INVESTIGATION OF THE ENTRAINMENT AND INFILTRATION RATES THROUGH AIR CURTAINS OF OPEN LOW-FRONT REFRIGERATED DISPLAY CABINETS

A Thesis Submitted for the Degree of Doctor of Philosophy

By

Ahmad Ali Al-Sahhaf

M. Sc.

School of Engineering and Design, Brunel University

January 2011

Abstract

The high energy demand associated with open multi-deck refrigerated display cabinets is a direct consequence of their open design. The interaction between the cold refrigerated air inside the cabinet and the relatively warm air of the supermarket takes place across the air curtain, which serves as a non-physical barrier between the customers and the products. It has been estimated that 70% to 80% of the cabinet's cooling load is due to ambient air infiltration into the cabinet refrigeration apparatus, which was previously entrained through the descending air curtain. A new generation of display cabinets has immerged in recent years, where the display-to-floor area has increased for the sake of maximizing sales. This modification leaves the air curtain with a larger display opening to seal against. Therefore, the design of such cabinets has now become more challenging, especially when attempting to ensure product integrity and temperature homogeneity while attempting to minimize their energy consumption.

In this work, advanced numerical and experimental techniques have been integrated to quantify and also minimize the entrainment rate through the air curtain and the infiltration rate into open low-front refrigerated display cabinets. Experimentally, the Particle Image Velocimetry (PIV) technique has been used to map the velocity profile along the air curtain while the Infrared (IR) Thermography technique has been used to map the temperature profile across the cabinet. The Computational Fluid Dynamics (CFD) technique has been used in both case and parametric studies after confirming its validation with experiment. CFD was found to be a valuable tool for the simulation of open low-front refrigerated display cabinets, and the credibility of the results was assured when the boundary conditions were fine-tuned by experimental data.

This thesis has demonstrated a systematic procedure where the entrainment rate through the air curtain can be quantified. The effect of various Discharge Air Grille (DAG) parameters was studied, and it was found that the entrainment rate is highly sensitive to the velocity profile and magnitude at the DAG. A velocity profile with a ramp shape having the maximum velocity near the cabinet yielded the minimum entrainment rate, hence the cabinet cooling load was reduced. In addition, two techniques were introduced for the determination of the infiltration rate of the cabinet. The first utilises the tracer-gas method to determine the specific amounts of ambient dry air and water vapour entering the evaporator coil, and the second uses psychrometrics to quantify the infiltration load as well as the other cooling load components by identifying the various heat transfer processes encountered during the operation of the cabinet. The ambient air infiltrated into the cabinet, although corresponds to 31% of the total mass flow rate, was found to be responsible for at least 85% of the total cooling load of the cabinet. This indicates that low-front cabinet suffer more from infiltration.

The contribution of this work is by providing a better understanding towards the entrainment and infiltration processes related to open refrigerated display cabinets. The new techniques introduced in this work can help designers to better assess the impact of different design parameters and quantify the amounts of the entrainment and infiltration rates associated with open low-front refrigerated display cabinets.

Dedication

To

My parents

Dr. Ali Al-Sahhaf and Fatima Al-Qattan

My wife

Fatima Al-Khamees

And my three beautiful children

Hawra, Jumanah, and Ali

Acknowledgement

I would like to convey my special thanks and sincere gratitude to the head of school of engineering and design, and my supervisor, Prof. Savvas Tassou for taking the time and effort to supervise this work. Not only did I learn from his expertise in the field, but also learned from him how to be an independent thinker; something I did not come with in the first place.

I would like to express my equally deep thanks to the deputy head of engineering and design, my second supervisor, Prof. Luiz Wrobel for his wisdom and uncompromised interest in the educational progress of students. His constant support and being there for me when the going got tough could not be more appreciated. And for that I am truly in debt.

Many thanks go to my new older brother, Dr. Abbas Hadawey. His friendship, encouragement, and support during those five tough years made all the difference. Thanks a million.

My friends back home and at Brunel University have made this journey more enjoyable, especially Dr. Yousif Al-Zelzelah, Mr. Mohammed Abbas, Mufeed Al-Shawaf, Ali Al-Rashood, Adel Al-Ruwaiyeh, P.C. George, Yaser Khalifa, Fuad Al-Khawaja, Ali Buabbas, Met'eb Altaf, Husain Madani, Abdul Rahman Ba Amir, Dr. Raed Bourisli, and many more.

I would like to thank my wife Fatima Al-Khamees (if I could) for her patience in taking care of our three beautiful children despite her health problem. And for that, I hope (I wish) I can make it up to her sometime in the remainder of my life. I would also like to extend a special thanks to my father and mother in-law, Mr. Jasem Al-Khamees and Sadeeka Al-Khalifa for their constant support.

Last and for most, I would like to thank my parents, Dr. Ali Al-Sahhaf and Fatima Al-Qattan, and my siblings for their support and encouragement over the years. I apologise for not being able to take good care of them during the past years, and hope they will forgive me for my selfishness and ignorance.

Table of Contents

Table of Figures

CHAPTER 1
Introduction

"You cannot teach a man anything;
you can only help him find it within himself"

(Galileo Galilei, 1564-1642)

1.1 Supermarkets

Supermarkets nowadays represent the main link between producers and consumers. Under one roof and in a friendly environment, consumers can easily manoeuvre between aisles, choosing from a large variety of products that make up nearly 90% of their needed commodities. The energy consumption of supermarkets is among the highest in the commercial sector, due to their high dependency on refrigeration, which places a burden on their overall operating efficiency. Moreover, the footprint of supermarkets on the environment is inevitably a large one, and the environmental consciousness that has risen in the past few years stimulated more research in an attempt to optimise their energy performance and reduce their impact on the environment.

1.2 Open refrigerated display cabinets

Supermarkets are heavily dependent on refrigeration, because food is basically perishable. The refrigeration systems serving all the refrigerated fixtures in a supermarket may account for between 30% and 70% of the electricity bill, and finding means to cut down the operating cost of refrigeration fixtures will result in higher profitability to the merchandiser. The refrigeration equipment found in supermarkets cover a wide range of temperatures to provide suitable storage and display environment for different food items. A typical supermarket features several combinations of equipment, including open and closed display cabinets, serve-over cabinets, and roll-in dairy cabinets to name a few. Vertical and horizontal display cabinets, both open and closed, are the backbone of the refrigerated-product aisles. Medium temperature, open, vertical, multi-deck, display cabinets can account for up

to 50% of the total refrigerated display cabinet line-ups. Although closed display cabinets are more efficient, open display cabinets are more appealing to the customer because the product is completely visible and easy to reach. However, due to their open design, the refrigeration load associated with them accounts for a large proportion of the energy bill. The total energy efficiency of such cabinets has gone through small incremental improvements over the past few years, but the pressure to design and manufacture more energy-efficient cabinets that permit displaying products at a lower running cost is increasing due to rising fuel prices. Many researchers and design engineers, in both academia and industry, are currently pursuing more efficient open display cabinet designs. In such a fiercely competitive industry such as the food retail sector, achieving even small enhancements will improve the profit margin of the merchandiser, not to mention maintaining more stable and homogeneous product temperatures leading to better product quality and longer shelf life. Improvements to the current design may be achieved by using better insulation and energy-efficient lights and fans. But these sources account for only around 10% of the total cooling load.

1.3 Air curtains and perforated back panels

The air curtain of open refrigerated multi-deck display cabinets is the main, yet most fragile, guardian against the influence of the surrounding environment. The amount of research that has recently been conducted to enhance its performance is justified by the fact that roughly 80% of the refrigeration load in such cabinets is a result of ambient air being entrained through the air curtain as it attempts to seal against the whole height of the display area. One of the main factors affecting the amount of ambient air entrainment through the air curtain is the shape of the velocity profile at the discharge air grille (DAG), which in turn, is a direct outcome of the geometrical shape of the cabinet design and air flow passages.

The majority of contemporary cabinet designs rely on a perforated duct situated at the back of the products from which cold air is directly ejected onto them. This flow, together with that of the air curtain, tend to “sandwich” the products with cold air, hence maintaining their temperature within prescribed limits. The optimum

distribution of air flow rate in the cabinet which is influenced by the cabinet design is still a matter of debate that exercises many researchers and manufactures.

1.4 Open, Low-front, multi-deck, refrigerated display cabinets

In order to maximize sales by increasing the display-to-floor area, a new design has recently emerged where the lower shelf (well tray) is further lowered. This design has become known as the low-front or low-deck open display cabinet, and attempting to lower its energy consumption constitutes a challenge to the design engineer, especially when the product temperature is to be maintained within acceptable limits. Since the air curtain on such cabinets has to seal against a larger display opening, its design to ensure product temperature integrity over a wide range of conditions and at minimum energy consumption has become more challenging.

1.5 Entrainment and infiltration

The interaction at the free boundary between the air curtain and the adjacent environment of the store has a major influence on the development of the flow in the air curtain. Among the various thermal loads on the open display cabinet (e.g. conduction through the cabinet walls, radiation from the store walls, the addition and removal of products, defrosting process, etc.), ambient air infiltration into the cabinet constitutes the largest energy loss. To minimize infiltration though, the turbulence action and hence mixing across the boundary must be minimized to preserve the momentum of the air curtain and its sealing ability against the ambient air. This calls for a thorough understanding of the structure and flow dynamics of the air curtain with the aim of quantifying the amount of ambient air entrained through it. To facilitate this, it is important to study the behaviour of the air curtain in isolation from the rest of the cabinet.

1.6 Research approach

The ability to predict the amount of entrained air through the air curtain and the portion that manages to infiltrate into the cabinet is vital to the analysis of the cabinet. Recent technological advances have made this task achievable through the use of numerical techniques such as Computational Fluid Dynamics (CFD). This technique has now reached a level of maturity and is capable of producing

quantitative rather than qualitative results. Moreover, recent rapid advances in sophisticated measuring devices have provided the accuracy needed to capture fine details in the flow of the air curtain. During the past decade, the Particle Image Velocimetry (PIV) technique has gained wide acceptance among researchers in the field. This non-intrusive technique can produce the air curtain velocity field with high accuracy if properly calibrated and synchronised. In addition, the Infrared (IR) thermography technique can be used to obtain the temperature field of the air curtain. In this work, the aforementioned numerical and experimental techniques have been used to analyze the entrainment and infiltration rates associated with air curtains of low-front refrigerated open display cabinets. Tecplot was used as a post-processing tool to analyze and present the data obtained from the CFD, PIV, and IR techniques.

1.7 Aims and objectives

The main aim of this work was to investigate the performance of low-front open refrigerated display cabinets using advanced techniques in order to identify, understand, and consequently optimize various design parameters affecting their temperature performance and energy consumption. The work included a number of sub-objectives as follows:

1. To modify an existing ordinary open multi-deck refrigerated display cabinet having a display height of 127 cm to arrive at a low-front design having an extended display height of 200 cm.
2. To employ advanced experimental techniques like PIV and IR thermography in the analysis of the airflow of open low-front display cabinets, and use their outputs to fine-tune and also validate the CFD modelling approach.
3. To identify design parameters of the DAG that can minimize the entrainment rate through the air curtain. This is done experimentally and numerically by isolating the functionality of the air curtain from the rest of the cabinet and allowing it to flow down a wall and solely interact with the ambient air through the entrainment process.
4. To develop new techniques for the determination of the infiltration rate into the cabinet and cooling load associated with it; the first employs the tracer-gas methodology during CFD simulations while the second utilises the well-established science of psychrometrics.

5. To test and optimize an existing low-front open display cabinet in order to meet the specifications set by the ISO standard.

1.8 Outline

This thesis is organized as follows:

Following this chapter, **Chapter 2** presents a review of previous work done on air curtains operating on open display cabinets, doors of cold stores, and doorways of buildings. The aim of including such a vast literature is to accommodate all findings affecting the functionality of the air curtain. In addition, the review covers the advanced methods used for the study of the thermo-fluid dynamics of open display cabinets over the past few years.

Chapter 3 illustrates, in a condensed form, many aspects dealt with during the experimental part of this work. This includes the test room utilised in controlling the environment, a modified cabinet representing a low-front design, together with the advanced measurement tools used to characterize the velocity and the temperature fields across the cabinet, namely, the PIV and the IR systems.

The basic CFD theory and the philosophy behind choosing different numerical algorithms used in this work are treated in **Chapter 4**. The various issues considered for pre-processing, solving, and post-processing the data are addressed. Boundary conditions together with turbulence, species, and radiation models used during the setup of the models are presented.

The validation process of the CFD results using the PIV and IR techniques is discussed in **Chapter 5**. A comparison is made between the numerical and experimental results, and conclusions are drawn as to the suitability of the CFD approach for the study of the entrainment rate through the air curtain.

Chapter 6 introduces a numerical method that can be applied to determine the entrainment rate through the air curtain. The effect of various DAG parameters on the entrainment rate is investigated, including the discharge velocity magnitude, velocity profile, turbulence intensity, and buoyancy effects.

Quantifying the amount of infiltrated air into the cabinet is the subject of **Chapter 7**. Two methods are introduced; the first is a numerical representation of the tracer-gas

method and the second utilises the science of psychrometrics in determining the cooling load due to infiltration together with the other components during cabinet operation.

Chapter 8 presents an optimization study performed on an existing open low-front display cabinet. Experimental results show that the cabinet could not perform in accordance with the ISO standard, and a validated three-dimensional CFD model was constructed and used for the optimization study.

Finally, summary, conclusions, and proposed future work related to the assessment and optimization of low-front open display cabinets are provided in **Chapter 9.**

CHAPTER 2
Background and Literature Review

"The true worth of every individual
is in what he does best"

(Imam Ali Bin Abi Talib, 598-661)

This chapter provides a comprehensive review of the literature for the most significant work done on air curtains so far, with emphasis on their role in open refrigerated display cabinets. After a brief introduction, a background for supermarkets in the food cold-chain and research done to minimize their energy consumption is presented. Then, the open display cabinet is presented and different aspects related to its design and operation are discussed. The operation of the air curtain is then presented in detail and the different parameters dictating its efficiency are considered.

2.1 Introduction

Air curtains of open refrigerated display cabinets act as non-physical barriers, virtually dividing the environment they operate in into sub-zones of two completely different thermal requirements: refrigerated and air-conditioned. Products stored in display cabinets are chilled or frozen at low temperatures in order to prevent them from rapid degradation and extend their shelf life. Thermal comfort of customers, on the other hand, necessitates maintaining the environment at acceptable temperature levels much higher than those required by products. Eventually, it is the role of air curtains to seal against the ambient air and minimize mixing between the refrigerated air enclosed within the cabinet and the conditioned air of the supermarket.

The effectiveness of air curtains has a paramount effect on the amount of cooling load required, and hence the energy consumed, by both the refrigeration and HVAC systems serving a supermarket. An inefficient air curtain allows the cold air in the cabinet to be spilled out and accumulate in the aisles, causing what is known as the "cold aisle effect". This phenomenon has a profound effect on the comfort level

experienced by customers and employees alike, and calls for other expensive measures to remedy the environment in the aisles. From another perspective, an inefficient air curtain allows the ambient air to intrude into the cabinet, adding both sensible and latent loads to it. Therefore, it is hardly surprising that the optimization of air curtains has gained considerable attention in recent years, especially in light of increasing energy prices. Moreover, maximizing sales pushed for the introduction of what has become known as “low-front” or “low-deck” open display cabinets, with the capability to accommodate larger quantities and varieties of products within the same store floor area. In such designs, the role of the air curtain has become more crucial due to the requirement to shield against a larger opening height.

2.2 The food cold-chain

The food cold-chain is the refrigeration process, by both chilling and freezing, required to preserve food products as they travel from the manufacturer to the consumer. This refrigeration process involves primary cooling at the manufacturing site, refrigeration during transportation, storage in cold rooms at the retailer site, refrigeration during retail display, and finally home storage by the consumer. Keeping the food products at a desired temperature throughout this chain is important in maintaining their safety, quality, and shelf life.

There is a direct relationship between the energy efficiency of the various refrigeration processes involved in the cold-chain and climate change. More efficient refrigeration systems and better understanding of each individual process along the cold chain will result in less weight loss, less energy use, prolonged shelf life, and better product quality. James and James (2010) stated that the cold-chain accounts for nearly 1% of all CO_2 production in the world. In addition, they estimated that 40% of all food requires refrigeration and 15% of the electricity consumed worldwide is used for refrigeration. Consequently, an effective and efficient cold-chain ensures delivering food with a better quality and shelf life.

2.3 Supermarkets and their energy consumption

Supermarkets, or as commonly known as “food retail stores” to specialists in the field, have become an integral part of modern societies, where consumers purchase nearly 90% of their foodstuffs from. The significant technological developments that

took place during the 1980's in the production and storage of foods caused an exponential increase in the number and variety of products, which encouraged the development of large supermarkets that could accommodate this large variety of products. In the UK alone, there are now over 6000 large supermarkets, approximately one for every 10,000 people, Baker and Shadow (2004), with an average sales area of 1400 m^2, Tassou (2006). Under one roof and a friendly environment, customers can conveniently manoeuvre from one section to another, choosing from over 100,000 products to purchase. Therefore, in today's fast pace life, shopping at supermarkets is a necessity rather than a luxury, offering time-efficiency to customers, where shopping time is on the average of 15 minutes, Purvis (2004).

Large supermarkets represent multi-million initial investment projects, and are responsible for 3% to 5% of the total energy consumption in developed countries, Tassou et al. (2007). The annual electrical energy consumed by supermarkets in the UK is estimated to be around 12 TWh, Tassou (2007), and the energy costs of running a typical supermarket for a year is about £150,000, as stated by Austin-Davies (2005). When compared to other buildings in the commercial sector, supermarkets are the largest users of energy, Walker and Baxter (2003), and with an estimated energy consumption of 1000 kWh/m^2, they consume two to six times more electrical energy per floor unit area than typical office buildings.

The thermal control of large supermarkets constitutes a real challenge for researchers and engineers. The store is a single wide open structure with high thermal loads distributed throughout the building, making them one of the most difficult single zones to be thermally controlled. Moreover, the enclosure of supermarkets constitutes a colony where diverse refrigeration and HVAC applications are brought together. The difficulty engineers find to control the environment within lies in the fact that it is hard to satisfy all stakeholders in this business. The merchandiser requires that the initial investment costs of the structure and equipment be as low as possible to achieve maximum profitability; the customer expects a well-organised and thermally acceptable environment to be in; the products need to be maintained at a predetermined temperature to avoid spoilage; and above all, standards and regulations require the whole process to be efficient and environmentally friendly.

The primary function of supermarkets, however, is to make a profit selling products. This is largely achieved by providing refrigeration to foods in the most attractive and economical way possible, and also assure that their temperature is safely maintained. Subsequently, the next task is to create a suitable environment where customers and products can coexist.

Supermarkets are heavily dependent on refrigeration, because food is basically perishable. The refrigeration and HVAC systems operating in supermarkets can account for about 50% and 10% of the electrical load, respectively, Kosar and Dumitrescu (2005). As for the refrigeration system, the compressors and condensers account for 30% to 35% of the total energy consumption, Walker and Baxter (2003), and the remainder is consumed by fans, display cabinet lighting, defrost heaters, and anti-sweat heaters.

From the above, a conclusion may be drawn that there is a tremendous potential for energy conservation in the supermarket industry. This justifies the considerable amount of research undertaken so far to cut the operating costs particularly those attributable to refrigeration.

2.4 Open refrigerated display cabinets

The need for alternative methods to display products began in the 1960s, when new refrigerated and frozen products started to appear. This sudden proliferation may be attributed to the dramatic enhancements in food technology and preservation of products, and the pursuit of more convenient life styles. In response to this, retailers of existing stores were obligated to find other alternatives to increase food display area. Moreover, since customers can now manoeuvre through the products and choose what they need, refrigerated and frozen products have to be displayed as clearly as possible and in the most attractive way and still preserve their low temperature. The result of this was the introduction of the open refrigerated display cabinet.

Display cabinets add to the customer's convenience and enhance the sales appeal of the product. On the merchandizing side, more sales and higher display-to-floor area ratio is desirable. Although closed display cabinets (with glass doors) are more energy efficient, open display cabinets are more appealing to the customer because

the food is more visible and easy to reach. There are well over a million refrigerated display cabinets currently in use in the UK alone (The Enhanced Capital Allowance Scheme, 2004).

The standard vertical and horizontal display cabinets have remained largely unchanged since they were introduced about fifty years ago, and their design is very much a compromise between the criteria set by the merchandiser and the energy-efficient design desired by the engineer. Merchandizing is defined as the displaying of products in an attractive manner that will encourage customers to purchase the products. This very definition is what often leads to conflict between the refrigeration engineer and the merchandiser. It has been mentioned previously that approximately 50% of a supermarket's energy bill is accounted for by refrigeration. In this regard, the general rule is that the best merchandising displays consume the most energy. For example, an open display cabinet consumes almost twice the amount of electricity as the same cabinet with doors. Nevertheless, the commercial benefits gained by using such open designs encourage designers and owners of refrigerated retail equipment to justify the additional cost of energy to run the equipment.

The total energy efficiency of open display cabinets has also gone through small improvements over the years. Many researchers and design engineers, in both academia and industry, are continuously pursuing better performance of such fixtures due to their high energy burden on the retail food industry. The energy consumption of cabinets form the same category may span across a very large range, with differences reaching up to 5- and 6-fold in chilled and frozen food retail cabinets, respectively (Evans et al. 2007). Therefore, a considerable amount of energy can be saved by simply replacing inefficient cabinets with more efficient ones. In such a fiercely competitive industry, achieving even the slightest enhancement in the cabinet design will improve the profit margin of the merchandiser, not to mention maintaining more stable product temperatures.

2.5 Types of open display cabinets

Refrigerated display cabinets can be classified by their purpose, geometry, design temperature, etc. The most common criteria however are the cabinet geometry and design temperature. There are two main types of open refrigerated display cabinets

that are in regular use in supermarkets today. The most common for medium temperature applications is the vertical multi-deck design shown in Figure 2.1.

Figure 2.1 A typical vertical multi-deck display cabinet

This design has become popular among merchandisers due to its large display-to-floor area ratio and ease of access for customers. The principle of operation can best be explained with reference to Figure 2.2. Air is forced over an evaporator by means of propeller fans located in the base of the cabinet. The cooled air then passes up into the back panel, which is perforated, allowing air to diffuse over the products. The remainder of the air then passes into the canopy and is discharged downwards from the discharge air grille (DAG) over the front of the products forming an air curtain. Air is then drawn back into the cabinet at the return air grille (RAG) located at the front of the base unit. The advantage of the air curtain is that a shield is formed to keep the warm ambient air out of the cabinet whilst still allowing a warm hand to penetrate it. The main disadvantage however, is that when this moving stream of air passes through the relatively still air of the environment, some of the ambient air will be entrained. The two streams of air will then mix, resulting in a mixture of cold and warm humid air, which is then infiltrated into the cabinet through the RAG. This adds an energy load to the evaporator, not only in the form of additional sensible

cooling, but also in defrost load as the humid air condenses on the evaporator coil and freezes.

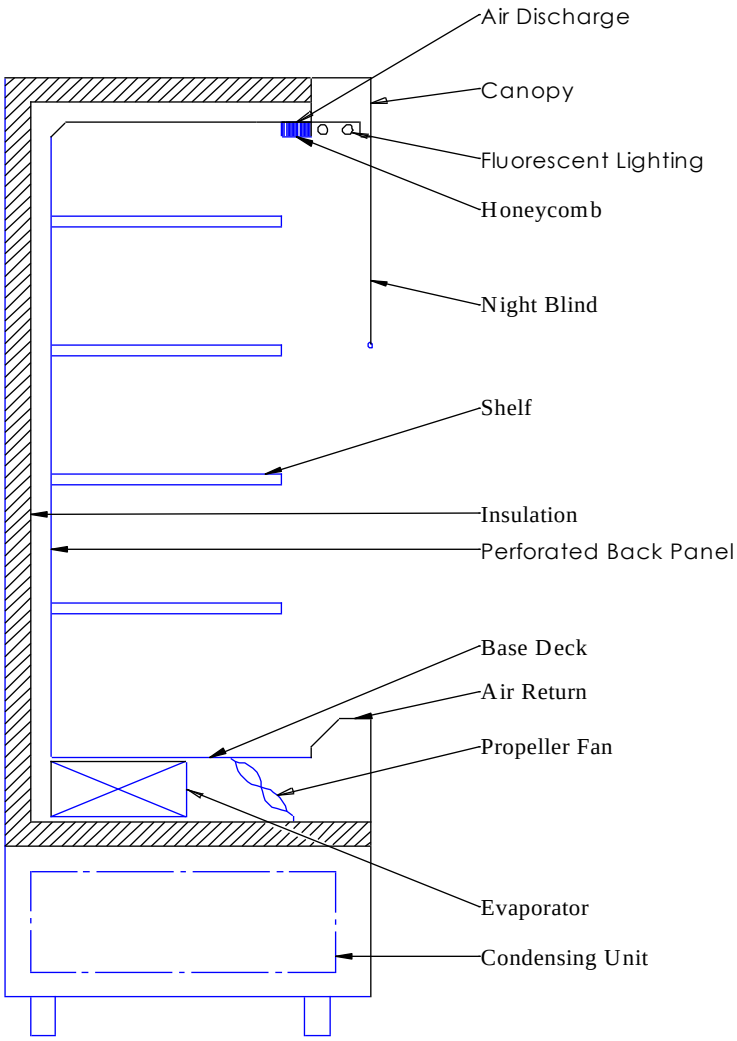

Figure 2.2 Cross section through a vertical multi-deck open display cabinet

The oldest design of a refrigerated cabinet is the horizontal well type, as shown in Figure 2.3. This is essentially a vertical cabinet laid on its back. The products are stacked in the cabinet up to the load line and a horizontal air curtain flows across the top. Since the display opening is oriented upwards, the cold refrigerated air gets stratified within the cabinet, hence spillage is minimised. Therefore, this design is more efficient when compared with the vertical cabinet. This type of cabinets has been traditionally used for the display of frozen food. However, vertical multi-deck cabinets have been increasingly used because of their better sales appeal.

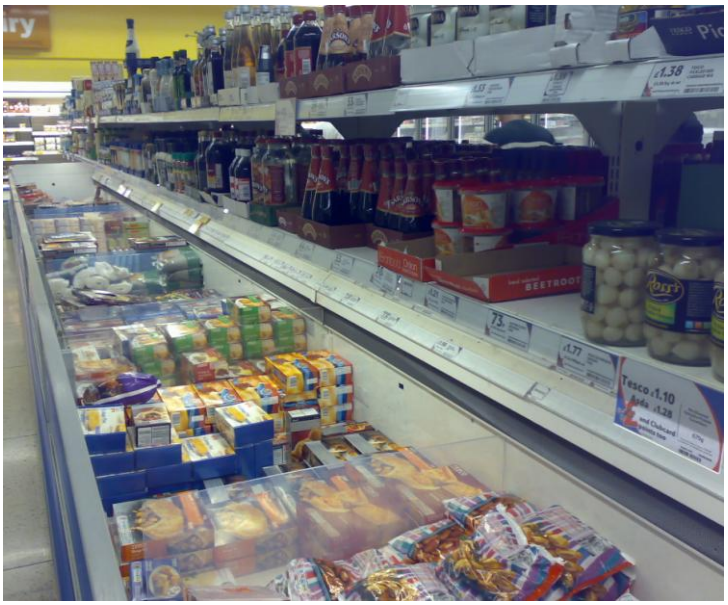

Figure 2.3 Horizontal (well) type cabinet

2.6 Air flow uniformity and temperature homogeneity

Achieving temperature homogeneity within the cabinet is highly crucial during operation, which is directly governed by the air flow pattern created by the air curtain and the perforated back panel. To emphasize the role of temperature homogeneity, within the usual temperature range for chilled meat (-1.5 ^{o}C to 5 ^{o}C), the microbiological growth rate can be as high as eightfold between the upper and lower temperatures (James and James (2010)). The heat stored in displayed products is primarily removed by convection (both free and forced). Consequently, to achieve optimum refrigeration of the products and prevent stagnation of thermal zones in the cabinet, the air flow must be uniform as much as possible. Moreover, cabinets with unwrapped products such as meats and cakes must have relatively low air flow velocities to minimize weight loss as much as possible and prevent them from drying out very quickly. Hadawey et al. (2005) studied the heat and mass transfer of fillings used in unwrapped sandwiches placed in open display cabinets to evaluate their display shelf life and dehydration rate, and concluded that the air velocity has a substantial effect on the drying rate.

From another perspective, having a uniform airflow across the whole span of the evaporator coil is necessary since it allows frost to form evenly throughout the evaporator. This delays the need for defrosting and minimises deterioration of heat

transfer due to frost build-up. In addition, the air mass flow rate determines the size and cost of the fans and hence the power consumption of the fan motors. Therefore, optimum airflow will lead to an efficient and economical unit. The forced air forming the air curtain acts as a non-physical barrier against the environment of the supermarket and aids in preserving acceptable thermal conditions within the displayed enclosure. From the above, it is clear that the airflow pattern is as important as the supplied air temperature in open display cabinets.

2.7 Cooling load components of open display cabinets

The flow of heat into and out of a display cabinet was expressed in detail by Howell (1993, a), and is represented by the equation:

$$\dot{Q}_{cab} = \dot{Q}_{walls} + \dot{Q}_{rad} + \dot{Q}_{sens} + \dot{Q}_{lat} + \frac{de}{dt} + \dot{Q}_{lights} + \dot{Q}_{ASW} + \dot{Q}_{def} \qquad (2.1)$$

Where $\dot{Q}_{cab}$ is the refrigeration or evaporator load on the cabinet, $\dot{Q}_{walls}$ is the heat transfer through the cabinet walls because of the temperature difference between the store and the cabinet, $\dot{Q}_{rad}$ is the radiant heat transfer to the cabinet, $\dot{Q}_{sens}$ is the sensible heat transfer by infiltration of ambient air into the cabinet through the air curtain, $\dot{Q}_{lat}$ is the latent heat transfer by infiltration of ambient air into the cabinet through the air curtain, de/dt is the energy change in the display cabinet due to restocking with products at an initially different temperature than the cabinet itself, $\dot{Q}_{lights}$ is the cabinet lighting load, $\dot{Q}_{ASW}$ is the cabinet anti-sweat heater load, and $\dot{Q}_{def}$ is the cabinet defrost energy load. Of all of the heat loads on a refrigerated display cabinet, only the term de/dt cannot be changed through the design process since the product must be replenished as it is purchased. The term $\dot{Q}_{walls}$ is also subject to limitations in the design of the cabinet, as the thickness of the insulation must be optimised against its capital cost. The terms $\dot{Q}_{lights}$ and $\dot{Q}_{rad}$ can be changed through design by moving or eliminating the lights which will affect both terms, or by changing the type of heating in the store for example, affecting the radiant element. The four terms $\dot{Q}_{sens}$, $\dot{Q}_{lat}$, $\dot{Q}_{ASW}$ and $\dot{Q}_{def}$ are related to ambient air

infiltration through the curtain. The only additional load which may be added to this equation is the heat dissipation from the fans.

A more detailed breakdown of the cabinet's cooling load is presented in Faramarzi (1999), where formulae used in the calculation of the various constituents of the cooling load are provided.

2.8 Energy consumption of open display cabinets

Open display cabinets account for up to 70% of the total refrigerated display cabinet line-ups in a supermarket. High operating costs for such fixtures have been historically reported to the extent that any product left in the cabinet for more than a few days is sold at a loss. This high operating cost is due to their open design, making infiltration the major contributor to the total cooling load, which may account for up to 80% of the total value. It is estimated that the refrigeration cost for frozen food open display cabinets is approximately twice that of the same cabinet with glass doors installed. Although replacing the air curtain with physical doors is not desired by both the merchandiser and the customer, this certainly constitutes an appealing step for the design engineer. Energy losses can be reduced by containing the chilled air flow within the cabinet either by the use of glass doors (Figure 2.4) or strips of clear plastic (Figure 2.5). Although these methods are effective, some merchandisers are reluctant to install them as they place a barrier between the product and the customer.

Figure 2.4 Closed (door) display cabinet

Faramarzi et al. (2002) explored the impact of retrofitting an existing open medium temperature display cabinet by installing conventional glass doors in place of the air curtain. The retrofitting reduced infiltration (convection) by nearly 80% (some infiltration was associated with the opening and closing action of the doors), radiation by 94%, while conduction through the body of the cabinet remained almost the same. This caused the total cooling load to decrease by 68%, refrigerant mass flow rate by 71% and as a result compressor power demand by 87%. The reduction in total cooling load was a result of reducing the sensible load by 59% and latent load by 90%. It also resulted in a reduction in product average temperature of 3.3 ^{o}C.

Figure 2.5 Clear plastic strips

2.9 Influence of supermarket environment on open display cabinets

The humidity level within a supermarket has a direct effect on the energy consumption of open display cabinets. The major source of moisture in supermarkets is the fresh outdoor air introduced, which is required to provide proper ventilation. Another source of moisture is the breathing and perspiration of customers and employees. In most supermarkets in the UK, humidity is not controlled but is allowed to float depending on ambient and store conditions. In general, humidity levels are in the range of 45% to 55% in the summer and lower in the winter (Tassou and Datta (1999)), and are usually homogeneous in the entire store. Orphelin and Marchio (1997) developed a global simulation method capable of coupling the energy requirements of both the HVAC and refrigerated cabinets. According to Orphelin, Marchio, and Bech (1997), the optimum relative humidity level proposed by their work was in the range of 45%. Attempting to achieve lower levels places a burden on the HVAC system, while allowing higher levels to take place overloads the refrigeration systems by increasing the rate of defrosting and re-cooling. Since the refrigeration system of display cabinets is less efficient in removing this moisture than the store air conditioning system, the overall energy consumption and demand of the cabinets will increase. Howell (1993, a and 1993, b) developed a procedure

that relates the relative humidity in supermarkets to the energy performance of open display cabinets. His results showed that reducing the relative humidity of the supermarket from 55% to 35% reduced the energy requirement of open display cabinets by 30%, defrost energy by 60% and anti-sweat heater operation by 70%, but increased the air conditioning energy requirements of the supermarket by 8%. High supermarket moisture levels can also result in food spoilage, condensation on display cabinets which demands more anti-sweat operation, frost build-up on products causing paper containers to deteriorate and label colouring to fade, and, in extreme conditions, damage to the refrigeration equipment.

Many studies have been conducted with the intension to remove excess moisture before it enters the store and becomes a load on the HVAC system and refrigerated cabinets. As early as the 1980's, Whitehead (1985) showed that using a separate dehumidification coil to treat outdoor air is more efficient than relying on the store's conventional HVAC system to handle it. The use of desiccant-based air conditioning systems to control humidity has been examined by many researchers and is justified over standard vapour-compression equipment whenever inexpensive (non-electric) energy is available for the regeneration of the desiccant materials. Macdonald (1983) studied the feasibility of utilising condenser heat from refrigeration systems to preheat the air used for desiccant regeneration and found that it enhances the efficiency of such application. Other researchers like Hill and Lau (1993) studied the performance of the store's air conditioning system when equipped with heat pipe heat exchangers and concluded that applying such technique to single-path air conditioning designs was effective in maintaining low indoor dew-point settings.

Although the effect of thermal radiation on product temperature has been ignored by many researchers in the field, it has a negative effect on both the temperature (and hence the integrity) of the products and the cooling load of the cabinet. Under nominal conditions, Orphelin and Marchio (1997) determined that the share of radiation on the cooling load of vertical multi-shelf and horizontal single shelf cabinets is approximately 7% and 37%, respectively. From another perspective, radiation has a very significant effect on weight loss of unwrapped products. The incident radiation heats up the surface of the products causing the stored moisture to evaporate. This in turn causes surface drying, leading to reduction of their

commercial value, Maidment et al. (1998). Nesvadba (1985) conducted an experimental study on the effect of product emissivity on the radiation heat transfer of products in refrigerated display cabinets. He concluded that the surfaces of chilled and frozen food products in cabinets have high emissivities in the range of 0.9, and radiation represents a significant part of the heat flux incident on the products' top layer and cannot be ignored. In addition, it was suggested that using metallic materials for wrapping products reduced the emissivity value to 0.2.

2.10 Environmental impact of open display cabinet

From an environmental standpoint, the effect of open display cabinets are twofold, pollution of the environment resulting from energy use, and usage of materials in their construction. Watkins et al. (2004, 2005) performed a life cycle assessment on open display cabinets and found that 93% of the environmental impact was associated with the energy use during the operation of the cabinet and only 6% was attributable to the materials used in construction. This suggests that lowering the environmental impact of display cabinets can be done through enhancing their efficiency to reduce their energy consumption during operation.

2.11 Air curtain of open display cabinets

The air curtain of open display cabinets is an incompressible turbulent plane jet of air, projected from a linear slot (or slots), which has sufficient momentum to reduce, or even prevent, transverse (or free) air flow from crossing it. The momentum created by the air curtain provides a virtual and non-physical barrier against heat and moisture, while facilitating unhindered access of customer's hands.

Open display cabinets utilise recirculating type air curtains where a jet of air is forced across the display opening, and a return air grille on the opposite side collects most of it and directs it back to the discharge air grille via the perforated back panel. This ensures that most of the previously treated air is drawn back to the evaporator, hence minimising energy loss. According to Johnson (1998), the efficiency of this type of air curtains is in the range of 90% to 95%, when compared to the efficiency of non-recirculating air curtains commonly used in doorways of many buildings, which have an efficiency of 60% to 80%. Hetsroni, Hall, and Dhanak (1963) and Hetsroni and Hall (1964) performed an early theoretical and experimental analysis of

the mechanism of heat transfer through this type of air curtains. The return air grille is placed about half a metre high from the floor to prevent dirt/particles from being drawn into the cabinet. Due to their vital role in the food retail sector, the amount of research done on them has dramatically increased during the past decade.

The performance of the air curtain operating on open display cabinets is dependent on many design parameters, as shown in Figure 2.6. Those are the 1) Discharge air velocity, 2) Discharge velocity profile, 3) Air curtain slot width, 4) Discharge angle, 5) Discharge air temperature, 6) Initial turbulence intensity, 7) Pressure differences on both sides of the air curtain (wind and stack effect), 8) Temperature differences on both sides of the air curtain (isothermal and non-isothermal cases), 9) Humidity ratio on both sides of the air curtain, 10) Height of the air curtain, 11) Offset distance between the DAG and the RAG, and 12) the width of the RAG.

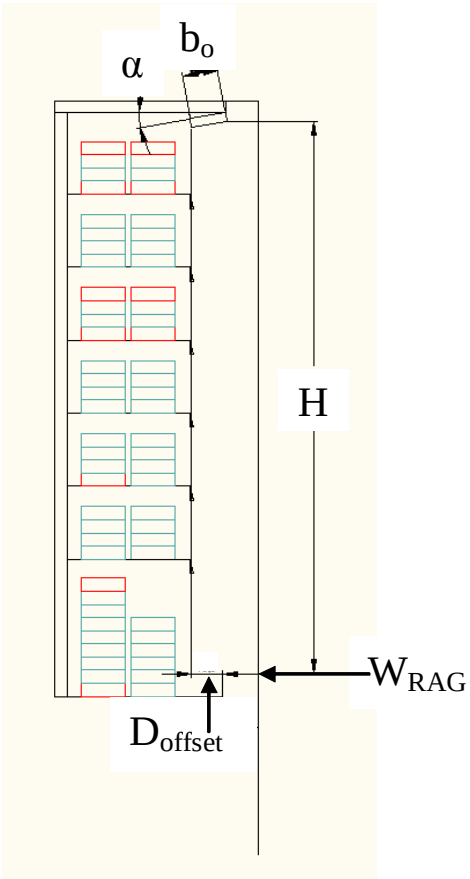

Figure 2.6 Physical parameters affecting the flow of the air curtain

An optimum air curtain is one that can seal the whole span of the opening it is attempting to protect with the least discharge velocity. Achieving optimum design

characteristics leads to minimal heat and mass transfer across the air curtain and assures complete coverage of the opening, which is the ultimate objective of an air curtain. Hayes and Stoecker (1969, a) developed mathematical models based on the mass, momentum and energy balance equations, to predict the rate of heat transfer and airflow across thin, high velocity, non-recirculating type air curtains subjected to temperature and pressure differences. The main contribution of their work lies in formulating a relationship between the temperature difference across the air curtain and the minimum momentum required to withstand this force and guarantee contact with the ground. The so-called "deflection modulus" was introduced as a dimensionless group that gives a measure of the sealing ability of the air curtain against transverse pressure forces. According to the aforementioned work, the most important parameters are the discharge air velocity, the air curtain slot width, and the discharge angle. By selecting two of those parameters, the third can be determined using plotted equations that represent the flow of the air curtain.

The second paper by Hayes and Stoecker (1969, b) was intended to be a guideline for design and installation of non-recirculating type air curtains installed at the opening of sealed enclosures. With the data provided, the heating or cooling load could be calculated once the slot width and discharge velocity were established. It was found that the axis of the jet deflection and the trajectory depends upon the nozzle discharge angle and whether air is taken from inside or outside the enclosure. Inclining the air curtain 30^{o} toward the warm side was found to provide a slightly more stable curtain than for a discharge angle of 15^{o}, but too large discharge angles may direct the jet out away from the door sides hence permitting leakage at those locations.

Howell, Van, and Smith (1976) numerically and experimentally investigated the heat and moisture transfer through turbulent recirculated air curtains. The total heat transfer across the air curtain was found to be directly proportional to the initial jet velocity and temperature difference across the air curtain. At a given initial velocity and temperature difference, the initial turbulence intensity was found to have a noticeable effect on the amount of heat and moisture transfer through the air curtain, especially in the range from 0% to 7%. However, this influence was found to diminish as the turbulence intensity was increased above 8%. Van and Howell (1976)

also reported that the length of the initial region of the air curtain as well as the turbulent mixing associated with it are strongly depended on the initial turbulence intensity of the jet. Howell and Shibata (1980) studied the relationship between the heat transferred through recirculating air curtains and the deflection modulus associated with them. The rate of heat transfer across the air curtain was found to be strongly affected by the initial turbulence intensity as well as the length of the air curtain. In addition, the heat transferred was found to be directly proportional to the initial jet velocity and the temperature difference across the air curtain. The experimental investigation revealed that for every air curtain configuration, there exists an optimum flow velocity associated with a minimum value of deflection modulus, which ensures minimum heat transfer across it. Later studies by Howell (1993, a and b) were dedicated to the effect of the relative humidity of the store environment on the performance of open display cabinets. He found that the air curtain's initial velocity and slot width are the most important parameters influencing the efficiency of the cabinet.

Costa et al. (2006) numerically studied the sealing efficiency of air curtains installed between two rooms of different ambient conditions. They concluded that air curtains working close to optimum deflection modulus values for summer and winter conditions provide energy savings up to 80%. In addition, a jet discharge angle of 15^{o}-20^{o} from the vertical oriented outdoors improved the sealing efficiency of the air curtain to about 70%. Pappas and Tassou (2003) numerically and experimentally studied different parameters affecting the performance of doorway air curtains functioning in air conditioned spaces. Their results show that if the air curtain jet has a sufficiently high velocity that ensures its contact with the floor, a 90 % reduction in air exchange between the two sides can be achieved. Lawton and Howell (1995) conducted an experimental study on the feasibility of installing air curtain devices on doorways of retail stores. They found that thicker jets with lower air velocities generate less energy transfer across the sides of the air curtain.

Based on the finite difference method, Ge and Tassou (2001) presented a comprehensive model capable of predicting and optimising the performance of air curtains of vertical multi-deck display cabinets. The total heat transfer across the air curtain was found to be linear with the difference between the jet temperature and the

controlled environment temperature. It was also found that the return air temperature increases as the curtain height was increased.

In open display cabinets, having an air curtain operating at optimal initial velocity is critical to the efficiency of the air curtain. Low discharge velocities result in a weak air curtain that is not capable of preventing ambient air from intruding the cabinet environment. Excessive velocity magnitudes at the DAG will produce high entrainment rates of the ambient air due to increased shear in an almost linear manner. According to the research conducted by Navaz et al. (2006), the discharge velocity can be characterized by the Reynolds number (based on the width of the DAG). They found that a Reynolds number in the order of 3,400 yielded optimum velocity magnitudes, claiming that this value delays the development of turbulence along the air curtain, yet has enough momentum to prevent premature spreading of the air curtain before it reaches the RAG.

Field and Loth (2004) studied the flow of air jets along walls using Particle Image Velocimetry (PIV) to investigate the dependence of their growth and velocity field on the discharge Reynolds number. Navaz et al. (2002) used PIV coupled with the CFD technique to investigate the effect of the air curtain velocity and temperature difference on the entrained air in open display cabinets. The experimental results from this approach were used to calibrate the CFD modelling of an open display cabinet.

Most air curtains have a single jet (single band) to deliver the air. This design is widely used in many applications due to its simplicity and low initial cost. When higher efficiency is required, air curtains are built by having multiple slots associated with different ducts, each having its own thermo-fluid conditions. In his PhD thesis, Stribling (1997) studied the effect of having double air curtains on the heat and moisture exchange in air curtains of medium temperature open display cabinets and found that incorporating a second outer air curtain with a lower velocity and higher temperature resulted in significant energy savings. Cortella et al. (2002) developed a 2D dynamic finite element model to analyse velocity and temperature distributions in vertical multi-deck open display cabinets having two air curtains. The main objective of their work was to reduce the external air infiltration and hence, energy

consumption of the cabinet. For frozen foods open display cabinets a more efficient design is necessary. D'agaro et al. (2006) studied the effect of having three air curtains on the performance of such cabinets and found that the third (outer) curtain being maintained at ambient temperature was necessary to reinforce the jet inertia and reduce the cold aisle effect in the store aisles. The drawback of this design however is the added cost and complexity during manufacturing.

2.12 Perforated back panel

A common feature of open vertical refrigerated display cabinets is the presence of a duct at the back of the shelves with many perforations delivering cold air from the evaporator directly to the products. This component is often called the perforated back panel, and plays an important role in the overall air distribution, and hence temperature homogeneity, within the cabinet. Delivering the optimum amount of air through the perforated back panel is critical, since it not only cools the products, but also serves as a cushion for the descending air curtain, and facilitates its flow by pushing it away from the shelves. The distribution of the perforations on the back panel can play a role in the air flow distribution and temperature homogeneity within the cabinet. The air leaving the perforated back panel does not have a constant discharge angle, but varies along the length of the back panel due to change in static pressure, as was found by El Moueddeb et al. (1997, parts 1 and 2) who numerically predicted the air flow in perforated ventilation ducts and validated their results against experiment. An experimental study by Gray et al. (2007) suggests allocating more perforations at the sides of the back panel in order to account for the arrangement of the supply air fans and the cooling coil.

2.13 The effect of placing front upstand

A modification to the design of the cabinet in order to minimise cold air spillage is to place a short barrier, commonly known as the front upstand, on the outer edge of the RAG, as seen in Figure 2.7. The base shelf of the cabinet can now be thought of as a well where cold air is collected. Moreover, introducing an upstand reduces the display opening without sacrificing customer access, and the air curtain has to seal against a shorter opening height. This in turn results in minimising mixing and hence heat transfer, leading to enhancement in air curtain efficiency. Stribling (1997)

carried out an analysis on the effect of using upstands and found that they can reduce the sensible refrigeration load up to 15%. It is worth mentioning that utilising an upstand to the cabinet does not completely prevent spillage, since the mass balance of air across the fans necessitates that the same amount of entrained ambient air into the air curtain must be overspilled.

Figure 2.7 Front upstand

2.14 Summary

This chapter provided a background to the many parameters affecting the performance of open display cabinets and the efficiency of air curtains protecting them. To date, no work in the open literature has been devoted to the study of the performance of air curtains in low-front cabinets. The air curtain in such designs is attempting to seal against a larger height, and more work must be done to understand the way it interacts with the environment and entrains ambient air. The following chapter presents the use of advanced experimental methods for the study of the air flow of air curtains serving low-front cabinets.

CHAPTER 3
Experimental Facility

"One must learn by doing the thing,
for though you think you know it,
you have no certainty until you try"

(Sophocles, 400 B.C.)

This chapter presents the test facility and experimental setup employed during the course of this project, and is subdivided into five main sections. The first section provides a summary of the ISO standard test procedure that was followed during the testing and assessment of the display cabinets under consideration. The second section is a brief description of the test room where controlled conditions were established for the tests. The third section presents the modification done on an ordinary open multi-deck refrigerated display cabinet to arrive at a low-front design having a large display height of 200 cm. The forth section discusses the advanced techniques used in this work to map the velocity and temperature fields across the air curtain, namely the Particle Image Velocimetry (PIV) and Infrared (IR) thermography techniques. The fifth section presents test results and discussion.

3.1 Introduction

The need for a controlled environment to test open refrigerated display cabinets stems from the fact that their performance must be assessed and classified based on unified testing conditions that can eventually be compared against a benchmark. In reality, however, display cabinets operate in the unpredictable environment of supermarkets and other retail food stores. Therefore, it is practically impossible to reproduce the many random ambient conditions experienced therein. The fluctuation of external temperature and humidity levels and also different HVAC set points, the irregular stacking pattern of products, and the warm hands penetrating the cabinet's air curtain, are all random events, among others, which cannot be taken into consideration in a single study. Therefore, in order to carry out work on the open

display cabinets and the air curtains associated with them, a test room was utilised to create and maintain a controlled environment around them. This allows for verification and comparison of results against those obtained by other researchers in the field, as well as validation of numerical results obtained from numerical techniques. More importantly, the boundary conditions assigned to the CFD simulations that were obtained from such controlled experiments develop a level of confidence in the numerical results obtained.

There has been a tremendous effort to unify the testing procedure of open display cabinets through what has now become the ISO standard test conditions. By utilising the test room, the specified thermal and flow conditions can be created to serve as a benchmark for testing the cabinets.

Advanced measurement techniques for the acquisition of velocity and temperature are becoming more popular as their prices are justified by the enormous advantages gained when used. The PIV technique used in this work, for example, provides a window of two-component velocity vectors rather than a velocity magnitude reading at a single point offered by a hot-wire anemometer. Moreover, the infrared thermography technique used to determine the temperature profile across the air curtain is considered a whole-field method allowing for the determination of the temperature in a one go.

3.2 ISO test standard

All the experiments in this work were carried out in accordance with the testing conditions laid down in the ISO (the International Organization for Standardization) standard: Refrigerated display cabinets- parts 23953-1:2005 (Vocabulary) and 23953-2:2005 (Classification, requirements, and test conditions). Part 2 is of particular relevance to this work because it is mainly concerned with the requirements for the construction, characteristics, and performance of refrigerated display cabinets used in the sale and display of foodstuffs. The following is a summary of the requirements that were complied with throughout the testing procedure in this work.

3.2.1 Test room thermal and air flow characteristics

During testing, a cross-flow parallel to the plane of the cabinet's display opening and to the longitudinal axis must be provided, as shown in Figure 3.1. With the cabinet switched off, the air velocity at the three points along the line shown in the figure must be 0.2 m/s.

The ambient temperature and relative humidity must be taken at a point midway along the length of the cabinet. At this cross section, the point must have a horizontal distance of 30 cm away from the canopy and a vertical distance of 15 cm higher than the Discharge Air Grille (DAG), as shown in Figure 3.2. For the testing of medium temperature cabinets, the temperature and relative humidity in the test room is usually in accordance with test room standard climate Class 3, which requires the temperature and relative humidity to be maintained at 25 ^{o}C and 60%, respectively. As will be explained shortly, the cabinet in this work was modified to yield a larger display area, which increased the load on the refrigeration system. For this reason, Class 0 was chosen for testing the cabinet, which specifies the temperature and relative humidity to be 20 ^{o}C and 50%, respectively. Table 3.1 shows the thermal requirements of climate classes 0 and 3, respectively.

Table 3.1 Climate requirements for testing the cabinet

	Class 0	Class 3
Temperature (^{o}C)	20 ±1	25 ±1
Relative Humidity (%)	50 ±5	60 ±3
Dew Point (^{o}C)	9.3	16.7
Humidity Ratio (kg/kg$_{da}$)	0.0073	0.012

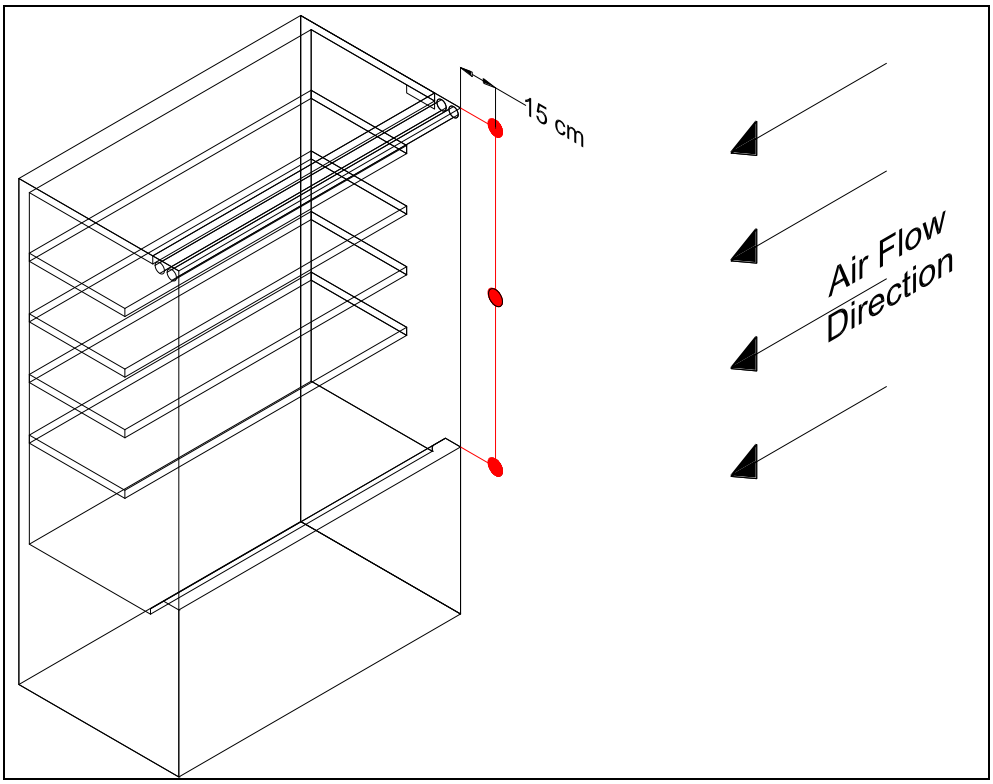

Figure 3.1 Air velocity measuring points

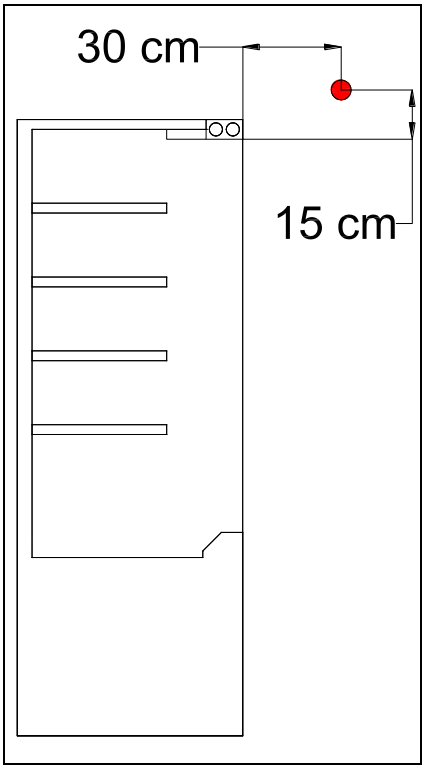

Figure 3.2 Climate measuring point

3.2.2 Cabinet positioning within the test room

The cabinet was located in the test room as shown in Figure 3.3. Table 3.2 gives the minimum required distances from the cabinet to the walls of the test room as required by the ISO standard.

Table 3.2 Cabinet location within test room

X	= 2 m
Y	≥ 1.5 m
A	≥ 0.8 m
B	≥ 1 m
C	≥ height of cabinet + 0.5 m

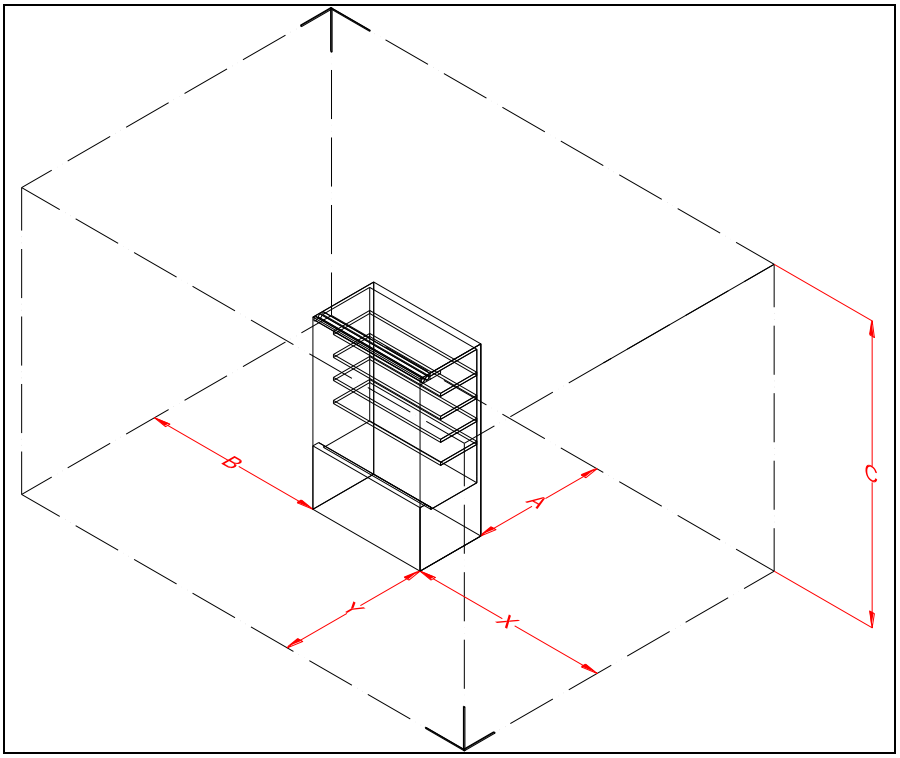

Figure 3.3 Display cabinet location within test room

3.3 Test room and air handling unit

The test room used in this study is a custom-built self-contained room positioned within the Refrigeration Laboratory at Brunel University, and is served by an air-handling unit, capable of creating and maintaining various test conditions as required by the ISO test standard. Figure 3.4 shows a photograph of the arrangement.

Figure 3.4 General arrangement of the test room and the air handling unit

The test room's overall internal dimensions are 7 m long, 3.5 m wide and 3 m high. The ceiling and walls are constructed from 10 cm thick modular cold room panels. The internal finish of the panels is made with good quality white steel sheeting, with an emissivity in the range of 0.9 to 1.0 to maintain adiabatic conditions. The walls and ceiling are insulated by 7.5 cm high-density expanded polystyrene sheets having thermal conductivity of 0.03 W/m.K, while the floor is made of concrete. A 2 m wide sliding door is positioned on one of the long sides of the room and a double glazed window is also positioned on the same side to allow for visual inspection without the need for interrupting test procedures.

To account for cross-flow, the opposite ends are partitioned off to create discharge and return air plenums, leaving a clearance of 5 m for the test area. The discharge air plenum wall (referred to as the discharge technical side wall in the ISO standard) is constructed from a bank of opposed blade dampers, allowing the velocity profile across the chamber to be adjusted as required. The return air plenum wall (referred to as the return technical side wall in the ISO standard) is constructed from panel filters, which create a pressure drop and hence a uniform face velocity can be achieved.

Figure 3.5 shows the supply and return air plenum walls, which were designed to create an even, horizontal air flow within the test room.

(a) Supply wall **(b) Return wall**

Figure 3.5 Supply and return air plenum walls

During test periods, lighting is provided by means of two 6-foot twin fluorescent tube lights fixed to the ceiling and giving a lighting level of 500 lx measured one metre above the floor (Stribling, 1997).

The climate in the test room is maintained by means of an air handling unit positioned on a purpose built support and located on the roof of the structure. The unit comprises a mixing box, a filter, a chilled-water cooling coil, an electric heater battery, a humidifier housing, and a centrifugal fan.

The cooling coil of the air handling unit is supplied with chilled water from a 9.9 kW chiller. The compressor is semi-hermetic and the evaporator is of the shell and tube configuration. A pump located within the chiller housing circulates chilled water around the cooling coil. The water flow through the coil is regulated by means of a three-port motorized diverting valve.

A robot available in the test room was used during PIV measurements in order to maintain a constant distance between the camera and the laser sheet and avoid frequent calibration of the PIV system. This robot consists of three servos that allow for three-axes movement with an accuracy within ±1 mm. The three servos are controlled by the SmartMove controller, which is a programmable high performance motion controller. In order to send the motion control commands from the host computer to the controller, the MINT language was used. MINT is a structured form

of the Basic programming language custom designed for motion control applications. cTERM, a terminal emulator was used to upload the commands (from the MINT program) to the controller with the aid of a computer.

3.4 Modification and loading of the cabinet

The main objective of this work is to study the performance of low-front open display cabinets. To fulfil this requirement, an existing medium temperature 120 cm wide cabinet of a leading brand using refrigerant R-404A was considered. The display opening height was originally 127.5 cm, but was retrofitted to have a display opening height of 200 cm, as shown in Figure 3.6. The Discharge Air Grille (DAG) was also altered to larger widths, and the figure shows a DAG width of 12 cm.

(a) **(b)**

Figure 3.6 Modified cabinet (a) idealisation and (b) with shelves

Throughout the tests, the cabinet was evenly loaded with 0.75 litre containers (filled with water to add thermal mass) up to the load limit prescribed in the ISO standard, as shown in Figure 3.6 (b). A 2.5 cm clearance was left between the container rows while a 3 cm clearance was left between the containers and the side walls. The loading height was equal to the free height between each two shelves.

At locations where the ISO standard requires that the temperature is to be monitored, the products were simulated by placing M-packs in the containers, as shown in Figure 3.7. The M-packs were prepared in-house by mixing hydroxyethylmethyl cellulose (Tylose), sodium chloride (salt), 4-chloro-m-cresol (anti-bacteria), with boiling water as specified by the supplier (Sigma-Aldrich company, Ltd). The M-packs were placed in the upper and lower layers of shelves 1, 3, 5, and 7 along three transverse sections, resulting in twelve measuring points on each shelf (a total of 48 M-packs in the cabinet). To abide by the ISO standard, the centre of the M-packages was carefully positioned at the centre of the cabinet as well as 7.5 cm from each end wall. Along the depth of the cabinet, the centre of the M-packages was located 5 cm from the perforated back panel and from the front edge of the shelves.

Figure 3.7 M-pack with a thermocouple

The product temperature was measured for shelves 1, 3, 5, and 7 at the right, middle, and left sections along the length of the cabinet. The location of the various M-packs along each shelf was further specified at the front or rear and top or bottom locations. Figure 3.8 illustrates the designations used to locate the M-packs. In order to identify the name of a specific M-pack, the order of the numbers in brackets was followed in the order given. For example, the code 3MFT refers to the M-pack located at the third shelf, across the middle section, at the front, and at the top layer. Table 3.3 gives the combinations of all designations used.

Table 3.3 Designations used to locate M-packs

(1) Shelf	(2) Cross-section	(3) Depth	(4) Layer
1	Right	Front	Top
3	Middle	Rear	Bottom
5	Left		
7			

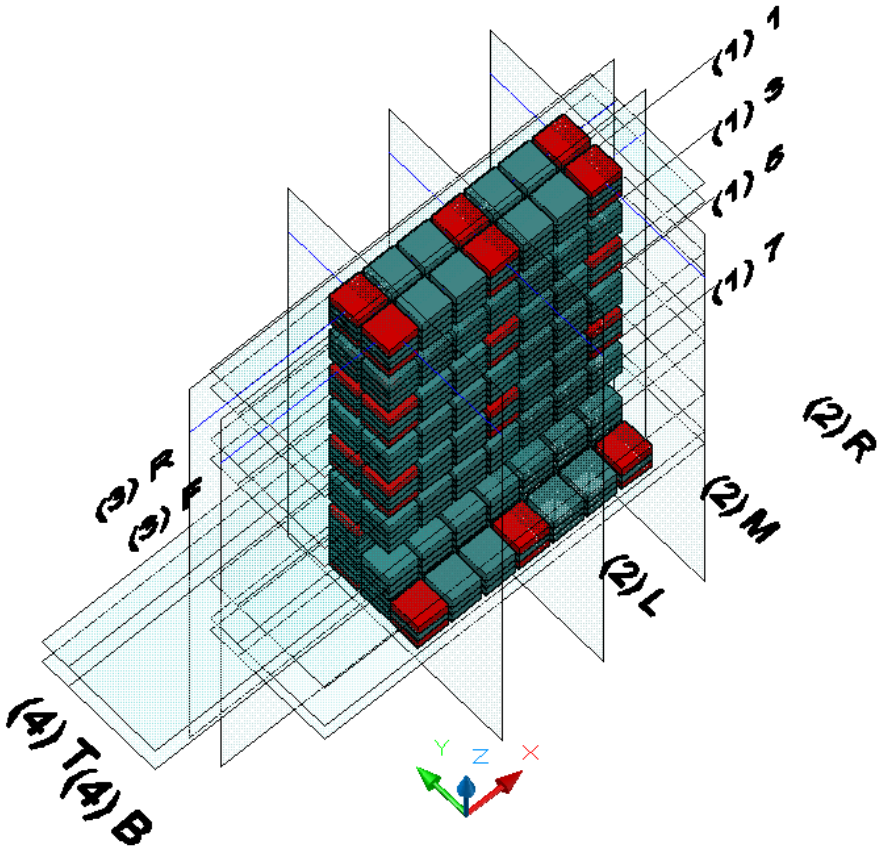

Figure 3.8 Designations used for the location of M-packs (shown in red)

3.5 Instrumentation

One of the unique aspects in this work lies in the utilisation of advanced techniques to measure temperatures and velocities at various locations of interest. The following presents the instrumentation used.

3.5.1 Measurement and data logging equipment

A total of 57 K-type thermocouples (having a temperature range -50 ^{o}C to 200 ^{o}C) were used to measure the temperature at 48 locations across the shelves together with three located at each of the air-on, air-off, and air curtain regions. Prior to use, the thermocouples were calibrated against a pool of ice and water, and were found to

have the prescribed tolerance of ±0.5 ^{o}C stated in the ISO standard. The thermal and flow conditions within the test room were measured using temperature and humidity sensors that provide analogue output signals. All the readings were logged into a computer by a data logging system comprising a multiple of Datascan modules and Labtech software, as shown in Figure 3.9. Data logging was carried out every 30 seconds over a 24-hour period.

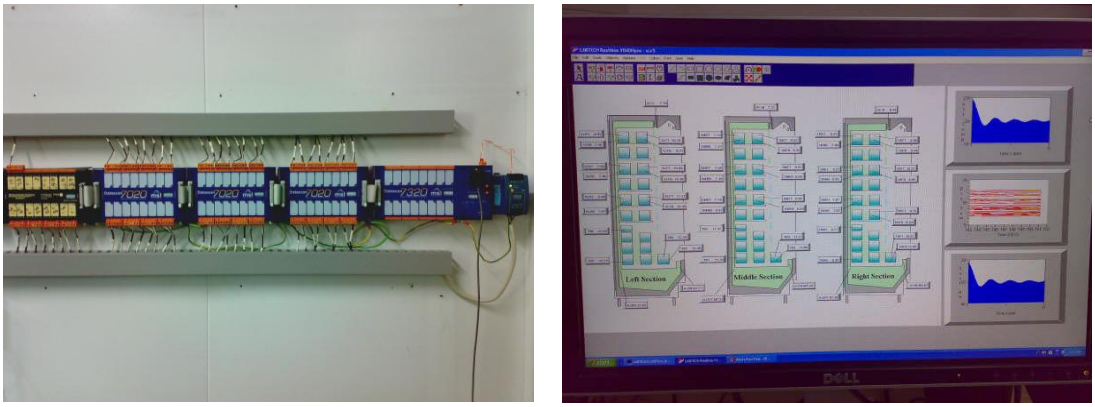

(a) Datascan hardware **(b) Labtech software**

Figure 3.9 Data acquisition system

A hot wire anemometer was also used for intermittent manual velocity and temperature measurements, and is shown in Figure 3.10.

Figure 3.10 Hot wire anemometer

3.5.2 PIV: principle and advantages, and equipment

In this work, the velocity map across the air curtain was experimentally obtained using the Particle Image Velocimetry (PIV) technique. The principle behind the PIV technique is fairly simple. A camera takes two consecutive snapshots of particles previously seeded into the flow, which are illuminated by a laser sheet. Knowing the time duration between the two snapshots and the distance travelled by the particles, the flow velocity can be obtained.

The main advantage of the PIV technique is that it is non-intrusive, and relies on optics to measure velocity by direct determination of its two fundamental dimensions: length and time. Moreover, it allows for measuring the flow velocity of a large cross sectional area within the flow field, which can extend up to a square metre. From another perspective, although the CFD technique has been proven to give reliable results in the study and optimisation of air curtains, it is still a simulation approach in the first place that demands many assumptions. The PIV technique on the other hand provides actual readings. If correctly calibrated and integrated with the CFD approach, PIV results can serve as an excellent validation tool as well as a source for setting realistic boundary conditions for further parametric studies using the CFD technique. Another advantage in using PIV is the immediate availability of the results and thus instant feedback during recording. This feature avoids the need to transfer the data to a spreadsheet, for example, and perform further calculations to reach final results.

The PIV equipment used in the tests was provided by Dantec Dynamics, and consists of a laser source, a digital camera, a laser arm, a computer, and an oil seeding generator. Figure 3.11 shows the lab setup of the PIV system used in this study.

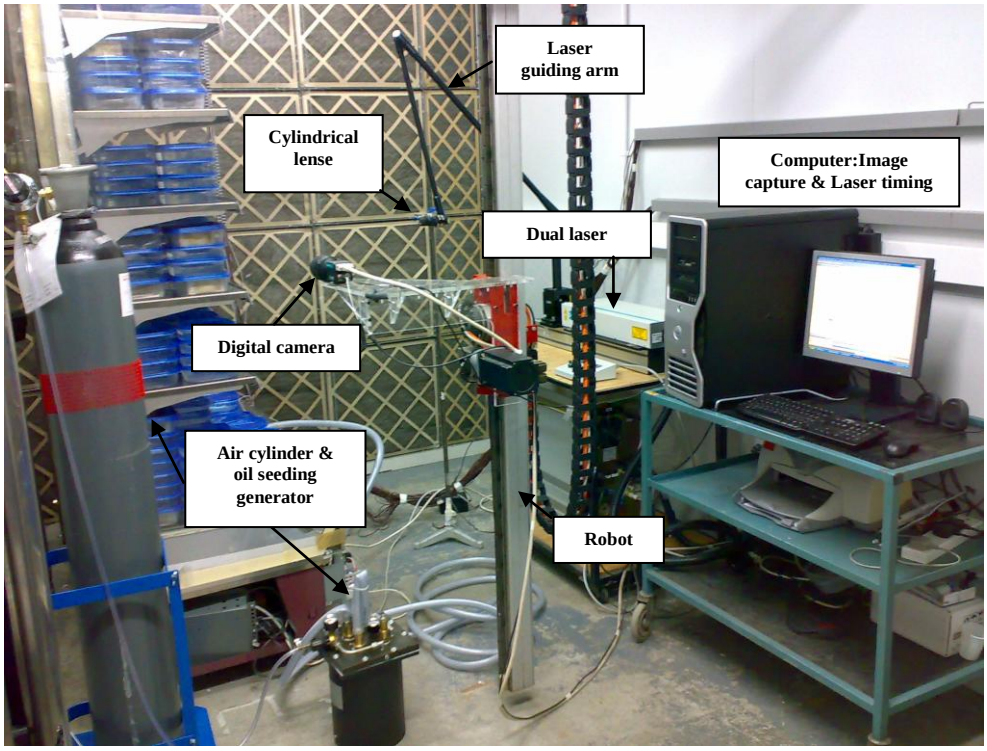

Figure 3.11 Photograph showing the setup of the PIV system

The software used for the acquisition and processing of the data is DynamicStudio v2.21, which is capable of performing process diagnostics, control of experiments, and analysis of image data. A personal computer is used for this purpose with a large storage capacity of 1.2 tera bytes.

The laser source is a dual pulsing Nd:YAG type, and is the most used laser source for conventional PIV applications, where high pulse energies at moderate repetition rates can be produced. The time between pulses and trigger rate suitable for the velocities encountered in this work were found to be 1500 μs and 4 Hz, respectively. The essential element for the generation of the thin laser sheet is a diverging cylindrical lens, which is placed at the end of the laser guiding arm. The thinner the light sheet produced, the better, since this allows the camera to capture particle images existing at the same plane. The light sheet produced in this work has a thickness in the order of 1 mm.

The high-speed digital camera allows for taking a single illuminated image for each illumination pulse, and has a resolution of 4 Mega pixel (2048 x 2048 pixel). Each individual image is subdivided into a number of interrogation areas to form a grid. In

the beginning of an analysis, a coarse grid of 64x64 pixels was used in order to produce results that allow for a qualitative evaluation of the flow field as well as running a check on the whole experimental setup. The grid was then refined by using a 32x32 grid size in order to capture fine details of the flow. Each consecutive pair of images is analysed by adaptive correlation to resolve a single velocity vector at each interrogation area in the final solution. A complete description is contained in Raffel et al. (2007).

The oil seeding generator consists of a closed cylindrical container where compressed air of 2 bar is used to agitate the oil, which in turn leaves at the outlet in the form of aerosols having 3 μm diameter.

3.5.3 Infrared thermography: Principle, advantages, and equipment

Infrared (IR) Thermography is a technique where a thermographic camera detects radiation in the infrared range of the electromagnetic spectrum (roughly 0.9–14 μm) and produces images of that radiation. Since infrared radiation is emitted by all objects based on their temperatures, according to the black body radiation law, thermography makes it possible to "see" one's environment with or without visible illumination. The amount of radiation emitted by an object increases with temperature, therefore thermography allows for detecting variations in temperature (hence the name). When viewed by a thermographic camera, warm objects stand out well against cooler backgrounds.

The infrared thermography technique was used here as a whole-field tool to visualise the air temperature across the air curtain. One advantage in using this technique is the instantaneous mapping of the temperature field, which, with flow results obtained from the PIV technique, can provide a comprehensive view of the thermo-fluid characteristics of the air curtain. Moreover, this technique is less intrusive than applying traditional measuring tools such as thermocouples, and only requires placing a sheet perpendicular to the flow to act as a screen for the IR camera.

The ThermaCAM^{TM} S60 infrared camera from FLIR was used in this work, and is shown in Figure 3.12(a). The built-in 24^{o} lens was substituted with an external 45^{o} lens to accommodate the extra height of the cabinet. In order for the IR camera to detect the temperature field of the air curtain, a sheet serving as a measuring screen

was placed perpendicular to the plane of the air curtain as shown in Figure 3.12(b). The dimensions of the sheet are 200 cm x 100 cm x 0.1 cm, and was kept perfectly stretched throughout the test procedure. After allowing sufficient time to pass to achieve equilibrium state with the flow of the air curtain, the camera was oriented perpendicular to the sheet to register images of the emitted infrared radiation. In order to drive the sheet temperature toward the temperature of the air curtain, it should have a low emissivity, so that its temperature depends more on convection with the air curtain and less on radiation exchange with the surroundings. However, a sheet with low emissivity introduces errors into the measurement of the sheet temperature by the infrared camera. Therefore, a black sheet with a relatively high emissivity of 0.86 (ThermaCAM^{TM} S60 infrared camera operator's manual, Emissivity Tables) was used. Figure 3.13 is a thermal image of the products and a sheet placed at the mid-section of the cabinet after reaching steady state conditions. The accuracy of the IR technique was confirmed by comparing the results with those obtained from thermocouple readings at the mid-section of the DAG, and the accuracy will be discussed in the subsequent section.

(a) IR camera **(b) Screen**

Figure 3.12 Infrared camera and screen

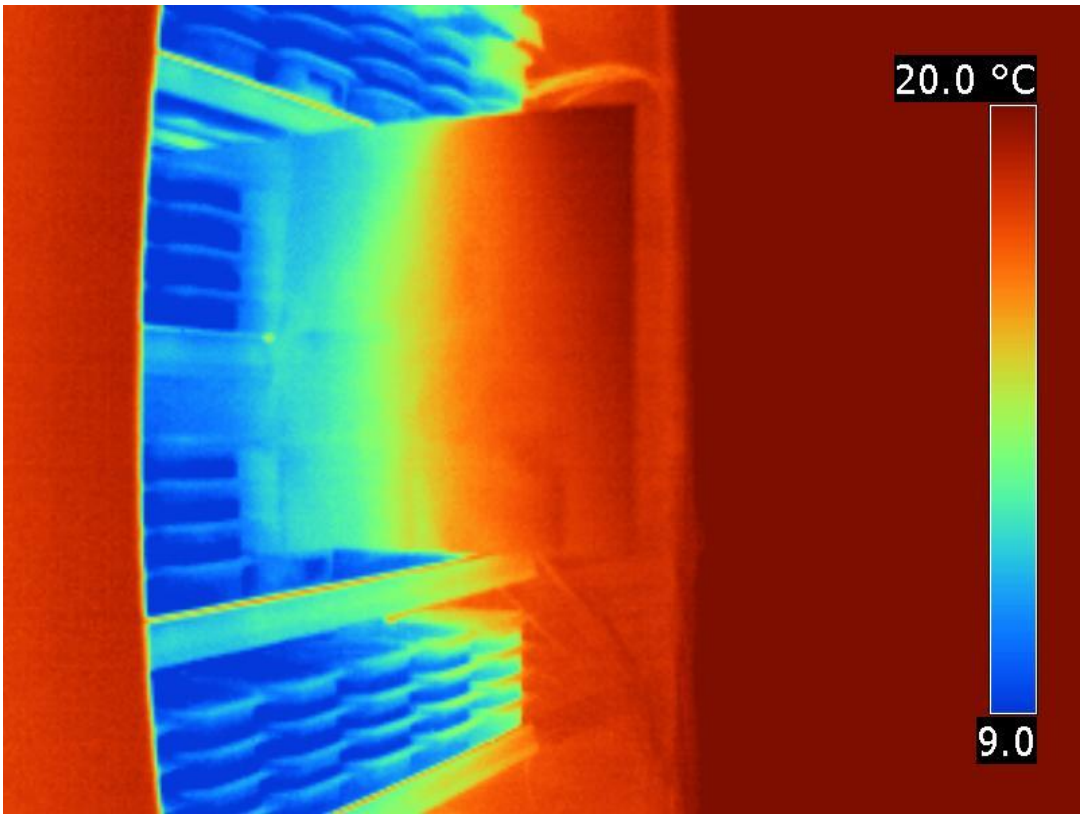

Figure 3.13 Thermal image taken by the infrared camera

3.6 Experimental results and discussion

The experimental results presented here are only those of the full cabinet configuration. Results pertinent to the idealised cabinet will be presented in Chapter 6, Quantification and minimisation of entrainment rate through the air curtain.

3.6.1 Test room environmental conditions

In order to guarantee compliance of the test conditions with those of the ISO 23953 standard, the temperature, relative humidity, and air velocity were measured at the prescribed locations shown in Figure 3.2. Figure 3.14 shows the temperature and relative humidity variations over a 24-hour period, and confirms that the values are fairly steady and the tolerances are within the ranges specified in the ISO standard (presented in Table 3.1). The small variation in relative humidity can be attributed to the evaporation of water from the condensate tray.

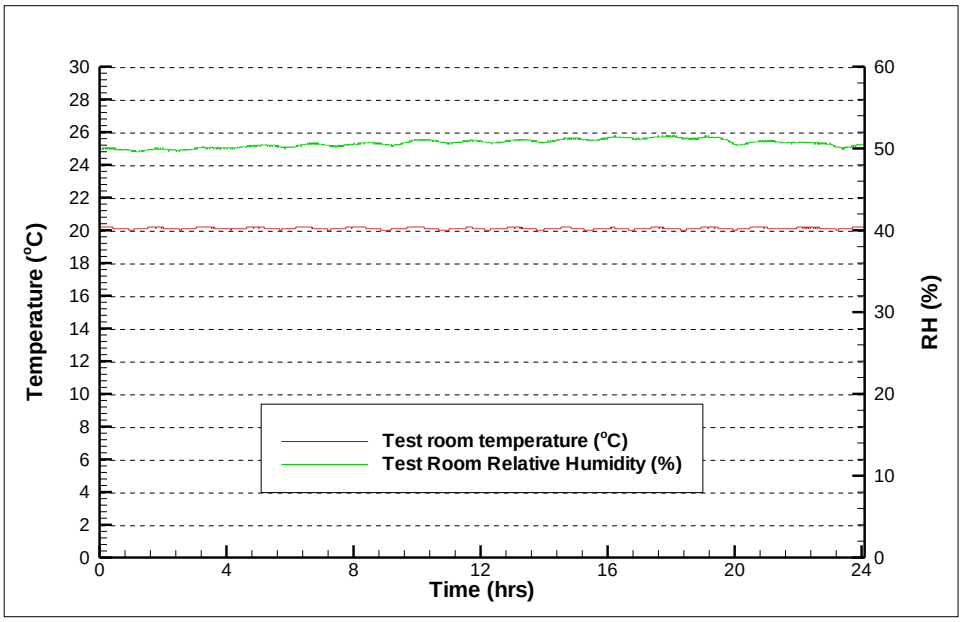

Figure 3.14 Test Room temperature and relative humidity over 24 hours

3.6.2 Air-side temperature of the display cabinet

After reaching steady-state conditions, the air temperature entering and leaving the cabinet was measured across the left, middle, and right sections along the span of the cabinet. Figure 3.15, 3.16, and 3.17 show the air-on, air-off, and air curtain outlet temperatures at the three sections, respectively. From the figures, it can be seen that the air-off temperature is higher than 0 ^{o}C. Therefore, the defrost cycle was not necessary, and was switched off to prevent it from adding unnecessary load to the cabinet. It is evident from the figures that the cabinet's right section (further away from the test room's supply air plenum) suffers from higher temperatures when compared to the other sections. This is attributed to the cross-flow effect which tends to disturb the air at this end of the cabinet. The temperature variation along the air-on location was in the order of 7 ^{o}C. This highly uneven temperature distribution was found to decrease to about 3 ^{o}C as the air passed the fans and the evaporator. This can be attributed to the enhanced mixing downstream of the fans, which were oriented downward to allow for better air mixing prior to entering the evaporator. By the time this air reached the honeycomb of the DAG, the temperature variation was further reduced to less than 2 ^{o}C. Moreover, an increase of approximately 1 ^{o}C was experienced as the air travelled from the air-off location to the DAG. This is due to the heat gain through the back and side walls of the cabinet.

Throughout the measurements, the temperatures at the middle section were found to be approximately the average of those at the two sides. For this reason, the measurements at the mid-section were used as boundary inputs for validation of the 2D simulation models developed. This assumption is valid since 2D models represent infinitely long cabinets without considering cross flow effects or heat transfer from the side walls.

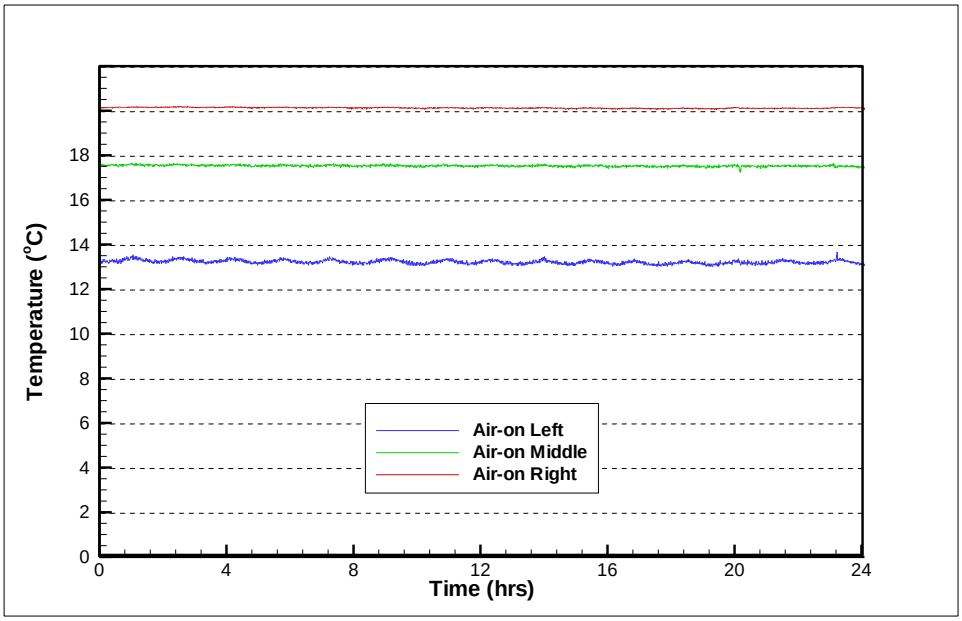

Figure 3.15 Air-on temperatures at the left, middle, and right sections of the cabinet

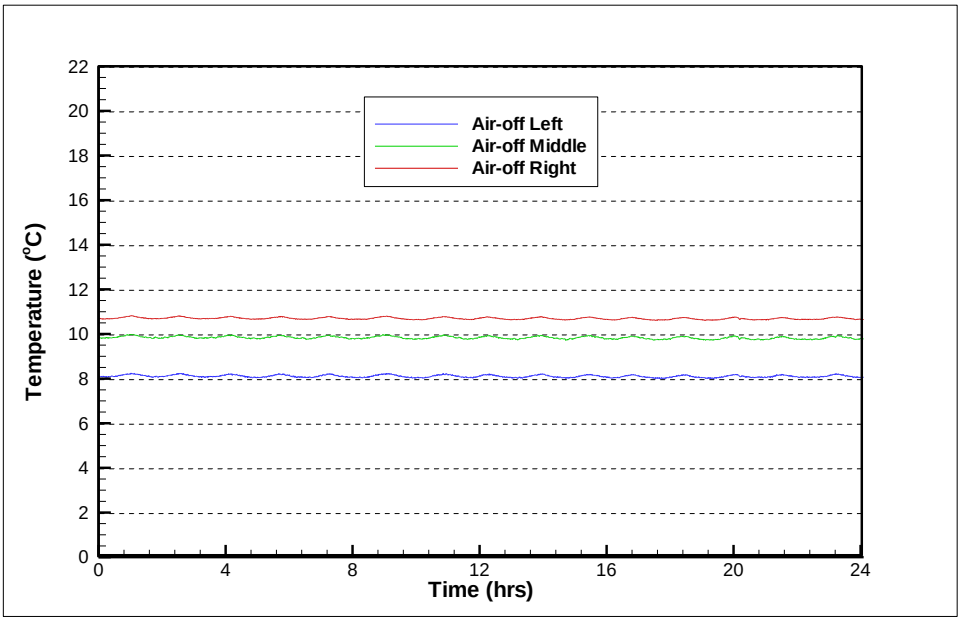

Figure 3.16 Air-off temperature at the left, middle, and right sections of the cabinet

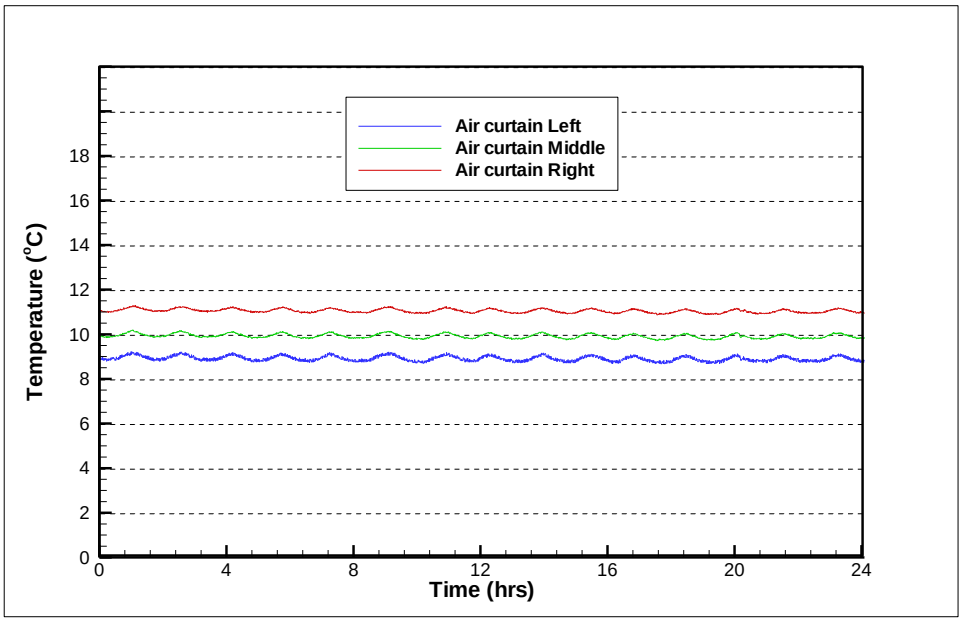

Figure 3.17 Air curtain temperature at the left, middle, and right sections of the cabinet

Figure 3.18 shows the IR temperature map at the middle-section of the cabinet, where the measured temperature at the honeycomb was found to be 10.1 ^{o}C. This is in close agreement with the 10 ^{o}C measured by the thermocouple at the same location. The figure also shows that the ability of the air curtain to cool the front products is diminished after the third shelf, although the DAG width used is relatively large (12 cm) and the average discharge velocity is approximately 1 m/s.

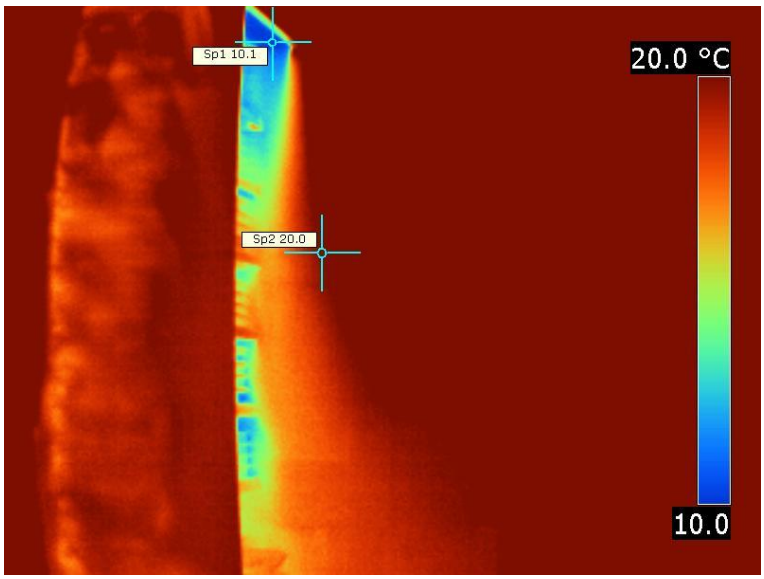

Figure 3.18 IR image of the air curtain at the mid-section of the cabinet

In order to determine the air-off mass flow rate, the velocity profile at the inlet to the perforated back panel was measured. This profile is shown in Figure 3.19, and it can be seen that the velocity at the sides of the cabinet is lower due to the shorter evaporator/fan box width (85 cm) compared to the cabinet width (120 cm). The average velocity was found to be 4.23 m/s, and this was used to calculate the mass flow rate supplied by the evaporator. This value was later used as an input for the air-off boundary condition in the CFD simulation of the cabinet.

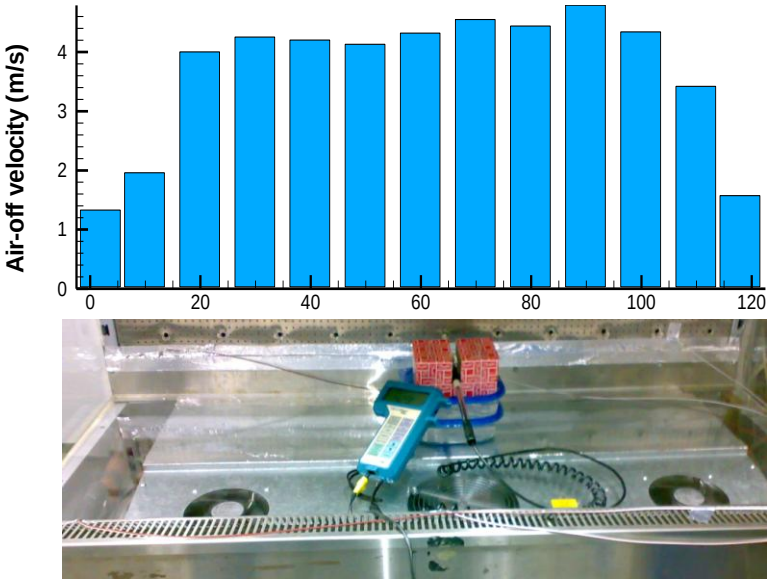

Figure 3.19 Air-off velocity variation along the air-off section

The PIV technique was used to map the velocity field in front of the cabinet. The first PIV image was taken 2.5 cm below the honeycomb since the reflection of laser light from the honeycomb influenced the image quality and prevented proper data acquisition much closer to the honeycomb.

Figure 3.20 shows a PIV velocity vector map superimposed on a side-view photograph of the cabinet. It is clear from the figure that the air curtain tends to breakdown as it reaches shelf 4, leaving shelves 5, 6, and 7 unprotected. In the vicinity of the RAG, the strength of the flow is gradually regained by the suction action created by the evaporator fans. However, this air is mainly ambient air, which constitutes the infiltration rate through the cabinet.

Figure 3.21 is a closer view near the DAG. The flow near the honeycomb can be seen to accelerate as it flows downward, showing the engagement of the negative-buoyancy effect. The upward flow at the outer edge of the air curtain suggests that a vortex action exists in this region, where ambient air starts to get entrained into the air curtain.

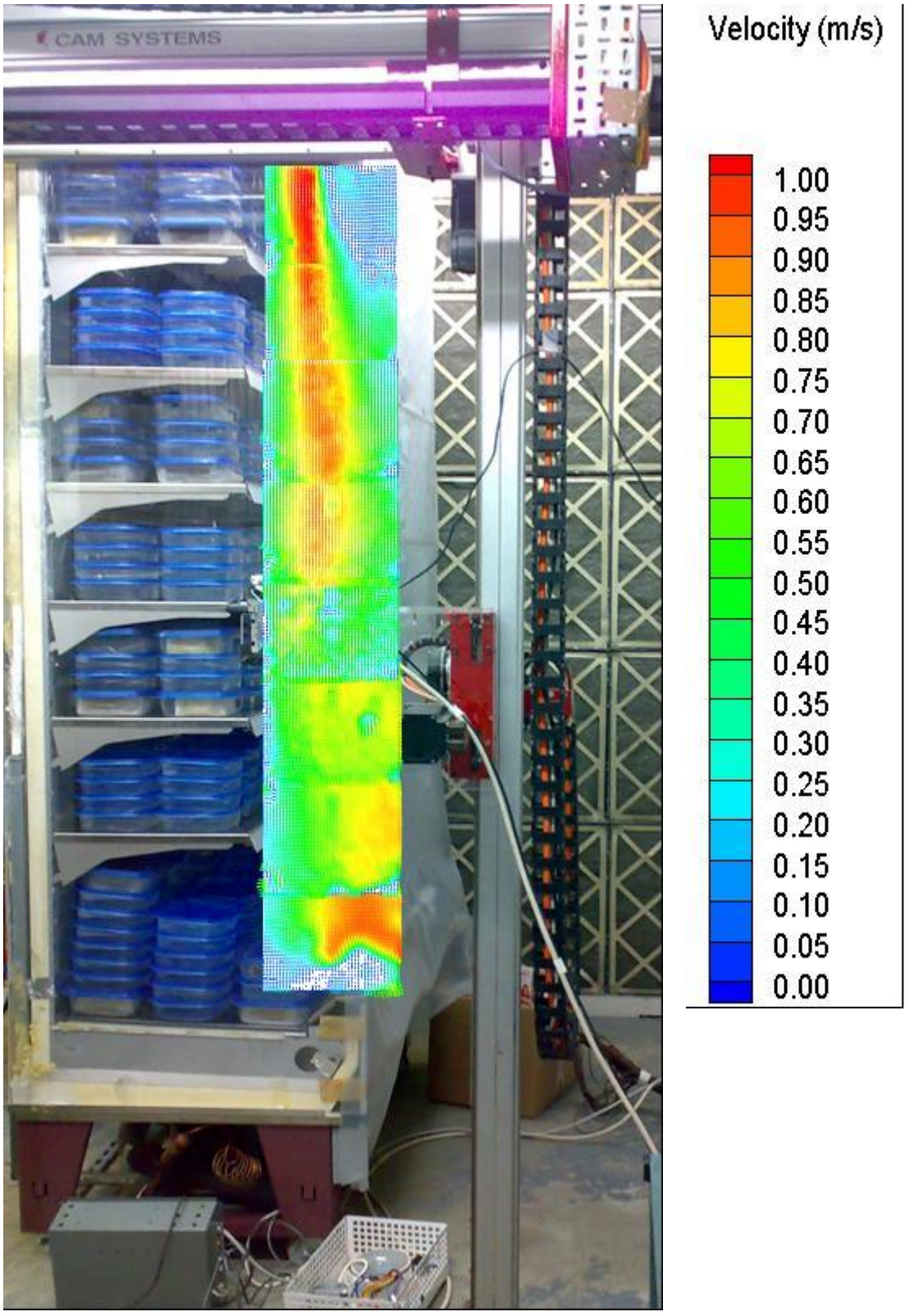

Figure 3.20 PIV velocity vectors (m/s) of the air curtain at the mid-section

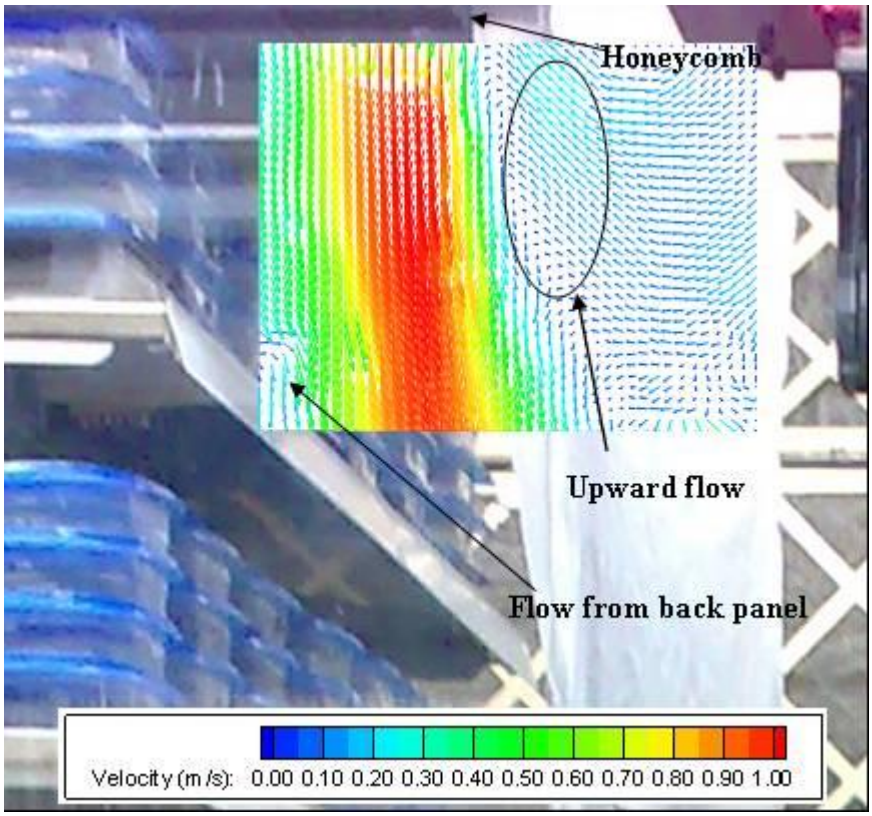

Figure 3.21 Velocity vectors near the DAG showing upward flow

The stream-wise (y-) velocity profile at the front and at the mid-height of each shelf was obtained from the PIV measurements, as shown in Figure 3.22. The measurements were taken 1 cm away from the shelves to prevent the reflection of laser light from affecting the quality of the results. Figure 3.23 shows the stream-wise (y-) velocity profiles at these locations, where the green lines/green triangles denote shelf height and the red lines/red squares denote mid-shelf height. It is noticed that the peak velocity is not progressively dampened in the flow direction, but momentarily increases at different heights due to the contribution of the flow emerging from the back panel. This is evident by looking at the graphs at the right-hand-side column, where the velocity profile at the front of each shelf (green) is followed by the velocity profile at the mid-height of the next shelf (red). The flow can be seen to be marginally boosted after each shelf. This behaviour is contrary to the marginal dampening that takes place as the flow travels from the shelves mid-height approaching the following shelf, as shown by the graphs on the left-hand-side column.

Also from the velocity profiles in Figure 3.23, the strength of the air curtain can be seen to be preserved until it reaches the forth shelf, beyond which, the velocity profiles start to depict an irregular shape, suggesting that the functionality of the air curtain is deteriorated. The counter-clockwise vortex created near the first shelf (due to the relatively high discharge velocity) produces an upward velocity vector at heights sh-0.5 and sh-1, as shown in Figure 3.23 (a). This flow feature is not observed near lower shelves, since the flow is not strong enough to create a vortex at the shear layer between the air curtain and the stagnant ambient air.

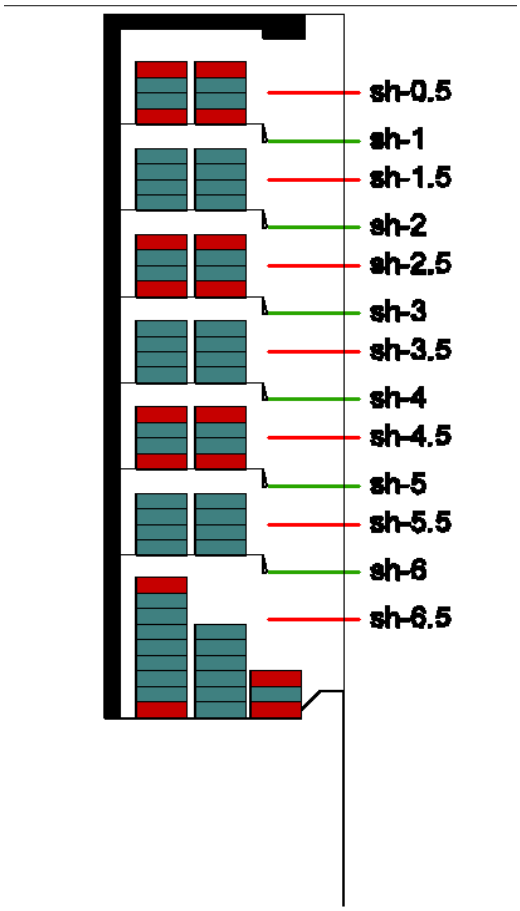

Figure 3.22 Locations of obtained velocity profiles

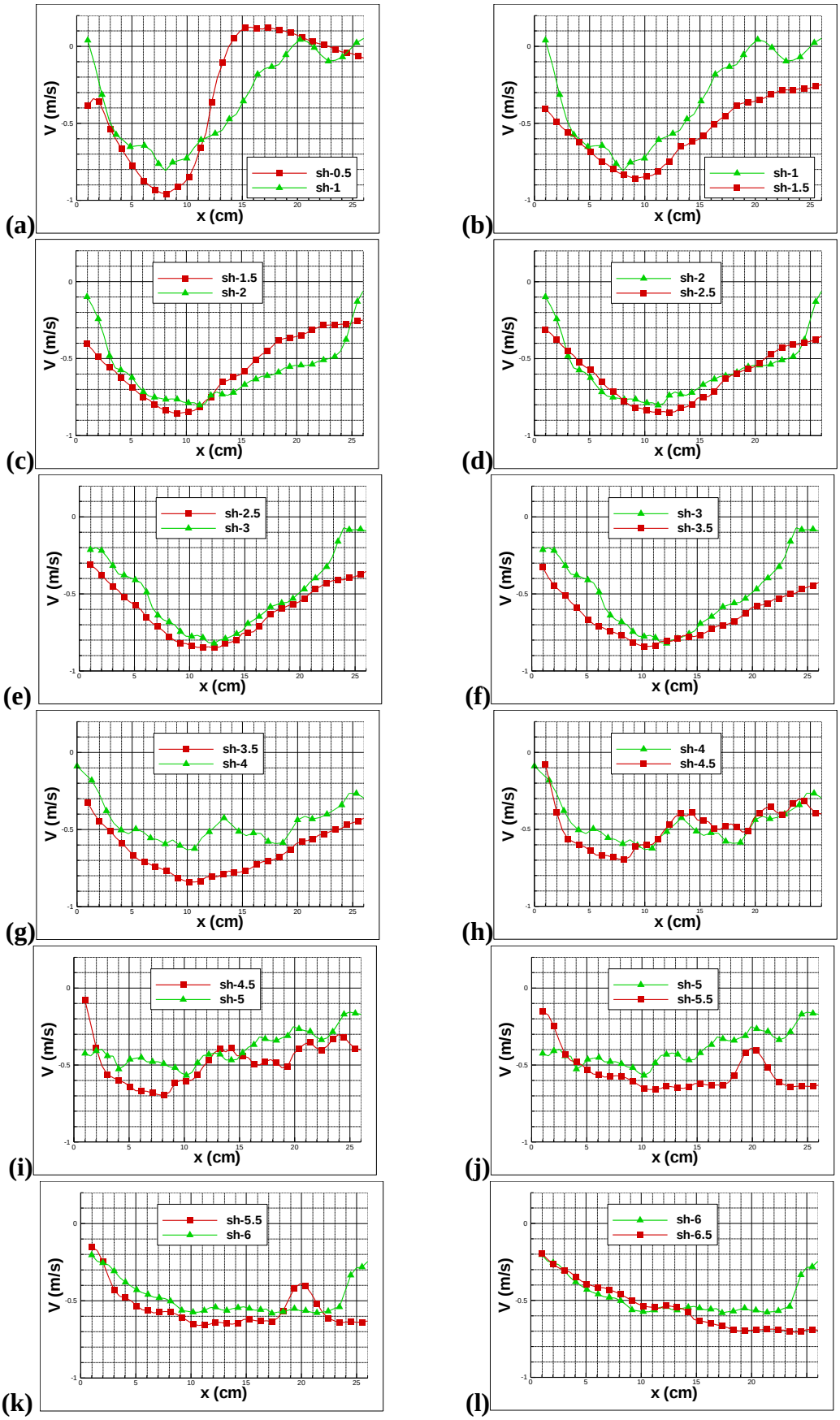

Figure 3.23 Stream-wise (y-) velocity profiles (m/s) at different shelf heights

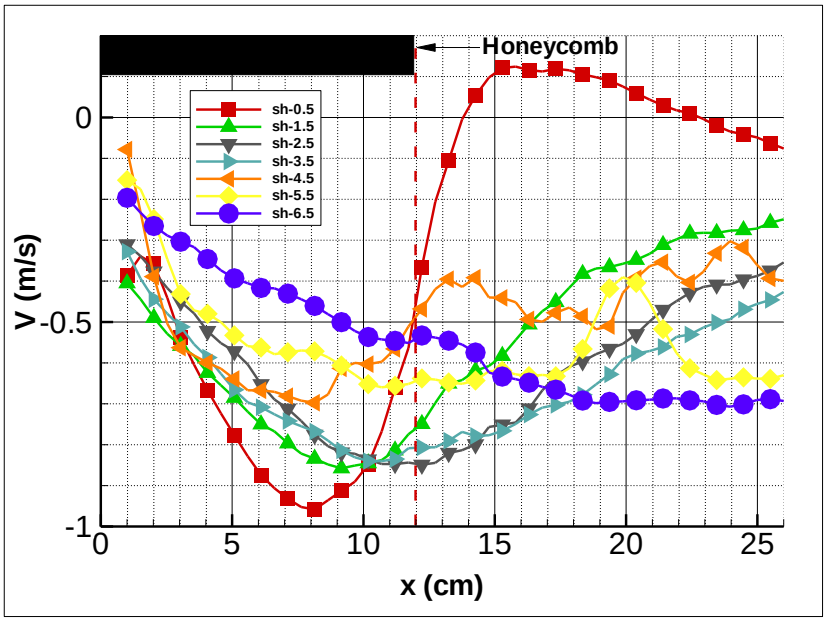

Figure 3.24 Stream-wise (y-) velocity profiles (m/s) at mid-shelf heights

Figure 3.24 shows the stream-wise velocity profiles at the mid-shelf heights only. It is clear from the figure that the interaction with the ambient air causes the air curtain to spread as it flows downwards. A consistent but insignificant decrease in peak velocity is seen, although the distance travelled is relatively high (2 metres). This is due to the contribution of air from the perforated back panel, which tends to augment the momentum along the flow path. The first four velocity profiles (i.e. mid height of shelves 1, 2, 3, and 4) seem to preserve their strength, with the peak shifting outwards as the air curtain travels downward. This trend is not observed for lower shelves, as the flow is weakened by the entrainment process.

3.6.3 Product temperature

Failing to achieve optimum air-off temperatures and sufficient mass flow rates resulted in a dysfunctional open display cabinet, which in turn hindered proper analysis of the results. Therefore, the conclusions drawn reflect those of a poorly designed cabinet and the results were only used to validate the CFD modelling in a later stage of this work.

Figure 3.25 through 3.27 present the product temperature variation at the locations referred to in Figure 3.8. Shelf-wise, the product temperature was found to increase downward further away from the DAG, with Shelf 7 having the maximum product

temperature among all the shelves. This clearly shows that the air curtain is inefficient in protecting against the outer environment at the lower shelves. As for shelf 1, being close to the DAG as well as receiving cold air from the perforated back panel enabled the products to be maintained at relatively lower temperatures.

The cross-flow created within the test room definitely has a strong effect on the product temperature. Products at the right cross-section (further away from the test room's air inlet) were found to exhibit higher temperatures, exemplifying the effect of cross-flow on such a short cabinet. This confirms the results of D' Agaro et al. (2006), who attributed this finding to the development of a vortex on the leading wall along the cross-flow direction, making the air deflect inward towards the display opening and hit the products at the far end of the cabinet.

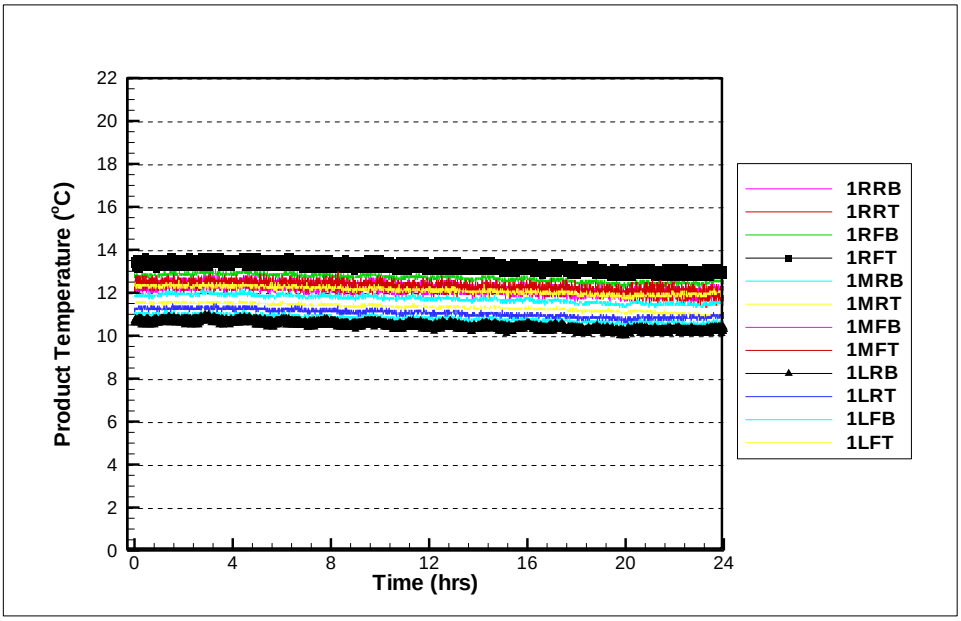

Figure 3.25 Product temperature variation at shelf 1

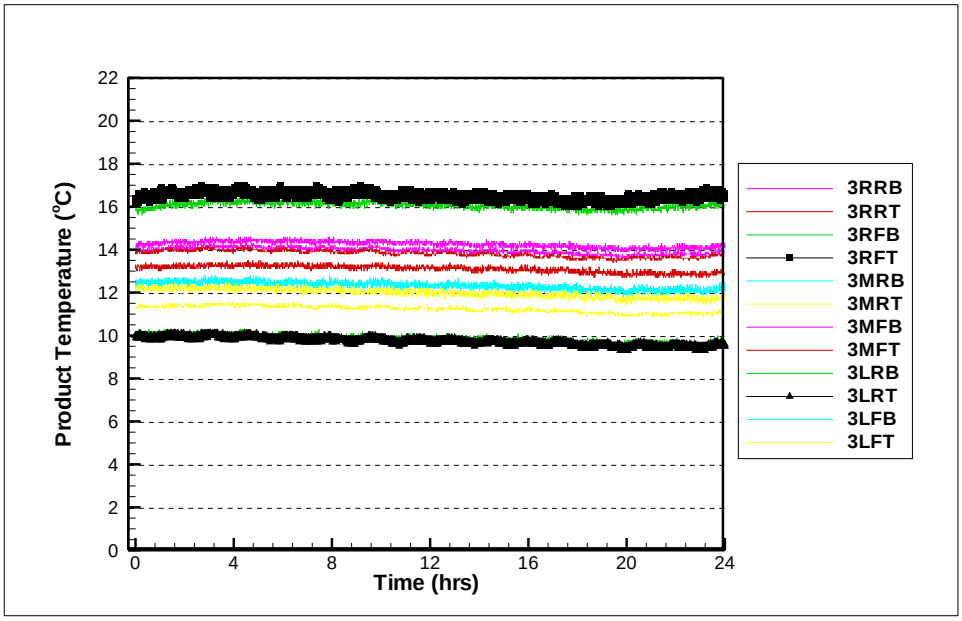

Figure 3.26 Product temperature variation at shelf 3

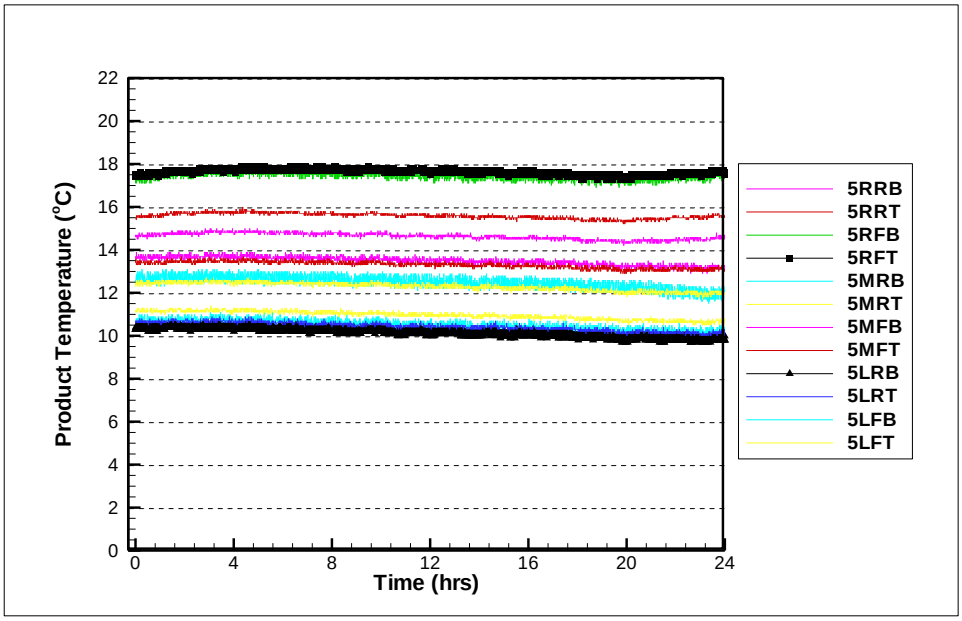

Figure 3.27 Product temperature variation at shelf 5

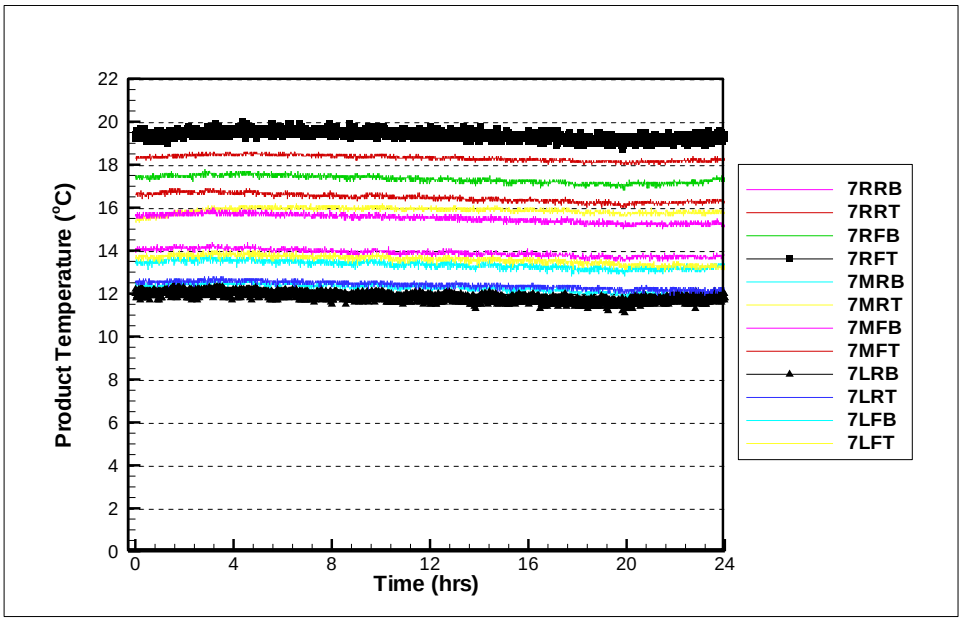

Figure 3.28 Product temperature variation at shelf 7

The variation in product temperature was also found to progressively increase from shelf 1 to shelf 7, with values of 3 ^{o}C, 6.5 ^{o}C, 7 ^{o}C, and 7.5 ^{o}C respectively. This observation strongly suggests that an efficient air curtain plays a dominant role in creating a homogeneous temperature distribution across shelves, and its efficiency must further be investigated.

3.7 Summary

This chapter presented the performance results of a modified low-front cabinet using advanced measurement techniques. The 150% increase in display area height resulted in a dysfunctional cabinet, which failed to comply with the Class 0 requirements (20 ^{o}C, 50% RH) of the ISO standard. Therefore, the experimental results in this chapter are only significant for validation purposes, and will serve as realistic boundary conditions for the CFD simulations utilised for the optimisation scheme in this work.

CHAPTER 4
CFD Model Setup

"Everything should be made as simple as possible,
but not simpler"

(Albert Einstein, 1879-1955)

The onset of this chapter is an introduction and overview of the Computational Fluid Dynamics (CFD) technique and the governing equations representing turbulent flows. Then, at the level of generality presented here, the various aspects touched upon during the model's setup stages, namely, pre-processing, solving, and post-processing, will be illustrated. Issues such as initial and boundary conditions, turbulence, radiation, and species modelling, and grid independence are presented. This is done with the aim of producing physically realistic and numerically accurate results.

4.1 Introduction

The term "Computational Fluid Dynamics" has been intensively used during the past four decades and is now part of many fields of academia, industry, and major research centres. CFD is defined by Versteeg and Malalasekera (2007) as "the analysis of systems involving fluid flow, heat transfer and associated phenomena such as chemical reactions by means of computer-based simulation". CFD is as much an art as a science, and there are an almost unlimited number of ways to conduct a CFD analysis. Proper implementation of CFD allows for the study of turbulent, three-dimensional, transient, and buoyancy-affected flows with complex geometries of practical applications. This makes CFD a suitable tool for the analysis and optimisation of the air flow and thermal characteristics of open display cabinets and the store environment surrounding them.

The ability of the CFD approach to rapidly provide relatively inexpensive, qualitative, and even quantitative results for both internal and external flows has made it the method of choice in commencing almost any new design. Furthermore,

rather than providing answers for a single quantity (i.e., temperature, velocity, etc.) at only one point or discrete points in the flow domain (as it is the case in many theoretical and experimental approaches), all parameters can be obtained at once across the entire field of study. This allows researchers and engineers in both research and development to have a comprehensive understanding of the flow regimes simultaneously taking place in the entire domain. This advantage is extremely vital in the study of open display cabinets, since the airflow pattern as well as its thermal properties dictate the cabinet's performance. Consequently, with the aid of the CFD technique, better understanding of the airflow mechanics around the entire cabinet results in the design of a better and more efficient one. The reviews by Norton and Sun (2006) and Smale et al. (2006) detail the application of CFD to predict the air thermo-fluid dynamics in refrigerated food applications including open display cabinets.

Besides the many merits in conducting a CFD analysis, there exist some drawbacks. No simulation can represent reality 100%. However, some simulations are better than others, especially when results are within engineering accuracy. Therefore, CFD predictions need to be validated against experimental results in order to assure the accuracy of the simulation results. Moreover, a thorough understanding and sufficient hands-on experience of the CFD technique is required in order to produce accurate results.

4.2 Thermo-fluid regimes of open display cabinets

The air flow characteristics in and around open display cabinets determine their operation and gauge their efficiency. This air is the working fluid that absorbs the heat (both sensible and latent) from the products and transfers it to the evaporator coil where it is removed. A complete CFD description of the physical processes taking place in a cabinet requires appropriate modelling and interpretation of various phenomena, including conduction, convection, and radiation. The interaction between the cabinet and the environment via the display opening is enormous and is by means of convection heat transfer (both free and forced) between the confined air in the cabinet and the air of the surrounding environment. Both laminar and turbulent regimes are involved, prompted by either momentum or buoyancy force or both.

Conduction heat transfer through the body of the cabinet takes place due to the relatively high temperature gradients across the cabinet walls. Radiation heat transfer between the products and the surrounding environment takes place due to the large temperature difference and cannot be ignored. All such thermo-fluid modes together with the numerical techniques employed for their solution result in a complex and demanding solution procedure. The following material briefly explains the CFD approach and provides the steps taken in the modelling setup.

4.3 The CFD approach

CFD modelling is commenced by sub-dividing the domain in question into a large number of cells (also called elements or control volumes) to form a mesh (or grid) overlaying the whole domain geometry. Each cell within the domain has a central node where information is stored. Using a computer, the iterative approach is used to calculate approximate solutions to the mathematical equations that describe the flow of the moving fluid for each control volume throughout the flow field. These equations are the governing equations of fluid dynamics, namely the conservation of mass (continuity equation), the conservation of momentum (Newton's second law of motion), the conservation of energy (first law of thermodynamics), along with an equation of state. These equations take the form of non-linear partial differential equations (PDEs) since a microscopic analysis of the distribution of the physical quantities (i.e. variables of mass, velocity components, pressure, temperature, concentration of species, turbulence, etc.) is necessary. Each PDE describes the conservation of one dependent variable within the field and this implies that there must be a balance among the various factors influencing this variable. The process of converting the PDEs and the auxiliary (boundary and initial) conditions into a system of discrete algebraic equations is known as discritisation, and is usually performed using either the Finite Volume Method (FVM), the Finite Difference Method (FDM), or the Finite Element Method (FEM). The FVM is commonly employed in CFD because it is easier to visualise the flow with it. Another significant advantage of the FVM is that it requires less computational resources and computer processing power. The key step of the FVM is the integration of all the governing equations in the partial differential form over each control volume to provide equations of discretised form at the nodal points. These discretised equations are then arranged to form a

system of algebraic equations that can be solved using matrix techniques to yield the distribution of the various properties at the nodal points.

4.4 Turbulence modelling

The flow of open display cabinets is characterised as a transitional regime (neither laminar nor turbulent) where turbulent kinetic energy is both created and destroyed, leading to random fluctuations in the air velocity. Those fluctuations are three-dimensional rotational flow structures, commonly known as eddies (or vortices), which promote the transported quantities of momentum, energy, and species concentration to mix and fluctuate. This phenomenon is mainly considered to be from the shear between different layers of the main flow and also from buoyancy forces affecting the flow. The onset of turbulence depends on the ratio of the inertia force to viscous force, which is generally indicated by the Reynolds number.

By introducing a general variable φ, the three-dimensional incompressible form of the governing equations for the conservation of mass, momentum, energy, and turbulent quantities can be presented by the so-called transport equation:

$$\frac{\partial \phi}{\partial t}+\frac{\partial (u\phi)}{\partial x}+\frac{\partial (v\phi)}{\partial y}+\frac{\partial (w\phi)}{\partial z}=\frac{\partial}{\partial x}\left[\Gamma \frac{\partial \phi}{\partial x}\right]+\frac{\partial}{\partial y}\left[\Gamma \frac{\partial \phi}{\partial y}\right]+\frac{\partial}{\partial z}\left[\Gamma \frac{\partial \phi}{\partial z}\right]+S_{\phi} \qquad (4.1)$$

By setting the variable φ equal to 1, u, v, w, T, k, or ε, and selecting appropriate values for the diffusion coefficient Γ and source terms S_{φ}, the partial differential equations for the conservation of mass (1), momentum (x, y, z), energy (T), turbulent kinetic energy (k) and turbulent dissipation rate (ε) can be obtained.

According to Reynolds (1895) averaging hypothesis, the instantaneous variables of a turbulent flow can be decomposed into a time-averaged component and a fluctuating component superimposed on it. For the x- velocity component, this gives

$$u=\bar{u}+u' \qquad (4.2)$$

and equations of similar form are given to the other variables in the flow (i.e. pressure, energy and species concentration). The time-averaged velocity is defined as

$$\bar{u}=\frac{1}{\Delta t}\int_{t}^{t+\Delta t} u\,dt \qquad (4.3)$$

and the time-average of the fluctuating velocity is zero, and is given as:

$$\overline{u'} = \frac{1}{\Delta t}\int_{t}^{t+\Delta t} u'\,dt = 0 \tag{4.4}$$

Figure 4.1 illustrates the average and fluctuating velocity in the x-direction for both steady and unsteady flows.

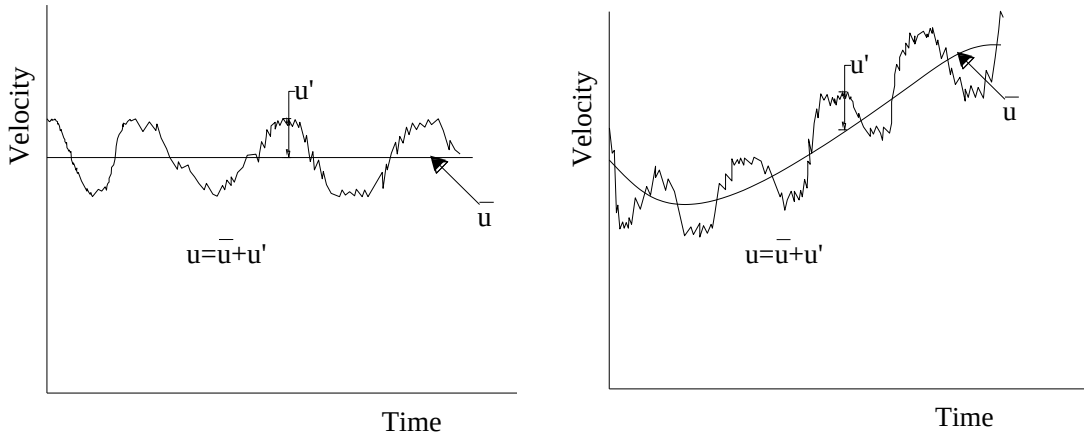

(a) Steady flow **(b) Unsteady flow**

Figure 4.1 Velocity components in the x-direction for a) steady and b) unsteady flows

Applying Reynolds averaging to the aforementioned governing equations of fluid dynamics yields the set of Reynolds averaged Navier-Stokes equations. New terms with mean signs appear representing the turbulent (Reynolds) stresses. With those variables, there are now more unknowns than equations, and additional equations are necessary to represent them (closure equations) before the momentum equations can be solved. This addition of equations to the Reynolds averaged N-S equations is called turbulence modelling. Turbulence models are usually classified based on the number of PDEs in the model. For example, the Prandtl algebraic model has no PDEs, and is referred to as a zero equation model. The k-ε model is a two-equation model and the Reynolds Stress Model (RSM) is a three- to five- equation model. It is worth mentioning here that turbulent effects that are smaller than the cell size cannot be simulated by solving the N-S equations, but are modelled using the aforementioned turbulence models. Therefore, turbulence modelling has been developed to account for these small-scale effects. Also, the need for a closure form to the governing equations is behind the development of turbulence modelling.

Turbulence representation can be divided into three groups: Direct Numerical Simulation (DNS), Large Eddy Simulations (LES) and Reynolds Averaged Navier-Stokes (RANS) turbulent transport modelling. It is theoretically possible to directly resolve the whole spectrum of turbulent scales using DNS without reliance on turbulence modelling. However, this technique requires an extremely fine computational grid (of the order of $Re^{9/4}$) and large computational resources, and can only be used for transient simulations with short time steps, which makes it impractical for large scale engineering applications. LES is an alternative that accounts for turbulent flows where the large, energy-carrying turbulent eddies are calculated directly and the effect of the small-scale eddies (below the computational grid size), which contribute to the turbulence energy dissipation, are modelled. To date, however, LES has rarely been applied to actual engineering configurations and still needs significant computer power and memory because of the mesh refining requirements. Most CFD applications use the RANS turbulent transport models, where the unknown Reynolds stresses and heat and diffusion turbulent fluxes are approximated by model assumptions in order to close the system of equations. The turbulence fluctuations are ruled out by a time-averaging process, leaving only the mean flow to be simulated.

Depending on how the Reynolds stresses and heat and diffusion fluxes are modelled, turbulent transport models are further classified as eddy-viscosity models and Reynolds-stress models. An early and popular eddy-viscosity model is the k-ε model from Launder and Spalding (1974) and a basic Reynolds Stress Model (RSM) is the one summarised by Launder (1989). The Reynolds-stress models are superior to the eddy-viscosity models because they do not involve the Bousinessq approximation, which links the Reynolds stresses to the mean rates of deformation. However, there is a penalty in terms of more computational time needed and a less stable numerical algorithm. Therefore, the eddy-viscosity based k-ε model will be used throughout this work.

4.5 The CFD code

All the CFD modelling in this work was achieved by going through three stages, namely, the pre-processing, solving (processing), and post-processing stages.

Figure 4.2 presents a framework illustrating the interconnectivity of the three stages within the CFD code.

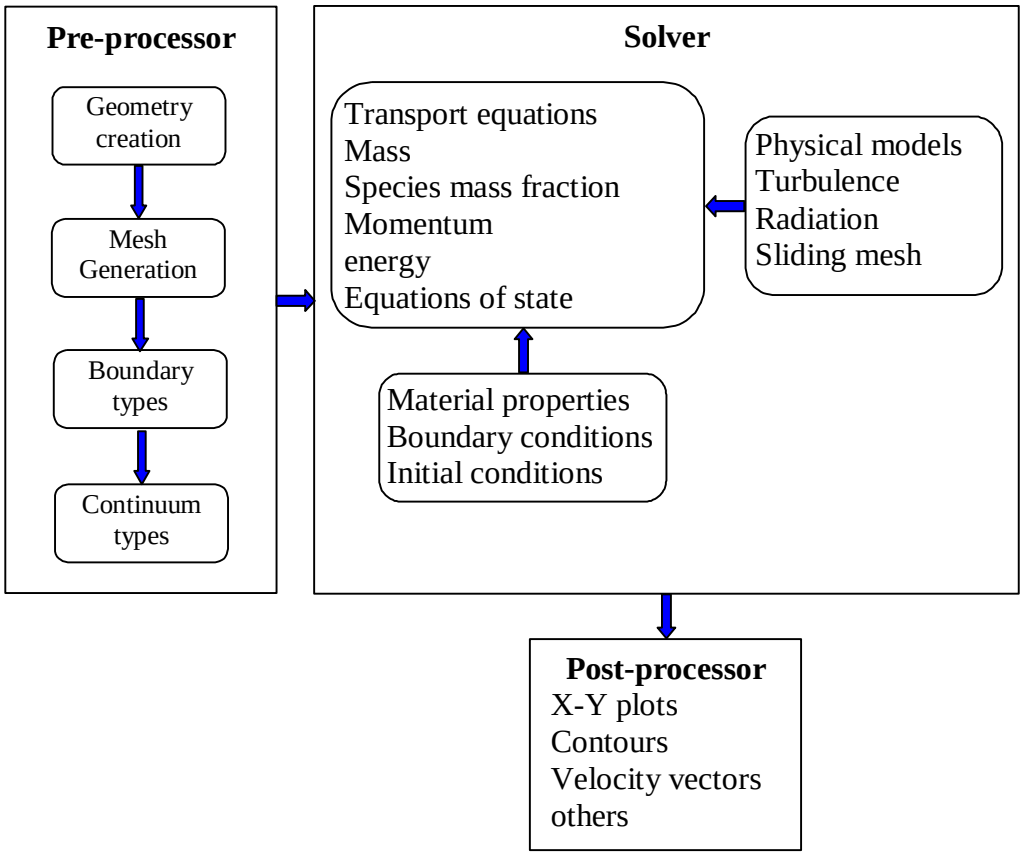

Figure 4.2 Interconnectivity functions of the three main elements within a CFD analysis framework

The pre-processor tasks were performed using Gambit v 2.3.16 (2006), a meshing tool provided by ANSYS Inc. capable of creating and meshing geometries of different complexities as well as defining the boundary conditions. The CFD software, ANSYS Inc., Fluent v 6.3.26 (2006), was used as the solver, which is responsible for grid importation, setting values at boundary conditions, setting of fluid properties, setting up of models to be used, and solution of the governing equations. It was also used for post-processing preliminary results. For more demanding tasks, however, the specialised post-processing software, Tecplot 360 (2008) was used for its capability to offer more specific and highly advanced representation of the results.

4.6 Pre-processing

4.6.1 Creation of geometry

The first step in commencing a CFD analysis is the creation and definition of the geometry under consideration. Whether modelling needs to be performed in a three-dimensional domain or can be simplified as a two-dimensional domain is a critical issue that needs to be addressed in the beginning since it has a direct impact on the computing power needed and the final accuracy of the results. During the study of open display cabinets, Stribling (1997) showed that the flow mechanics along the span of sufficiently long cabinets is generally the same; hence, the computational domain can simply be considered as a two-dimensional with reasonable accuracy. Moreover, D'Agaro et al. (2006) compared the refrigeration power of two- and three-dimensional computational results and concluded that dimensionality issues are significant only at the side walls of short cabinets being subject to cross flow. In this study, 3D modelling was initially used in the validation scheme with the experimental results since the interaction of the cross flow with the side walls initiates 3D secondary vortices that affect the air curtain and could not be ignored. 2D modelling was then assumed in the study of entrainment through the air curtain since variations in the direction of the DAG length can be considered negligible if cross flow is not considered or a cabinet of a large span is assumed. Details of this modelling will be addressed in Chapter 6, Quantification and minimisation of entrainment rate through the air curtain.

Another aspect that should be considered in early stages is whether the actual size and fine details of the original domain must be represented exactly as they are in reality or can be altered without lose of accuracy. To eliminate backflow into the domain of 2D models and achieve stable convergence, the flow must be fully developed at all boundaries. Since the most important flow is that in the vicinity of the air curtain, the domain boundary was further distanced away from the air curtain in 2D models to eliminate its influence on the air curtain and also prevent backflow from occurring at the boundary. After many trials, a distance 2.5 times the air curtain height was found to be sufficient and still manageable for the CFD calculations. This lead to the use of a 5 m-wide domain instead of the actual 3.5 m-width of the test

room. The 3 m-height of the test room was kept unchanged throughout the 2D and 3D modelling.

When using CFD to model engineering problems, it is the exception rather than the norm to represent the geometry exactly. Many cabinet details that are not of interest and/or have minimal or no effect on the overall air flow were not modelled and were removed without affecting the final results. Excluding such unnecessary details, especially in 3D modelling, reduced the complexity of the meshing process by not introducing extra cells to accommodate for the transition from areas of fine mesh to areas of coarse mesh. The outcome of this simplification was faster and more stable solutions.

4.6.2 Mesh generation

Mesh generation constitutes one of the most important and time-consuming steps during the pre-processing stage. The accuracy of the solution is governed by the shape, size, and number of cells scattered in the mesh in order to resolve details in areas of interest. Although a large number of cells reveal more details of the flow and generally provide a more accurate solution, the simulations are limited by the computational cost and calculation turnover time. The quality of the mesh also has significant implications on the convergence and stability of the numerical simulation.

Both structured and unstructured meshes were used in this work. In the former, all interior nodes have an equal number of adjacent elements. This implies rectangular elements for 2D simulations and hexahedral elements for 3D simulations. Unstructured meshes, on the other hand, allow any number of elements to meet at a single node, for both 2D and 3D simulations. The choice of the type of the grid depends on the geometrical complexity and on the physics encountered near those regions. Aligned structured elements were constantly used near the walls of the cabinet and the products as shown in the window of Figure 4.3, since they are more suitable in solving for momentum and heat transfer in near-wall boundary layers. Also, structured mesh usually yields faster conversion of the solution. Rapid change between adjacent cells deters the smoothness of the mesh and leads to truncation error (the difference between the exact solution of partial derivatives in the governing equations and their discrete approximations). This was of high concern

through the modelling procedure, and a mesh expansion rate of no more than 20% was always applied. The shape of a cell is assessed by its skewness and aspect ratio. Skewness, defined as the difference between the cell's shape and the shape of an equilateral cell of equivalent volume, was limited to 0.4 and 0.8 for 2D and 3D simulations, respectively. Aspect ratio is a measure of the stretching of the cell, and was always kept under 5:1. The aforementioned expansion rate, skewness, and aspect ratio values are recommended by the Fluent manual to reduce truncation errors.

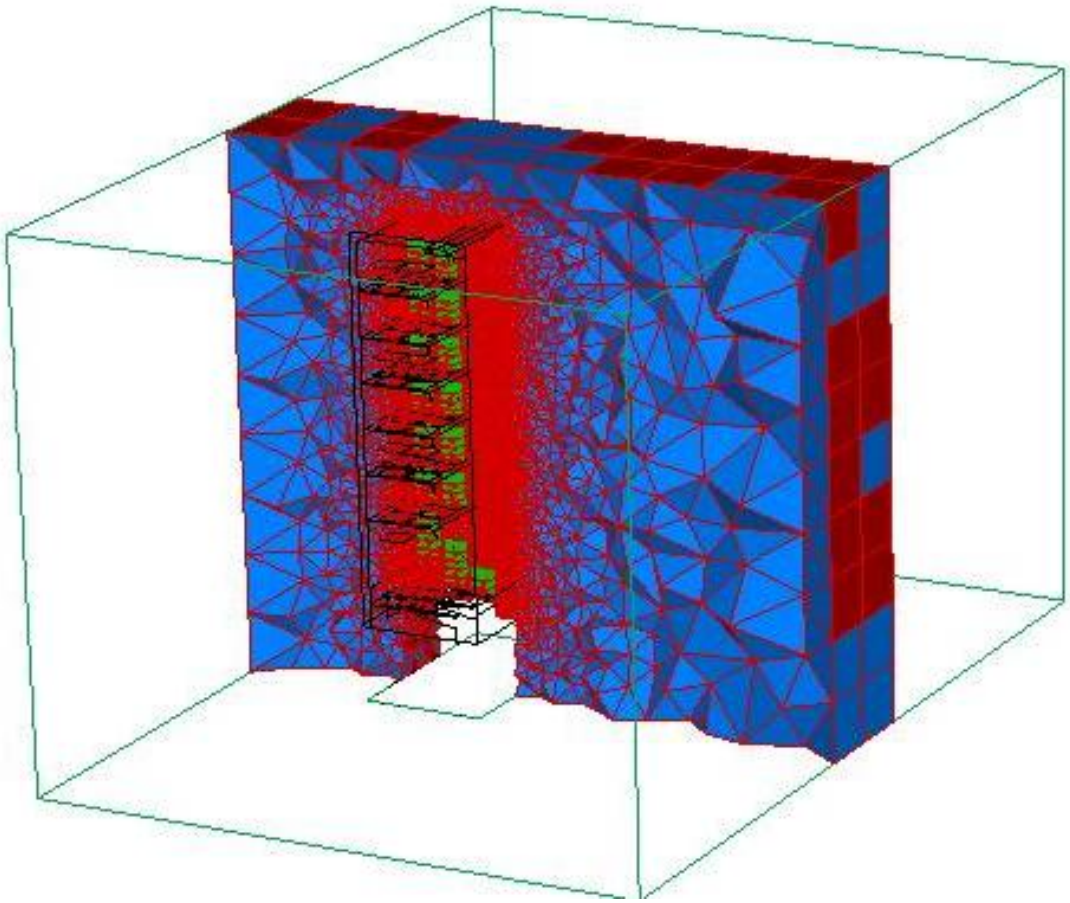

Figure 4.3 3D domain of the test room showing the mesh at the mid-section of the cabinet

4.7 Solver

The solution procedure within the frame of Fluent (solver) consists of the following processes: initialisation, solution control, monitoring solution, CFD calculation, and checking for convergence. Prior to performing iterations, all the discrete values of the flow properties (i.e. velocity, pressure, temperature, etc.) were initialised by setting them with values close to that of the air curtain in order to achieve faster and

more stable convergence. The calculations were performed using a double-precision (dp) accuracy, where 15 significant figures are used to present each variable, rather than the single precision default option which uses seven significant figures only. This choice was deemed necessary in the study of entrainment, to reduce round-off errors resulting from the difference between the computer accuracy and the true value of the variables, although a slight increase in calculation time was experienced.

In order to calculate the surface fluxes of the transport variables at each face between the control volumes, interpolation schemes must be used. Some of the schemes offered by Fluent are the First-order Upwind, Second-order Upwind, and the Quadratic Upstream Interpolation Convective Kinetics (QUICK). Throughout this work, the QUICK scheme, which is a third-order interpolation scheme, was used since it offers a higher level of accuracy. However, using this scheme for the momentum equation was found to yield transient-like results at the boundary of the air curtain, which introduced difficulties in calculating the entrainment rate. Therefore, the momentum equation was solved using the First-order Upwind scheme, while all other transport variables (e.g. the turbulent kinetic energy, dissipation rate, species, and energy) were solved using the QUICK scheme.

The need for correct linkage between the pressure and the velocity in CFD calculations stems from the fact that there is no independent equation for pressure in the solution of the governing equations. The SIMPLE (Semi-Implicit Method for Pressure-Linking Equations) scheme developed by Patankar and Spalding (1972) has been extensively used in the literature due to its robustness and rapid stabilisation. The PISO (Pressure Implicit with Splitting of Operators) algorithm proposed by Issa (1986) was found to improve the robustness and convergence rate of the iterative process, especially when the mesh had a relatively high skewness, hence it was used throughout this work.

At the start of each iteration run during the process of solving the system of algebraic equations for the transport variables, an imbalance (error) exists in the discretized equations, and equality is not satisfied. This imbalance is known as the “residual”, and is introduced to monitor the convergence behaviour of the numerical process. Convergence is defined as the solution of the system of algebraic equations

approaching the true solution of the partial differential equations having the same initial and boundary conditions as the refined grid system, and is deemed to be achieved so long as the global residual satisfies a specific convergence tolerance during the advancement of the iterations. In the present work, the iterative process was terminated when the residual of the various variables reached a plateau of $1x10^{-4}$. However, stricter convergence considerations were required for the transport variables of energy and species, and convergence tolerances of $1x10^{-6}$ and $1x10^{-5}$ were needed to achieve energy and species balances, respectively.

Other variables, such as the temperature at the RAG, were monitored during the iteration process to ensure that convergence has been achieved. The iteration process was terminated when no appreciable change in temperature was observed. In addition, the overall imbalance in mass flow rate, total heat transfer rate, and radiation heat transfer rate for the entire domain were routinely checked to be as low as possible to ensure adequate property conservation.

4.8 Grid independency and adaption

The resolution of the mesh at high gradient regions has a large impact on the stability and convergence of the numerical procedure. It also significantly affects the accuracy of the final computational results. Therefore, a grid independence study must be made to provide assurance that the final values are not being excessively affected by the cell size. Most of the grid independence studies in the literature have been performed by 1) making a simulation with a coarse grid, 2) making another with a finer grid (more elements), and 3) comparing the average values of the two at locations of interest. If the comparison shows that the values are close enough for the application, then the simulation with the coarse grid is sufficiently independent of cell size for the specific application. This however introduces grid points at locations of no interest, hence increasing the computational demand.

In this work, grid-independent solutions were achieved by extensively applying mesh adaptation during the post-processing stage. This feature mainly depends on the preliminary solution obtained with the original mesh to find zones of high gradients for a specific variable. The maximum gradients for temperature and velocity were limited to 1.0, and adjacent cells with gradients higher than that were refined to

produce a mesh that is fine enough and adequate for representing the important features of the flow. This fulfils the requirement of improving the resolution of flow features in particular zones of interest by judiciously adding more cells without excessive increase in computational effort. In addition, this step saved time by not having to go back to Gambit (pre-processor) for further grid refinement. By obtaining identical solutions of different variables (e.g. values of velocity, temperature, etc.) at a certain point in the domain, the final results were then taken to be "grid independent" and the coarser mesh was then put into consideration. Figure 4.4 shows a mesh before and after adaption, where the cells on both sides of an air curtain are refined.

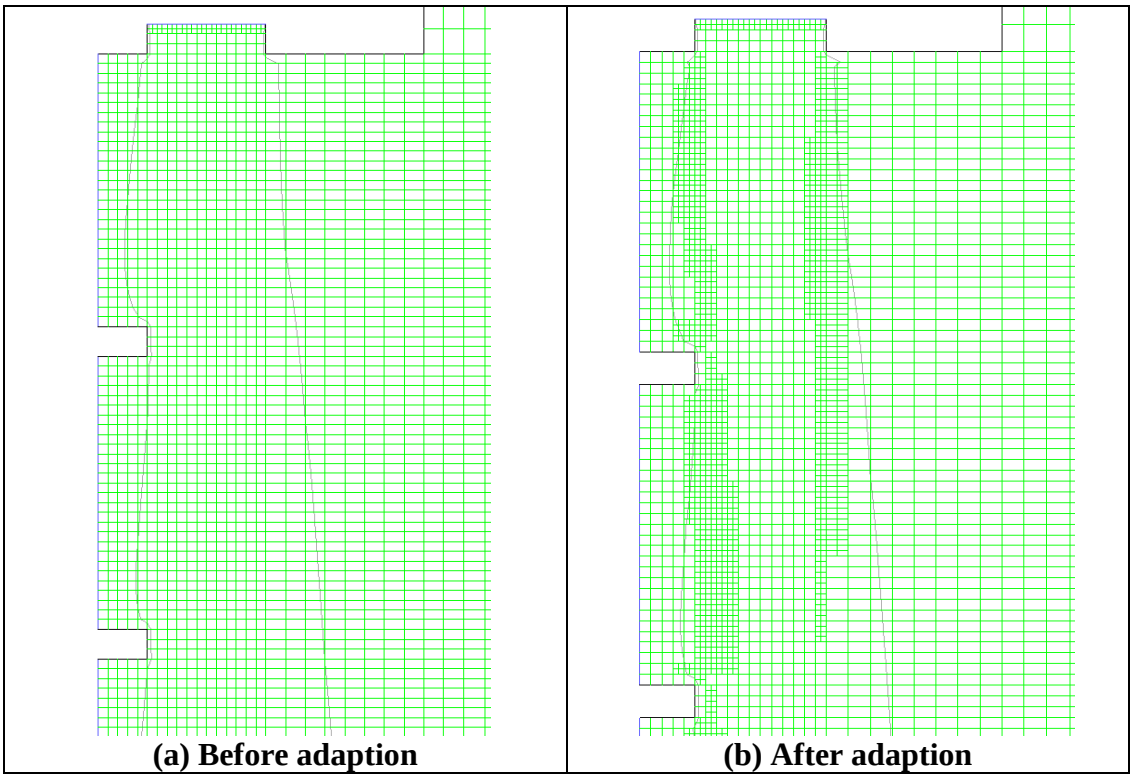

Figure 4.4 Mesh adaption at the edges of the air curtain

4.9 The k-ε model

In this work, the k-ε model has been applied because of its acceptable accuracy and relatively low computational demand when compared to other turbulence models (Stribling (1997), Xiang (2003)). The k-ε model is a two-equation, semi-empirical, eddy-viscosity model in which the Reynolds stresses are assumed to be proportional to the mean velocity gradients, with the constant of proportionality being the

turbulent viscosity, μ_t. This assumption, known as the Boussinesq hypothesis, provides a correlation between Reynolds stresses with mean velocity gradients. The strength of this model stems from the fact that it uses the generation of turbulence kinetic energy, k, to describe the turbulence velocity and its dissipation rate, ε, as an implicit scale.

An enhancement over the standard k-ε model is the Renormalization Group (RNG) k-ε method developed by Yakhot and Orszag (1986). One of the difficulties with the standard k-ε model is the inadequate representation of the effect of small-scale turbulence, which is not usually very significant in high Reynolds number flows but its effect begins to be prominent in low Reynolds number flows or in some local domains of high Reynolds flows, such as close to a surface where the large eddies are reduced by the damping effect of the surface. In this model, they represent the effects of the small-scale turbulent motion by a large-scale turbulence and a modified viscosity. The RNG model introduces an additional term in the ε-equation, compared to the standard k-ε model, which improves its performance. The basic idea behind the RNG model is to systematically filter out the small-scale turbulence to a degree that the remaining scales can be resolved. In his PhD thesis, Xiang (2003) used the RNG k-ε model in the study of open display cabinets and compared results with the standard k-ε model. He concluded that the RNG k-ε model provided results of better accuracy and is more suitable for such application. It is worth mentioning that the computational effort associated with the RNG k-ε model is only marginally higher than that for the standard k-ε model.

In flows where the mean strain rate is considerably large (as in near wall conditions), the standard and RNG-based k-ε models yield negative values for the normal (Reynolds) stresses, which by definition are positive quantities. Moreover, although the aforementioned models can accurately predict the spreading rate in planar jets, they poorly predict the spreading rate for axisymmetric jets (ANSYS Inc., Fluent v 6.3.26 (2006) manual). This is mainly due to deficiencies in modelling the turbulence dissipation rate. The Realizable k-ε model proposed by Shih et al. (1995) was intended to address these deficiencies. The term "realizable" means that the model satisfies certain mathematical constraints on the normal (Reynolds) stresses, consistent with the physics of turbulent flows. As a result, a new equation for the

turbulence dissipation rate based on the dynamic equation of the mean-square vorticity fluctuation together with a new eddy-viscosity formula were introduced to rectify these deficiencies. These enhancements allow this model to accurately predict the spreading rate of planar jets similar to the air flow of the air curtain. The different variants of the k-ε model will be compared in the next chapter and the most accurate one will be used for the simulations.

The flow around the cabinet exhibits both natural and forced convection and proper representation of the buoyancy effects in the k-ε turbulence equations is crucial for accurate results. The turbulence kinetic energy tends to be augmented by the negative buoyancy effect. In places where stratification exists (e.g. between products in a shelf) buoyancy tends to suppress turbulence. In Fluent, the effect of buoyancy on the generation of k is always included when the gravity field and/or temperature gradients are included in the simulations. However, the buoyancy effect on ε is not included by default, and was included in this work by incorporating the "Full Buoyancy Effects" in the viscous modelling step.

4.10 Near-Wall Treatment and wall functions

Capturing the correct thermo-fluid mechanics near the products and the body of the cabinet is crucial for the accurate representation of the thermal and flow behaviour of the cabinet. The accuracy of the solution is highly dependent on the ability of the grid to resolve and transfer solution data from those near-wall regions to the core of the flow field and vice versa. The mean velocity field is affected through the no-slip condition that has to be satisfied at the wall. Unfortunately, all variants of the k-ε turbulence model are only effective for turbulent flows not affected by solid walls, and a special treatment needs to be done to include near-wall situations, especially near the products.

It has been well established that the boundary layer at near-wall regions can be largely subdivided into three layers. In the innermost layer, called the viscous sub-layer, the flow is almost laminar, and the (molecular) viscosity plays a dominant role in momentum and heat and/or mass transfer. In the outer layer, called the fully-turbulent layer, turbulence plays a major role. Finally, there is an interim region

between the viscous sub-layer and the fully-turbulent layer where the effects of molecular viscosity and turbulence are equally important.

Although it is possible to use turbulence models that can be applied all the way to the walls, those models are computationally expensive. The near-wall region can be estimated by adopting the wall functions. Through this approach, the difficult near-wall region is not explicitly resolved within the numerical model but rather is bridged using wall functions (Launder and Spalding 1974). Those functions have been most widely used for industrial flows.

The distances and velocities dealt with in the near-wall boundary layer region are too small, and can be magnified using dimensionless variables with respect to the local conditions at the wall. If y is the normal distance from the wall and U is the time-averaged velocity parallel to the wall, then the dimensionless velocity U^+ and wall distance y^+ are described as:

$$U^+ = \frac{U}{u_\tau} \tag{4.5}$$

And

$$y^+ = \frac{y\rho u_\tau}{\mu} \tag{4.6}$$

The wall friction velocity u_τ is defined with respect to the wall shear stress τ_w as

$$u_\tau = \sqrt{\tau_w / \rho} \tag{4.7}$$

The soul purpose of the near-wall treatment is to include a sufficient number of cells within the boundary layers surrounding walls of importance in order to resolve the turbulent effects of such walls on the mean flow and heat transfer characteristics around the products. The Standard Wall Functions approach uses semi-empirical formulas called “wall functions” to bridge the viscosity-affected region between the wall and the fully turbulent region.

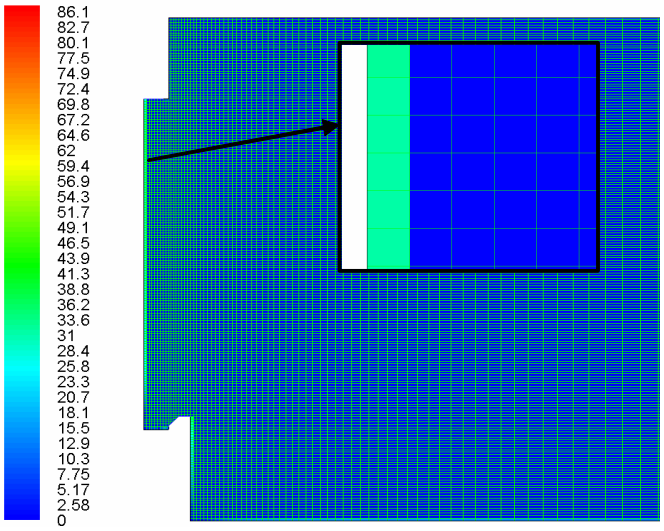

Figure 4.5 Computational grid near the cabinet walls having a y+ of 30

The acceptable distance between the cell centroid and the wall for wall-adjacent cells for the standard wall function, each wall-adjacent cell's centroid should be located as close as possible to the lower bound (y^+=30) within the log-law layer, $30 < y^+ < 300$.

4.11 Boundary conditions

During simulations, the accuracy of the results is as good as the specified values at the boundaries since the solution of the governing equations is initiated from them. Therefore, the boundary conditions in this work are those obtained from experiment in order to faithfully mimic the real physical representation of the thermo-fluid flow of the cabinet.

4.11.1 Wall boundary conditions

Wall boundaries are solid surfaces where the tangential component of velocity is considered to be zero. This hypothesis is usually termed the no-slip condition, where the fluid adheres to the wall boundary of the flow domain. The no-slip hypothesis (u=v=0) necessitates the production of high velocity gradients near walls, and the mean velocity field is inevitability affected where viscous damping near walls reduces the tangential velocity fluctuations, while kinematic blocking reduces the normal fluctuations. Toward the outer part of the near wall region, however, the turbulence is rapidly augmented by the production of turbulence kinetic energy due to the large gradients in mean velocity. Throughout the CFD simulations, the wall

boundary condition is assigned for the test room's walls, floor, ceiling, as well as the body of the cabinet and containers.

4.11.2 Inlet boundary conditions

When air is introduced to the domain (e.g. through the air curtain, air supply of the test room, etc.), its velocity, temperature, moisture fraction and turbulence quantities have to be specified. Those variables are case-specific and are either known from previous experiments or calculated from other quantities, and are usually taken as being uniformly distributed across the inlet boundary.

The turbulence associated with the air curtain controls the performance of the open display cabinet since it determines the level of mixing between the environment and the enclosure. The initial values of k and ε at the domain inlets are specified in term of turbulence intensity, which is defined as the ratio of the root-mean-square of the velocity fluctuations, u', to the mean flow velocity, $\bar{u}$. Generally speaking, a turbulence intensity of 1% or less is considered low and a turbulence intensity greater than 10% is considered high.

Another physical quantity used to assign the turbulence at inlets is the turbulence length scale, *l*, which is related to the size of the large eddies in the flow. The largest eddies that can exist in a fully-developed flow may have a maximum length of 7% of the opening from which they cross. In this work, the turbulence length scale was obtained by multiplying the opening of the DAG by a factor of 0.07, and in cases where a honeycomb is used, the turbulence length scale was found by multiplying this factor by the diameter of the honeycomb conduits (3 mm). Many researchers reported on those issues and found that the turbulence intensity at the honeycomb is in the range of 5 to 10%, which is enough to represent a fully-developed turbulence flow. Furthermore, Xiang (2003) and Navaz et al. (2005) both showed that the entrainment rate and the final solution are not influenced by the change of turbulence intensity in that range. Hence, a turbulence intensity of 5% at the honeycomb outlet is used throughout this study.

4.11.3 Ambient boundary condition

The boundary representing the environment was simulated by a pressure inlet boundary condition. This boundary allows both inflow and outflow, where the

pressure value is taken as the total pressure based on the normal component of the velocity when the flow direction is entering the domain, and the static pressure when it is leaving the domain. At boundaries where air exits the domain, the condition of choice was the pressure outlet (pressure specific) or outflow (mass flow specific). The former is more stable since the pressure is known beforehand at the boundary and the simulation is performed from the pressures at these boundaries. Other variables such as velocity, temperature, moisture fraction, and turbulence intensity are specified at such outlets should there be any backflow from the boundary, otherwise they are not involved in the calculations.

The air mass flow rate through the RAG must match that of the air-off section, and was prescribed in this work by using the "mass flow inlet" boundary condition with a negative sign direction. Physically, specifying the mass flux permits the total pressure to vary in response to the interior solution. This is in contrast to the "pressure outlet" boundary condition where the static pressure is fixed while the mass flow rate varies. Another advantage in using this boundary condition is the elimination of the trial-and-error process in obtaining the exact mass flow rate through the RAG. After performing few iterations only, the mass flow rate from the air-off section was obtained and this value in turn was assigned to the RAG. Temperature and turbulence quantities are irrelevant here since no flow is introduced from the RAG boundary to the domain.

4.12 Radiation modelling

Radiative heat transfer is often overlooked in the CFD simulation of open display cabinets. When products are included in the simulations, and the cooling load is to be determined, radiation modelling is inevitable since it has the tendency to strongly influence the heat transport and the overall fluid dynamics within the cabinet. The significance of thermal radiation on the cabinet is due to the large temperature difference between the products and the surrounding environment, which can be as high as 25^{o}C. The fourth-order dependence of the radiative heat flux on temperature implies that the share of radiation in the thermodynamic balance of the cabinet is comparable to that of convection and conduction, and may contribute to as high as 7% of the sensible cooling load through heating the front part of the products as well

as the inner body of the cabinet (Orphelin et al., 1997). The radiation heat being transferred from the environment is in the form of electromagnetic waves, hence it is not restricted to visible light emanating from sources such as the lightings of the cabinet and the supermarket, but can also be from people, walls, ceilings, floors, and any other objects of relatively higher temperatures surrounding the cabinet.

Among the different radiation models offered by Fluent, only the Discrete Transfer Radiation Model (DTRM) by Shah (1979) and the Discrete Ordinates (DO) model by Chui and Raithby (1993) are appropriate for the application in hand. The choice of a radiation model strictly depends on the optical thickness (or opacity) of the participating medium, given as:

$$(a+\sigma_s)\, s \tag{4.8}$$

where a is the medium absorption coefficient, σ_s is the scattering coefficient, both of which have units of m^{-1}, and s is an appropriate length scale. The absorption coefficient of air is 0.01, and since the ambient air in the test chamber holds small amounts of water vapour, the scattering coefficient can be considered negligible. Finally, taking the length scale s to be the length of the test chamber (5 m), this would result in an optically thin situation ($(a+\sigma_s)\, s << 1$), restricting our choice to be from the two aforementioned radiation models. Although the DTRM model was shown by Xiang (2003) to produce results in good agreement with experiment, it was decided not to use it in this work. Before commencing an iteration run, a file must be created to save the ray tracing, which will then be read during iterations. This step is time consuming, especially in three-dimensional simulations. Therefore, the DO model will be used throughout this work for the modelling of radiative heat transfer.

When considering the interaction with solids, surface emissivity ε is defined as the ratio between the heat flux emitted by a real surface and a black surface at the same temperature. Throughout the course of CFD modelling of shelved cabinets, the body of the cabinet, walls, ceiling, floor, as well as inlet and outlet boundaries were all assigned emissivities, and hence contribute to the calculation of the radiation process.

4.13 Buoyancy effect

When the gravitational force and temperature gradients are included in the simulation of the air curtain, the relatively low temperature of the air curtain jet allows it to

descend to the ground even when no sufficient momentum is employed. This is known as the negative-buoyancy effect where the gravitational force acts on the higher density of the cold air of the air curtain. In this case, FLUENT accounts for the generation of kinetic energy, k, due to buoyancy and the corresponding contribution to the production of the dissipation rate, ε, in the k-ε model.

There are several ways to account for buoyancy effects in the simulations by considering density as a function of temperature. The Boussinesq approximation model has been intensively used by many researchers mainly because of its simplicity and the fast convergence associated with it. This model treats density as a constant value in all solved equations, except for the buoyancy term in the momentum equation. The accuracy of this model is acceptable as long as changes in actual density are small. In this work, however, the use of this model was found to be not feasible since it cannot be used together with species modelling, which is necessary to account for the moisture content in the air that takes part in the calculation of the cooling load of the cabinet.

Another way to address buoyancy in the calculations is by linear interpolation, (Stribling (1997), Xiang (2003) and Hadawey (2006)). This procedure is performed by feeding FLUENT several temperature values and their corresponding densities. Although this method is straightforward and reasonably accurate, it is time consuming and error is likely to take place.

In this work, the incompressible ideal gas model for the density of air is used and was found to give more accurate results than the two previously mentioned methods. Moreover, at pressures below 10 kPa, water vapour can be treated as an ideal gas regardless of its temperature with a negligible error of less than 0.1 percent (Cengel and Boles, 2007). This allows for modelling the water vapour as an incompressible ideal gas as well in this study.

The flow regime at the moment when air leaves the air curtain is forced convection and is governed by the dimensionless Reynolds number, which represents the ratio of internal forces to viscous forces acting on the fluid. The flow regime far away from the DAG is natural convection, and is governed by the dimensionless Grashof number, which represents the ratio of the buoyancy force to the viscous force acting

on the fluid. The flow in open display cabinets can best be described as a mixed convection flow and the importance of the buoyancy forces can be assessed by evaluating the ratio of the Grashof and the Reynolds numbers. A buoyancy driven flow is considered to be dominant when this ratio approaches or exceeds unity. Conversely, buoyant forces may be ignored if this ratio is small.

4.14 Modelling the honeycomb

Using a honeycomb at the DAG has a significant effect on the shape of the initial velocity profile of the air curtain, which dictates the amount of ambient air entrainment through the air curtain. Modelling the fine details of the honeycomb passages hinders the meshing process by calling for impractically high number of cells to accommodate for the transition from extremely small cells in the passages to the large cells of the domain. Therefore, simulating the pressure loss through the honeycomb rather than geometrically representing it is more practical from a modelling point of view.

Within Fluent, the honeycomb was simulated by the porous media model, which adds a momentum source/sink in the governing momentum equations. This special fluid zone is composed of a viscous loss term and an inertial loss term. No viscous resistance takes place through the honeycomb, and only resistance to momentum takes place, resulting in a pressure drop across the honeycomb that is proportional to the fluid velocity in the cells. The pressure drop for each component direction across the honeycomb can be expressed as:

$$\Delta p = C_2(\frac{1}{2}\rho u^2)\Delta m \tag{4.9}$$

where C_2 is the inertial resistance factor (m^{-1}) per unit thickness that provides a correction for the inertial losses in the porous medium, *u* is the velocity (m/s) at each component direction, and Δm is the honeycomb thickness. The research conducted by Patel (1996) on such honeycomb configuration revealed that the loss coefficient per unit thickness along the direction of the passages was in the order of 100 m^{-1}. The two other component directions were assigned relatively higher values (in the order of 10^5 m^{-1}), since no flow is allowed to take place along them.

4.15 Modelling the perforated back panel

Properly modelling the perforated back panel plays an integral part in the accurate prediction of product temperature and also the accurate amount of air being passed to the DAG. Many researchers have attempted to model the perforated back panel as either a velocity-inlet boundary condition for the entire back panel (Foster et al. (2005)) or as small segments at intermittent locations to represent the perforations (Yu et al. (2007)). Although this might provide the right mass flow rate, it does not take into account the upwardly directed air being ejected or the pressure deterioration along the height of the back panel. However, to model the small geometry of the extremely large number of perforations would require an impractically large number of cells, and attempting to use the porous media model to simulate its very small thickness (1 mm) will result in an extremely large number of elements with poor aspect ratio. Instead, the effect generated by the perforated back panel was picked up using the "porous jump" model, which is essentially a 1D simplification of the porous media model, but uses cell interfaces rather than cell zones. Although this model is mainly suited for situations in which the flow is exactly perpendicular to the porous jump surface, it was adopted since it was a simple and effective way to simulate the flow pattern of air leaving the perforated back panel.

4.16 Species modelling

Throughout the simulations in this work, the humidity in the air was represented by enabling the species model to account for the moisture content. Although including moisture content in the calculations doesn't have an effect on the entrainment or infiltration rates, it allows for directly calculating the total cooling load by including the latent part in the calculations. Further details of using the species model will be presented in Chapter 7, Infiltration rate into the cabinet.

4.17 Post-processing

The ability to present the computational results effectively helps to better analyse and visualise the physical characteristics of the flow. In this work, the specialized post-processing software, Tecplot 360, 2008 was used for the graphic representation of the CFD results. Tecplot 360 allows for visualising and analysing the data through high quality plots, as will be seen in the following chapters.

4.18 Summary

This chapter provided an overview of the CFD approach and laid the ground for the construction and assessment of the CFD modelling of the cabinets. Relevant issues in grid generation, specifying appropriate boundary conditions, and turbulence modelling have been discussed, among others that dictate the accuracy and sensitivity of the results. Effective modelling necessitates that only the combination of mathematical models significant to the physics of the problem are included, and inclusion of models that are not of importance add to the complexity of the model and could be a source of error. The next logical step is to validate the numerical predictions against experimental results, which is the subject of the next chapter.

CHAPTER 5
CFD MODEL VALIDATION

"The truth is generally seen,
rarely heard"

(Baltasar Gracian, 1601-1658)

In this chapter, the ability of the CFD approach to reproduce the thermo-fluid dynamics of the cabinet is examined. PIV and IR data were used to validate the numerically derived CFD results. Two cabinet configurations were considered. The first is an idealisation of a fully packed low-front display cabinet where an isothermal air curtain is allowed to flow down a wall and only interacts with the ambient air. The second configuration is that of a low-front refrigerated cabinet with shelved products. Using the ideal cabinet configuration, simulations were performed to evaluate different variants of the k-ε turbulence model. A 3D model is used for the evaluation of the standard configuration.

5.1 Introduction

Chapter 4 introduced some of the theory behind CFD, and the different mathematical models that have been used in the simulation of open refrigerated display cabinets. However, for any CFD simulation to be credible, a validation study needs to be performed in order to quantify the modelling and numerical uncertainties in the simulation. This develops a level of trust in the CFD results and assures that the assumptions and mathematical models used for the simulations are appropriate. The validation procedure depicted here is commenced by experimentally obtaining velocity and temperature profiles at the cabinet's mid-section using the PIV and IR techniques. Then, based on the geometry and boundary conditions obtained from experiment, two- and three- dimensional CFD models are produced and the results are compared with their experimental counterparts.

Two cabinet configurations were used for validation, as introduced in Chapter 3, Experimental Facility. The first is a simplification of an open refrigerated display

cabinet where the shelves are fully loaded with products. The final flow domain can be represented by an air curtain flowing down a wall resembling the flow of a wall plane jet. The second configuration is that of an ordinary cabinet having products on the shelves. The DAG width in both configurations is chosen to be 12 cm, and the display height is 200 cm. The validation study performed on the ideal situation was isothermal. Therefore, cross flow was not used to control the thermal conditions of the test room.

5.2 Results of the idealised configuration

5.2.1 Flow visualisation

The flow details at the boundary of the air curtain can be seen during PIV experimentation when only the air curtain is seeded by particles while the ambient air is maintained with no or low particle density. This allows for qualitative visualisation, and clear images are possible in the beginning of the test runs when the ambient air is not yet contaminated with particles, hence, the camera detects the reflected laser light from the particles flowing with the air curtain only. Figure 5.1 shows sequential PIV frames of 0.1 second intervals along a flow window of 30 cm by 30 cm below the DAG. Since the laser light used is green, the obtained images are also green, but the displayed colours were altered here for better visualisation. Many vortices of different sizes coexist at the interface between the air curtain and ambient air. It is noticed that small eddies are initially formed, then grow in size as they migrate down the air curtain, and finally disperse as they merge with the downward stream of flow. The arrow in the images tracks a single eddy as it goes through its creation and destruction history. At first, an indentation is formed where ambient air is entrained into the air curtain and in the same time part of the air curtain intrudes into the ambient air (Figure 5.1 (a)). This flow pattern occurs as a result of the instability at the edge, which encourages the size of eddies to increase as they flow down with the stream (Figure 5.1 (d)). As time elapses, each eddy constitutes a lump that is separated from the main flow of the air curtain and is diluted in the ambient air, while the engulfed ambient air is also diluted within the stream of the air curtain. It is this entrained ambient air that becomes a cooling load when infiltrated into the cabinet. It is worth mentioning that no such structure exists across the main core of

the air curtain, and only takes place at the boundary. This observation explains the preference of using a wider air curtain over a thin one of similar mass flow rate, since the line of interaction would be further away from the front part of the shelved products, as will be seen in Chapter 6, Quantification and minimisation of entrainment rate through the air curtain.

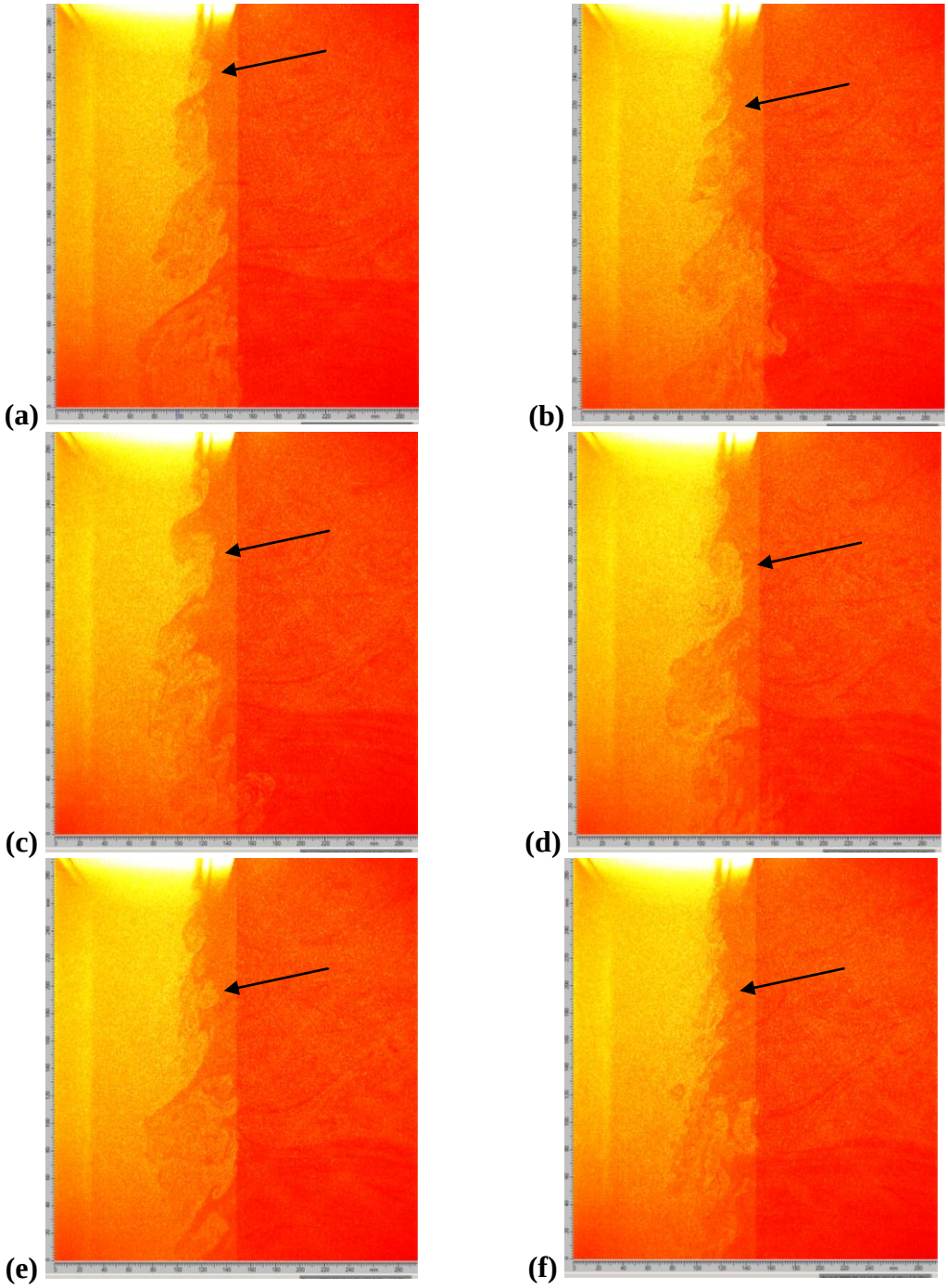

Figure 5.1 Sequential PIV images showing eddy action at the air curtain boundary (Image size=30x30 cm, Time interval=0.1 sec)

Figure 5.2 shows streamlines of the air curtain which were obtained from the time-averaged PIV data and the steady-state CFD simulations. The results obtained from both techniques highly match, assuring confidence in the CFD technique. As can be seen from both techniques, the streamlines approach the cabinet at the upper part with the same intensity, showing the entrainment action of ambient air through the air curtain. At the lower part, air spillage is observed where the streamlines leave the vicinity of the display opening. Since the air curtain and the ambient air both have the same temperature (isothermal flow), it tends to immediately spread after discharge and no inward deflection is experienced as a result of negative-buoyancy.

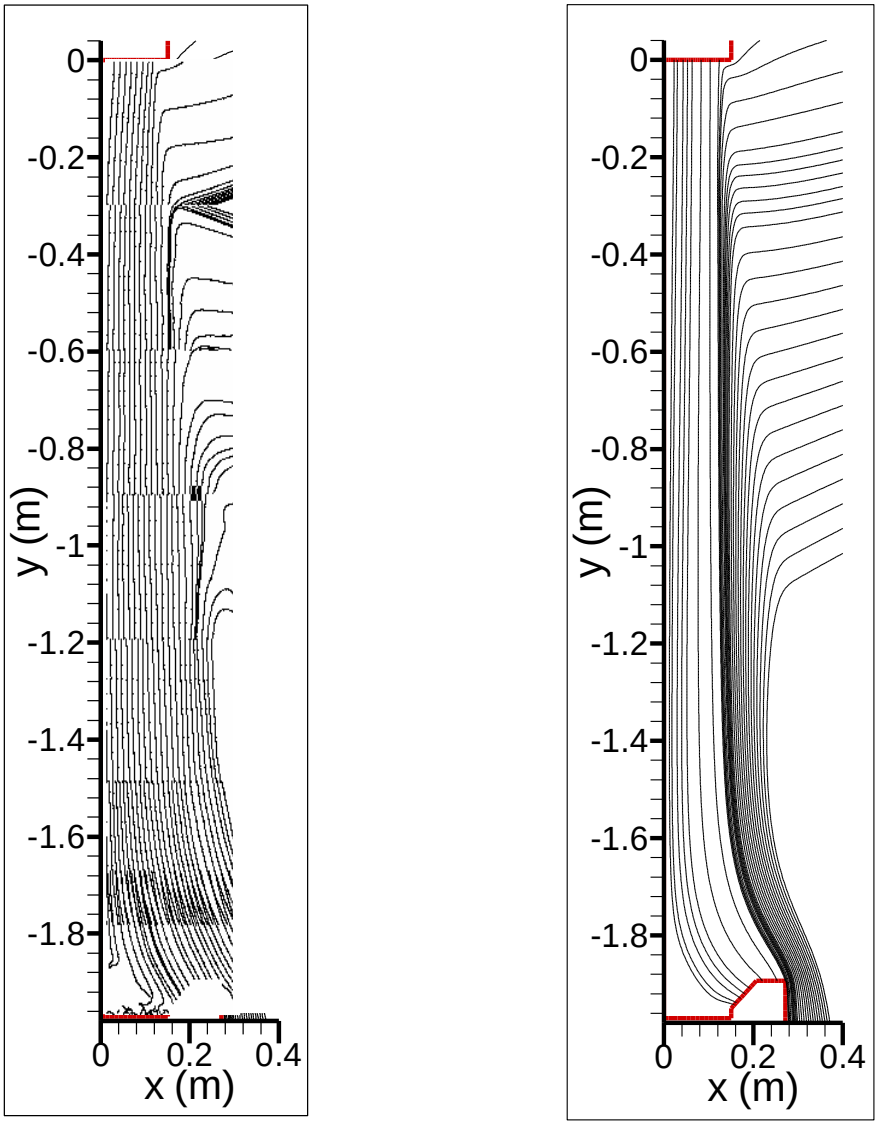

(a) PIV **(b) CFD**

Figure 5.2 Streamlines of the air curtain from a) time-averaged PIV results and b) steady-state CFD results

At this point, it is imperative to emphasise the difference between streamlines and velocity contour lines, since they can be misleading in the explanation of the thickness of the air curtain. Streamlines are paths traced by massless particles placed at arbitrary locations in a steady-state simulation that can exemplify the nature of the vector field flow in a particular region in the domain. Velocity contour lines, on the other hand, are lines of constant velocity magnitude, showing regions of distinct velocity gradients. Figure 5.3 shows lines of velocity contours (black) and streamlines (green) obtained from the PIV and CFD techniques, respectively. From the figure, the boundary of the air curtain can be identified using velocity contours, which show an immediate spreading of the air curtain after discharge. The streamlines on the other hand illustrate the entrainment action at the boundary of the air curtain, which depict an inward deflection through the air curtain's boundary. Comparing the air curtain widths at the bottom of the figure, it can be seen that the one measured by PIV is slightly wider than that predicted by CFD. This may be due to the deficiency of the k-ε turbulence model in accurately predicting the expansion rate of free jets, as will be shown later in this chapter.

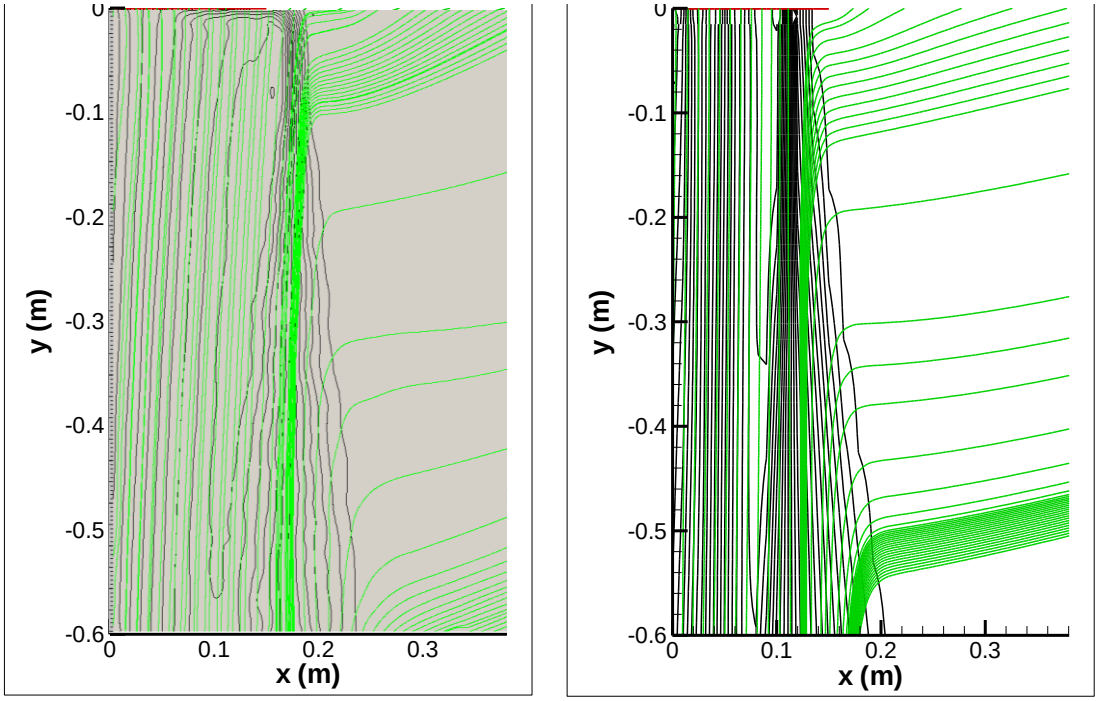

(a) PIV **(b) CFD**

Figure 5.3 Velocity contours (black) and streamlines (green) from the a) PIV and b) CFD results

5.2.2 Comparison of turbulence models

Being able to accurately reproduce the velocity distribution in CFD simulations is critical for the analysis of the entrainment process through the air curtain. This is because entrainment is mostly momentum driven, even though it can also be slightly influenced by buoyancy effects when a refrigerated air curtain is encountered. In this section, the PIV data are compared with CFD results obtained by using the Standard k-ε, the RNG k-ε, and the Realizable k-ε turbulence models in order to determine the turbulence model that can best reproduce the flow mechanics of the air curtain. All variants of the k-ε turbulence model involve two equations to solve for the turbulent kinetic energy and dissipation rate. As mentioned earlier in this work, the flow behaviour of air curtains is complex due to the simultaneous presence of entrainment and mixing at the boundary of the air curtain. Implementing an accurate turbulence model capable of faithfully predicting the contribution of the turbulence activity at the boundary is therefore critical. Most of the CFD work done on the analysis of the flow mechanics of air curtains mainly used either the Standard k-ε or the RNG k-ε models. The Standard k-ε model is known for its stability and robustness. Earlier CFD studies conducted by Stribling (1997) concluded that the Standard k-ε model has difficulties in accurately simulating the air curtain. The main drawback of the Standard k-ε model was found to be its tendency to overestimate the length of the potential core and underestimate the jet expansion (Fernandez et al. (2007)). The RNG k-ε model is a more sophisticated turbulence model that includes a modification to the transport ε-equation, which responds to the effects of rapid rate of strain and stream curvature that cannot be properly represented by the Standard k-ε model. According to the Fluent manual, the Realizable k-ε model is a relatively recent development and is more capable of accurately predicting the spreading rate of both planar (e.g. air curtain) and round jets. The same reference also claims that this model is more likely to provide superior performance for flows involving recirculation, similar to the flow structure at the outer edge of the air curtain.

The consideration in finding a suitable turbulence model here is different from that considered by Stribling (1997) and Xiang (2003), where the model of choice there was based on the accurate prediction of the product temperature and the overall cooling load of the cabinet. Here, however, a turbulence model is considered

accurate if it can faithfully reproduce the velocity and turbulent kinetic energy fields of the air curtain, and more importantly is capable of producing the right air curtain thickness.

The computational domain used to validate the idealised configuration is shown in Figure 5.4. The path taken by the air prior to being ejected into the atmosphere certainly has an effect on the velocity profile downstream of the DAG. Therefore, the flow of air leaving the evaporator (air-off) and passing through the back panel, canopy, and honeycomb is considered. The significant geometrical details in the path of the flow were closely depicted in the geometry, and dimensions as small as 0.5 cm were included during the construction of the domain.

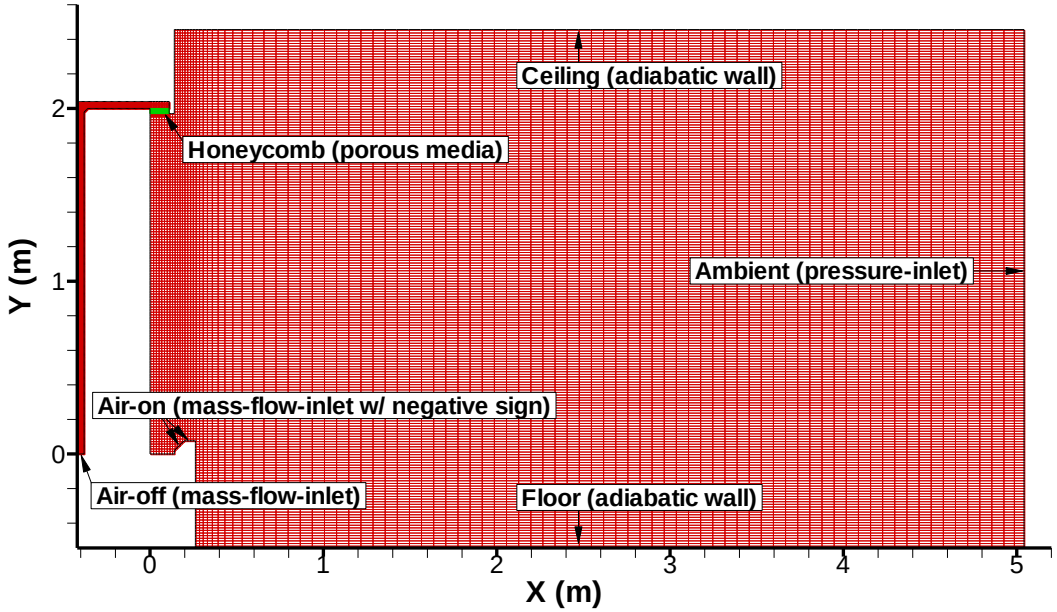

Figure 5.4 Computational domain of the idealised configuration

Since the aim here is to simulate the flow mechanics along the air path, the honeycomb was represented by the porous media model in order to pick up the effects of creating pressure drop, straightening of the air, and suppressing the turbulence kinetic energy through the honeycomb. The air-off mass flow rate per unit cabinet length (0.11 kg/s.m) was found by superimposing the discharge velocity profile of the PIV data on a velocity-inlet boundary of a separate model where the DAG was the inlet of the domain. Since no data is available for the amount of turbulence intensity after the air has left the evaporator (air-off location), the model assumes a fixed turbulent intensity of 10% and a turbulent length scale of 7% of the

inlet width (Stribling 1997). The PIV technique could have been used to experimentally determine the turbulence intensity at this location, however, an intensive modification to the cabinet would have been necessary in order to eliminate the reflection from the surrounding surfaces, and was thought to be out of the scope of this work. Furthermore, the work of Navaz et al. (2005) showed that for the range of Reynolds numbers dealt with in open display cabinets, the turbulence level at the back panel has minimal or no effect on the final shape of the velocity profile at the DAG, and does not contribute much to the overall entrainment through the air curtain. The turbulence intensity at the honeycomb (which is represented by a porous media zone) was found to be nearly 5%, which is close to the 6% turbulence intensity experimentally obtained by Navaz et al. (2002).

Figure 5.5 shows stream-wise (-y) velocity contours of the numerical and experimental results. The PIV result shows a transient nature at the outer edge of the air curtain. Results closer to the steady-state regime would have been possible if more that 50 images were averaged for every view. However, this was constrained by the available memory capacity of the computer used for the experiments. It can be seen from the figure that the three numerical models show less expansion rate than what was found experimentally. Moreover, all the simulations overestimate the length of the potential core region, which is a direct consequence of a smaller expansion rate and a lower transversal diffusion of momentum. It is important to note that the experimental PIV results are three-dimensional (although are presented in a two-dimensional domain), whereas the numerical results assume two-dimensionality. This puts a limit to the expansion process in the third dimension; hence, the potential core region throughout the simulations is not allowed to decay as is experienced in reality.

Figure 5.6 compares PIV and CFD results of the velocity magnitude extracted from a vertical line 10 cm from the wall where the peak velocity is located. The PIV profile is actually a cluster of seven frames, and producing a smooth line was not possible due to the gaps and overlaps between the frames. The numerical and experimental results show an overall good agreement except for the near-discharge region. All variants of the k-ε model overestimate the velocity magnitude along the first 50 cm from discharge, and fail to reproduce well the deceleration regime at this region. The

Standard k-ε model however shows the closest results to the experimental data, and the Realizable k-ε model has the worse performance for all the investigated models. Obtaining accurate results at the bottom part of the air curtain near the RAG was difficult because of the existence of the solid body of the RAG together with the large amounts of laser light being reflected from the body of the cabinet. This is shown in the bottom of the figure as an instability in velocity profile.

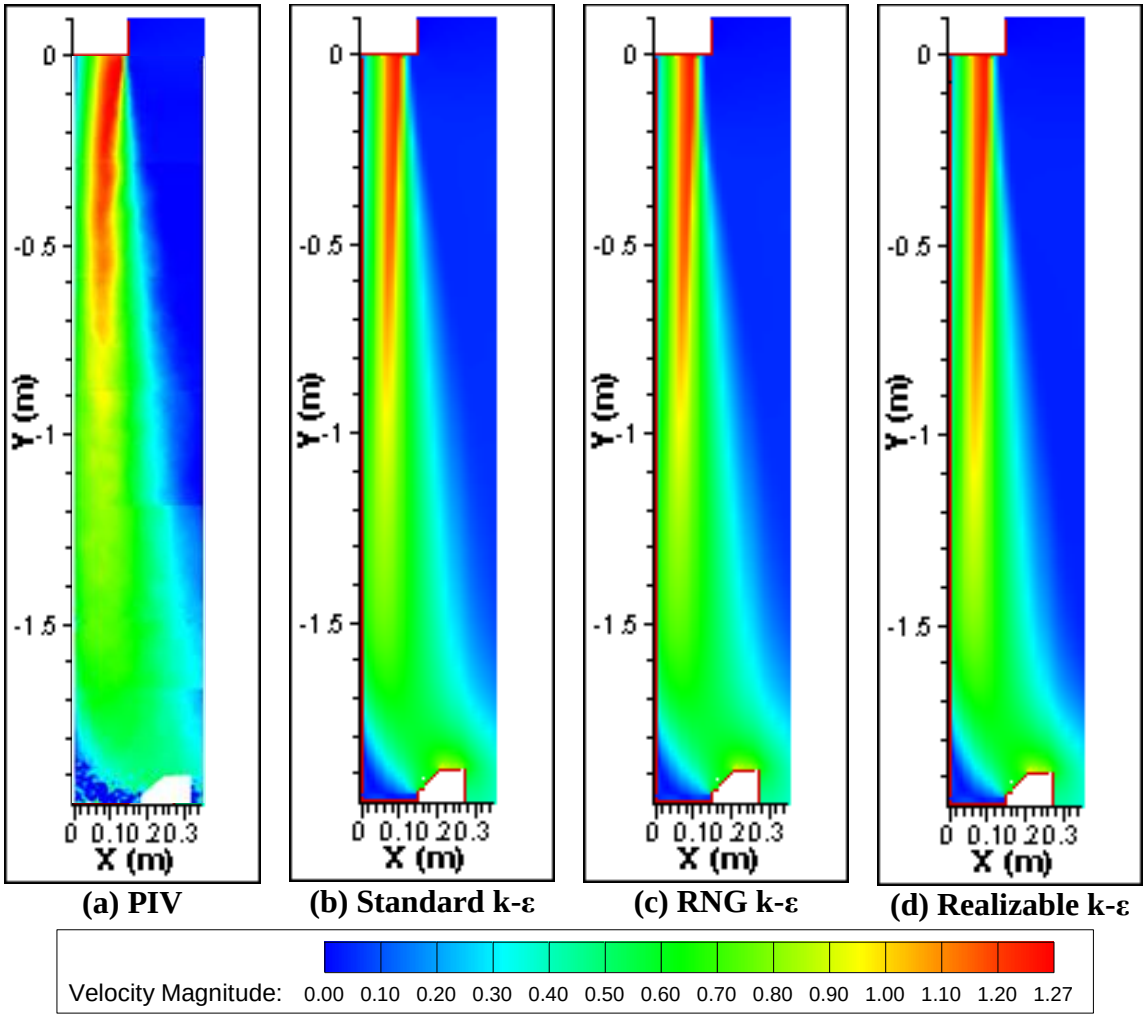

Figure 5.5 Stream-wise (y-) velocity contours for the PIV and CFD results

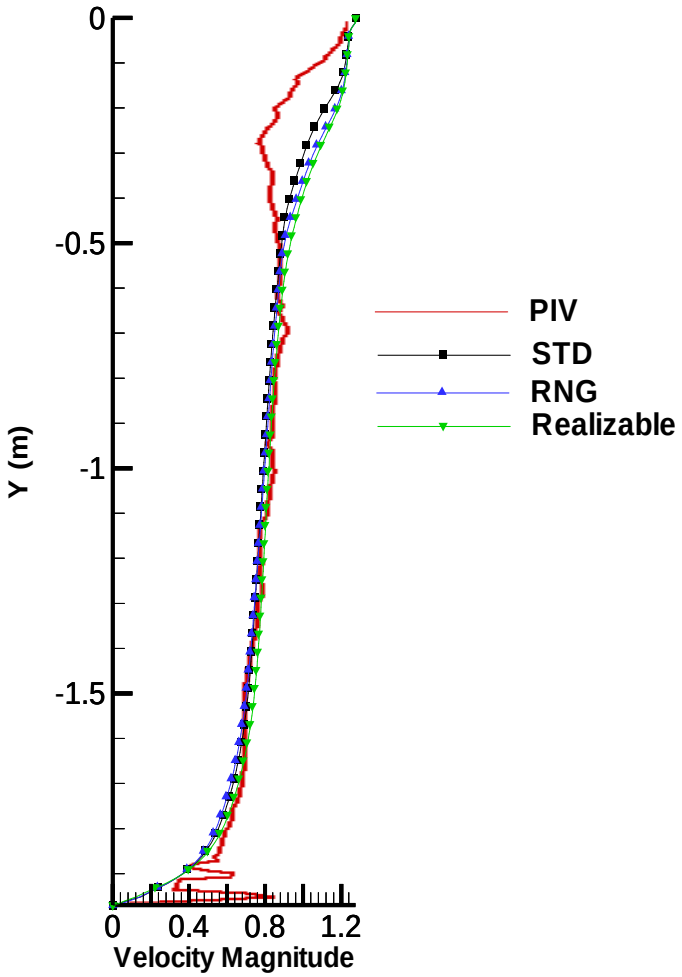

Figure 5.6 Velocity magnitude along a vertical line 10 cm from the wall as measured by PIV and predicted by different turbulence models

Figure 5.7 compares the x- and y- velocity profiles for the CFD predictions and the experimentally obtained PIV data, taken at a horizontal line 10 cm downstream of the DAG. In the figure, the velocity magnitudes of the x- and y- components differ by a factor of 10, so the x- component is much smaller than its y- component counterpart. It is clearly seen that the predicted y- velocity component is in close agreement with the measured PIV results, and the peak magnitude only differs by a value of 0.03 m/s. The predicted peak location is off by less than one cm, showing that the simulation predicts the experimental results well, and it can be concluded that the simulation was successful in predicting the magnitude and location of the peak velocity downstream of the honeycomb. The x-component velocity profiles also show good agreement between the CFD and PIV data. At this height (10 cm below

the DAG), the relatively high downward velocity tends to induce (draw) ambient air towards the air curtain. This is clearly shown in the figure by a negative (x-) velocity component along the entire distance from the back wall. The marginal decrease in the (x-) velocity component at the boundary of the air curtain (at about x=11 cm) is a clear indicator of the mixing process taking place at this location.

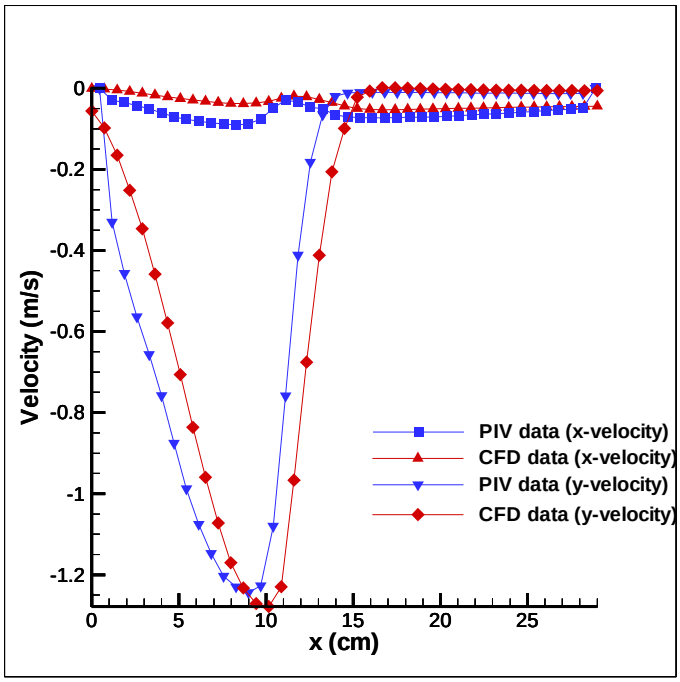

Figure 5.7 CFD and PIV comparison of velocity component profiles 10 cm below the DAG

Figure 5.8 shows stream-wise (y-) velocity profiles obtained from the PIV and CFD techniques at 10 cm intervals from the DAG. The velocity profiles spread immediately after discharge. This spreading is a consequence of the interaction at the boundary, which causes damping of the air curtain velocity and acceleration of the ambient air. The peak velocity however is mostly preserved along the height of the air curtain, and starts to deteriorate only after about 150 cm from the DAG. This observation was also noticed by Field and Loth (2006), who reported that the peak velocity was not significantly decreased along the 160 cm height studied therein. From the figure, it can be seen that the spreading rate measured by the PIV technique is slightly more pronounced than that predicted by CFD, and even though the match of the PIV and CFD results is not perfect, the accuracy of the numerical predictions was considered acceptable in view of the low relevant computational costs and the

engineering application in hand. Therefore, it can be concluded that all variants of the k-ε model produce similar results. This might be attributed to the low velocity magnitudes dealt with in this case. However, the Standard k-ε model offers the closest results with experiment and therefore will be used for further investigations in this work.

The accuracy of numerical solutions is directly dependent on laying an adequate number of grid points near regions of interest for the sake of acquiring a sufficient amount of information. The amount of heat and mass transfer during the entrainment process at the boundary of the air curtain is intense and needs to be simulated with accuracy. Moreover, being able to accurately reproduce the convection process near the products is vital in reproducing the experimental results. Therefore, the aforementioned regions must be properly meshed since the solution there determines the capability of the simulation to accurately represent the experimental results. Having sufficient amounts of grid points near such areas also ensures the stability and convergence during iterations.

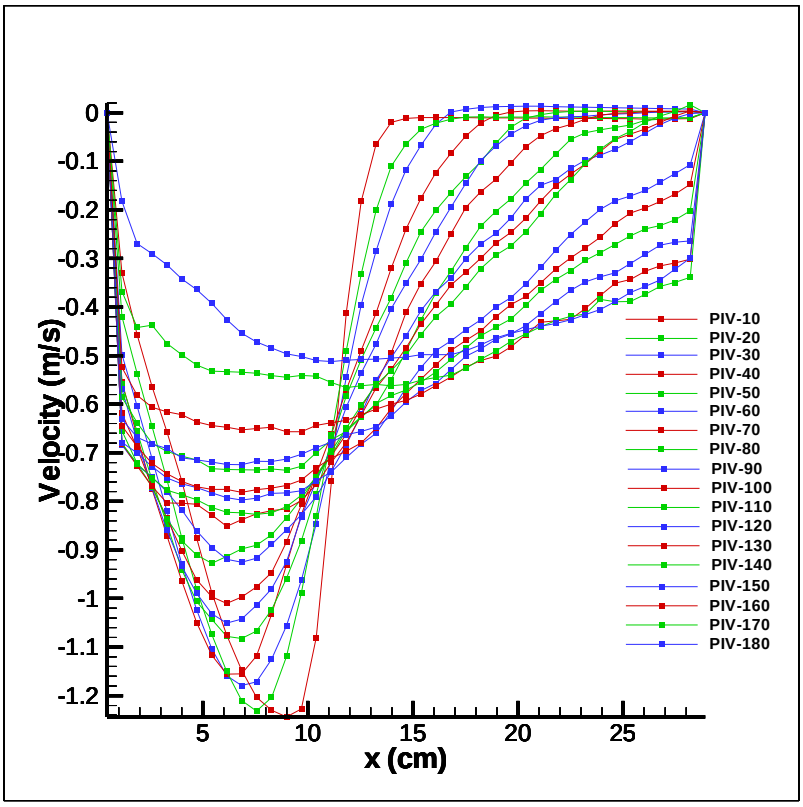

(a) PIV

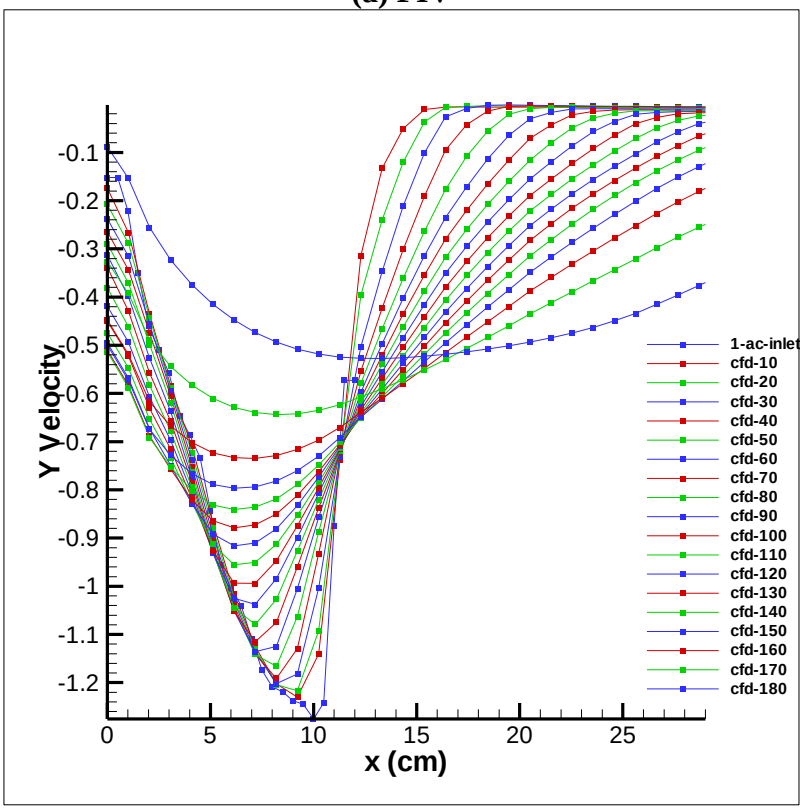

(b) CFD

Figure 5.8 Evolution of stream-wise (y-) velocity profiles at 10 cm intervals from the DAG

In order to make sure that the final solution is independent from the mesh size used, a practice that is widely adopted is the "mesh independency test", where the grid is doubled twice in each direction after which results are compared. The produced grid is considered satisfactory if the solution is not enhanced by further refinement. This method however introduces extra grid points where they may not be needed. The meshing process in this work was given particular attention from the beginning of the pre-processing stage. However, performing a grid independency test is crucial in building confidence in the results. Instead of arbitrarily locating more grid points in the domain, refining the mesh was performed based on a converged initial solution, after which the mesh adaption tool was used to locate adjacent grid points of velocity gradients higher than a prescribed value. Figure 5.9 (a) shows the mesh as generated during the pre-processing stage, while Figure 5.9 (b) and (c) illustrate the solution adaption for areas of velocity gradients higher than 0.25 and 0.1, respectively. It is evident from the figure that the elements at the air curtain's outer edge have velocity gradients higher than the prescribed maximum thresholds, and were consequently divided in order to produce a smoother velocity gradient in this region. This is presented by the high-density grid points clustered in this region. The grid points near the back wall were masked to prevent them from being refined. This was necessary in order to preserve the near-wall-treatment condition of the Standard Wall Function, which demands that those elements have y^+ values in the range from 30 to 300, as was discussed in the previous chapter.

Figure 5.10 shows the stream-wise (y-) velocity profiles 10 cm below the DAG and for a distance of 20 cm from the back wall for the corresponding grid distributions. The grid size increased from 22,897 in the base mesh, to 22,993 in the 0.25 velocity gradient, to 24,127 in the 0.1 velocity gradient. The figure shows that the additional refinement made after a maximum velocity gradient of 0.25 did not provide any advantage since the solution is nearly the same and the peak velocity is only marginally increased after this refinement. This shows that the mesh created during the preliminary stage, which originally had a velocity gradient of 0.5, was sufficient in representing the flow details of the air curtain. It can be concluded that using adaption helps to place additional grid points where needed to resolve important

fluid-flow details without adding excessive grid points at areas of no interest in the domain.

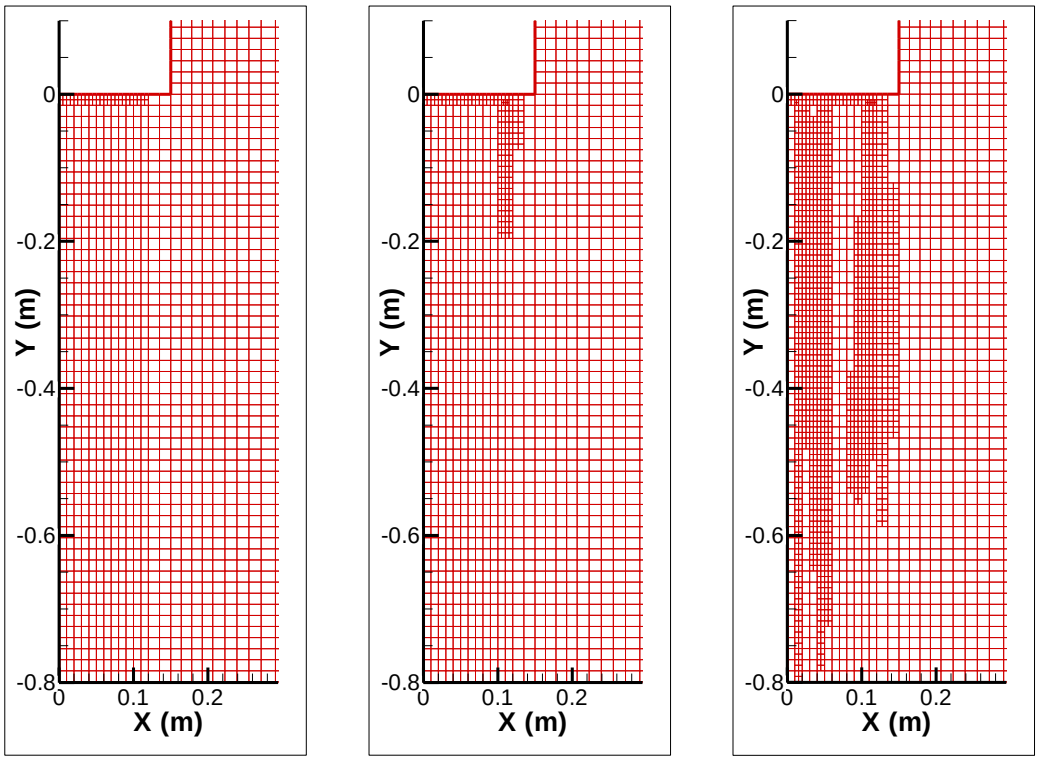

Figure 5.9 Solution adaption of velocity gradients of a) 0.5, b) 0.25, and c) 0.1

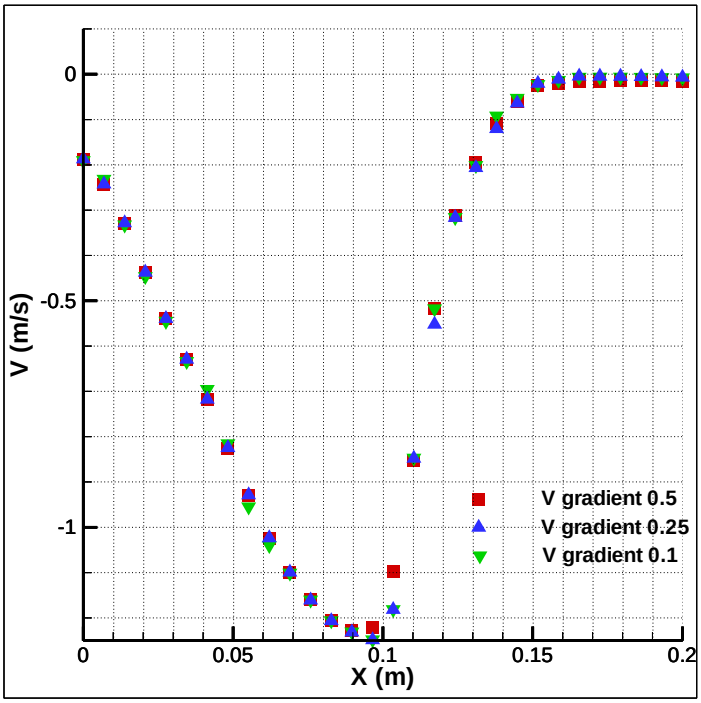

Figure 5.10 Stream-wise (y-) velocity profiles 10 cm below the DAG for grid distributions having velocity gradients of 0.5, 0.25, and 0.1

5.3 Validation of the shelved low-front cabinet

This section presents the validation of the numerical simulations for the shelved low-front refrigerated display cabinet. In order to carry out tests under controlled conditions as specified by the ISO standard, the test room must be capable of maintaining temperature and humidity conditions. Therefore, a cross-flow must constantly be supplied to fulfil this task. This necessitates the use of a three-dimensional computational domain where the dimensions of the test room and the cabinet can both be represented.

According to the ISO standard, the mean horizontal air cross-flow within the test room must be 0.2 m/s and measured at designated points near the leading edge of the cabinet, as was illustrated in Chapter 3. This requirement was initially fulfilled before data acquisition. However, placing the laser equipment (e.g. the digital camera, robot, personal computer, and air cylinder, etc.) upstream of the cabinet decreased the cross-sectional area, which in turn increased the cross-flow velocity at the specified locations to a value of 0.34 m/s. Locating the equipment upstream of the cabinet was inevitable to protect them from being damaged by the oil droplets (seeding particles) needed for the PIV measurements. More importantly, having the camera facing the cross-flow (by locating it downstream of the cabinet) would have allowed oil droplets to accumulate on the laser filter, leading to the contamination of the results. Therefore, the cross-flow velocity applied at the inlet of the test room was taken to be 0.34 m/s during the validation procedure in order to perform a comparison between simulation and experiment. The temperature and humidity ratio of the test room were measured during testing to be 293 K and 0.0073 kg_w/kg_{da}, respectively.

The total mass flow rate through the cabinet was calculated by finding the average face velocity at the inlet of the back panel. A hot wire anemometer was used at 13 measuring points, and the average velocity was found to be 4.24 m/s. Knowing the cross sectional area and the air-off density, the calculated mass flow rate was 0.15 kg/s. The average air-off temperature and humidity ratio were also measured as explained in chapter 3, and were 283 K and 0.0065 kg_w/kg_{da}, respectively. Table 5.1 shows the experimentally obtained conditions that were used as inputs to the 3D CFD model.

Table 5.1 Experimentally obtained inputs to the CFD model

Parameter	Model input
Air-off mass flow rate (kg/s)	0.15
Air-off average temperature (K)	283
Air-off humidity ratio kg_w/kg_{da}	0.0065 (RH=85%)
Test room velocity (m/s)	0.34 m/s
Test room temperature (K)	293
Test room humidity ratio kg_w/kg_{da}	0.0073 (RH=50%)

Analogous to the grid size requirements of CFD simulations, the size of the interrogation area used during the PIV measurements had to be checked to ensure that there is no data dropout, and the flow dynamics of the air curtain is accurately captured. In order to achieve this, the distance travelled by the seeding particles must cover a fraction in the range from 25 to 50 % of the interrogation area. Using a very small interrogation area makes the particles travel a large fraction of the interrogation area and the particles might even leave the interrogation area, leading to a loss of information. Using a very large interrogation area on the other hand allows the particles to travel a small fraction of the interrogation area, which prevents the camera from recognising the flow pattern of the seeding particles. Clearly, using a small interrogation area offers better resolution since more vectors are produced. In order to retrieve the information near the edges of the interrogation areas, an overlapping of 25% in both the vertical and horizontal directions was performed, which generated additional vectors, as was described in Chapter 3. Figure 5.11 shows vector maps of a 30x30 cm area below the DAG using three interrogation area sizes (measured in Pixels), namely 32x32 (85x85 vectors), 64x64 (42x42 vectors), and 128x128 (21x21 vectors). From the figure, it can be seen that the 32x32 pixel interrogation area produced erroneous results at the ambient side due to the low velocity, while the 128x128 pixel interrogation area failed to show details near the outer edges of the air curtain. Therefore, it can be concluded that a 64x64 interrogation area offers a good compromise between the required distance to be travelled by the particles and the spatial resolution required to produce the details of the flow.

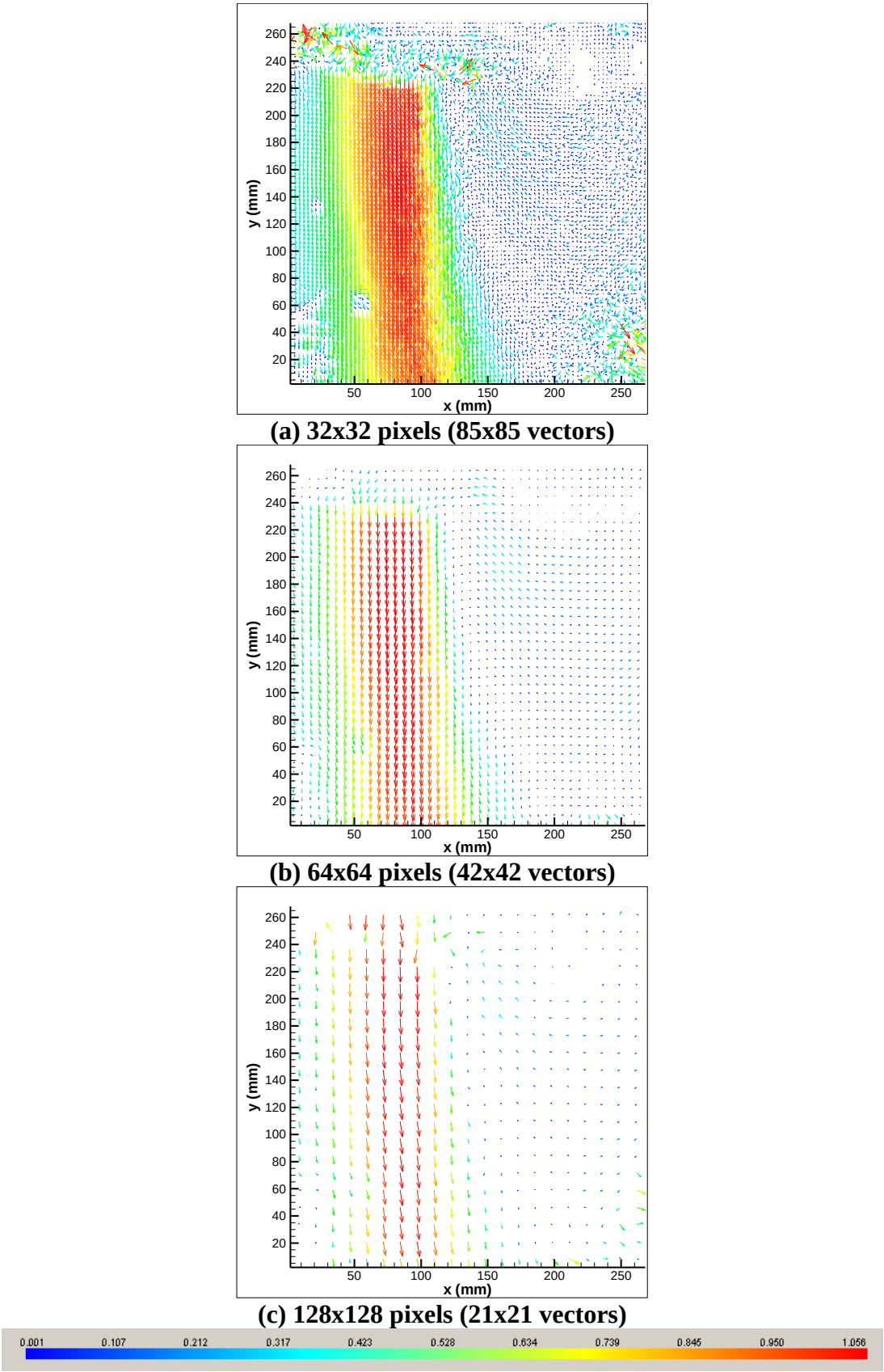

(a) 32x32 pixels (85x85 vectors)

(b) 64x64 pixels (42x42 vectors)

(c) 128x128 pixels (21x21 vectors)

Figure 5.11 Vector maps of a 30x30 cm area under the DAG obtained using different interrogation area sizes

5.3.1 Comparison of flow patterns

Figure 5.12 shows the stream-wise (y-) velocity vectors of the experimental and numerical results. It is clearly seen that the CFD simulation successfully reproduced the air flow patterns obtained from experiment. At the DAG, both the magnitude and location of the peak velocity are accurately predicted. A common feature of non-isothermal air curtains is the tendency to bend inward towards the cabinet due to the density difference (and hence pressure difference) between the air curtain and the adjacent ambient air, as confirmed by Field and Loth (2006). The 10 ^{o}C temperature difference between the two air streams was supposed to produce such effect, but the figure shows that the air curtain is dragged away from the shelves. The cross-flow creates a recirculation region as it flows around the side wall, hence creating an area of low pressure that tends to drag the air curtain away from the cabinet. It is noticed that the air curtain is broken near the forth shelf. At this height, the downward momentum of the air curtain deteriorates by the cross-flow, where the air changes its direction to the direction of the cross-flow. The downward flow regains its strength again near the RAG as a result of the suction of the evaporator fans.

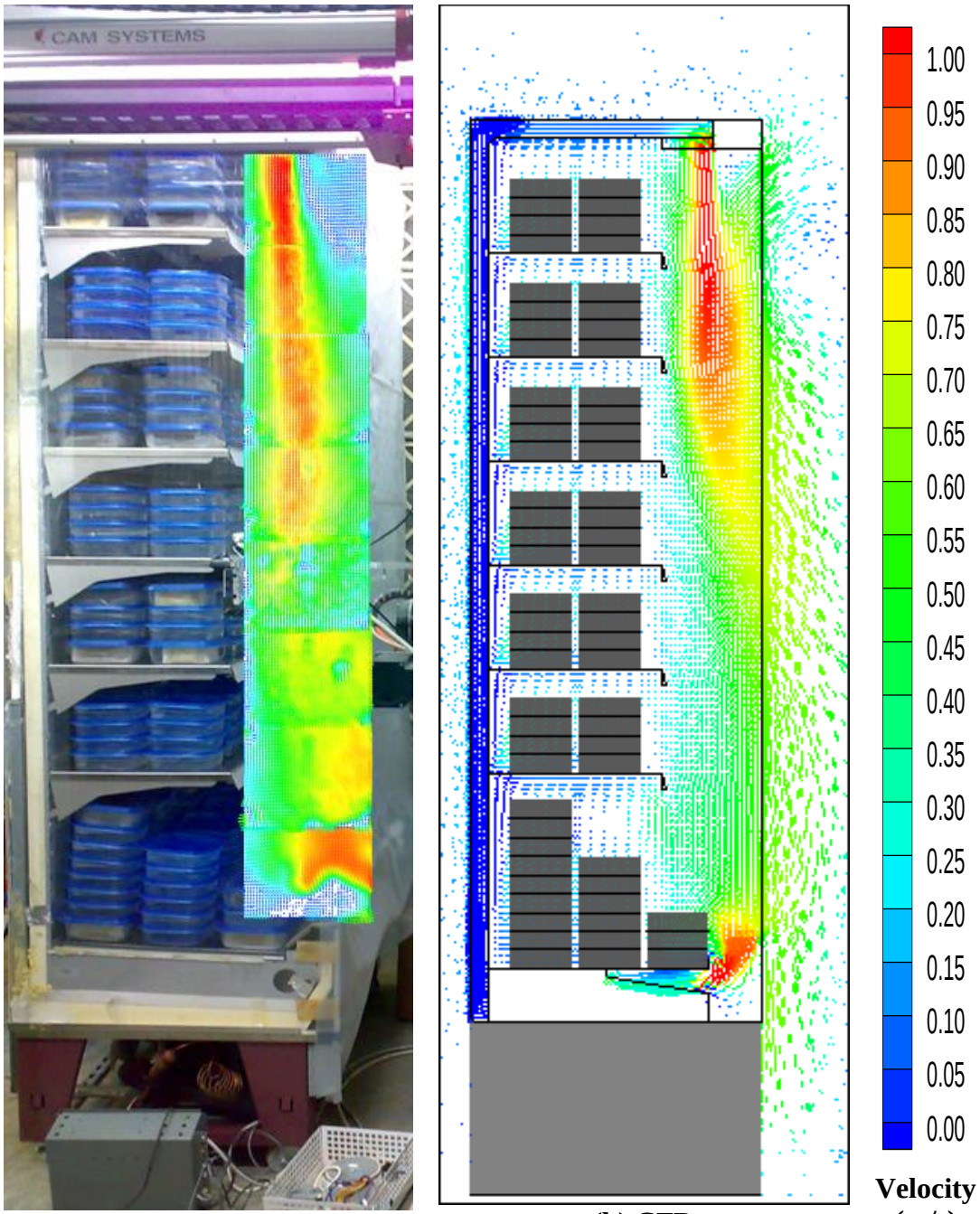

(a) PIV **(b) CFD**

Figure 5.12 Stream-wise (y-) velocity vectors obtained from (a) PIV and (b) CFD at the mid-section of the cabinet

The applied cross-flow has a strong influence on the performance of the cabinet. Figure 5.13 shows the interaction between the air curtain (shown by an iso-surface having a y- velocity magnitude of 0.55 m/s) and the transverse ambient air at three horizontal surfaces taken at the mid-heights of shelves 1, 3, and 5. It is noticed that a vortical structure is formed near the cabinet's leading sidewall, which tends to

withdraw the air curtain away from the cabinet. This effect is amplified as the air curtain loses its momentum while flowing downward. The arrows in the figure show the vortices as they get bigger while migrating downward. As the flow reaches shelf 5, the ambient air is entrained into the cabinet raising the product temperatures at this height onwards. Therefore, it is established that having an air curtain of insufficient mass flow rate will result in its breakage.

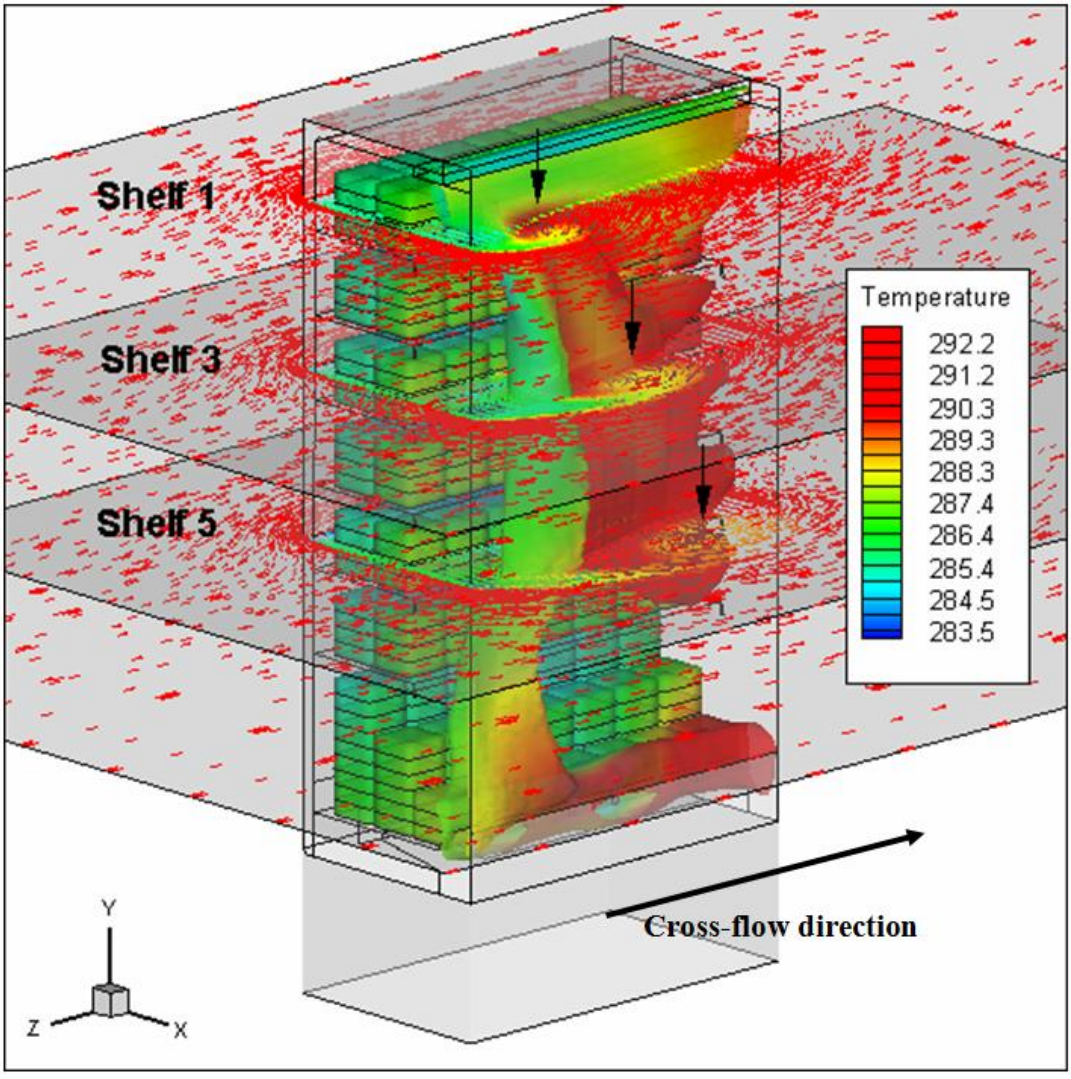

Figure 5.13 Flow field showing cross-flow velocity vectors at horizontal surfaces through shelves 1, 3, and 5. The air curtain is presented by an iso-surface of a constant y- velocity of 0.55 m/s

5.3.2 Comparison of temperature distribution

The temperature field at the cabinet's mid-section was determined experimentally using infrared thermography. Although the IR camera was recently calibrated by the

manufacturer, the emissivity of the screen, which is made of black cardboard was not known. Figure 5.14 shows a comparison of the temperature distribution between the IR and CFD results, and a general similarity can be noticed between the two. The CFD results under predicted the minimum and maximum temperatures at the air curtain and the ambient air by nearly 1 ^{o} C.

Three distinct regions at the display opening section can be identified and further analysed. The temperature of the air curtain is preserved after discharge, and its cooling effect is noticeable only until reaching the third shelf. This indicates that the unacceptable high discharge temperature (283.1 K) is rapidly consumed by the warm entrained ambient air, and its cooling capacity is rapidly compromised. The CFD result was successful in predicting the experimentally obtained IR image in this region. After that, both the measured and predicted results show that the cooling effect of the air curtain is deteriorated at the third shelf (75 cm from the DAG), beyond which, the front side of the products was left unshielded. By comparing the temperature map in Figure 5.14 with the stream-wise velocity in Figure 5.12, it is noticed that the air momentum has the tendency to go further down and its effect is seen all the way to the forth shelf (100 cm from the DAG). This shows that a distinction must be made between the air curtain's flow pattern and its cooling-ability, and it might be concluded that entrainment has a more detrimental (dampening) effect on the temperature gradient at the air curtain's boundary than on the velocity gradient.

Finally, the numerical approach showed deficiency in accurately predicting the temperature map near shelf 7 (base well), and a 4 ^{o}C difference in temperature was encountered. The air leaving the evaporator and entering the back duct makes a 90-degree turn, which results in creating a vortex flow and hence a low-pressure region near the lower part of the perforated back panel. Figure 5.15 presents velocity vectors at the air-off section coloured by static pressure at the cabinet's mid-section. The vortex flow causes the air in the shelf to be induced to the back duct, resulting in less air injection to the lower shelf. To minimise this effect in practice, the lower part of the back panel is designed to have a solid wall of approximately 10 cm in height. The drop in pressure in this region was only partially predicted in the CFD simulation. This deficiency was responsible for delivering more cold air to the upper part of shelf

7 than what is found in reality, which in turn participated in decreasing the product temperatures to lower levels than those found in the experiment.

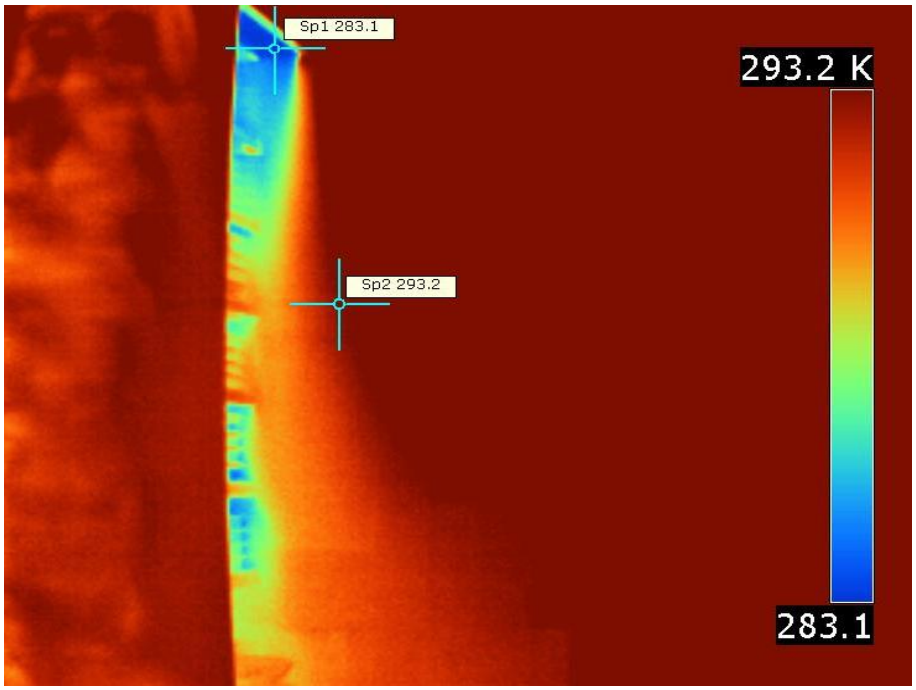

(a) IR image

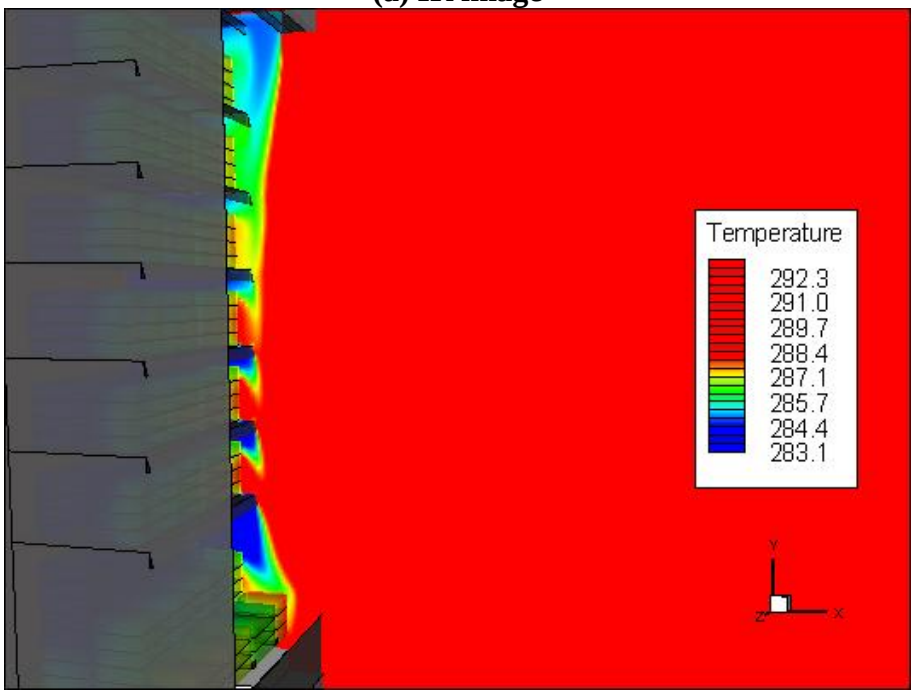

(b) CFD simulation

Figure 5.14 Temperature distribution along the mid-section obtained from a) IR thermography and b) CFD

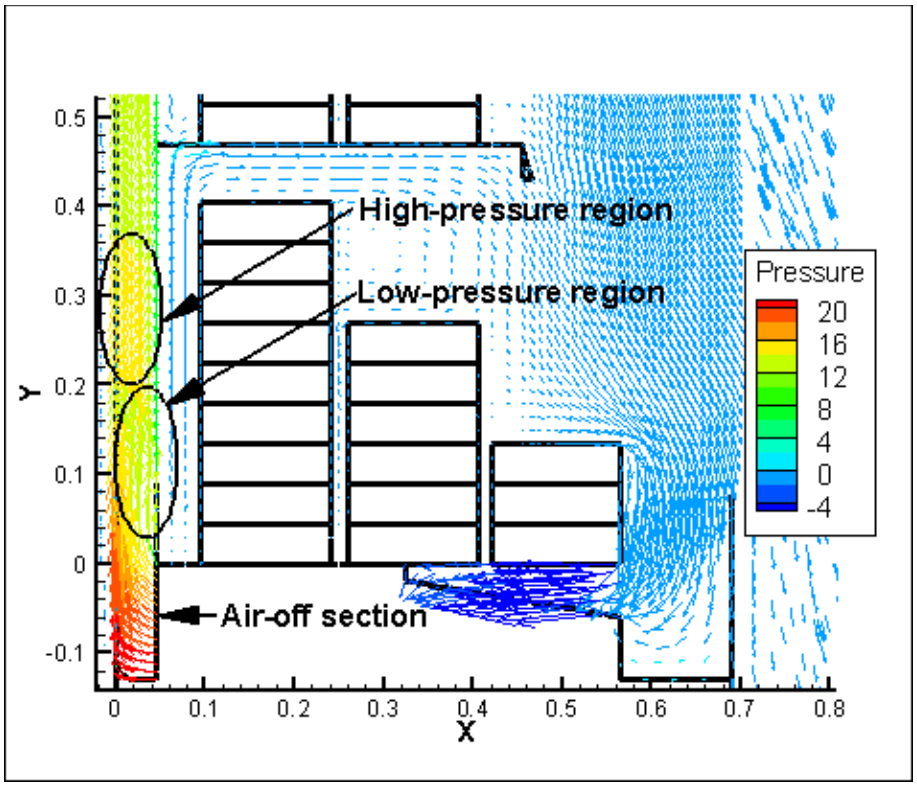

Figure 5.15 Velocity vectors coloured by static pressure (Pa) at the mid-section of the cabinet

5.3.3 Comparison of product temperature

Figure 5.16 shows the predicted temperature contours superimposed on the products together with an isothermal surface of 288.1 K at the display opening of the cabinet. It can be seen that the display opening is not properly shielded at the right-hand-side, and the ambient air is allowed to intrude the cabinet as a result of the cross-flow, affecting the product temperatures at this location. Figure 5.17 is an IR image showing the increased product temperature at shelf 6 (shown by an arrow). This confirms that the CFD simulation was successful in predicting the locations of high product temperatures within the cabinet.

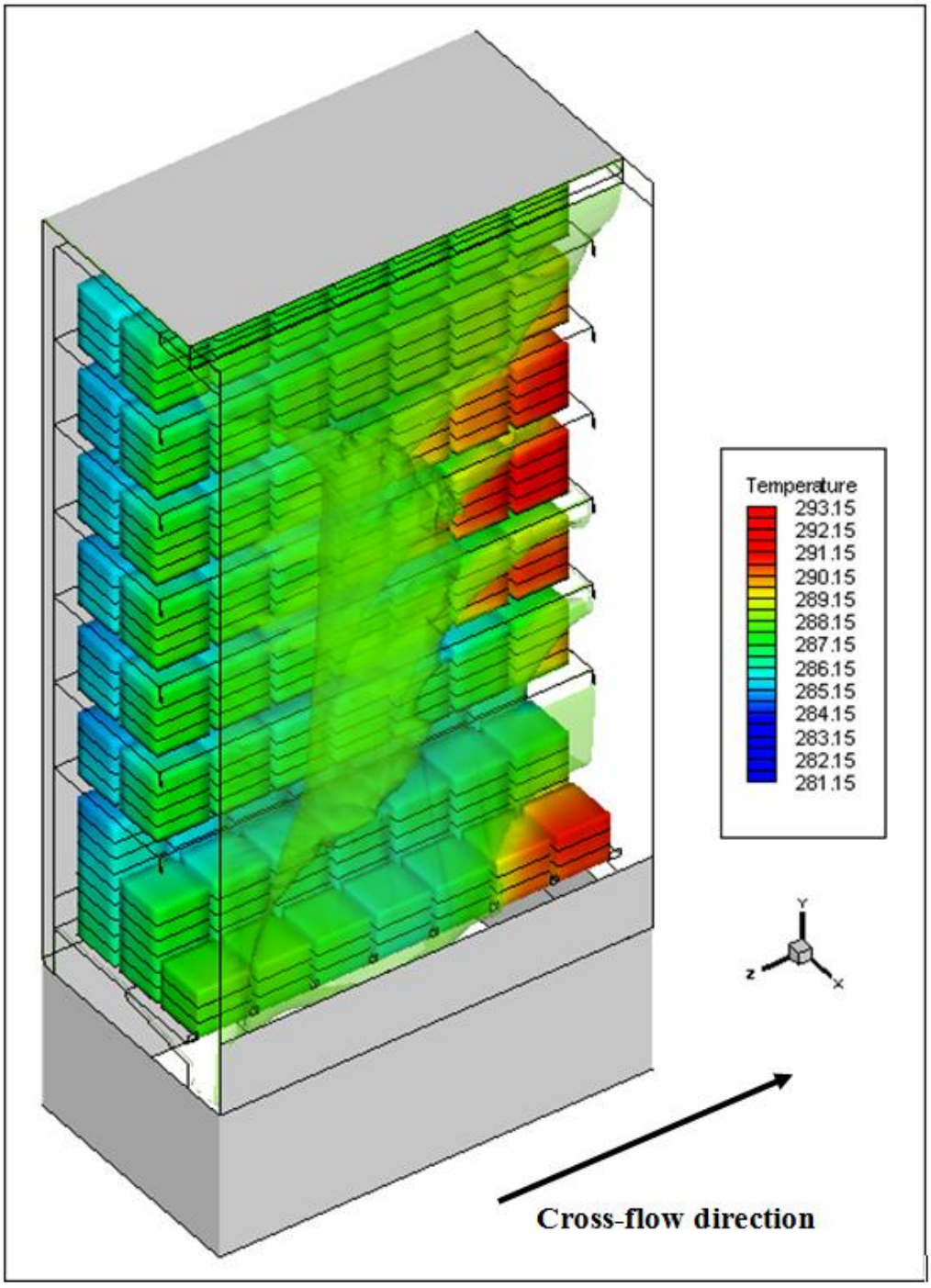

Figure 5.16 Temperature contours superimposed on the products and an isothermal surface (288.15 K) showing the location of the air curtain

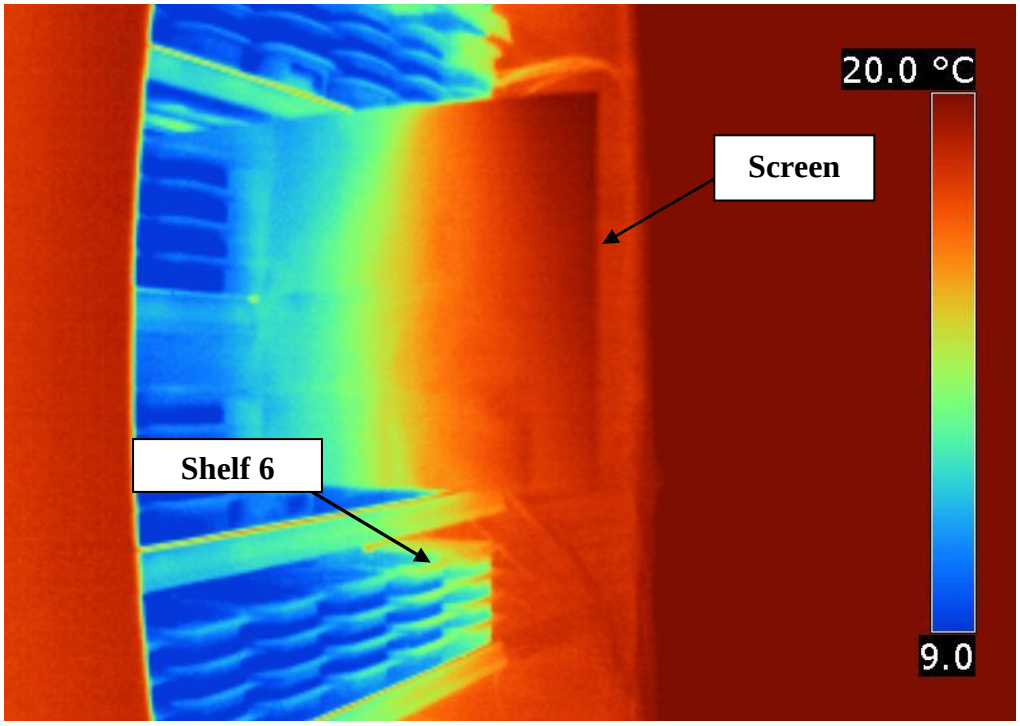

Figure 5.17 IR image showing products at lower shelves and a screen at the cabinet mid-section

Figure 5.18 to Figure 5.21 show the measured and predicted product temperatures of the 48 M-packages located on shelves 1, 3, 5, and 7. The location of the M-packages can be found in Figure 3.8. It can be seen that the product temperatures and also the temperature distribution across each shelf are well predicted, showing a maximum temperature difference of less than 2 K (an error of 12%). The exception was for the three top products at the rear side of shelf 7, where the deviation from experiment was as high as 4 K (an error of 20%). As was mentioned previously, this discrepancy might be attributed to ejecting more cold air at the upper part of shelf 7 as a result of not accurately representing the pressure drop across the porous jump, which was used in the simulations to represent the perforated back panel.

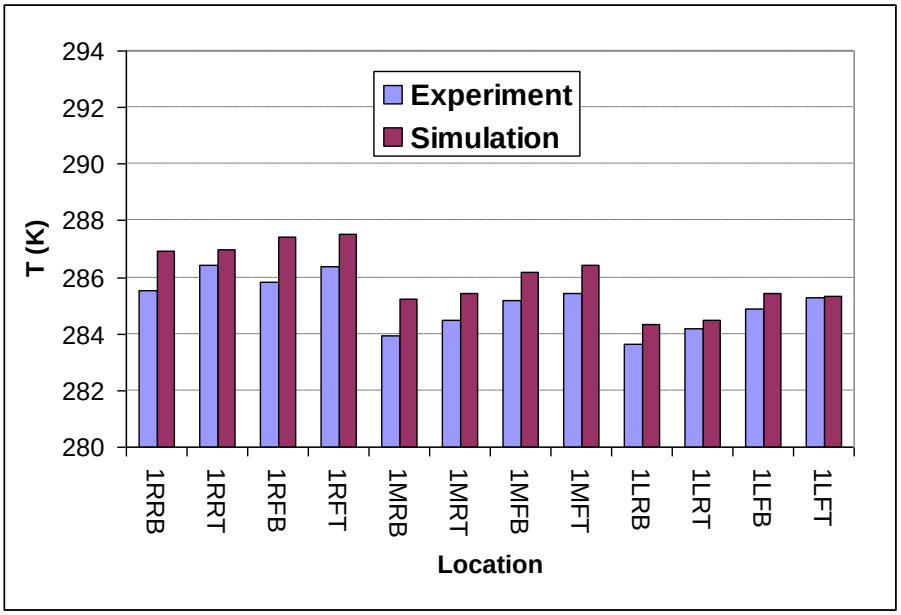

Figure 5.18 Experimental and computed product temperatures for shelf 1

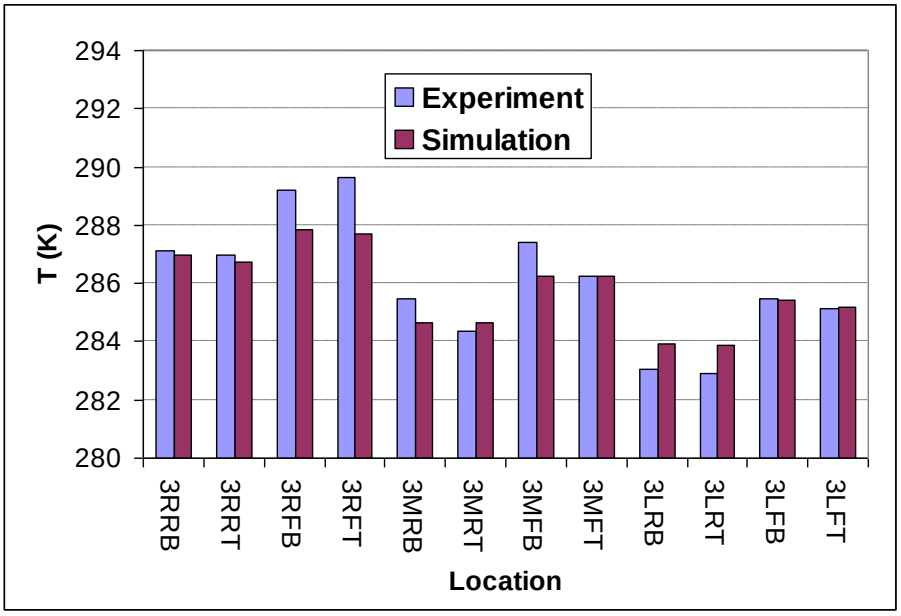

Figure 5.19 Experimental and computed product temperatures for shelf 3

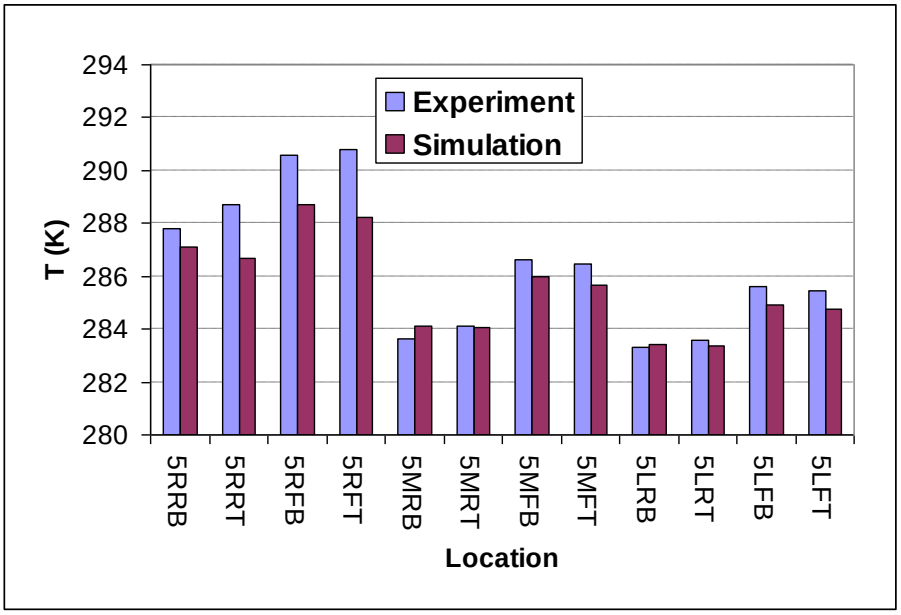

Figure 5.20 Experimental and computed product temperatures for shelf 5

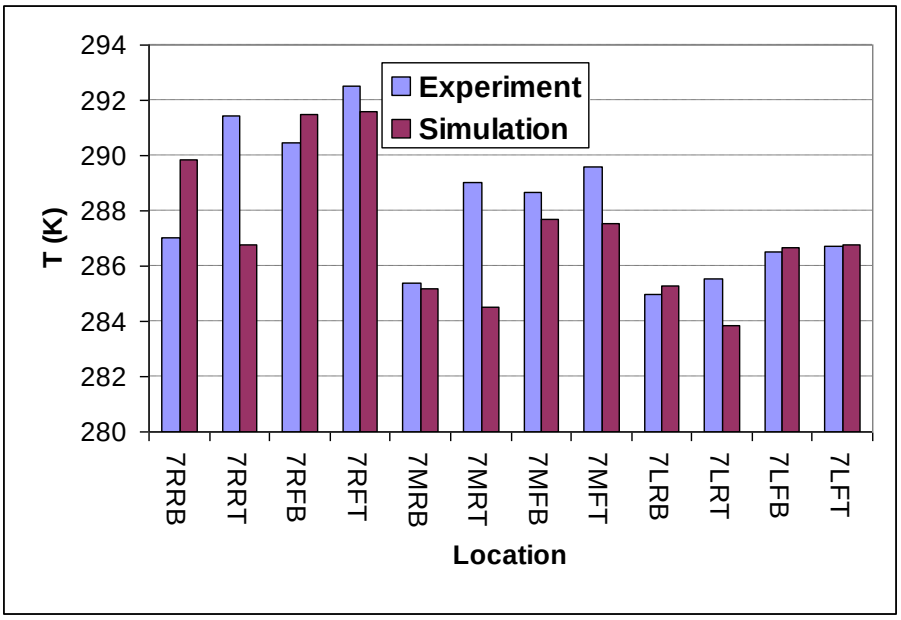

Figure 5.21 Experimental and computed product temperatures for shelf 7

5.3.4 Comparison of sensible cooling load

The sensible cooling load from the experiment and the simulation was determined by averaging the temperatures at the left, middle, and right sections of the air-off and air-on sections, as shown in Figure 5.22. As expected, the air-on temperature at the right side of the cabinet was high due to the intrusion of ambient air at this location, which in turn resulted in higher air-off temperature when compared with the left side.

The sensible cooling load was found to be 1111.5 W from the experiment and 1103.8 W from the simulation. This yields an error of less than 1%, which represents very good simulation accuracy.

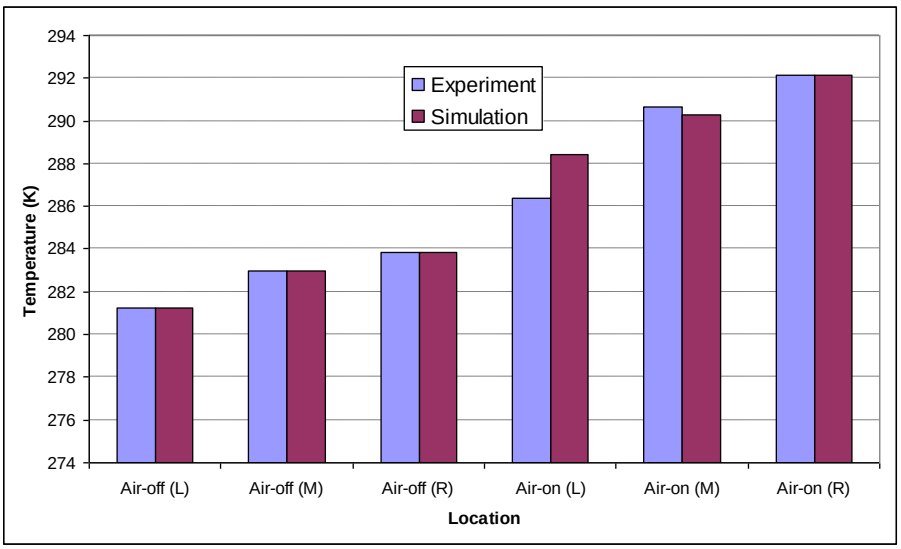

Figure 5.22 comparison of the air-off and air-on temperatures at the left, middle, and right sections of the cabinet

5.4 Summary

This chapter presented the use of advanced experimental tools in the validation of 2D and 3D simulations. Utilising experimentally obtained data to assign boundary conditions in CFD simulations aided in gaining more confidence in the numerical results, which will be used to conduct parametric studies later in this work. The PIV technique produces two-dimensional results of a three-dimensional flow, and the third (z-) velocity component is not represented in the results. For the application of open display cabinets, where the average velocity in the vicinity of the display area is in the order of 1 m/s, an interrogation area of 64x64 pixels having an overlap of 25% was found to offer the best results when the camera was placed about 1 m away from the laser sheet. Although the IR camera used here was calibrated, the emissivity of the screen, which was made of cardboard, was not known beforehand, and a value of 0.85 gave the closest results with the CFD simulation. Placing the screen at the cabinet's mid-section was necessary for the acquisition of the IR images. This affected the accuracy of the results by blocking the cross-flow in the air curtain region, hence weakening the cross-flow effect. Therefore, caution must be taken when comparing CFD results with their IR counterpart. All variants of the k-ε turbulence model underestimated the air curtain's expansion rate and overestimated the stream-wise (y-) peak velocity, especially at the initial region. The Standard k-ε model showed the closest results to experiment whereas the Realizable k-ε model had the worse performance. Cross-flow has a detrimental effect on the performance of low-front open display cabinets, and more work needs to be done on the air curtain of these cabinets in order to minimise the entrainment rate and provide better sealing against the environment. This must be tackled in view of both the structure of the cabinet and also the parameters dictating the efficiency of the air curtain itself. In addition, the infiltration rate into the cabinet must be determined and also minimised since it constitutes the largest contributor to the cooling load, which will be the subject of the next chapter.

CHAPTER 6
Quantification and minimisation of entrainment rate through the air curtain

"Have confidence that if you have done a little thing well, you can do a bigger thing well too."

(David Storey, 1933-present)

This chapter deals with the interaction at the boundary between the air curtain and the surrounding environment, commonly referred to as entrainment. Since entrainment cannot be prevented, it should be accurately predicted and minimized in order to optimize the performance of the air curtain and ensure proper operation of the open refrigerated display cabinet. The flow of the air curtain results in an induction action that increases the withdrawal of the adjacent stagnant air into the moving stream, and finding means to quantify it and ultimately reduce it is the aim of this chapter. After providing a brief introduction to the theory of turbulent air curtains, particular attention is paid to the entrainment mechanism and how to quantify it. The CFD technique is used to determine the entrainment rate as a function of different parameters governing the efficiency of the air curtain.

6.1 Introduction

Entrainment is the process of exchanging air between a moving fluid (either liquid or gas) and the stagnant air adjacent to it. This phenomenon occurs either naturally or artificially, and is considered to be a problem in many engineering applications. Although invisible and difficult to quantify, entrainment takes place in air curtain applications as they interact with the adjacent ambient air. Figure 6.1 is a steady-state CFD simulation showing the entrainment process during the moving stream of the air curtain. The flow of an air curtain functioning on an open display cabinet differs from other types of fluid flow because it is bounded on one side by a free boundary of the same fluid (air), while the other side is bounded by flow ejected from the back panel, not to mention shelves containing randomly stacked products. This, with the

high temperature differential across its sides makes the entrainment process even more difficult to analyse. This interaction between the cold air curtain and the outer boundary has a dominant impact on its overall flow development. The literature has only a handful of reviews related to the entrainment process associated with air curtains serving open display cabinets, and those are mainly the works of Field and Loth (2006) and Navaz et al. (2006).

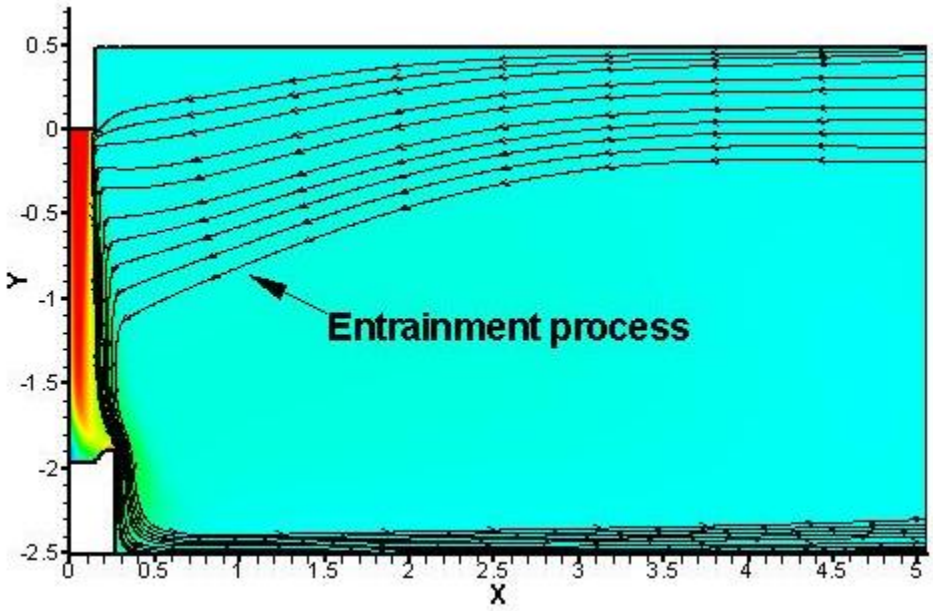

Figure 6.1 Velocity contours with streamlines showing entrained air into an air curtain

6.2 Theory of turbulent air curtains

The theory of air jets is well established in the literature due to the large number of engineering applications they represent. Depending on the geometry of the opening and the existence of surfaces in the vicinity of the jet, air jets may further be classified as free air jets and wall air jets. Awbi (2003) describes a free air jet as "a flow of air issuing from an opening or a nozzle into an air space where there are no solid boundaries to influence the flow pattern and where the static pressure within the jet is the same as the static pressure of the surrounding space". A wall air jet, on the other hand, "is produced when the flow is bounded by a flat surface on one side and the velocity at the exit from the opening is parallel to the surface". When the jet is issuing from a rectangular opening of aspect ratio greater than 40, it is commonly

approximated by what is known as a plane jet, as variations in the direction of the opening length are negligible.

The fluid dynamics behaviour of an air curtain is largely similar to that of a plane jet produced by an infinitely long rectangular opening so that only lateral change in the properties of the jet occurs in the plane normal to the opening length. Therefore, the flow of an air curtain can be treated as two-dimensional, consisting of a core region and a fully developed region, as shown in Figure 6.2. The core region is the region immediately downstream of the discharge air grille (DAG), where mixing between the air curtain and the surrounding air is not complete.

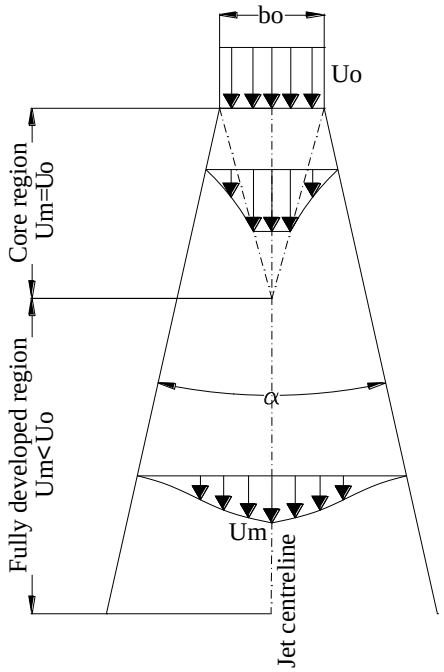

Figure 6.2 Sketch of the two regions of an air curtain

The length of the core region depends on the supply velocity magnitude, U_o, the width of the discharge air grille, b_o, and the discharge turbulent intensity, TI. This region strongly affects the development and structure of the jet as was shown by the modelling and experimentation done by Van and Howell (1976). The centreline velocity, U_m, is constant in this region and equals to the supply velocity, U_o. After the consumption of the core region by the free shear layer, the centreline velocity begins to gradually decay, forming the fully developed region. The extent of this region also depends on the characteristics of the DAG, and is dominated by a highly

turbulent flow generated by viscous shear at the edge of the shear layer. The spread angle α of this region is almost constant and its value is dependent on the geometry of the DAG.

6.3 Mechanism of Entrainment

Entrainment takes place in both laminar and turbulent regimes. In laminar flows, the shear stress, τ, is given by:

$$\tau = \mu \times \frac{\partial U}{\partial y} \tag{6.1}$$

where μ is the dynamic viscosity, U is the stream-wise velocity, and y is the direction normal to the flow direction. For larger shear stresses, the fluid can no longer sustain the viscous shear stress and turbulence spots develop. After the appearance of turbulence spots, the turbulence expands rapidly to the entire shear flow. The shear stress in the turbulent flow is expressed by Chanson 1996 as:

$$\tau = \rho \times (\nu + \nu_T) \frac{\partial U}{\partial y} \tag{6.2}$$

where ρ is the fluid density, ν is the kinematic viscosity ($\nu=\mu/\rho$) and ν_T is a factor depending upon the fluid motion and is commonly known as the eddy viscosity or momentum exchange coefficient.

In the hypothetical situation where entrainment is absent, the interface between the air curtain and the ambient air is well defined and continuous as shown in Figure 6.2, and the heat flux and mass exchange between the two streams will take place across a single line represented by a free surface. However, when entrainment is introduced, the exact location of the interface between the moving stream of the air curtain and the stagnant surrounding environment becomes indistinctive. The free surface now represents a layer consisting of air from both streams. In other words, the air exchange in this layer includes both the entrainment of ambient air into the air curtain and the detrainment (or escape) of air from the air curtain to the ambient air. This boundary is commonly called the “free surface boundary” or the “free shear layer” in the literature. Figure 6.3 is a sketch of the air curtain edge where the entrainment action is involved.

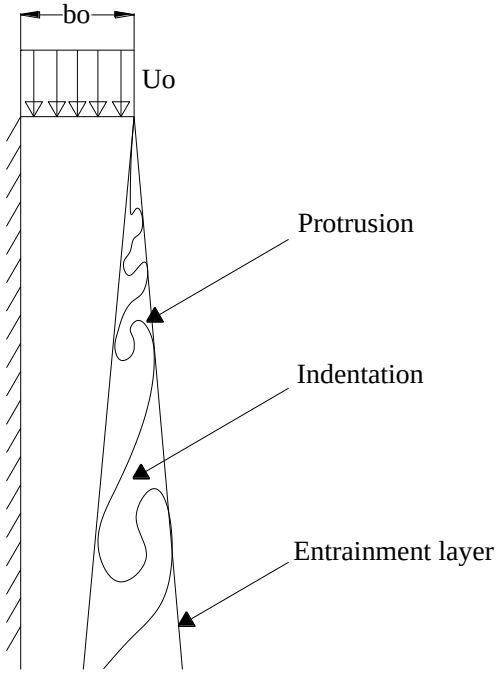

Figure 6.3 Sketch showing the entrainment process at the edge of an air curtain

The shear layer develops as the air of the curtain leaves the DAG because of the velocity discontinuity at the boundary. The flow is characterised as a shear flow where a velocity gradient in the direction normal to the mean flow direction is present. Similar to a boundary layer flow along a flat plate (where the velocity is zero at the plate and equals to the free-stream velocity away from the plate), the momentum is satisfied from the high-velocity region of the air curtain to the low-velocity region of the ambient air. Therefore, the air tends to resist the shear associated with the transfer of momentum, where the shear stress is proportional to the rate of transfer of momentum. This results in a growth of the air curtain thickness and the generation of eddies with the axial distance from the DAG. The shear layer interface is dominated by strong vortex structures representing combinations of protrusions and indentations, forming a wavy pattern along the outer layer of the air curtain. The entrained ambient air into the curtain is the amount of air mass being drawn into the indentations, which gets mixed and starts migrating along the stream of the air curtain until it reaches the return air grille (RAG), forming the infiltration load.

6.4 Detrimental effect of entrainment on the air curtain

Among the negative effects of entrainment on the dynamics of the air curtain are the reduction of the jet momentum (and consequently the length of the air curtain) and the triggering of mixing with the warm ambient moist air. The thermal loss through a properly working air curtain is due the turbulence generated entrainment-spill process. In addition, the relatively fast moving air of the air curtain loses momentum to speed up the stationary surrounding air. Due to the entrainment of the surrounding air, the velocity gradients decrease in magnitude in the flow direction and ultimately, this causes the mean velocity at the centreline to decrease. Excessive entrainment rates also result in raising the temperature of the front part of products, especially those placed on the lower shelves of the display cabinet. Moreover, inducing moisture during the entrainment process increases the latent load on the evaporator and hence more frequent defrosting cycles are inevitable. In effect, the entrained air into the air curtain may constitute up to 75% of the total refrigeration load of the cabinet, depending on the amount of this entrained air that manages to infiltrate into the cabinet (Adams 1985).

6.5 CFD technique for the determination of the entrainment rate

In the following, a process is developed to determine the entrainment rate through an air curtain of a simplified open display cabinet, as shown in Chapter 3. The geometry adopted for this study mostly resembles that proposed by Field and Loth (2006), where the products are replaced by a solid vertical wall mimicking a fully-packed cabinet. This assumption was considered valid in order to isolate the thermo-fluid dynamics of the air curtain from the effect of the physical body of the cabinet. Furthermore, no flow from the back panel was introduced and the air curtain was allowed to freely descend on the wall, and solely interacts on one side with the ambient air. The width of the DAG, b_o, was chosen to be 12 cm, similar to that used by Field and Loth (2006). Although this width might not be the optimum for the display height in hand (200 cm compared to 160 cm used by Field and Loth (2006)), this choice was deemed necessary for the verification of the results, at least to a certain distance from the DAG. From another perspective, the Reynolds number associated with air curtains is usually based on the width of the DAG, and using the aforementioned width in finding the Reynolds number (and the average velocity

associated with it) allows for running a comparison check with the entrainment results numerically generated by Navaz et al. (2005). Initially in this work, the Reynolds number at the DAG of an isothermal air curtain was calculated using values of density (1.18 kg/m^3) and molecular viscosity (1.85x10^{-5} kg/m.s) at 298 K. After specifying a Reynolds number of 6000 for the 12 cm DAG, the average discharge velocity was found to be 0.78 m/s and the calculated mass flow rate was 0.11 kg/s. Since the simulations are two-dimensional and no cross-flow is introduced, the air of the domain is assumed stagnant prior to the ejection of the air curtain (at the initiation of the calculations) and was then allowed to freely respond to the flow of the air curtain. In their work, Bhattacharjee and Loth (2004) specified a co-flow ambient velocity parallel to the air curtain direction having a magnitude 6.6% of the mean air curtain velocity. They rationalized this assumption to be consistent with the entrained air from above the air curtain in most display cabinets. Applying this assumption however was thought to interfere with the flow of the air curtain and introduce discrepancies in the calculation of the entrainment rate. In order to focus on the entrainment process, the conduction from the body of the cabinet and the radiation heat exchange with the environment were neglected as well as the latent heat in the humid air. Those assumptions were considered reasonable since the refrigeration load was not considered in the analysis.

The complexity of the negative-buoyancy effect was initially overlooked by setting the temperature of the air curtain as well as the ambient air to 298 K creating an isothermal case. Although the air curtain of working open display cabinets is usually cooled to temperatures near the freezing point, this assumption was justified by results obtained from Field and Loth (2006) showing that the effect of density gradients on the entrainment rate is minimal when sufficient inertia forces are applied at the DAG. Moreover, entrainment takes place even when the air curtain has the same temperature as the ambient air. Ultimately, assigning isothermal conditions simplified the numerical as well as the experimental procedure, since no refrigeration requirements were required for the analysis.

To distinguish between the two air streams, the species model was used to designate different names for the air of the curtain and the ambient air. Assigning different names for the two streams served as a tracer gas process, allowing for the

determination of the infiltration rate as a mass fraction quantity directly from the CFD model. This proposed modelling is contrary to that assumed by Bhattacharjee and Loth (2004), who numerically studied an isothermal air curtain by specifying different temperatures for the curtain and the ambient air streams solely for the sake of visualization of the thermal and mass mixing processes. Although this step is numerically possible by setting gravity to zero (in order to discard buoyancy effects), it is physically not possible and was not considered in this work.

As the air of the curtain travels from the DAG to the RAG, the total mass flow rate unceasingly increases in the stream-wise direction due to the continuous entrainment of the surrounding ambient air into the air curtain. The calculation of the net mass flow rate of the ambient air being entrained into the air curtain is initiated by creating horizontal surfaces (or lines) evenly spaced along the height of the air curtain. Since the case in hand is two dimensional, each line actually represents a surface with a unit length spanning into the domain. The vertical distance between the surfaces was taken to be 10 cm, and the width of each surface must initially cover the entire local thickness of the air curtain. Therefore, the surfaces were initially chosen to be 50 cm long and could be even longer for wider air curtains. At each individual surface, the maximum stream-wise (-y) velocity (based on the vertex minimum criterion) is directly found during the post-processing stage. The iso-clip option offered by Fluent was then utilised to cut each of the original surfaces at the location where the local stream-wise velocity reaches 25% of the maximum velocity at this location (smaller percentages were tested without much gain in accuracy). Doing so, the local thickness of the air curtain is determined as was proposed by Bhattacharjee and Loth (2004). This procedure was taken a step further by directly determining the mass flow rate across each of these newly created surfaces. The net entrainment mass flow rate, $\dot{m}_{ent}$, at each of these locations is calculated by subtracting the amount of air supplied at the DAG, $\dot{m}_{DAG}$, from the total mass flow rate, $\dot{m}_{tot}$, passing through each of those new surfaces along the height of the air curtain. This can mathematically be written for each -y distance from the DAG as

$$\dot{m}_{ent} = \dot{m}_{tot} - \dot{m}_{DAG} = \int_0^x \rho\, u\, L\, dx - \left(\int_0^x \rho\, u\, L\, dx \right)_{DAG} \tag{6.3}$$

where x is the local width of the surface, and since the simulations are two dimensional, L is taken as the unit depth into the domain (mass flow area=$x \times L$).

Figure 6.4 is a stream-wise (-y) velocity vector plot showing the surfaces where the entrainment rate was calculated and the location of the air curtain boundary that was obtained as a result of the 25% reduction in the stream-wise velocity. It is worth mentioning here that the last horizontal surface near the RAG represents the spillage surface, and since mass is conserved through the air curtain, the mass flow rate through this surface is identical to the entrainment rate through the air curtain.

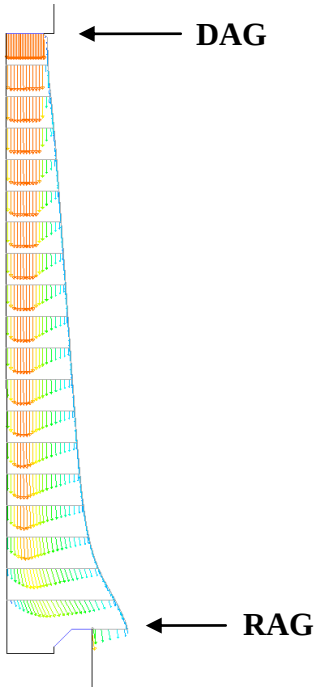

Figure 6.4 Air curtain boundary with flux lines at 10 cm intervals from the DAG

6.6 Modelling results and discussion

6.6.1 Entrainment rate of laminar and turbulent air curtains

The efficiency of an air curtain is highest for a laminar regime since no turbulent diffusion (and thus turbulent viscosity) is allowed to participate in the mixing process at the boundary with the ambient air, and therefore, only laminar (molecular) diffusion takes place. A proposal for conducting this comparison was made by Navaz et al. (2005), who suggested that creating a laminar flow at the DAG with a velocity

profile that resembles a laminar flow is helpful in reducing the entrainment and infiltration rates through the cabinet.

Initially in this work, a comparison between a laminar and a turbulent isothermal air curtain was deemed necessary to assess the difference between their flow characteristics. Although the laminar flow assumption is not realistic, it is helpful in gaining insights into how far off the efficiency of a turbulent air curtain is when compared to such an ideal-case scenario. Both flows were assumed isothermal to eliminate the complexity of the negative-buoyancy effect. In order to reveal more clearly the difference between the characteristics of the laminar and turbulent simulations, the conditions at the boundaries of both models (i.e. the velocity magnitude and profile at the DAG and the domain) were assigned the same values, except for turbulence-related quantities that are not applicable to the simulation of the laminar regime.

Figure 6.5 shows forty streamlines in the laminar and turbulent simulations computed from a horizontal rake of 25 cm width placed 75 cm below the DAG. There is a distinct difference between the flow pattern in the laminar air curtain and its turbulent counterpart. Namely, the streamlines emanating from the DAG in the laminar simulation were generally kept closer to each other all the way to the RAG. On the other hand, since the turbulent transport mechanism is dominant in the turbulent air curtain (instead of the molecular transport mechanism in the laminar air curtain), the ability of the turbulent air curtain to entrain the surrounding ambient air is much larger than that of the laminar air curtain. This is evident by analysing the turbulent air curtain (Figure 6.5 (b)) which experiences more entrainment and hence more spreading of the streamlines. The increased amount of entrainment is also obvious by comparing the number of streamlines being spilled from the turbulent air curtain. It is noteworthy that the streamlines approaching the air curtains tend to travel upwards as they reach the air curtain boundary. This observation is due to the counter-clockwise vortex flow in the vicinity of the air curtain, which was also experimentally confirmed by Field and Loth (2006). Moreover, by analysing the density of the incoming streamlines at the upper part of the air curtains, it is obvious that the entrainment action happens sooner and is more pronounced in the turbulent

air curtain where more streamlines manage to approach it crossing the same rake length.

Figure 6.6 compares contours of the stream-wise (-y) velocity for the laminar and turbulent air curtains. It is noted that the centreline velocity is preserved until about 1.6 m from the DAG and there is no appreciable difference between the length of the potential core region in the simulations. This was expected due to the one-sided interaction with the ambient air. This finding is consistent with experimental measurements, which showed the peak velocity not to decrease significantly in this range. However, the core region of the turbulent air curtain narrows and disappears more rapidly than its laminar counterpart.

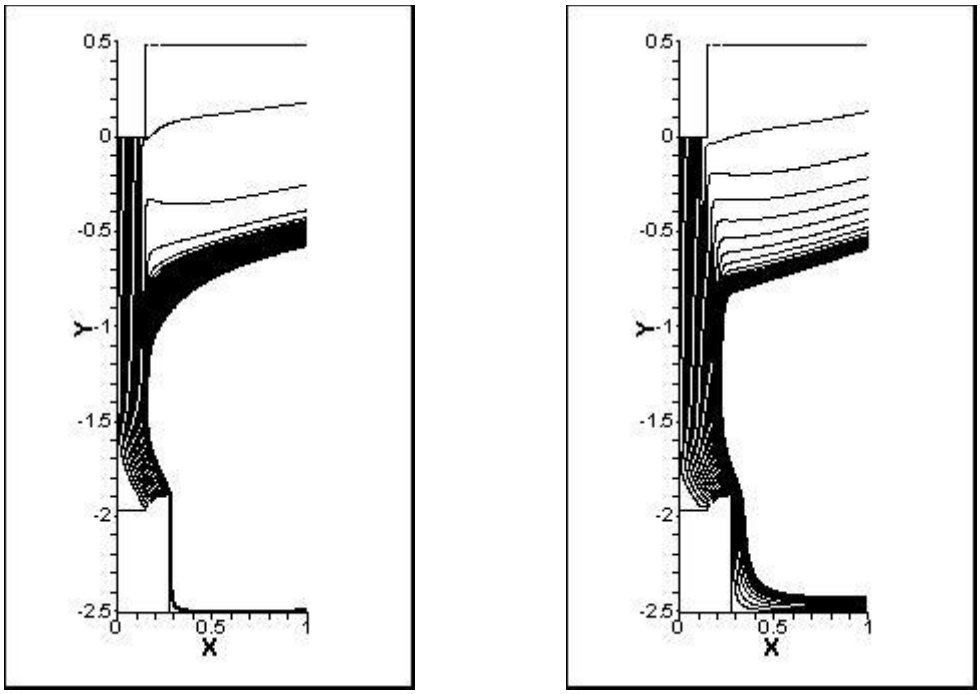

(a) Laminar flow **(b) Turbulent flow**

Figure 6.5 Streamlines passing through the same cross sectional area while approaching the air curtain for the (a) laminar and (b) turbulent simulations

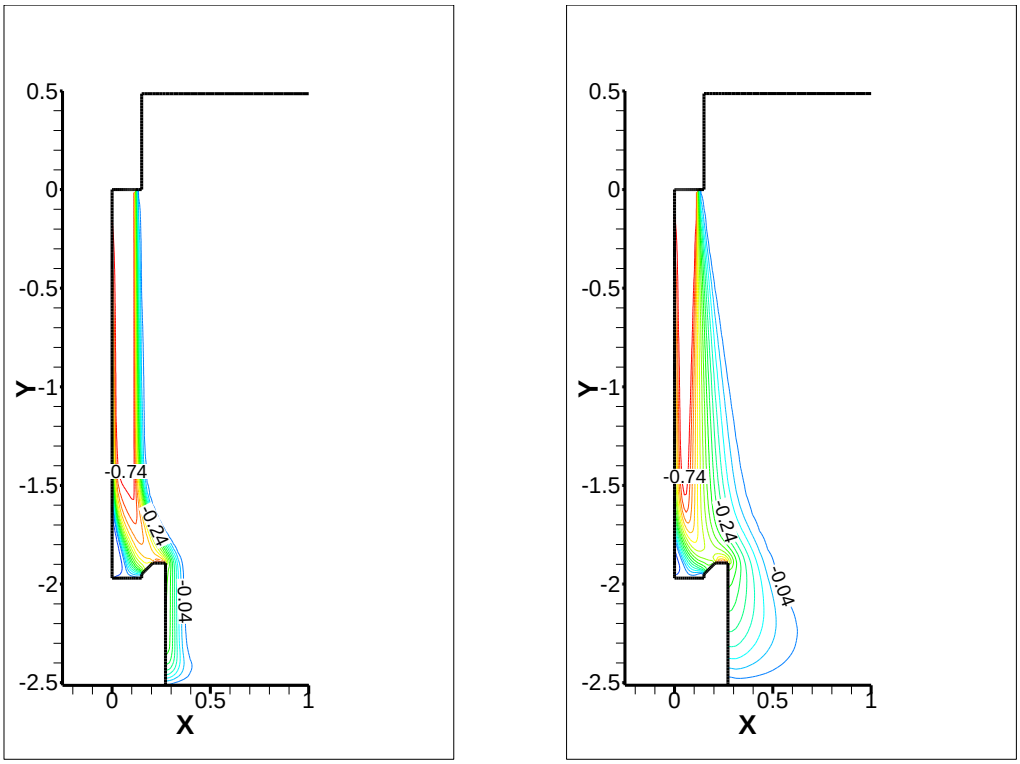

(a) Laminar flow **(b) Turbulent flow**

Figure 6.6 Contours of stream-wise (-y) velocity for the (a) laminar and (b) turbulent simulations

Comparison of the entrainment mass flow rates for the laminar and the turbulent air curtains is shown in Figure 6.7. The amount of entrained air for the laminar and turbulent regimes is almost the same for the distance of 10 cm from the DAG. This is attributed to the fact that there is not enough time for the turbulent air curtain to entrain enough ambient air. In the turbulent air curtain, the entrainment rate is found to increase almost linearly with the distance from the DAG. This however is not the case for the laminar air curtain, where the entrainment rate remains fairly low up to a distance of around 140 cm downstream the DAG after which it increases exponentially. The exponential entrainment rate experienced at this height might be as a result of the offset distance between the wall and the RAG, which increases the length of the entrainment borderline between the air curtain and the ambient air. This effect however is not observed in the turbulent air curtain since the curtain-ambient interface does not follow the physical body of the cabinet, but forms an almost straight oblique line from the DAG to the RAG.

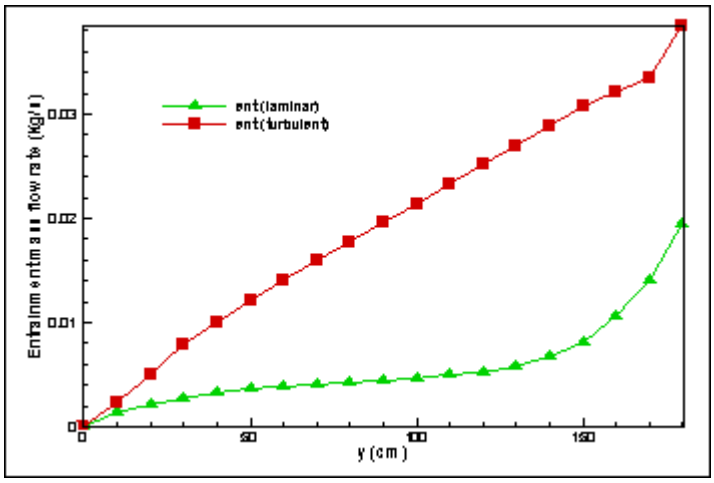

Figure 6.7 Entrainment mass flow rate of the laminar and turbulent simulations

Figure 6.8 shows the air curtain thickness for both regimes. The spreading of the turbulent air curtain is much pronounced, especially half way down the DAG. The local thickness at the lowest point reflects the amount of spillage (and also entrainment) associated with the air curtains, and it is clearly evident that the turbulent air curtain spills more air to the ambient. Therefore, the air curtain must be designed to be as laminar as possible in order to minimise entrainment.

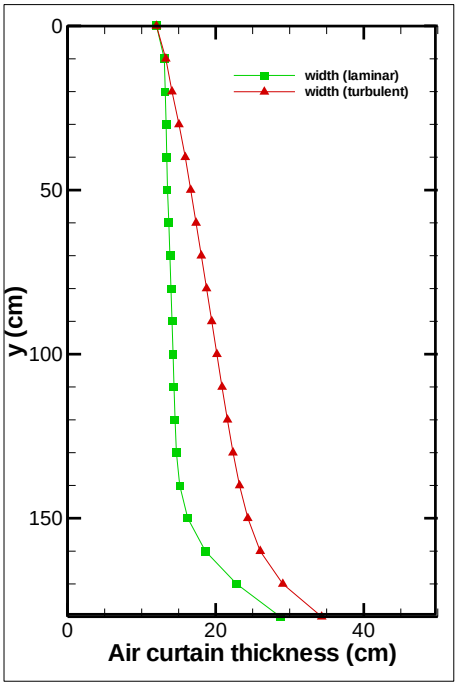

Figure 6.8 Air curtain thickness for the laminar and turbulent simulations

6.6.2 Effect of velocity magnitude on entrainment

As mentioned earlier, the relatively fast moving air of the air curtain loses its momentum to speed up the stationary air of the environment. Navaz et al. (2005) demonstrated that using low Reynolds numbers at the DAG tends to reduce the amount of entrained air into the air curtain, which ultimately leads to less infiltration into the cabinet.

In order to build confidence in the numerical results obtained here, the thickness of an isothermal air curtain with a Reynolds number of 6000 was verified with the experimental data presented by Field and Loth (2006), as shown in Figure 6.9. In this figure, the zero Richardson number represents an isothermal air curtain for the Reynolds number range from 3800 to 8500 (shown by white circles). The CFD prediction here (shown by red squares) tends to follow the same trend of the experimental results, but a systematic bias can be observed at a distance x/H of 6. This bias can be mainly explained by the difference in the velocity profiles used in the two cases. Moreover, the increased spreading of the air curtain thickness predicted by Field and Loth (2006) might be a consequence of the offset distance of the RAG. Another explanation for this is that the obtained PIV results might not have been averaged using a sufficient number of images. Nevertheless, the results in both cases were shown to be roughly independent of the Reynolds number and the air curtains grow nearly linearly with x/H.

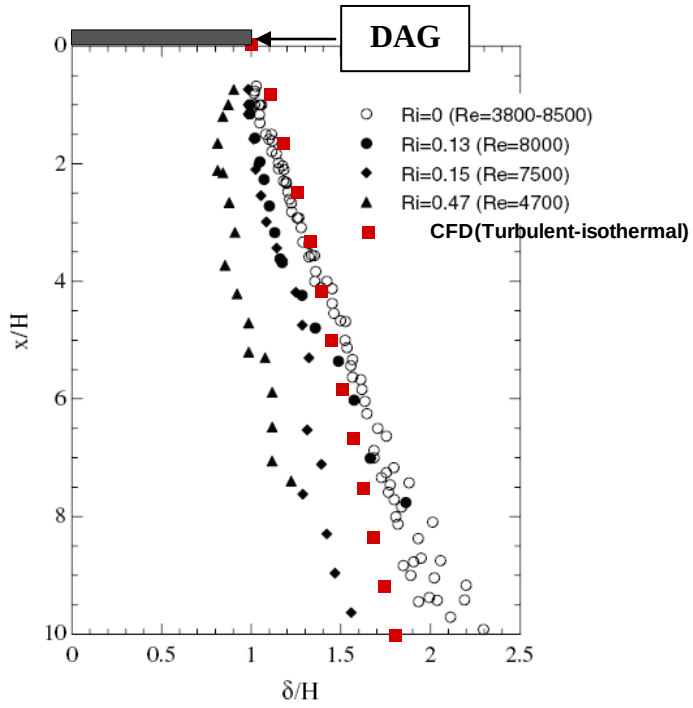

Figure 6.9 Comparison of air curtain thickness between numerical results (red squares) and experimental results of Field and Loth (2006)

Figure 6.10 shows CFD results of the air curtain thickness for six discharge Reynolds numbers, namely 500, 1500, 3000, 4500, 6000, and 7500. It can be seen that the air curtain thickness is decreased with the increase of the Reynolds number. This might be explained by the fact that the momentum is more focused and hence less spreading takes place. This however is contrary to the results produced by Bhattacharjee and Loth (2004), which revealed a proportional relationship between the thickness and Reynolds number for the turbulent air curtain but a decrease in thickness with the increase of Reynolds number for the laminar air curtain. They postulated that the entrainment rate would always be least for flow conditions when the flow just begins to change from the steady laminar regime into the early transitional regime.

At this stage, it is necessary to revisit the definition of the Reynolds number ($Re=\rho Ux/\mu$), since it has been a source of debate in the field for its suitability to characterise the performance of the air curtain. The Reynolds number is a dimensionless number that gives a measure of the ratio of inertial forces to viscous forces in the flow, and consequently it quantifies the relative importance of these two types of forces for given flow conditions. It is also used to characterise the flow

regime, i.e. either laminar or turbulent. A laminar flow occurs at low Reynolds numbers, where viscous forces are dominant, and is characterised by smooth, constant fluid motion. A turbulent flow, on the other hand, occurs at high Reynolds numbers and is dominated by inertial forces, which tend to produce random eddies, vortices and other flow fluctuations. In the flow over a flat plate, an initially laminar flow would turn into a turbulent flow after a certain distance from the leading edge, as the laminar boundary layer will become unstable and turns to a turbulent one. This distance is called the characteristic length, and the Reynolds number is meaningless without the selection of a proper characteristic length. The flow velocity is the free stream velocity of the fluid outside the boundary layer.

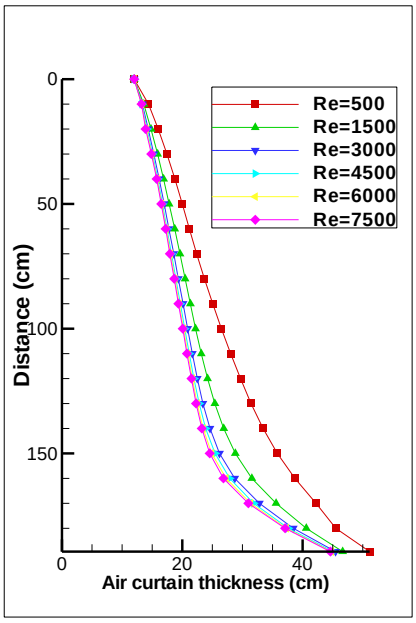

Figure 6.10 Air curtain thickness for different Reynolds numbers

In the case of the air curtain, the flow is already turbulent at the DAG, and characterising it with a Reynolds number might be misleading. Navaz et al. (2005) recommended a DAG Reynolds number in the range of 3200 to 3400 to minimise ambient air entrainment when the DAG width is taken as the characteristic length. This results in a large Reynolds number for a very wide DAG even when the discharge velocity is insufficient in producing a turbulent flow. Therefore, it can be concluded that when the characteristic length is taken as the DAG width, the Reynolds number can be a dimensionless quantity relating the discharge velocity

with the DAG width for a specific case, and cannot be generalised to yield an optimum design number for all air curtains operating on open display cabinets.

Figure 6.11 shows the entrainment mass flow rate of the six air curtains. The last values represent the total amount of entrained air, and since the Reynolds numbers used here are equally varied by a fixed amount of 1500, it can be postulated that the entrainment rate is linearly proportional to the DAG Reynolds number. Therefore, the discharge velocity must be as low as possible given that its momentum is sufficient in sealing against the entire display height.

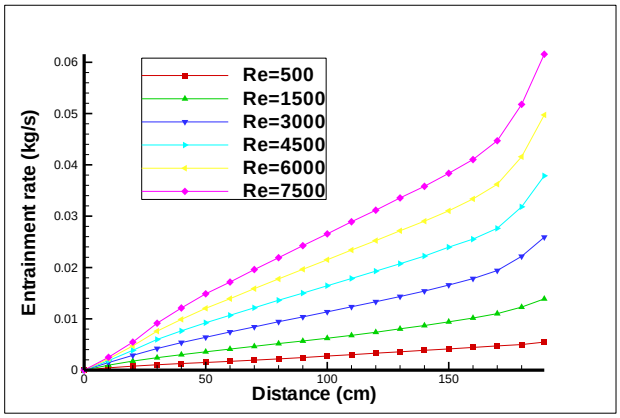

Figure 6.11 Entrainment mass flow rate for different Reynolds numbers

6.6.3 Effect of discharge turbulence intensity on entrainment

The turbulence intensity at the DAG can potentially affect the amount of entrained air through the air curtain since it invokes mixing and initiates the formation of eddies at the boundary. On the contrary, achieving near-laminar flow situations is believed to suppress this activity. Initially at the air-off location, the air turbulence intensity is high because of its passage through the evaporator; however, this high intensity is dampened as the air travels through the back panel to reach the DAG. Honeycombs have long been used to reduce the turbulence intensity at the DAG, where it is further reduced to values as low as 5% downstream. The parametric study conducted by Navaz et al. (2005) suggests that reducing turbulence intensity at the DAG can reduce the entrainment rate, especially for Reynolds numbers (based on the DAG width) greater than about 3200. An attempt is made here to compare the effect of turbulence intensity in the vicinity of this range. Figure 6.12 and Figure 6.13 compare the thickness and entrainment mass flow rate of an air curtain having a

discharge Reynolds number of 6000 but with three turbulence intensities, namely, 5, 10, and 15%. It is evident from the figures that the air curtain thickness and entrainment rate are insensitive to the turbulence intensity in this range. Since turbulence is a micro activity, its effect, as previously suggested by Navaz et al. (2005), might be exaggerated at higher Reynolds numbers not experienced in open display cabinets, i.e. over 10,000. This is shown by examining the results of the previous authors, where the entrainment rate is almost unchanged in the range from 1500 to 7500 when the turbulence intensity was varied between 0 to 60%. Therefore, it can be concluded that the turbulence intensity at the DAG has a weak impact on the performance of the air curtain especially in the range of velocities dealt with in open display cabinets.

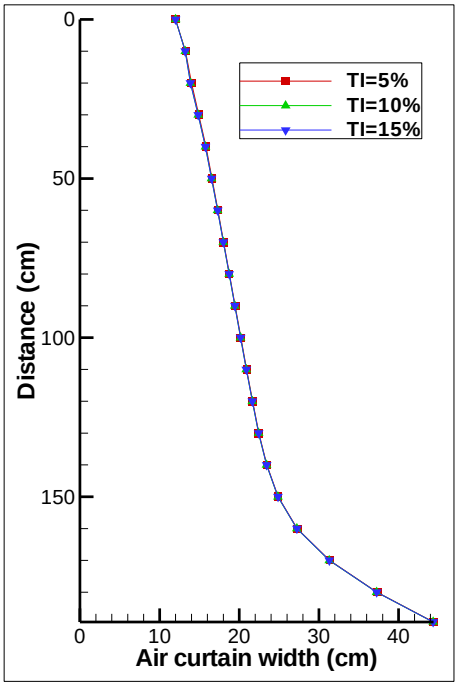

Figure 6.12 Air curtain thickness for different discharge turbulence intensities

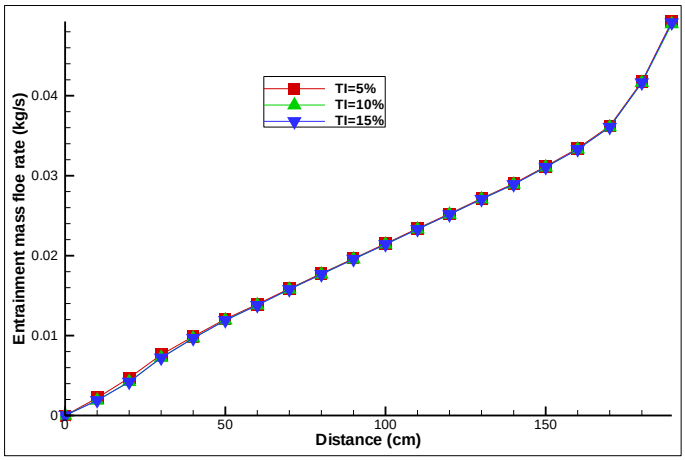

Figure 6.13 Entrainment mass flow rate for different discharge turbulent intensities

6.6.4 Effect of buoyancy force on entrainment

A cooled air curtain experiences acceleration due to the influence of the gravitational force working on its highly dense air. This negative buoyancy effect takes place at the top of the air curtain, where mixing is not yet complete and density differences between the air of the curtain and the ambient air are large.

The thickness for an isothermal and a refrigerated air curtain is shown in Figure 6.14. As can be seen, shrinkage in thickness is noticed for the refrigerated air curtain at the distance from 20 to 70 cm below the DAG, while the isothermal air curtain spreads immediately after discharge. Those results strongly match the PIV results of Field and Loth (2006), which show a necking action at this height. After that, the refrigerated air curtain behaviour is similar to the isothermal air curtain, and its thickness increases again further down the display height.

Figure 6.15 shows the entrainment rates for the isothermal and refrigerated cases. The noticed increase in entrainment rate for the refrigerated (non-isothermal) air curtain can be explained by the preservation of the momentum intensity (i.e. velocity) for a longer distance in the flow direction. As for the isothermal air curtain, the flow tends to dampen more rapidly, which is reflected on the amount of entrained air through the curtain. This means that buoyancy acceleration encourages flow instabilities at the edge of the air curtain, which lead to more entrainment. Since the amount of entrained air is equivalent to that spilled, Figure 6.14 depicts this by showing more air curtain thickness at the bottom of the figure.

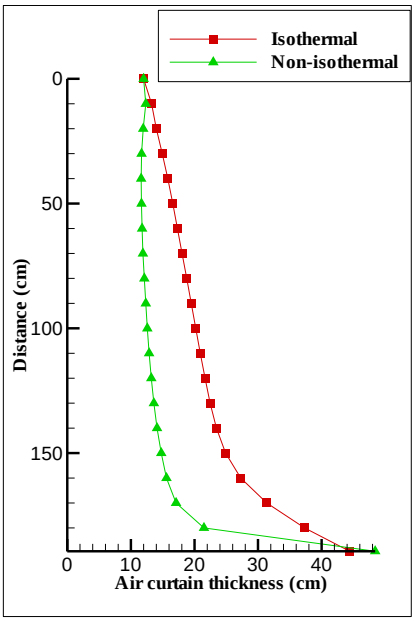

Figure 6.14 Air curtain thickness for the isothermal and non-isothermal cases

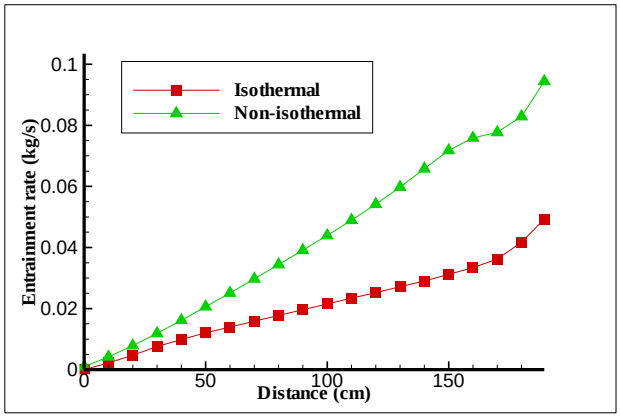

Figure 6.15 Entrainment mass flow rate for the isothermal and non-isothermal cases

6.6.5 Effect of velocity profile shape on entrainment

Given a constant mass flow rate, the shape of the initial velocity profile at the DAG has a strong effect on the amount of ambient air being entrained through the air curtain. This is due to the mixing intensity between the two airstreams at the borderline, which is an indicator of the steepness of the velocity gradient at this location. The shape of the velocity profile is a direct outcome of the geometrical shape of the cabinet body (e.g. the back panel, the canopy, and the honeycomb) prior to the air being ready to depart from the DAG. The velocity profile that can achieve minimum entrainment rate is expected to have higher velocities near the products to

ensure good mixing on the cabinet side and lower velocities near the ambient air to minimise turbulent mixing. This involves configuring the plenum prior to the DAG to align the air streams and encourage low-velocity laminar flow near the ambient air, as demonstrated by Navaz et al. (2006). Another way to achieve this is by imposing an artificial velocity gradient with two or more air curtains of different velocities to have the effect of smoothing out the velocity profile. Figure 6.16 shows a DAG configuration where the outer air curtain is equipped with a screen to create higher pressure drop and achieve lower discharge velocity near the outer side. This improvement enhances the performance of the air curtain by reducing the entrainment rate and eventually reduces the infiltration load of the cabinet.

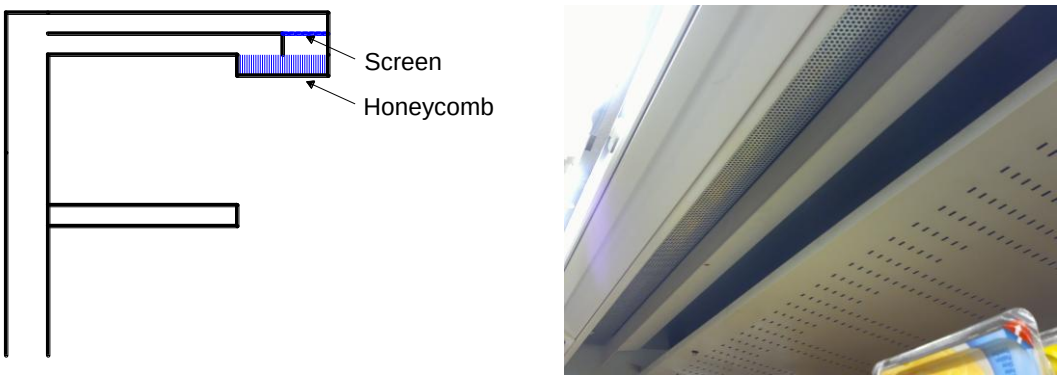

Figure 6.16 A screen used to maintain lower velocity magnitudes at the outer edge of the air curtain (honeycomb not yet installed in real picture)

Analysing the effect of the velocity profile on the entrainment rate was found to be the most demanding among the cases studied herein, mainly for the identification of the air curtain thickness at the top of the air curtain. As mentioned earlier in this work, the air curtain thickness along the height is measured from the wall to the location where the stream-wise velocity reaches a 25% depreciation of the maximum local velocity for each given height. This assumption is relatively easy to obtain for the whole height of the air curtain, except for the DAG location.

Four velocity profiles were analysed, namely, a) uniform, b) parabolic, c) ramp, and d) inverted-ramp. The uniform profile is similar to the plug flow at an exit, the parabolic profile is similar to a fully-developed flow regime between two flat plates, the ramp profile represents a gradual increase in velocity starting from the outer edge of the DAG, and the inverted-ramp represents a gradual increase in velocity starting

from the inner edge of the DAG. Figure 6.17 shows the initial velocity profiles at the DAG coloured by the velocity magnitude, all having the same mass flow rate.

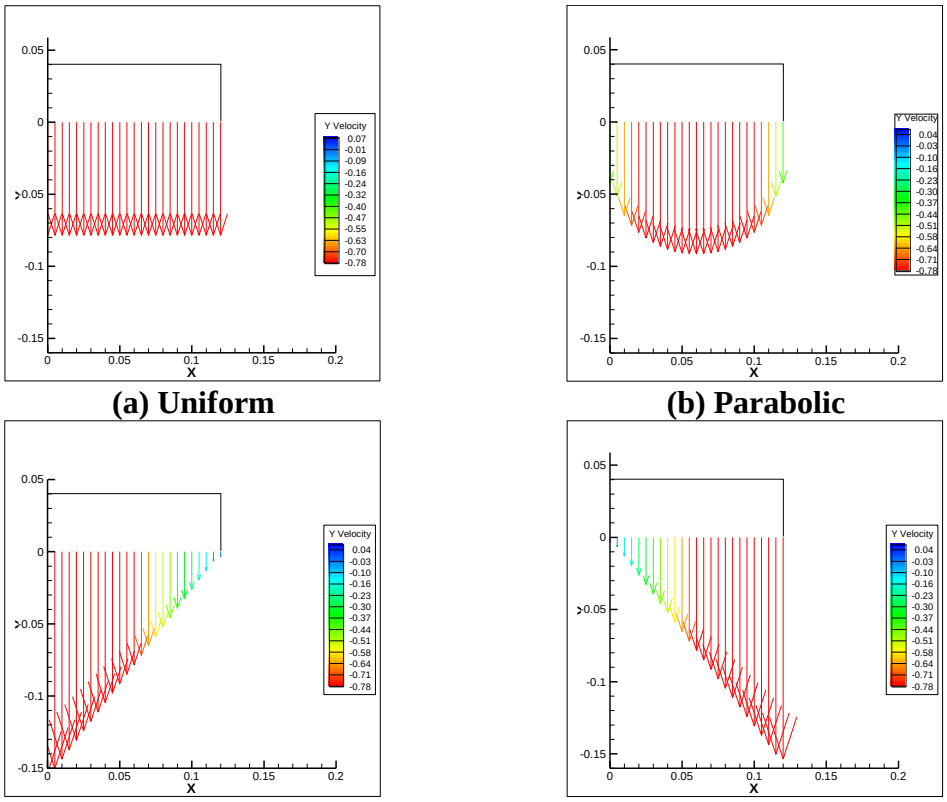

Figure 6.17 Discharge velocity profiles

For the uniform profile (Figure 6.17 (a)), an abrupt change in velocity exists at the outer edge, hence the air curtain thickness is taken to be as the DAG width (12 cm) and the mass flow rate was accordingly calculated through this width. This notion was also considered for the inverted-ramp profile (Figure 6.17 (d)), due to the similar circumstance at the outer edge. On the contrary, the gradual change in velocity near the outer edge for the parabolic and ramp cases introduced some scepticism as to whether the air curtain thickness at this location should be taken as the DAG width or the 25 % decrease in velocity should be applied. Taking the air curtain thickness at the DAG width would give the right mass flow rate at this height, nevertheless, the entrainment rate along the air curtain will show negative values, which is not physically possible. This is because the air curtain thickness gets less than the DAG width downstream, and so does the mass flow rate. It was finally decided that the 25% reduction in velocity is to be applied even for the DAG location. Although this

yields less mass flow rate than what is actually discharging (since the line of mass flow rate is now shorter), the entrainment rate obtained along the air curtain is correct since this reduced amount is repeatedly subtracted from the local mass flow rate of all cross sections.

Looking at Figure 6.18 and Figure 6.19, it is immediately recognised that the profiles with high velocity gradients at the outer edge of the air curtain, namely the uniform and inverted-ramp profiles, entrain more ambient air. The amount of entrained air is much more in the case of the inverted-ramp profile (Figure 6.19), due to the enlarged velocity gradient. On the other hand, the ramp profile has the least entrainment rate followed by the parabolic profile. From the above, it can be concluded that, since the discharge velocity profile of actual open display cabinets is close to that of an inverted-ramp shape, there is plenty room for improvement.

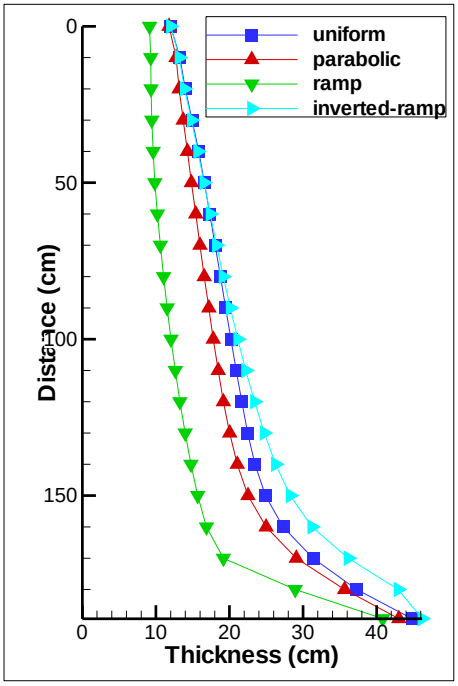

Figure 6.18 Air curtain thickness for different velocity profiles

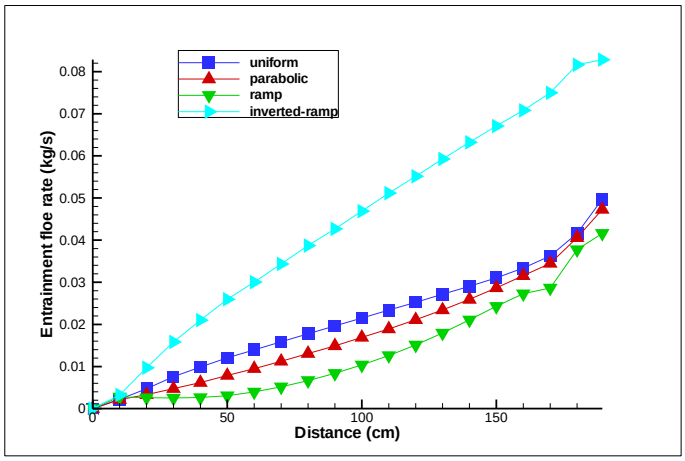

Figure 6.19 Entrainment rate for different velocity profiles

6.6.6 Effect of the DAG width on entrainment rate

The effect of changing the DAG width on the entrainment rate while holding the mass flow rate constant (0.11 kg/s) is examined here. Four DAG widths were examined, namely 8, 12, 16, and 20 cm. Figure 6.20 shows stream-wise (y-) velocity contours for the different DAG widths. It is obvious that for the specified mass flow rate, the 20 cm DAG does not have sufficient momentum to seal against the entire opening height. In order to compare the change in air curtain thickness due to entrainment along the height of the opening, the air curtain thickness in each case was normalised with the DAG width, as shown in Figure 6.21. Excluding the 20 cm DAG curtain, the 8 cm DAG entrains the most. This is because for the same mass flow rate, the discharge velocity is higher, causing more ambient air to be withdrawn into the air curtain.

Figure 6.22 shows the entrainment rate associated with the four DAG widths. It is noticed that the amount of entrained air is not linearly proportional with the DAG width, but has a sudden increase as the width changes from 12 to 8 cm. The average discharge velocities for the 8, 12, and 16 cm DAG widths are 1.17 m/s, 0.78 m/s, and 0.59 m/s, respectively. The aforementioned results reinforce the fact that the level of entrainment is strongly dependent on the velocity magnitude at the DAG.

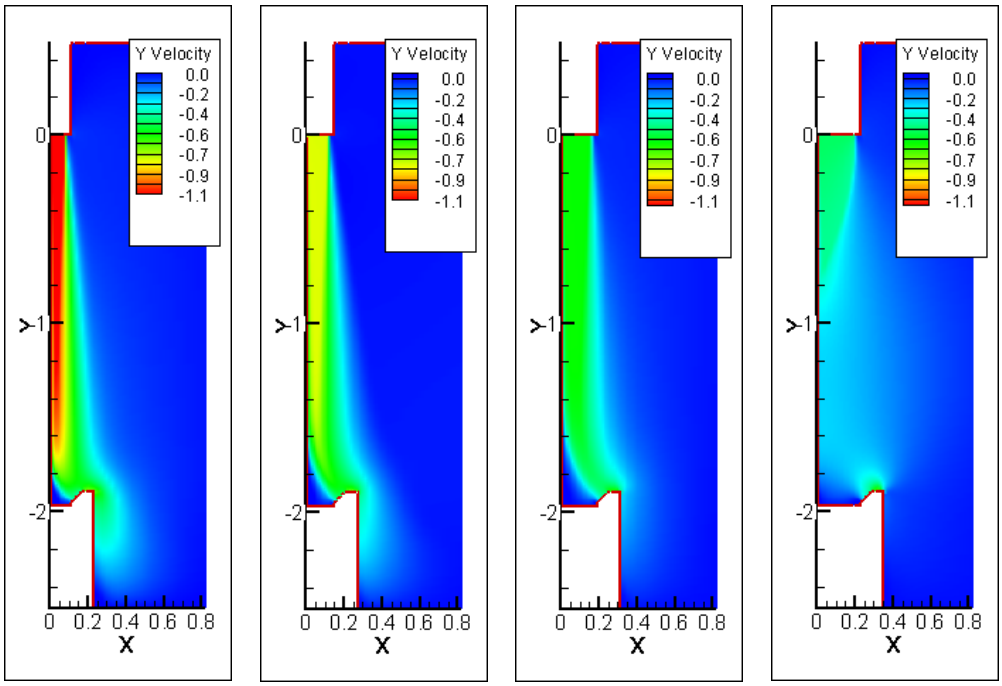

(a) 8 cm **(b) 12 cm** **(c)16 cm** **(d) 20 cm**

Figure 6.20 Stream-wise (y-) velocity contours of different DAG widths

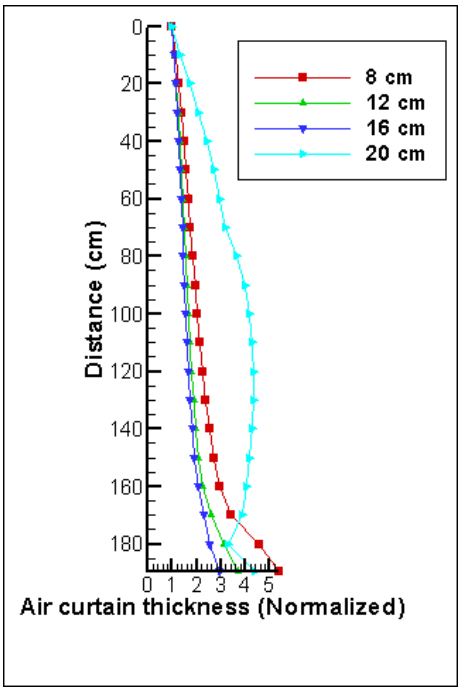

Figure 6.21 Normalized air curtain thickness for different DAG widths

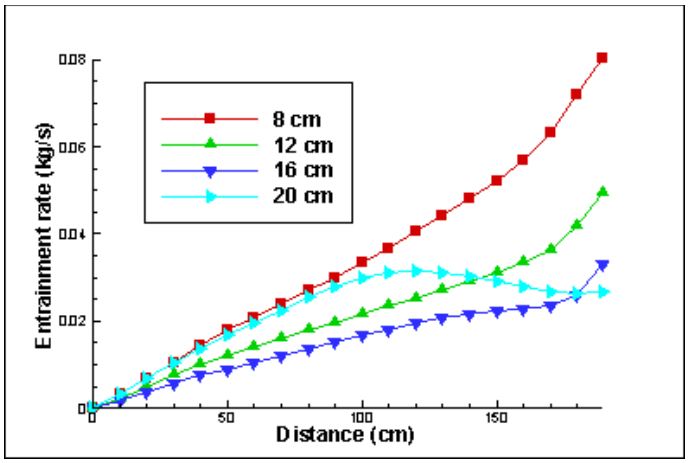

Figure 6.22 Entrainment rate for different DAG widths

6.7 Summary

This chapter provided a reliable numerical method where the entrainment rate through the air curtain can be accurately quantified. An idealisation of the open display cabinet was used, where the products were modelled as a solid wall resembling a fully packed cabinet. The effect of many discharge parameters were examined, including the discharge velocity, velocity profile, temperature, turbulence intensity, and DAG width. It was found that within the typical range of each of the aforementioned parameters, the velocity profile has the most profound effect on the entrainment rate, followed by the velocity magnitude. This emphasises the fact that a high velocity gradient at the air curtain borderline triggers mixing, leading to the enhancement of the entrainment action. This, combined with the impact of velocity magnitude suggests that entrainment is predominantly momentum driven. It is also reconfirmed here that the amount of entrained ambient air is proportional to the distance travelled by the air curtain. As a result, low-front open display cabinets (with display opening heights larger than 150 cm) have more tendency to suffer from entrainment than cabinets of typical display height (in the range of 125 cm). The use of the Reynolds number as a parameter to gauge the performance of the air curtain was shown to be misleading, especially when the DAG width is used as the characteristic length. Quantifying the amount of the entrained air that manages to infiltrate into the cabinet, hence forming part of the cooling load, is the subject of the next chapter.

CHAPTER 7
Infiltration rate into the cabinet

"It's just a job. Grass grows, birds fly, waves pound the sand.
I beat people up."

(Mohammed Ali Clay, 1942-present)

In this chapter, the refrigeration duty required for the shelved low-front cabinet presented in Chapter 5 to meet climate classes 0 and 3 of the ISO standard will be determined, with emphasis on complying with M-package temperature class M1. Then, the various components that go into making the total cooling load of the cabinet will be analysed. Infiltration of the warm ambient air into the cabinet is well known to constitute the dominant share of the cooling load. After presenting some techniques that have been implemented in the literature for the determination of the infiltration rate into open refrigerated display cabinets, two other techniques will be presented. The first one is a numerical technique that is conceptually similar to the tracer-gas method which aims at directly determining the sensible and latent components of the infiltration load by tracking the specific amounts of dry air and water vapour from the test room to the air-on section of the evaporator coil. The second technique utilises psychrometrics to quantify the infiltration load as well as the other cooling load components of the cabinet through the identification of the various heat transfer processes encountered within the cabinet.

7.1 Introduction

The modification done on an open vertical refrigerated display cabinet was presented in Chapter 3 with the aim of producing a low-front configuration. Contemporary low-front cabinets found in supermarkets and retail stores have display openings in the order of 150 cm in height. Here however, the cabinet under consideration has a display opening height of 200 cm (a 150% increase in display area over the original design). Since no modification was done to the refrigeration system, the cabinet failed to comply with the requirements of class M1 ($-1\ ^{o}C \leq T_{prod} \leq +5\ ^{o}C$) of the ISO

standard, even when tested against the least demanding conditions of climate class 0 (T_{db}=20 ^{o}C, R.H.=50 %). This was mainly because the air curtain struggled to seal against the extended height and could not effectively cool the front part of the products, especially the ones placed on the lower shelves. As a result, the refrigeration system could not cope with the excessive amounts of warm ambient air being directly infiltrated into the RAG. Therefore, there must be an optimum amount of cold air that, if appropriately distributed within the cabinet, is capable of 1) forming an efficient air curtain, 2) minimising the infiltration and entrainment rates, 3) minimising the energy consumption, and 4) maintaining the products within the required temperature range.

Although the terms entrainment and infiltration are sometimes used synonymously in the literature, they are two different entities in the explanation of the air flow dynamics of open refrigerated display cabinets. In buildings, for example, infiltration is defined by ASHRAE (2009) as "the rate of uncontrolled air exchange through unintentional openings that occurs under given conditions". In open display cabinets, however, the RAG is an opening that is "intentionally" placed at a preset location to retrieve most of the refrigerated air that would have been spilled otherwise. The infiltrated ambient air into the RAG is inevitable due to the entrainment process that previously took place at the boundary between the air curtain and the ambient air. This however does not necessarily mean that increased entrainment leads to increased infiltration, since only a portion of the entrained air is infiltrated into the display cabinet. Therefore, even a 100% efficient air curtain entrains ambient air, but will not allow any of it to infiltrate into the cabinet. Navaz et al. (2005) conducted a study on an open display cabinet having a display height of 100 cm, and estimated a 30 to 35% of the entrained air to be infiltrated into the cabinet. Since the ambient temperature is higher than the refrigerated cabinet air temperature, the warm ambient air being infiltrated can account for a large fraction of the total cabinet cooling load. Faramarzi et al. (2002) evaluated the performance and energy impact of installing glass doors on an open refrigerated display cabinet, and found that the cooling load was reduced by 68%. Implications of excessive infiltration rates include 1) higher refrigeration system capital cost to deal with the extra cooling load, 2) long operation periods that in turn increase the energy consumption of the cabinet, and 3) longer and

more frequent defrost periods in order to remove the frost formed on the evaporator coil. Quantifying and minimising the infiltration rate into the evaporator coil is therefore imperative since it constitutes the largest contributor to the cooling load of the cabinet.

7.2 Refrigeration capacity requirement for climate classes 0 and 3

This section aims at finding the refrigeration capacity needed to meet the cooling load requirements of classes 0 and 3 of the ISO standard using the CFD approach, without conducting further modifications on the physical configuration of the cabinet. Starting with the validated model of the shelved cabinet (see Chapter 5), the boundary conditions of the test room were kept the same, except for the conditions at the test room's inlet, which was assigned as a velocity-inlet boundary condition with temperature and relative humidity of 20 ^{o}C and 50% for climate class 0 and 25 ^{o}C and 60% for climate class 3.

In order to follow the ISO standard, it is important to note that the cross-flow velocity parallel to the span of the cabinet must be 0.2 m/s at the locations shown in Figure 3.1, and not on the test room's inlet. This necessitates that the horizontal velocity of the air prior to reaching the cabinet's leading side-wall, which is about to interact with the air curtain, should have a value of 0.2 m/s. During 3D simulations, the air near the domain's boundaries (walls, ceiling, and floor) is slowed down to zero in order to satisfy the no-slip condition imposed at those walls. As a result, the air velocity away from those boundaries is slightly increased to satisfy the continuity equation. Figure 7.1 shows the cross-flow velocity contours at the middle height of the domain. It is clear that the cross-flow velocity near the walls approaches zero, while a velocity increase is experienced right after entry. Therefore, the velocity at the domain's inlet boundary was reduced to 0.1 m/s (by performing a trial-and-error process) to ascertain that the cross-flow velocity at the designated locations in the ISO standard (Figure 3.1) is equal to 0.2 m/s.

As for the cabinet, the air-off temperature and relative humidity in all the simulations were fixed at -2 ^{o}C (271.1 K) and 90%, respectively. These thermal conditions are usually encountered during normal operation (i.e. non-defrosting periods) when refrigerant R-404A is used, and were found by Maki and Tassou (2005) to yield a

good compromise between the required air flow and the evaporator and compressor power consumption.

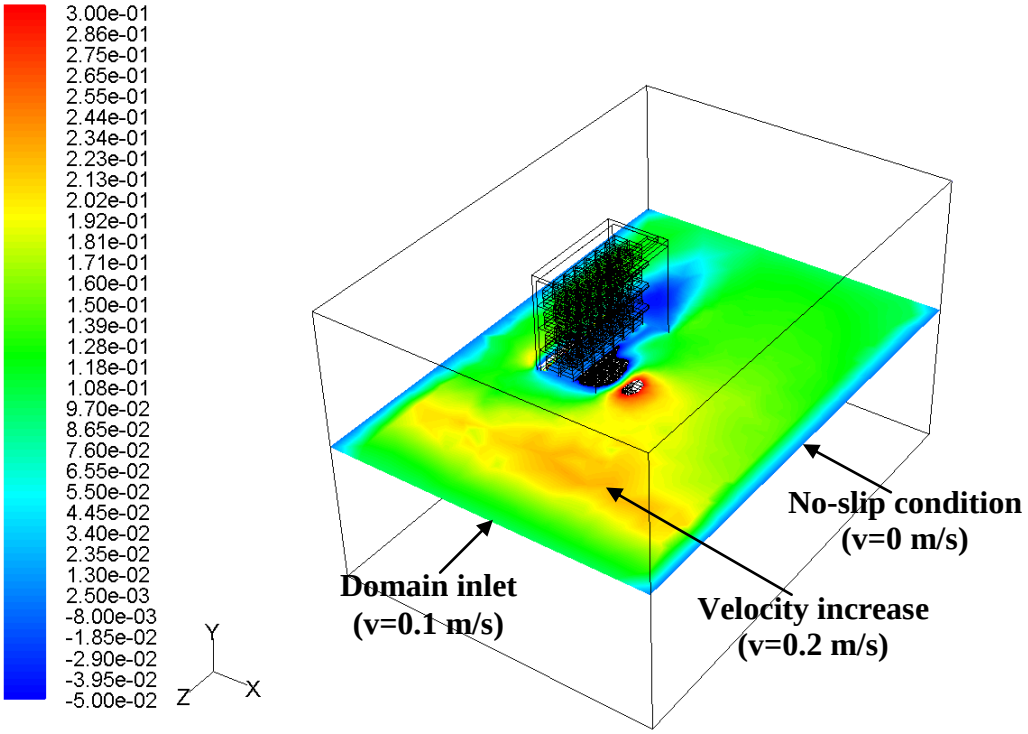

Figure 7.1 Velocity contours at the cabinet's mid-height showing a sudden increase in velocity as a result of the no-slip condition at the walls

During operation, it is logical to find the maximum product temperature at the front side of the cabinet where products are totally exposed to convection and radiation heat exchanges with the environment (Evans et al. (2007)). Furthermore, the experimental results obtained in this work showed that the products at the lowest shelf (shelf 7) suffer from the highest rise in temperature because of the absence of the air curtain's cooling effect at this location. In addition, the interaction between the cross-flow and the cabinet's leading side wall causes the warm ambient air to intrude the cabinet at the trailing side wall and further temperature rise is experienced by the products at this location. From the above, the product (M-package) positioned at the right-front-top side of shelf 7 (bottom shelf), which was designated as T_{7RFT} in Chapter 3, seems to suffer the most and its temperature will be taken as an indicator for the required amount of air-off mass flow that is sufficient for the proper operation of the cabinet. The air-off mass flow rate was gradually increased by increments of

0.01 kg/s until all the products were in accordance with class M1 of the ISO standard.

Initially, the experimentally obtained air-off mass flow rate of 0.15 kg/s was examined to see if it was sufficient to cool the products when the new aforementioned thermal conditions were applied at the air-off section ($T_{air\text{-}off}$=-2 ^{o}C, R.H.=90 %). Figure 7.2 (a) shows an isothermal surface of 5 ^{o}C at the display opening superimposed by stream-wise (y-) velocity contours for the experimentally obtained mass flow rate (0.15 kg/s). The average downward velocity at the DAG was found to be 0.47 m/s, which was not sufficient to create a properly functioning air curtain for such display height (note that the DAG width is 12 cm). It is clear from the figure that the products at shelf 7, and especially those ones located at the right-hand side, are unprotected by the air curtain, which allowed the warm ambient air to heat the M-packages to an unacceptable temperature of 8 ^{o}C. Therefore, it can be concluded that even when the air-off temperature is decreased to -2 ^{o}C, the cabinet was still unable to pull the temperature of all the products below the targeted 5 ^{o}C.

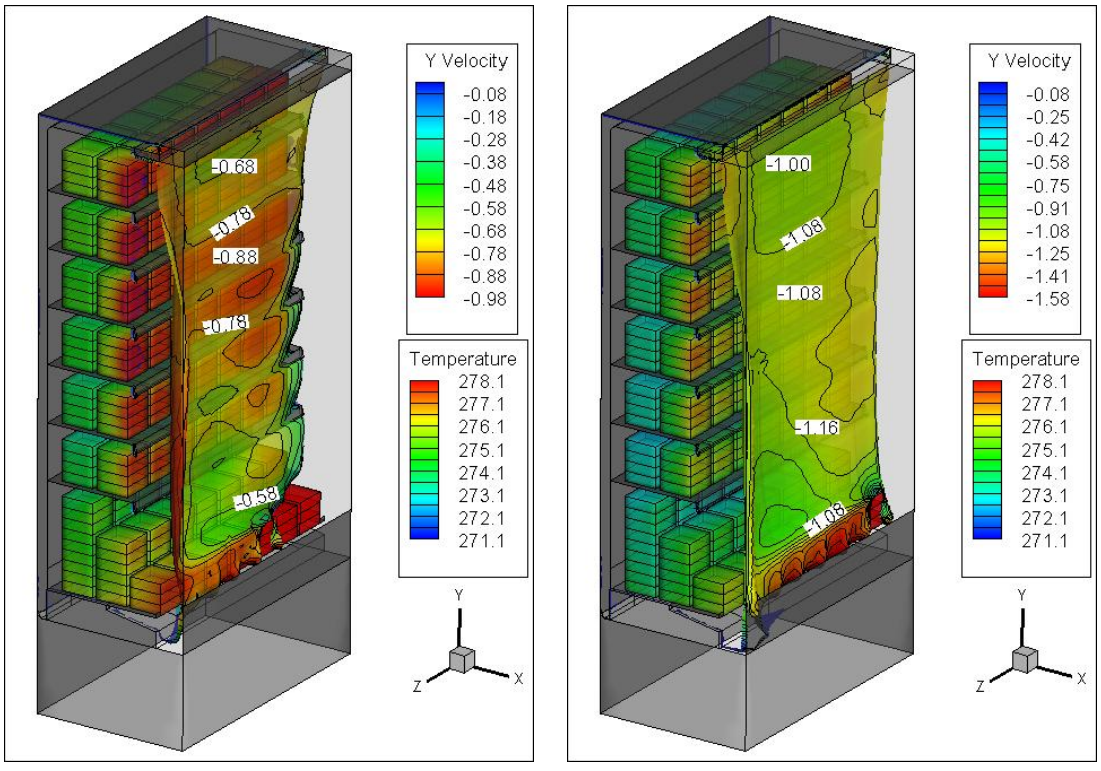

(a) $\dot{m}_{air-off}$ **= 0.15 kg/s** **(b)** $\dot{m}_{air-off}$ **= 0.24 kg/s**

Figure 7.2 Cabinet tested against climate class 0 and different air-off mass flow rates. An isothermal surface of 5 ^{o}C is shown at the display opening

After performing a number of trials to meet the requirements of climate classes 0 and 3, the cabinet managed to work in accordance to M-package class M1 when the air-off mass flow rates were 0.24 kg/s and 0.30 kg/s, respectively. Table 7.1 summarises the cabinet's total cooling load together with other details for the three cases under consideration. For climate class 0, the average discharge velocity had to be increased from 0.47 m/s to 0.77 m/s. Figure 7.3 shows the temperature contours of the cabinet when tested against climate class 3. A 5 ^{o}C isothermal surface at the display opening is shown and superimposed by the stream-wise (y-) velocity contours. The average velocity at the DAG (associated with the 0.3 kg/s mass flow rate) was 0.97 m/s. The need to increase the flow rate at the DAG is mainly due to the higher temperature and relative humidity values compared to climate class 0 conditions.

The total cooling load of the cabinet was increased by 58.2% when tested against the more demanding requirements of climate class 3. This is mainly because of the 25% increase in the cabinet's mass flow rate. Revisiting Table 7.1, the latent component was increased by 92% while the sensible component was increased by 41%, showing that the latent load has a more detrimental effect when comparing the cabinet's performance in the two climate classes considered here.

Table 7.1 Comparison of cabinet performance with climate classes 0 and 3

Climate class	$\dot{m}_{air-off}$ (kg/s)	V_{DAG} (m/s)	T_{7RFT} (K)	T_{air-on} (K)	R.H.$_{\text{air-on}}$ (%)	$\dot{Q}_{sen}$ (W)	$\dot{Q}_{lat}$ (W)	$\dot{Q}_{tot}$ (W)
0	0.15	0.47	281.1	281.0	69.9	1,492	739	2,231
0	0.24	0.77	277.8	279.0	74.5	1,905	953	2,859
3	0.30	0.97	277.9	280.0	82.0	2,693	1,832	4,525

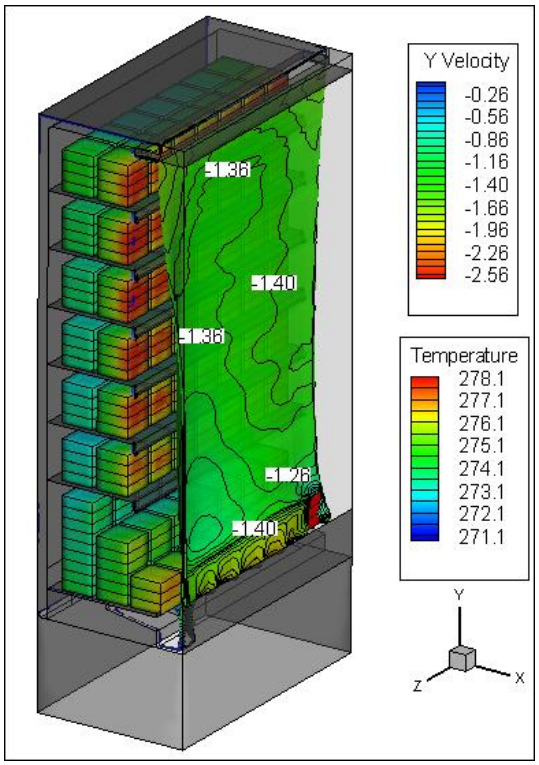

$\dot{m}_{air-off}$ **= 0.30 kg/s**

Figure 7.3 Cabinet tested against climate class 3 and air-off mass flow rate of 0.3 kg/s. An isothermal surface of 5 ^{o}C is shown at the display opening

In order to gauge the credibility of the aforementioned results, the performance of the cabinet was further assessed by comparing the Total (electrical) Energy Consumption (TEC) per Total Display Area (TDA) with the figures provided by the Energy Technology Criteria List for Refrigerated Equipment (2009), which is part of the ECA (Enhanced Capital Allowance) scheme. This scheme is part of a government programme that is concerned with encouraging businesses to invest in low carbon, energy-saving equipment. The ratio of TEC to TDA is termed by the ECA as the Energy Efficiency Index (EEI), which, for integral and remote open refrigerated display cabinets operating under M1 conditions, must be less than or equal to 11.95 and 11.45 kWh/day/m^2, respectively.

For the cabinet considered here, TEC and TDA, which were calculated in accordance with sections 5.3.6.3.3 and A.2.2 of the ISO 23953-2 standard (2005), were found to be 40.91 kWh and 2.46 m^2, respectively. This resulted in an EEI of 16.63 kWh/day/m^2, indicating that the cabinet does not comply with the criteria set by the ECA scheme.

7.3 Cooling load components

It was mentioned earlier in this work that analysing the thermo-fluid dynamics of open refrigerated display cabinets is highly complicated due to the involvement of coupled conduction, convection, and radiation heat transfer processes. In this section, the focus is to perform a cooling load breakdown for the low-front cabinet tested against climate class 3 conditions in order to understand and also rank the magnitude of the different parts of the cooling load. This is done by comparing the numerically obtained cooling load components with the manually calculated values using the first law of thermodynamics (energy balance) and the conservation of mass (mass balance) equations.

The energy balance in open refrigerated display cabinets was addressed in detail by Howell (1993, (a)) and Faramarzi (1999). The flow of heat into and out of a display cabinet can be represented by:

$$\dot{Q}_{tot} = \dot{Q}_{cond} + \dot{Q}_{rad} + \dot{Q}_{\inf} + \dot{Q}_{fan} + \dot{Q}_{lights} + \dot{Q}_{ASH} + \dot{Q}_{def} + \dot{Q}_{pulldown} \qquad (7.1)$$

where $\dot{Q}_{tot}$ is the total refrigeration load on the cabinet taken across the evaporator coil, $\dot{Q}_{cond}$ is the heat transfer by conduction through the back, side, and top walls driven by the temperature difference between the cabinet and the environment, $\dot{Q}_{rad}$ is the radiation heat transfer from the surrounding walls of the test room to the products and also to the inner and outer walls of the cabinet, $\dot{Q}_{\inf}$ is the infiltration load due to the air exchange across the air curtain (entrainment) that manages to infiltrate into the RAG, $\dot{Q}_{fan}$ is the load due to heat dissipation from the fans, $\dot{Q}_{lights}$ is the load due to the lights, $\dot{Q}_{ash}$ is the cabinet's anti-sweat heater load required to eliminate condensation on the walls of the cabinet, $\dot{Q}_{def}$ is the defrost energy load required for removing the ice build-up on the evaporator coil, $\dot{Q}_{pulldown}$ is the energy required to reduce the product temperature down to the required value after each defrost cycle.

The external loads of the cabinet at steady state conditions are conduction, radiation, and infiltration. These can represent anything between 80% to 90% of the total load

of the cabinet, and will be considered in greater detail in this chapter. Neglecting internal loads such as lights and fans, the total load of the cabinet can be given by:

$$\dot{Q}_{tot} = \dot{Q}_{cond} + \dot{Q}_{rad} + \dot{Q}_{\inf} \tag{7.2}$$

The total cooling load that will be satisfied by the evaporator coil is hence,

$$\dot{Q}_{tot} = \dot{m}(h_{air-on} - h_{air-off}) \tag{7.3}$$

where $\dot{m}$ is the air mass flow rate through the evaporator coil, $h_{air\text{-}on}$ and $h_{air\text{-}off}$ are the air enthalpies at the air-on and air-off sections, respectively. For the cabinet considered at climate class 3 conditions, this yields a total cooling load of 4356 W, which is considered high when compared to the load of cabinets with lower display heights. The sensible cooling load, $\dot{Q}_{sen}$, can be determined from:

$$\dot{Q}_{sen} = \dot{m} c_p (T_{air-on} - T_{air-off}) \tag{7.4}$$

where c_p is the specific heat of moist air, and $T_{air\text{-}on}$ and $T_{air\text{-}off}$ are the temperatures at the air-on and air-off sections, respectively. This gives a sensible cooling load of 2671 W for the cabinet considered. The latent cooling load, $\dot{Q}_{lat}$, can be obtained from:

$$\dot{Q}_{lat} = \dot{Q}_{tot} - \dot{Q}_{sen} \tag{7.5}$$

or:

$$\dot{Q}_{lat} = \dot{m}(w_{air-on} - w_{air-off}) h_{fg} \tag{7.6}$$

where $w_{air\text{-}on}$ and $w_{air\text{-}off}$ are the humidity ratios (kg_w/kg_{da}) at the air-on and air-off sections, respectively, and h_{fg} is the latent heat of vaporisation of water based on the average temperature of the air-on and air-off sections. The latent load predicted was 1686 W. Table 7.2 summarises the sensible and latent loads obtained from the manual calculations and their percentages relative to the total cooling load. It is clear that they are in good agreement with the CFD results presented in Table 7.1, with a discrepancy of less than 4%.

Table 7.2 Contribution of sensible and latent loads

	Refrigeration load (W)	Percentage (%)
$\dot{Q}_{sen}$	2670.5	61.3
$\dot{Q}_{lat}$	1685.8	38.7
$\dot{Q}_{tot}$	4356.3	100

7.3.1 Conduction heat transfer

When the cabinet is in operation, heat is transferred by conduction from the warm ambient air to the cold air inside the cabinet through the back, top, and side walls. The temperature difference across the walls is the driving force, and is roughly 27 ^{o}C for climate class 3 conditions when the cabinet's air-off temperature is -2 ^{o}C. Consequently, the air leaving the evaporator coil gets gradually heated as it flows through the back duct and the canopy before reaching the DAG. In addition, the cabinet's cold air is further heated up in the vicinity of the products by conduction heat transfer through the cabinet's side walls.

Conduction heat transfer through the different walls of the cabinet was obtained directly from the CFD simulation and also by manual calculations using:

$$\dot{Q}_{cond} = U\, A_{wall} (T_{amb} - T_{air-off}) \tag{7.7}$$

Here, A_{wall} is the total surface area of each individual wall and U is the overall heat transfer coefficient given as

$$\frac{1}{U} = \frac{1}{h_i} + \frac{L}{k} + \frac{1}{h_o} \tag{7.8}$$

where L is the wall thickness, k is the thermal conductivity, h_i and h_o are the convective heat transfer coefficients of the inner and outer walls, respectively. Since the inner and outer surfaces experience forced and/or free convection, an air film layer is developed, and the convective coefficients associated with them must be included in the calculation of the conduction load. However, determining the exact values of these quantities is out of the scope of this work and values of 9.0 W/m^2.K and 11.0 W/m^2.K were used for the outer and inner surfaces, respectively. Table 7.3 shows the manually and numerically obtained conduction cooling loads of the cabinet. A good agreement between the two approaches is evident for the heat

transfer through the back and top walls, but a large deviation is noticed for the side walls. Considering that the flow is impinging the left-side wall while recirculating at the right-side wall (refer to Figure 7.1), heat transmission through these walls must be low. This suggests that the manually obtained heat transfer of 373.5 W is an over prediction. Therefore, the total cooling load due to conduction was taken from the CFD results as 212 W, which accounts for 4.9% of the total cooling load of the cabinet.

Table 7.3 Conduction heat transfer through the walls of the cabinet

	K (W/m.K)	L (m)	A (m^2)	$h_{i,\,eqn}$ (W/ $m^2.^oC$)	$h_{o,\,eqn}$ (W/ $m^2.^oC$)	U_{eqn}	$\dot{Q}_{eqn}$ (W)	$h_{i,\,CFD}$ (W/ $m^2.^oC$)	$h_{o,\,CFD}$ (W/ $m^2.^oC$)	U_{CFD}	$\dot{Q}_{CFD}$ (W)
Back wall	0.035	0.05	2.59	11.0	9.0	0.61	42.9	3.4	0.97	0.36	37.5
Top wall	0.035	0.05	0.69	11.0	9.0	0.61	11.4	2.6	1.0	0.36	10
Right side wall	0.2	0.01	1.49	11.0	9.0	3.93	159.6	15.2	5.4	3.3	72.5
Left side wall	0.2	0.01	1.49	11.0	9.0	3.96	159.6	9.7	4.26	2.5	92
Total	-	-	6.26	-	-		373.5	-	-	-	212

7.3.2 Radiation heat transfer

The cabinet's cooling load due to radiation is a function of 1) the temperature difference between the products' surfaces and test room's walls (including ceiling and floor), 2) the emissivities of the product surfaces and the test room walls (including ceiling and floor), 3) the product surface area, and 4) the view factor between the products and the test room walls. Previous studies by Stribling (1997), Faramarzi (1999), and Hadawey (2006) used a simplified equation for determining the radiation load by applying

$$Q_{rad} = \frac{\sigma A_{display}(T_{surr}^4 - T_{prod}^4)}{\frac{1}{\varepsilon_{surr}} + \frac{1}{\varepsilon_{prod}} + \frac{1}{F} - 2} \tag{7.9}$$

where σ is the Stefan-Boltzmann constant (5.67×10^{-8} $W/m^2.K^4$), $A_{display}$ is the cabinet's display opening area, T_{surr}, ε_{surr}, T_{prod}, and ε_{prod} are the temperatures and emissivities of the surrounding walls and the products, respectively, and F is the view factor between the cabinet and the test room.

The view factor is a fraction ranging from 0 to 1 that parameterises the thermal power leaving the relatively warm walls of the test room and reaching the products and the cold inner walls of cabinet. Since the cabinet is totally enclosed by the test

room, a view factor of 1 was used for the calculations. The perforated back panel is made of polished stainless steel having an emissivity of 0.04, which is nearly an order of magnitude smaller than that of the products. This relatively small value makes the radiation exchange with the surrounding walls of the test room less significant when compared with that of the products.

Using equation (7.9), the cooling load due to radiation was found to be 209 W, which is higher than the numerically obtained value of 126 W. This over-prediction is due to the use of the cabinet's display opening area (2.27 m^2). Although radiation exchange takes place between the surrounding walls of the test room and the actual products' outer surface area exposed to radiation (14.27 m^2), only the front part of the products facing the test room heavily interacts with the surroundings. The manually produced radiation load was closer to the CFD results when the front surface area of the products (1.5 m^2) was used instead of the display opening area of the cabinet, yielding a value of 138.6 W. The 126 W obtained due to radiation heat transfer was found to be 2.9% of the cabinet's cooling load. The results presented here show the dependency of the cabinet's cooling load due to radiation on the size of the display opening area, and emphasises the importance of this parameter when analysing the performance of low-front refrigerated open display cabinets.

7.4 Measurement techniques of the infiltration rate

The infiltration rate through open refrigerated display cabinets has been traditionally determined by the knowledge of either the thermal conditions or the concentration of a tracer gas at both sides of the evaporator coil. Both numerical and experimental techniques were used, and the merits and disadvantages of each technique depend on its accuracy and ease of implementation.

7.4.1 Condensate collection technique

Knowing the amount of condensed water dripping off the evaporator and accumulating in the condensate tray during operation can be used to determine the amount of infiltrated ambient air into the cabinet. The amount of this condensate water (kg_{water}) is proportional to the humidity ratio ($kg_{water}/kg_{dry\ air}$) of the ambient air, which in turn can be determined with the use of a psychrometric chart if the ambient air temperature and relative humidity are known. The mass of the infiltrated air can

simply be calculated from the humidity ratio and the knowledge of the time duration at which this condensate water was collected. This technique however is described by Amin et al. (2009) to be time consuming, since the collection of the condensate water requires lengthy periods of experimentation. Another concern is the accuracy in reading the amount of condensate water collected, since some of it might evaporate during testing.

7.4.2 Enthalpy measurement technique

The enthalpy measurement technique establishes a correlation between the infiltrated warm ambient air through the cabinet and the enthalpies (or temperatures) at the DAG, RAG, and the ambient air. By drawing a control volume around the air curtain region (extending vertically from the DAG to the RAG and horizontally from the shelves to the ambient air), the inlets and outlets may be specified as shown in Figure 7.4. After applying the conservation of mass and the first law of thermodynamics equations to the air leaving from and returning to the open display cabinet and also the air entraining into and the air spilling from the air curtain, the fraction of infiltrated ambient air into the cabinet, which is sometimes known in the literature as the thermal entrainment factor, α , can be determined by:

$$\alpha = \frac{h_{RAG} - h_{DAG}}{h_{Amb} - h_{DAG}} \tag{7.10}$$

where h_{RAG}, h_{DAG}, and h_{Amb} are the enthalpies at the return air grille, discharge air grille, and ambient air, respectively. This factor ranges from 0 to 1, and can serve as a good indicator for the quantitative assessment of the air curtain. However, determining the air enthalpies during experiment is not straightforward and is difficult to obtain. Another alternative is to use the temperatures at those locations instead of the enthalpies by assuming a constant specific heat for all temperatures. However, a recent study by Gaspar et al. (2010) showed that this assumption makes the aforementioned technique provide different judgments when based on enthalpy than when based on temperature. Using temperature instead of enthalpy resulted in a 16% decrease in the results, due to the absence of latent load (moisture content) when using temperature alone.

The aforementioned technique (based on temperature) was used by Navaz et al. (2005), but was found to be time-consuming and indirect, since it requires the knowledge of the average temperatures at the DAG, RAG, and ambient air. In addition, it principally relies on the thermal conditions of the various air streams involved, and cannot be used to determine infiltration during isothermal operation, e.g. defrost cycles.

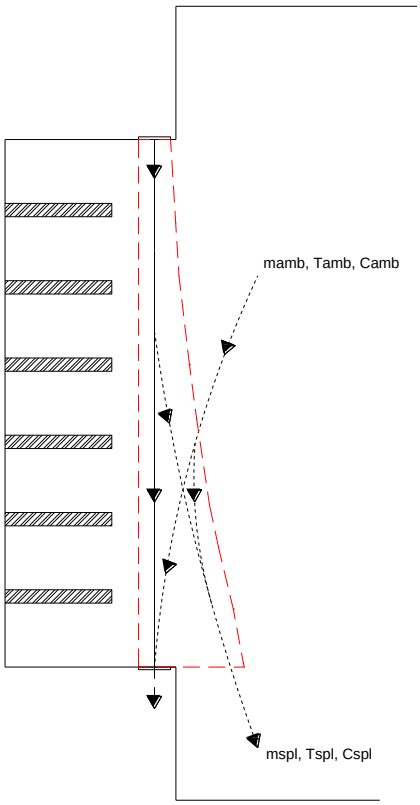

Figure 7.4 Control volume around the air curtain

7.4.3 Tracer-gas technique

The tracer-gas technique has been proven to be reliable in determining the infiltration rate through doors of refrigerated facilities, and recently, through open display cabinets. This technique was first pioneered by Gosney and Olama (1975) who developed correlations based on measurements of air infiltration for doors of cold stores. The procedure is commenced by mixing a tracer gas (usually CO_2) at the coil air-off section, and then measuring its concentration at the coil air-on section after it has travelled from the perforated back panel and the DAG to the RAG. By running an analysis on the conservation of mass across those locations, a relationship can be

established between the tracer gas concentration and the infiltration rate. Unlike the enthalpy measurement technique, no thermal properties need to be known along the process, and the infiltration rate can be directly determined solely from the tracer gas concentration levels. This technique may be analogous to the enthalpy measurement technique if the high concentration of the tracer gas at the DAG is compared with the temperature of the cold air at the DAG, and the low concentration ambient air is compared with the temperature of the warm ambient air. Amin et al. (2009) have successfully used this technique to determine the infiltration rate in open display cabinets by introducing a Non-dimensional form of Infiltration Rate, NIR, defined as:

$$NIR = \frac{\dot{m}_{\inf}}{\dot{m}_{RAG}} = \frac{C_{DAG} - C_{RAG}}{C_{DAG} - C_{Amb}} \tag{7.11}$$

where C is the mass concentration of the tracer gas. In the limit of no infiltration, the concentration at the RAG section is equal to that at the DAG, leaving NIR with a value of zero. On the other hand, when the concentration at the RAG is that of the ambient, NIR is equal to 1.

7.4.4 CFD-tracer-gas method

In this section, the CFD approach is used to directly determine the infiltration rate into the cabinet by a methodology similar to the experimental tracer-gas technique. Using the species transport modelling during the simulation, the moist air streams entering the domain via the test room's inlet and the cabinet's air-off inlet are further decomposed into their dry and moist parts. This breakdown is impossible to execute in reality, but is achievable with CFD, showing one of the unique advantages of simulation over experiment. Since dry air and water vapour are pure substances when existing under low atmospheric pressure, they can be considered as incompressible perfect gases in the calculations. As a result, the developed model deals with four species at the same time, namely, the mass fractions of dry air and water vapour emanating from the two aforementioned domain inlets. The essence of this method is to determine the total amount of infiltration rate, and more importantly, to provide the breakdown of the cooling load components (sensible and latent) by specifically quantifying the mass flow rates of the ambient dry air and water vapour infiltrating into the cabinet.

In order to trace the individual air and water vapour species from their sources to the RAG, their fractions at the cabinet's air-off section are distinctively named as cabinet-air and cabinet-H_2O, respectively, and the air and water vapour fractions entering the test room are named room-air and room-H_2O, respectively. During the course of setting up the model, the mass fractions (and not the mass flow rates) of the species at each individual boundary inlet must sum up to unity. The total mass flow rate at the evaporator coil air-off section for the cabinet considered is known to be 0.3 kg/s before hand. The dry air and water vapour mass fractions making up this total mass can be determined from the humidity ratio at the air-off thermal conditions (T=-2 ^{o}C and R.H.=90%). Similarly, the test room's humidity ratio, which is obtained at a dry-bulb temperature of 25 ^{o}C and 60% relative humidity can be used to determine the air and water vapour mass fractions at this condition. Table 7.4 lists the mass fractions used in the model. It is important to mention that these mass fractions were obtained from a computer-based psychrometric chart, which is constructed such that the humidity ratio (along with enthalpy and volume) is presented per unit mass of dry air, and not per unit mass of moist air. This benefits from the fact that the quantity of dry air is always constant, and it is the moisture content that explicitly changes.

Table 7.4 Mass fractions of different species at the air-off and test room inlets

	Air-off section	Test room inlet
Dry bulb temperature (^{o}C)	-2	25
Relative humidity (%)	90	60
Humidity ratio (kg_w/kg_{da})	0.0028728	0.0118962
Total mass (kg)	1.0028728	1.0118962
Water vapour mass fraction	0.0028646	0.0117563
Air mass fraction	0.9971354	0.9882437
Total mass fraction	1.0	1.0

Table 7.5 shows the mass flow rates of the different substances entering the air-on section. The infiltration rate into the cabinet can be determined by directly summing the mass flow rates of the ambient dry air and water vapour:

$$\dot{m}_{\inf} = \dot{m}_{room-dryair} + \dot{m}_{room-H_2O} \tag{7.12}$$

which results in a value of 0.093 kg/s. This mass flow rate, when divided by the total mass flow rate of the cabinet (0.3 kg/s), yields the mass fraction of ambient air

infiltrating into the cabinet, and was found to be 31.1%. This percentage is within the range proposed by other researches for cabinets of ordinary display heights (Navaz et al. (2005)). Also from Table 7.5, the humidity ratio (kg_w/kg_{da}) at the air-on section can be determined by dividing the sum of the water vapour mass flow rates by the dry air mass flow rates:

$$w_{air-on} = \frac{\dot{m}_{cab-H_2O} + \dot{m}_{room-H_2O}}{\dot{m}_{cab-dryair} + \dot{m}_{room-dryair}} \tag{7.13}$$

which yields a value of 0.00566 kg_w/kg_{da}.

Table 7.5 Mass flow rates of various substances crossing the air-on section

Substance	Mass flow rate (kg/s)
Cabinet-water vapour	0.0005923
Cabinet-dry air	0.2061461
Test room-water vapour	0.0010964
Test room-dry air	0.0921652
Total	0.3

The cooling load attributed to infiltration can be found by

$$\dot{Q}_{\inf} = \dot{m}_{\inf}[(h_{amb} - h_{air-off}) - (w_{amb} - w_{air-off})h_w] \tag{7.14}$$

where h_w is the enthalpy of water at evaporator coil temperature. This yielded an infiltration cooling load of 4,027 W, which accounts for 89% of the total cooling load of the cabinet.

The method presented here highlights two important points. Firstly, infiltration is not temperature dependent, and takes place even when the cabinet is working under isothermal conditions, i.e. when the refrigeration system is turned off. Secondly, the detrimental effect of infiltration on the cooling load of the cabinet can be directly related to both the amount of infiltrated ambient air and the difference between its temperature and that of the cabinet.

7.4.5 The psychrometric method

In this section, a new graphical approach is introduced where the cooling load due to infiltration as well as conduction and radiation is predicted using a psychrometric chart. Psychrometrics uses the thermodynamic properties of moist air to analyse conditions and processes during the operation of air conditioning systems, and it is

intended to be used here to assess the performance of the open display cabinet. Knowing the air's bulk average thermal conditions at the air-off, air-on, and ambient locations along with the cabinet's total mass flow rate, the various thermal processes that the cabinet air goes through can be laid down on a psychromentric chart, and the cooling load due to infiltration can therefore be determined. The approach can be applied during experiment by measuring the temperatures and relative humidities at the aforementioned locations, or by obtaining them from a CFD simulation. Initially in this work, this procedure was performed manually using a printed ASHRAE psychrometric chart at standard sea level pressure. However, readability was found to be difficult and the precision of laying down and also accurately reading the state points and the energy transfer was deteriorated. Therefore, it was decided to resort to the ASHRAE Psychrometric Analysis software (2002), which is capable of allocating the various state points and calculating the energy transfer of the various processes involved with high accuracy.

To illustrate this approach, the discussion presented here is based on the results obtained from the numerical simulation of the low-front cabinet tested against climate class 3 conditions previously introduced in this chapter. The procedure of determining the infiltration load and percentage from the psychrometric chart is straightforward, and is illustrated through Figure 7.5 and Figure 7.6. First, the air-off (Air-off), air-on (Air-on), and ambient air (Amb) state points are plotted on the psychrometric chart as shown in Figure 7.5.

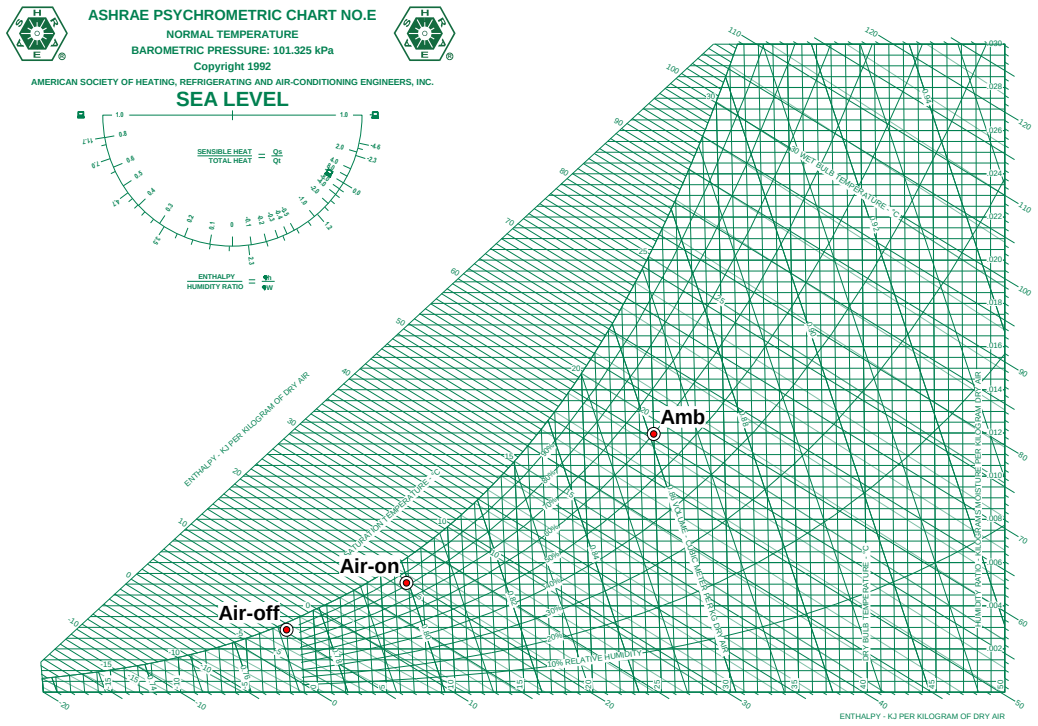

Figure 7.5 Psychrometric chart showing air-off, air-on, and ambient air state points

Then, a continuous line starting from (Amb) and crossing (Air-on) is drawn as shown by the blue line in Figure 7.6. In the hypothetical situation where the cooling load due to infiltration is excluded (e.g., when doors are installed on the display opening of the cabinet), the air leaving the evaporator coil air-off section is mainly affected by the conduction and radiation loads of the cabinet, which are purely sensible. This suggests that a horizontal line can be drawn starting from (Air-off) and extends to the right of the chart representing the sensible heat picked from the walls of the cabinet and also from the products as a result of radiation, as illustrated by the red line in Figure 7.6. The intersection of the blue and red lines, (Cab), is the state point of the cabinet air which is not known before hand. The length of the line from (Air-off) to (Cab) represents the cooling load attributed to the conduction and radiation heat transfers through the cabinet.

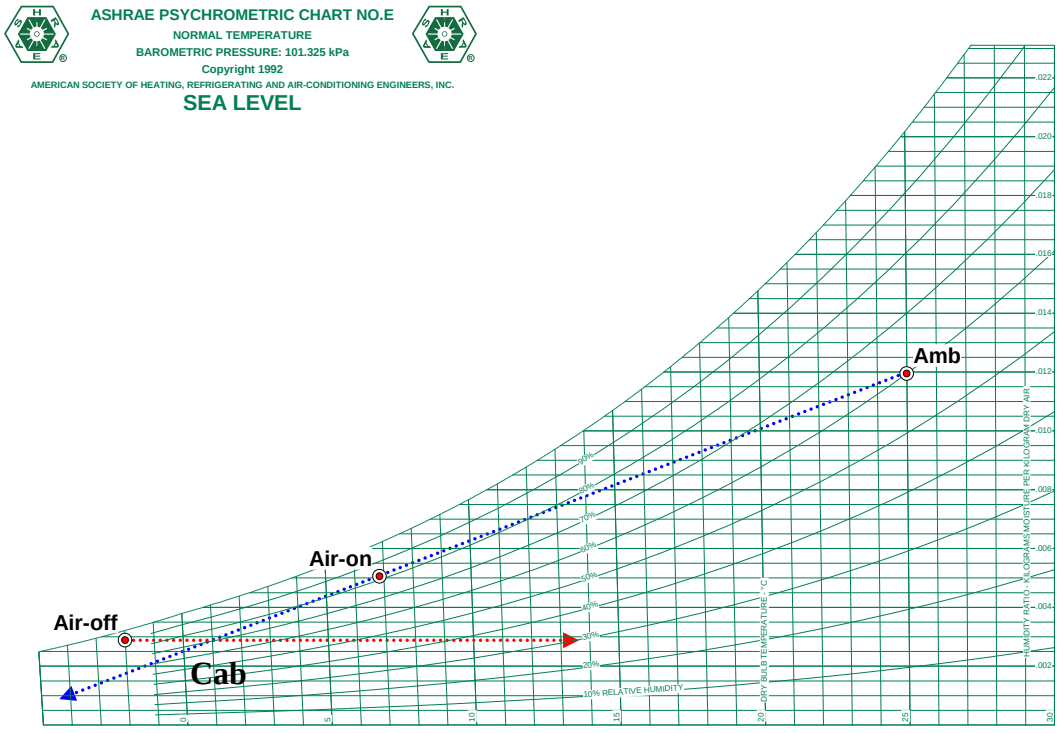

Figure 7.6 Process lines, red representing conduction and radiation, blue representing infiltration

The infiltration load is directly related to point (Air-on), which is a mixture of air from points (Amb) and (Cab). According to the rules of the psychrometric chart, those three state points must lie on a straight line. The location of (Air-on) is such that it divides the straight line joining (Amb) and (Cab) in the inverse ratio of the masses of the two moist air streams, namely $\dot{m}_{Amb}$ and $\dot{m}_{Cab}$.

The process taking place at the display opening (the boundary between the air curtain and the ambient air) is an adiabatic mixing process of different quantities of moist air coming form the cabinet and the test room. Entrainment along the air curtain can be thought of as an adiabatic mixing process between the two moist air streams of the cabinet and the ambient air, forming a uniform mixture entering the evaporator coil. This process is illustrated in Figure 7.6 by line Cab-Air-on-Amb, and is governed by three equations:

$$\dot{m}_{cab}\, h_{cab} + \dot{m}_{amb}\, h_{amb} = \dot{m}_{air-on}\, h_{air-on} \tag{7.15}$$

$$\dot{m}_{cab} + \dot{m}_{amb} = \dot{m}_{air-on} \tag{7.16}$$

$$\dot{m}_{cab}\, w_{cab} + \dot{m}_{amb}\, w_{amb} = \dot{m}_{air-on}\, w_{air-on} \tag{7.17}$$

Eliminating $\dot{m}_{cab}$ gives:

$$\frac{\dot{m}_{amb}}{\dot{m}_{air-on}} = \frac{h_{air-on} - h_{cab}}{h_{amb} - h_{cab}} \tag{7.18}$$

Since the Air-on point must lies on the line that connects state points Cab and Amb, the ratio of the infiltration rate to the total mass flow rate through the cabinet is equal to the ratio of segment Air-on-Cab to segment Cab-Amb, that is:

$$\frac{\dot{m}_{\inf}}{\dot{m}_{tot}} = \frac{L_{Air-on-Cab}}{L_{Cab-Amb}} \tag{7.19}$$

which is analogous to the thermal entrainment factor discussed earlier in this chapter.

The psychrometric chart in Figure 7.7 shows the complete process by showing the different loads of the cabinet and the cooling duty needed from the evaporator coil to meet the refrigeration requirements of the cabinet.

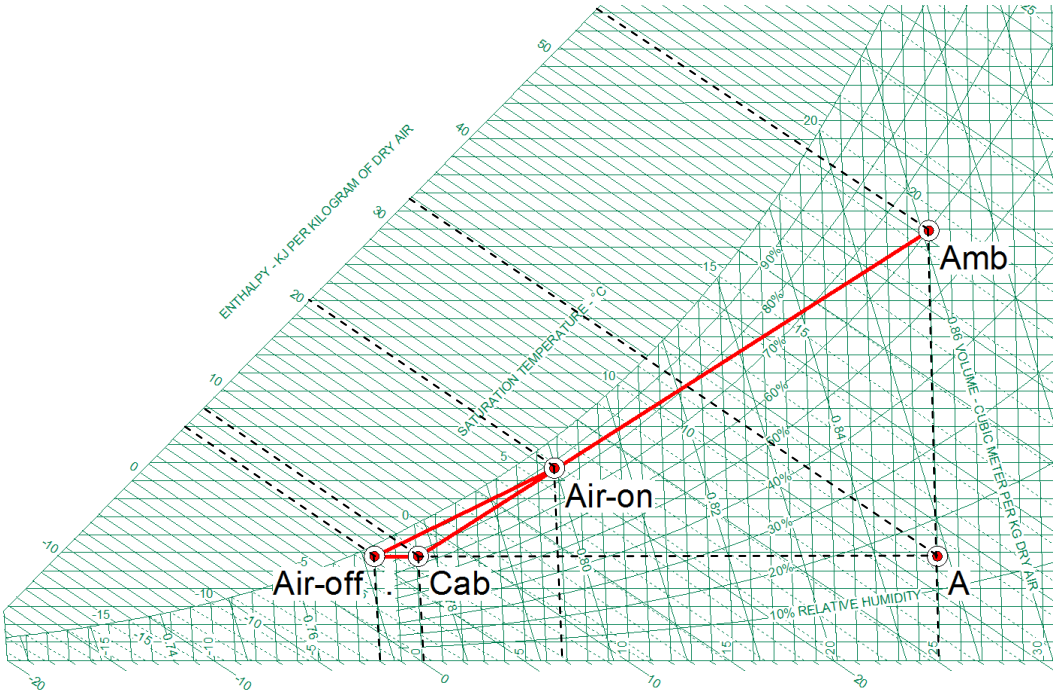

Figure 7.7 Complete process of the cabinet

Three assumptions were made in the analysis. Although in actual practice the air's thermal properties may not be uniform across the DAG and RAG, complete mixing (due to high turbulence levels at the fan section) was assumed, leading to

temperature homogeneity at the air-off and air-on sections. As a result, the air-off and air-on temperatures were assumed not to vary along the length of the cabinet. In addition, it was assumed that the products do not contribute to the latent load due to respiration (weight loss), since in the large majority of cases they are fully sealed from the cabinet (as required by the ISO standard). Finally, it was assumed that the path from the air-off section to the DAG section is air-tight and allows no ambient air infiltration into the cabinet. A good approximation to the cooling load due to conduction from the outer walls of the cabinet is by finding the heat gain to the air from the air-off section to the DAG. Therefore, if the cabinet is not properly insulated, the conductive heat being transferred to the cabinet is reflected on the psychrometric chart by a longer Air-off-Cond segment.

Table 7.6 Air properties at different locations

	T (K)	R.H. (%)	W (kg_w/kg_{da})	h (kJ/kg_{da})
Ambient	25.0	60	0.01195	55.55
Air-off	-2.0	90	0.00289	5.20
DAG	-0.64	80.4	0.00289	6.57
Air-on	6.85	82	.00505	19.59
Cab	0.10	75.7	0.00289	7.32

From Table 7.6 and Figure 7.7, the cabinet's total cooling coil load, $\dot{Q}_{tot}$, is 4,517 W, from which, 2,672 W is sensible and 1,845 W is latent. The load due to infiltration was found to be 3,851.5 W, which is 85.3% of the total cooling load. The sensible and latent shares due to infiltration are 2,430 W and 1,421.5 W, respectively.

The ambient air being infiltrated through the evaporator coil was found to be 25.4% of the total amount, which is about 6% less than the value obtained by the CFD-tracer-gas method (31.1%). More accurate results could have been acquired if the heat rejected from the fans was taken into consideration, which would have added an extra sensible cooling load, $\dot{Q}_{fan}$, at the RAG section. This can experimentally be determined by reading the temperatures before and after the fans. However, it is important to stress that this added accuracy does not change the infiltrated fraction, since the amount of ambient air intruding the cabinet at the RAG is not affected by the heat gained from the fans.

7.5 Summary

Conventional techniques used in the measurement of the infiltration rate into open refrigerated display cabinets have been presented, but they are either indirect, inaccurate, or difficult to implement. Two new approaches have been introduced in this chapter. The first utilises the tracer-gas technique in CFD simulations, with the advantage of being independent of the operation of the cabinet refrigeration system. The second approach utilises psychrometrics in determining the infiltration load together with providing an estimate of the other cooling load components. This approach can be applied during experimentation, and results can be rapidly obtained if the cabinet mass flow rate and the state points at the air-off, air-on, and ambient conditions are known. The results found in this chapter suggest that low-front open refrigerated display cabinets are more affected by cross-flow effects than cabinets of ordinary height, especially those with short lengths. The ambient air entering the RAG was found to be 31.1% of the total mass flow using the CFD-tracer gas method and 25.4% using the psychrometric method. This corresponded to an infiltration load of 89% and 85.3% of the major cooling load components for the aforementioned new methods, respectively. Those results show that the infiltration rate of low-front open display cabinets is relatively high when compared to cabinets of ordinary height.

Low-front cabinets seem to benefit from higher ratios of air curtain-to-perforated back panel flow rate when compared to cabinets of ordinary height. This is due to the need of supplying more air through the DAG in order to form an effective and efficient air curtain that is capable of sealing the entire display height. Moreover, such cabinets suffer more from conduction due to the larger outer surface area, and more infiltration and radiation through the larger display area.

CHAPTER 8
Optimisation of open low-front refrigerated display cabinets

"panta rei"
([given enough time] everything flows)
(Heraclitus, 535 BC-475 BC)

This chapter presents an optimisation study performed on an existing low-front open multi-deck display cabinet. Experimental results show that the cabinet was not able to meet the M1 requirements when tested against climate class 3 of the ISO standard. A steady-state, three-dimensional CFD model was constructed and validated with the experimental data. Then, an optimisation study was performed while focusing on the canopy and DAG sections, and solutions to enhance the performance of the cabinet are proposed.

8.1 Introduction

Achieving and maintaining product temperatures within the preset M1 requirements (-1 ^{o}C$\leq T_{prod} \leq$5 ^{o}C) of the ISO standard when tested against climate class 3 (T=25 ^{o}C, *R.H.*=60 %) is a real challenge for low-front, multi-deck open display cabinets. This new generation of cabinets may be characterised by display openings that are 150 cm or higher, for the purpose of maximising the display-to-floor area ratio so that more products can be displayed for the same floor area in a supermarket. The extended display height increases interaction with the outer environment by entrainment and radiation. This leads to high energy demand and calls for greater levels of flow optimisation to minimise the effect of infiltration on the energy performance of the cabinet.

8.2 Cabinet tested

The cabinet considered is a remote, low-front, open, multi-deck cabinet as shown in Figure 8.1, with the condensing unit (Figure 8.5 (a)) located outside the laboratory.

The 375 cm long cabinet consists of six shelves (including the base), and has a display opening height of 150 cm. The base (lowest shelf) is 33 cm above the floor level, and is equipped with a 6 cm thick upstand to minimise spillage. The 7.5 cm wide DAG is equipped with a 1.5 cm thick honeycomb of 0.6 cm cell diameter. The back panel is perforated by 2 cm× 0.2 cm rectangles vertically spaced by 0.6 cm and repeated in a uniform grid every 4.6 cm across the back panel except for the lower part, which was a solid wall 11 cm high. Details of the honeycomb and the perforated back panel are shown in Figure 8.2. The cabinet defrost method was “off cycle” (air recirculation with refrigeration system off), and therefore no defrost heaters were used. One feature of the cabinet was the shorter depth of the first (top) shelf, which was measured to be 43 cm compared to 53 cm for the other shelves. This leaves only the first shelf to be vertically aligned with the inner edge of the DAG.

Figure 8.1 Low-front open display cabinet

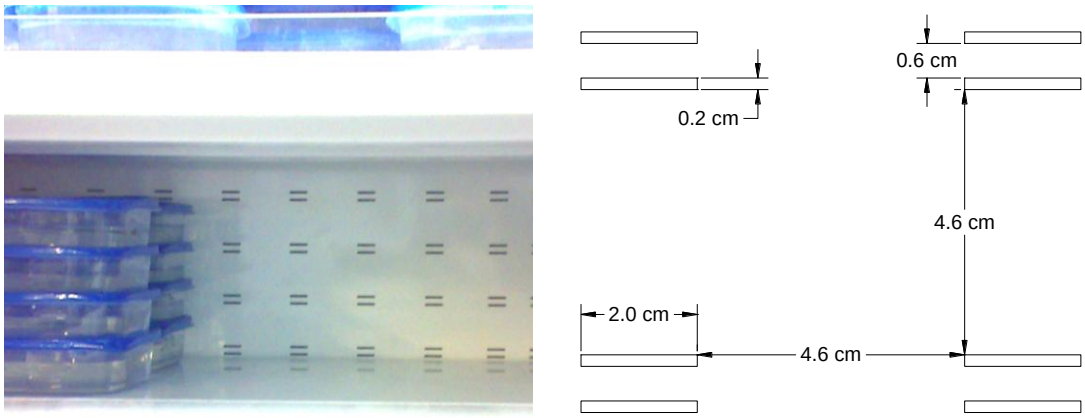

(a) Photograph **(b) Dimensions**

Figure 8.2 Perforated back panel

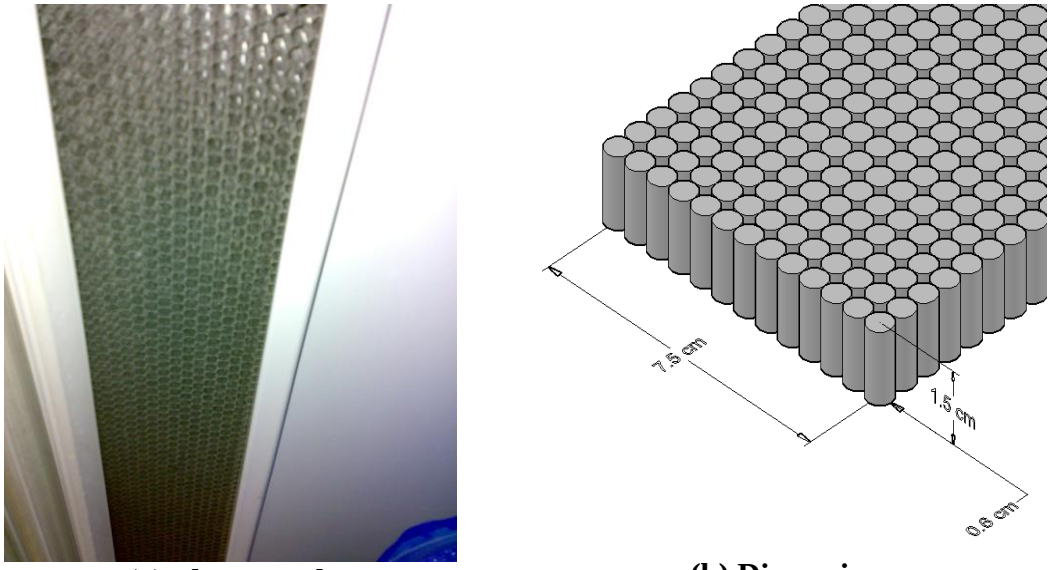

(a) Photograph **(b) Dimensions**

Figure 8.3 Honeycomb

8.3 ISO standard test

The cabinet was tested in the test room in accordance to climate class 3 (T = 25 ^{o}C and R.H. = 60 %) of the ISO standard over a 24-hour period. A cross-flow of 0.2 m/s was measured at three locations near the cabinet leading side wall. The temperature and relative humidity at the prescribed location were measured during the test period as shown in Figure 8.4. The cabinet was loaded with 1278 containers filled with water. At locations where product temperature was measured, M-packages were used with T-type thermocouples, resulting in 12 product measurement points at each of shelves 1, 3, 5, and 6 (a total of 48 thermocouples were used for the M-packs).

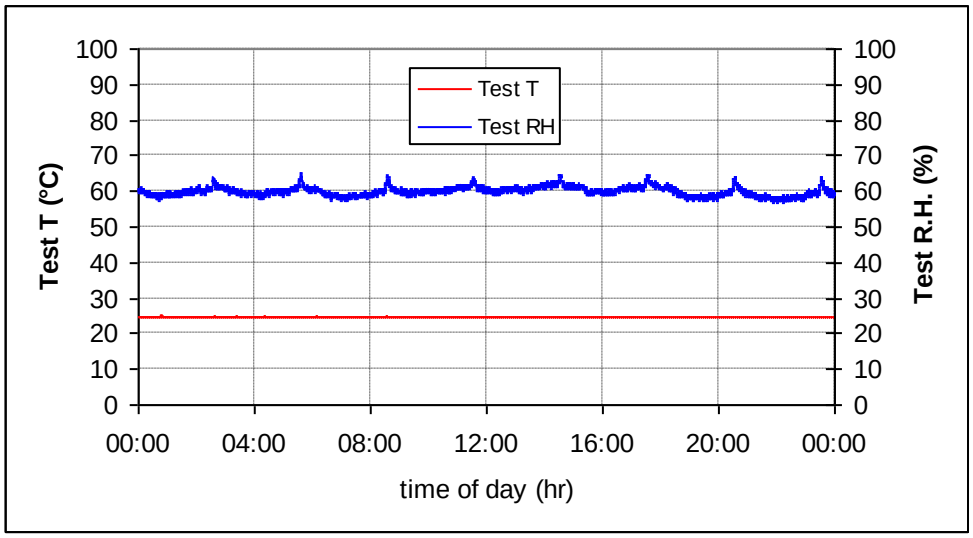

Figure 8.4 Test room temperature and relative humidity

During the tests, the refrigeration system, which was served by Refrigerant R-404A, was closely monitored by mounting thermocouples on the evaporator coil inlet and outlet tubes (Figure 8.5 (b)), a flow meter in the refrigeration cycle (Figure 8.6 (a)), and pressure transducers on the discharge and suction lines (Figure 8.6 (b)). Figure 8.7 shows the refrigerant mass flow rate, discharge and suction pressures, and evaporator coil inlet and outlet temperatures for the 24-hour test period, and the average values are given in Table 8.1.

a) Condensing unit

b) Evaporator coil

Figure 8.5 Cabinet condensing unit and evaporator coil

a) Flow meter **b) Pressure transducers**

Figure 8.6 Flow meter and pressure transducers

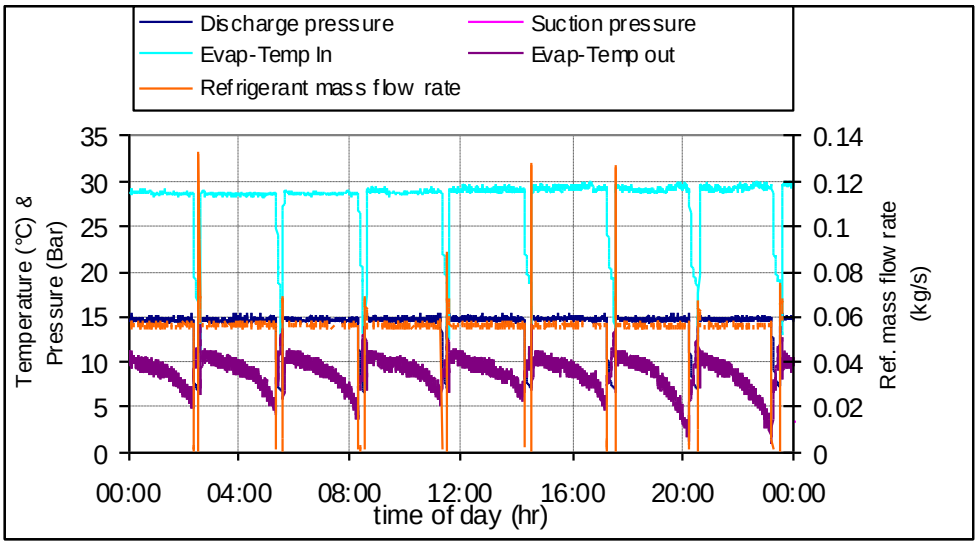

Figure 8.7 Discharge and suction line pressures and temperatures

Table 8.1 Average refrigeration cycle pressures and temperatures

Refrigerant mass flow rate (kg/s)	0.051
Discharge pressure (Bar)	15.07
Suction pressure (Bar)	4.65
Evaporator coil inlet temperature (^{o}C)	27.73
Evaporator coil inlet temperature (^{o}C)	8.87

The evaporator coil saturated suction temperature was measured over a 24-hour period as shown in Figure 8.8. It is clear that the -2 ^{o}C temperature is not sufficient for the operation of the cabinet if the targeted product temperature is to be maintained between -1 and 5 ^{o}C.

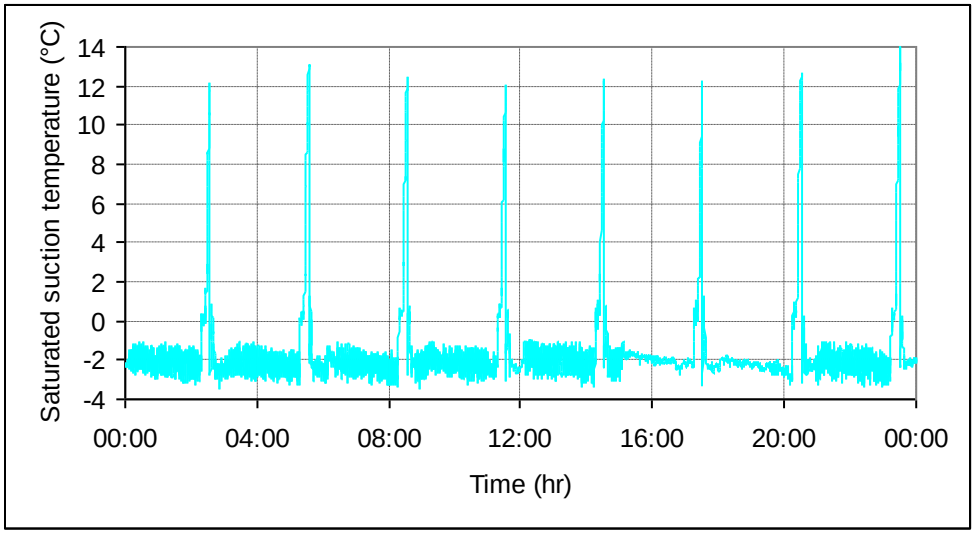

Figure 8.8 Saturated suction temperature over a 24-hour period

The average cooling load over the 24-hour test period was found from the refrigerant side by using a P-h diagram of refrigerant R-404A, and was found to be 7.4 kW as shown in Figure 8.9. In addition, the power consumption of the five evaporator fans and the lighting was monitored during the test. Figure 8.10 shows the power consumption of the fans and the lighting, where the lights were switched off for twelve hours within the 24-hour test period as specified by the ISO standard. The cabinet TEC/TDA was found to be 12.04.

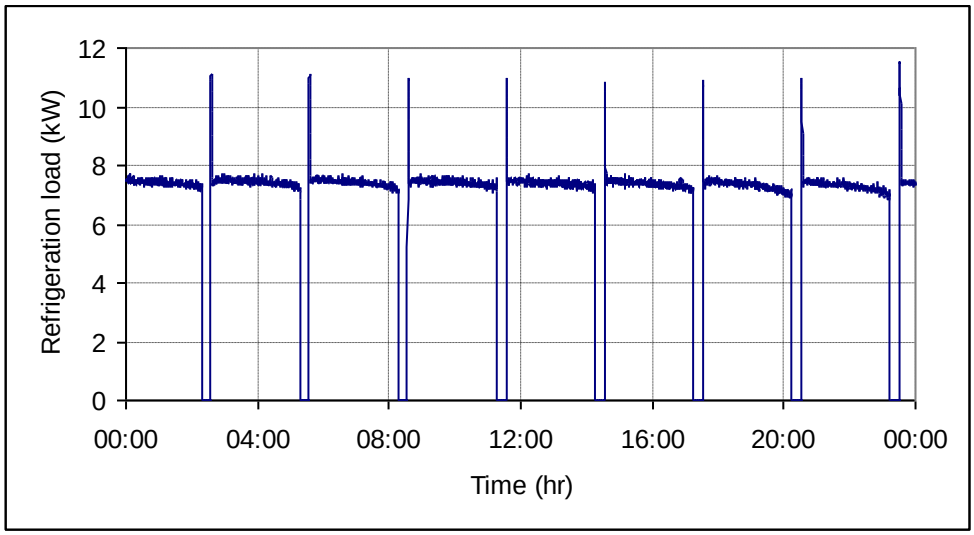

Figure 8.9 Cabinet refrigeration load over the test period

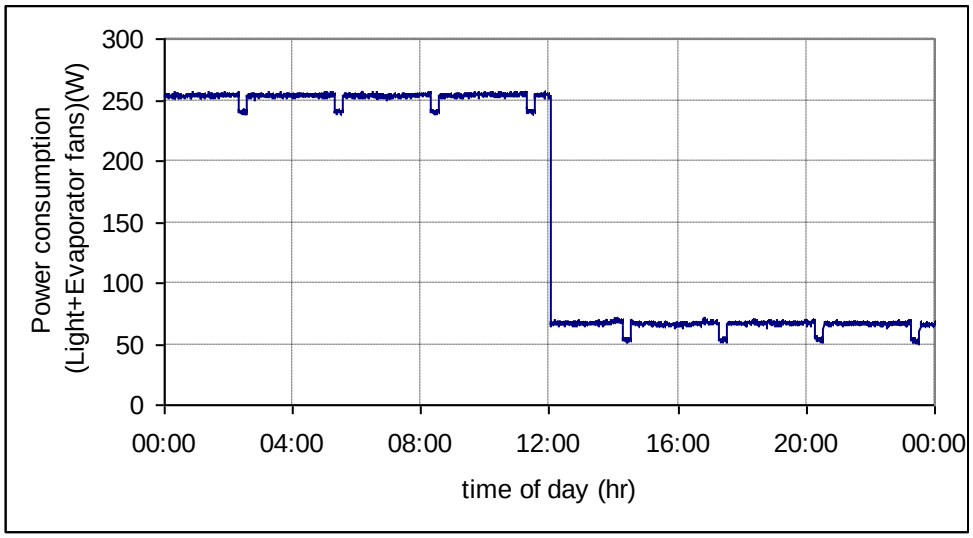

Figure 8.10 Direct energy consumption (DEC) of lighting and fans

The air temperatures at the air-off, air on, and DAG sections were also measured along the cabinet right, middle, and left sections as shown in Figure 8.11, and the average values are given in Table 8.2.

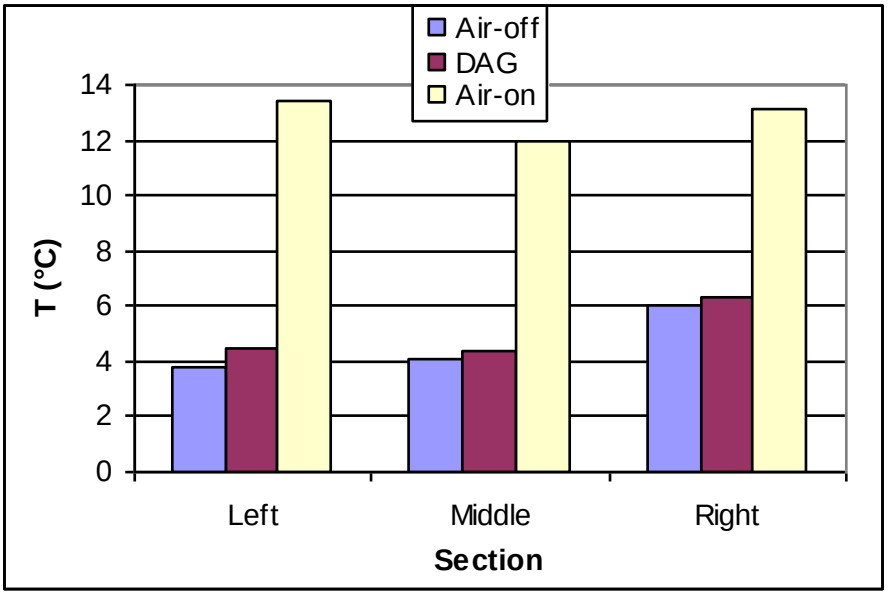

Figure 8.11 Average temperatures at the right, middle, and left of the air-off, DAG, and air-on sections

Table 8.2 Air-off, DAG, and air-on temperatures at three sections and their average

	Left	Middle	Right	Average
Air-off	3.8	4.0	6.0	4.0
DAG	5.4	6.1	6.3	5.0
Air-on	13.4	12.0	13.1	12.0

The cabinet average air mass flow rate was found using a hot wire anemometer for the measurement of the average air velocity at the inlet of the back duct. This yielded an average mass flow rate of 0.81 kg/s. In addition, the relative humidity at the air-off and air-on sections were found to be 93% and 82.2%, respectively.

The infiltration rate was determined using the Psychrometrics method introduced in Chapter 7. Applying the experimentally obtained average values at the aforementioned cabinet locations (Table 8.2), the psychrometric chart representing the cabinet operation is shown in Figure 8.12. The amount of ambient air being infiltrated into the cabinet was found to be 35% of the total mass, which is considered to be on the high side of the acceptable range (from 30% to 35%) proposed by Navaz et al. (2005).

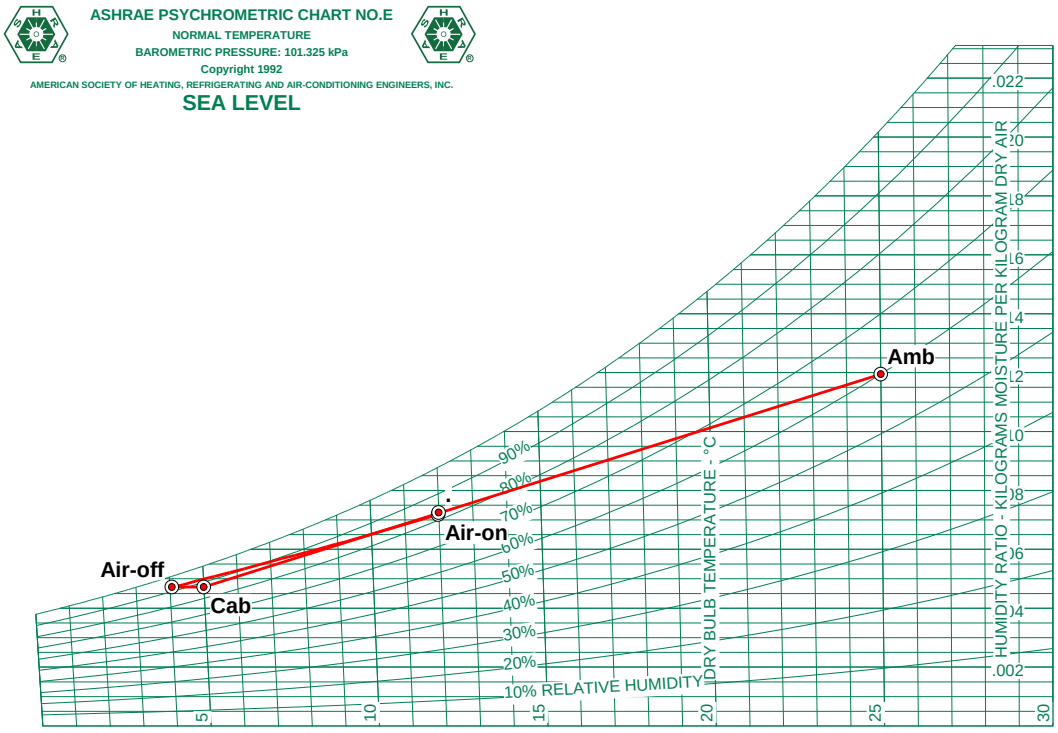

Figure 8.12 Psychrometric chart presenting the cabinet operation

8.4 CFD simulation and validation

A three-dimensional representation of the cabinet and the test room was considered by a model using a total of 1,100,000 structured and unstructured elements, as shown in Figure 8.13 . Within the cabinet, a high quality mesh using 400,000 hexagonal elements was laid to arrive at a fully structured mesh. The size function scheme was used to mesh the rest of the domain by increasing the element size further away from the cabinet by a step size of 20%.

The thermo-fluid conditions measured from experiment (and previously given in section 8.3) at the test room and air-off sections were applied in the model. Since the temperature at the air-off section was experimentally measured at three locations, the model air-off section was subdivided accordingly in order to apply those three temperatures to the CFD model. Within the products, it was assumed that heat conduction is the only mode of heat transfer, and therefore, the M-packs and products were modelled as solids having the thermal properties of lean beef (as specified by the ISO standard) and water, respectively.

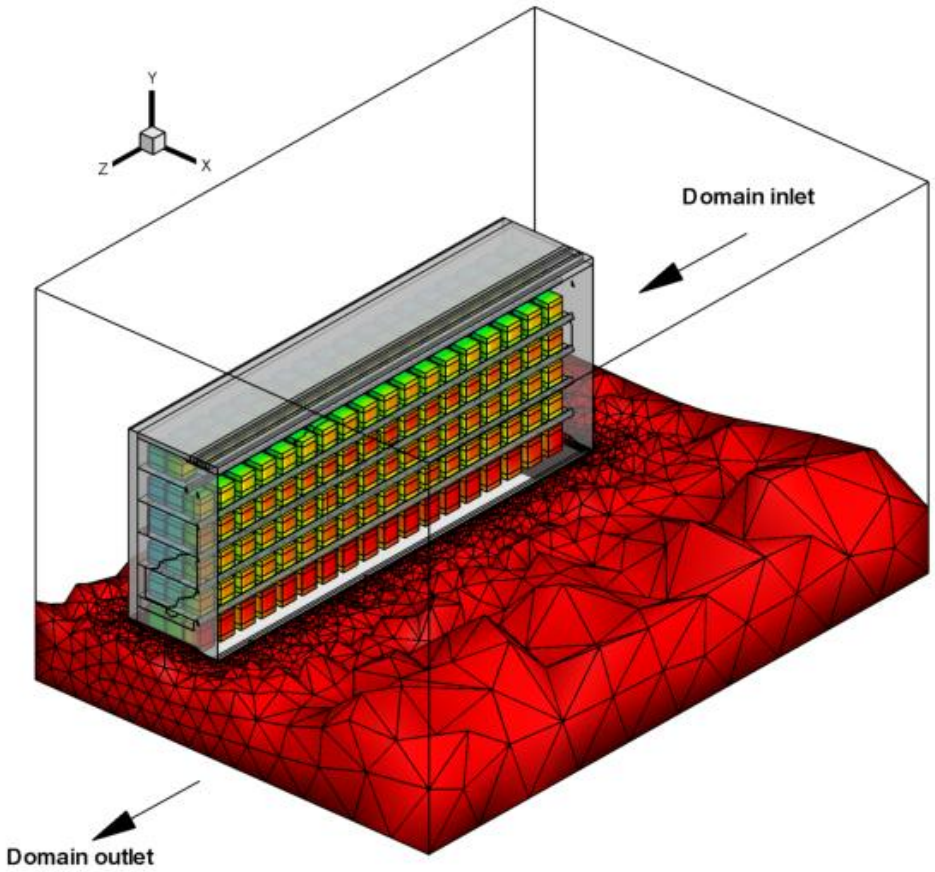

Figure 8.13 Three-dimensional computational domain

8.5 Comparison of product and air temperature distribution

Figure 8.14 shows the product temperatures at the specified M-packs locations obtained from experiment and simulations. The results are generally in good agreement showing a maximum variation of 0.8 ^{o}C except for the M-packs located at the right side of shelf 3. This location seams to suffer the most from the cross flow effect and also the inefficient air curtain, which is diverted away form the cabinet by the blockage of the upper shelf (shelf 2). Therefore, it could be suspected that the steady-state simulation used here could be unsuitable for the representation of the highly random flow at this location. More importantly, however, the temperatures of M-packs P-6RFT and P-6RFB (products at the lowest shelf at the right front of the cabinet), which have the highest temperatures of all the products, are in excellent agreement between the experiment and the simulation. This importance stems from the fact that the ability of the cabinet to perform against the M1 specification is

gauged by the highest product temperature, which is located at the aforementioned locations.

Revisiting Figure 8.14 , almost all the products have temperatures over 6 ^{o}C, with some having temperatures below 5 ^{o}C that are located at the rear part of the shelves. This strongly suggests that the air curtain was not able to deliver cold air to the front products, especially the ones at the lower shelves.

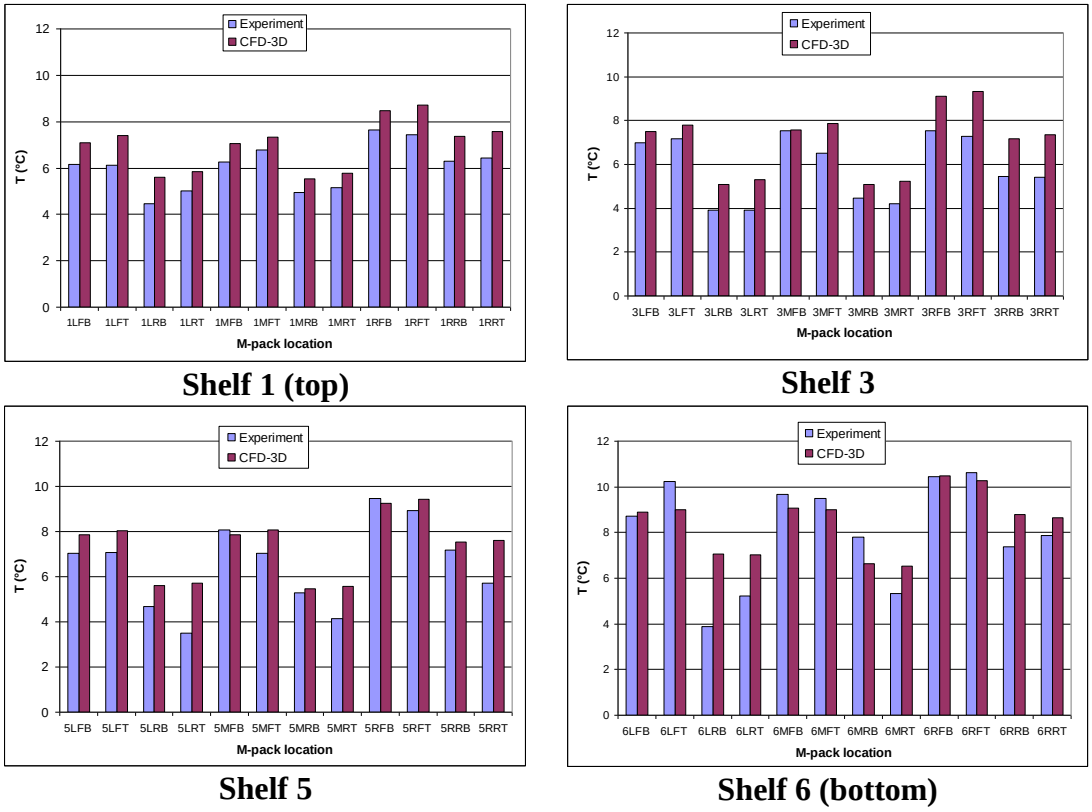

Shelf 1 (top) **Shelf 3**

Shelf 5 **Shelf 6 (bottom)**

Figure 8.14 Comparison of product temperature between experimental and CFD results

Figure 8.15 shows a thermal image taken at the middle cross section of the cabinet. Although the cabinet is not properly cooling, the borderline of the air curtain with the ambient air is clearly shown. An abrupt deflection of the air curtain away from the cabinet is evident in the region of the second shelf, instead of the gradual increase of air curtain thickness usually found in open display cabinets. This suggests that the downward momentum that is expected to seal the whole display height is dissipated by interacting with the second shelf, and an optimisation study is therefore needed.

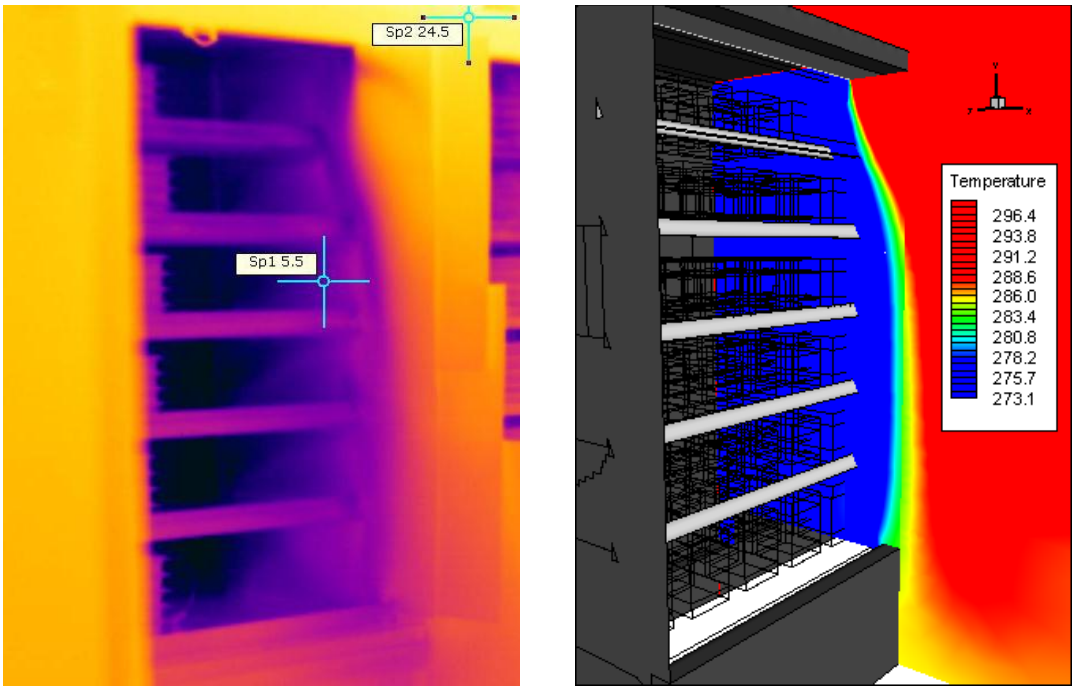

Figure 8.15 IR image at the middle cross section of the cabinet

8.6 Comparison of flow patterns

The PIV technique was used to visualise the flow dynamics across a section 136 cm from the leading side wall. Running the PIV tests at the cabinet middle section (187.5 cm) was not possible due to the restriction in moving the robot carrying the digital camera further down the test room. Figure 8.16 shows the PIV setup in the test room. Eight field views were needed to cover the entire display height and also the near-floor region, each of which having an area of 30×30 cm, as shown in Figure 8.17.

Figure 8.16 PIV experimental setup

By analysing Figure 8.17, it is obvious that the flow tends to divert away from the cabinet immediately after discharge. This is contrary to what has been experienced in previous works on other tested cabinets, where the air curtain deflects towards the cabinet due to the pressure differential between the ambient and cabinet air. After close examination to the honeycomb, it was noticed that the cell (conduit) length to diameter ratio was 2.5 (honeycomb thickness = 1.5 cm, conduit diameter = 0.6 cm), which is lower than the optimum value of 10 suggested by Loehrke & Nagib (1976). This resulted in allowing a portion of the air to eject outwards, offering less guidance to its momentum. Figure 8.17 also shows that the integrity of the air curtain was corrupted by shelf 2, and its flow pattern was not allowed to continue all the way down protecting the lower shelves. The effect of this can be noticed by comparing the product temperatures at shelf 1 and shelf 6, where a difference of more than 3 ^{o}C is experienced.

Figure 8.18 shows the stream-wise (-y) velocity profile taken 5 cm below the honeycomb starting from the inner edge of the DAG and extending 25 cm towards the test room. Excellent agreement can be seen between the PIV and CFD results, especially for the location of the peak velocity. However, the CFD result could not closely represent the upward (positive) flow at the boundary of the air curtain as provided by the PIV result. This dome-shaped positive velocity represents the entrainment process at this location (as referred to in the figure by the red arrow), and the PIV result was more accurate in capturing this phenomenon than the CFD approach. By examining the velocity profile, it is clear that the peak occurred at a distance of 6 cm from the DAG inner edge. The relatively high velocity magnitude of 1.1 m/s is more likely to generate more turbulent kinetic energy at the outer edge of the air curtain. To minimise entrainment through the air curtain, a more efficient velocity profile would be to shift the peak near the cabinet. This finding was discussed in Chapter 6, and will be implemented here in the optimisation study.

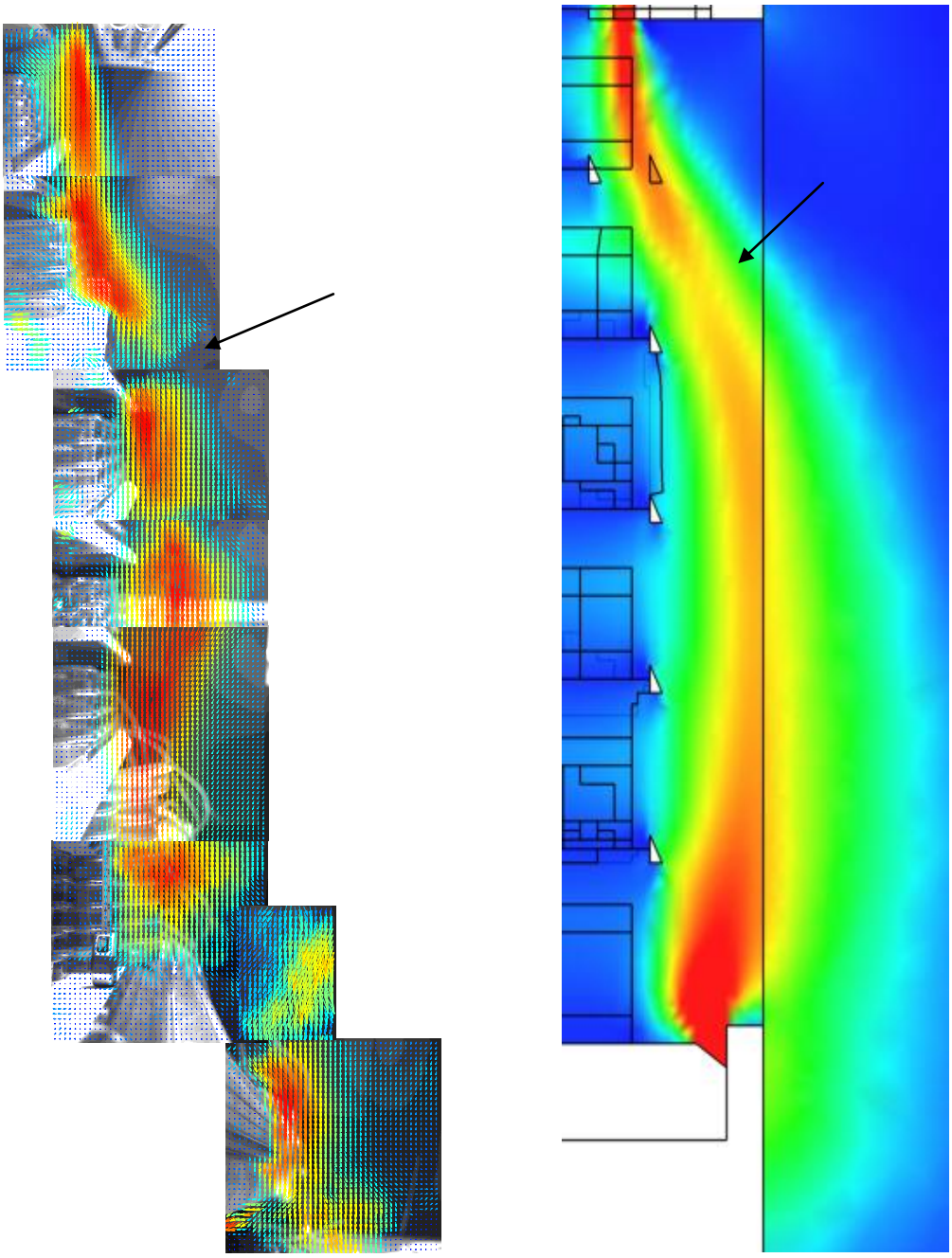

(a) PIV (b) CFD

Figure 8.17 Stream wise (-y) velocity vectors at the cabinet mid-section. The arrows show the breakage of the air curtain near shelf 2

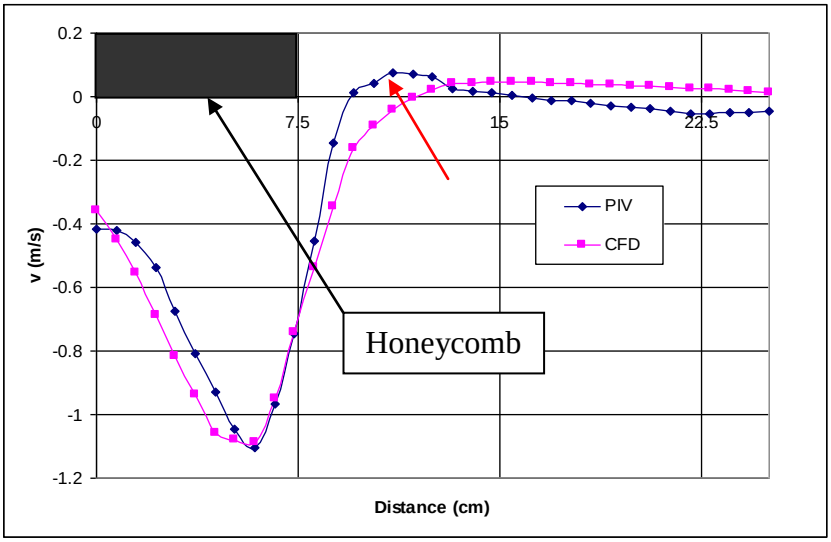

Figure 8.18 Downward (-y) velocity profile 5 cm below the honeycomb

Figure 8.19 is a top view showing an iso-surface of 5 ^{o}C near the cabinet (green) and velocity vectors on a slice at the mid-height of the display opening. A large vortex is predicted at the leading wall, where spillage and therefore infiltration is intense. It is clear from the figure that the cross flow has an effect on the air curtain only at this location, while the rest of the air curtain was kept intact for the majority of the display opening. This observation supports the finding of D'Agaro et al. (2006), who conducted a study on a relatively shorter cabinet having a length of 240 cm, and concluded that cross flow effects have a significant influence only on the performance of short cabinets. Therefore, it can be concluded that a 2D representation of the cabinet would produce satisfactory results for the prediction of power consumption and product temperatures at the mid-section of the cabinet.

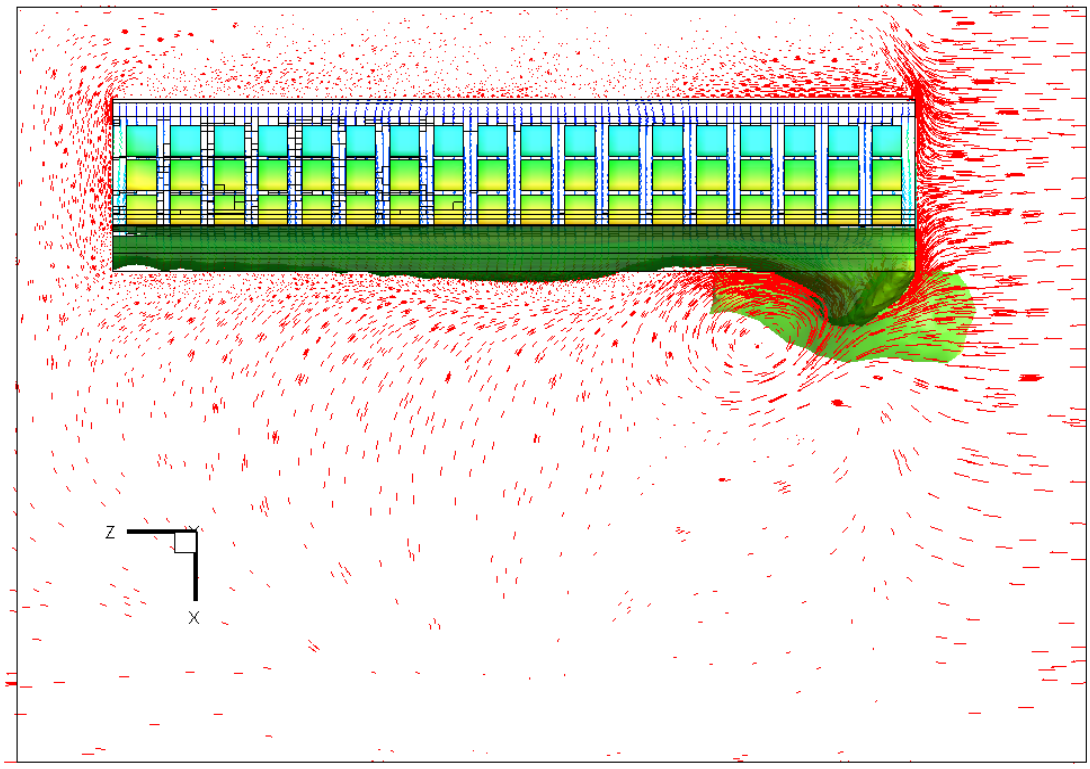

Figure 8.19 Top view showing an iso-surface of 5 ^{o}C (green) and velocity vectors on a slice at the mid-height of the display opening

8.7 Optimisation of the cabinet

8.7.1 Air-off thermal conditions changed to -2 ^{o}C and 93%

The first step towards the optimisation of the cabinet was to set the air-off thermal conditions to the operating conditions normally found in functioning cabinets while maintaining the same air mass flow rate. The entire air-off section was assigned a constant temperature and relative humidity of -2 ^{o}C and 93%, respectively. Figure 8.20 shows the effect of this change on the product temperatures. It is obvious that the product temperatures are all within the ISO standard specification of 5 ^{o}C. This indicates that the cabinet mass flow rate is sufficient, however, the ambient air infiltrating into the cabinet participated in raising the air-off temperature to unacceptable levels. In order to rectify this shortcoming in reality, a larger refrigeration system would be required. This modification, although would satisfy the product temperatures, will increase the energy consumption of the cabinet. In addition, it can be seen that all the M-packs had a temperature higher than -2 ^{o}C, satisfying the lower temperature limit of the ISO standard.

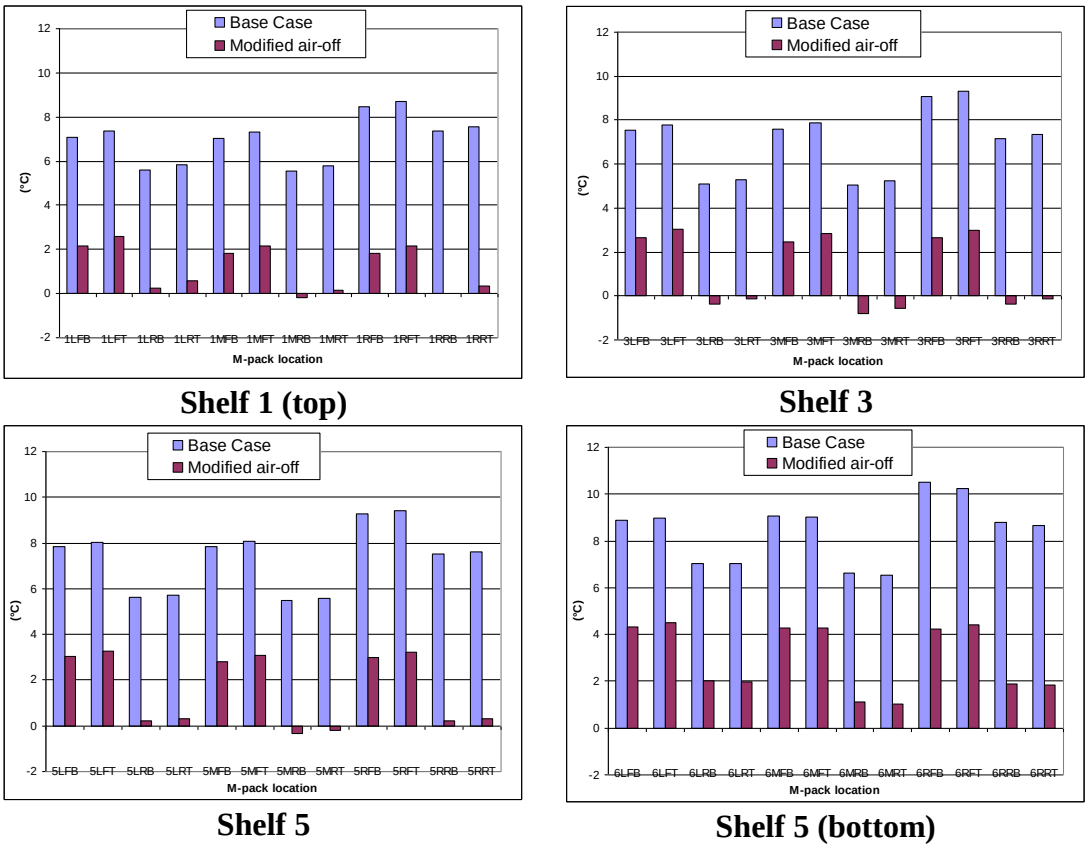

Shelf 1 (top) **Shelf 3**

Shelf 5 **Shelf 5 (bottom)**

Figure 8.20 Comparison of product temperature from CFD predictions for the base case and the modified air-off thermal conditions

8.7.2 Shifting the DAG outwards

As mentioned before, the inner side of the DAG was only aligned with the first (top) shelf, leaving the air curtain to be disrupted at the second shelf, as shown by the velocity vectors in Figure 8.21. Figure 8.22 shows the behaviour of the air curtain in the original and modified configurations through an iso-surface having a downward (-y) velocity magnitude of 0.85 m/s. It is obvious that the air curtain in the original design is completely broken near the second shelf. This deficiency prevents it from providing proper sealing to the products at the right side of the cabinet where the cross flow effect is the highest. However, the cold air being discharged from the perforated back panel and descending from the second shelf onwards participated in creating an air curtain.

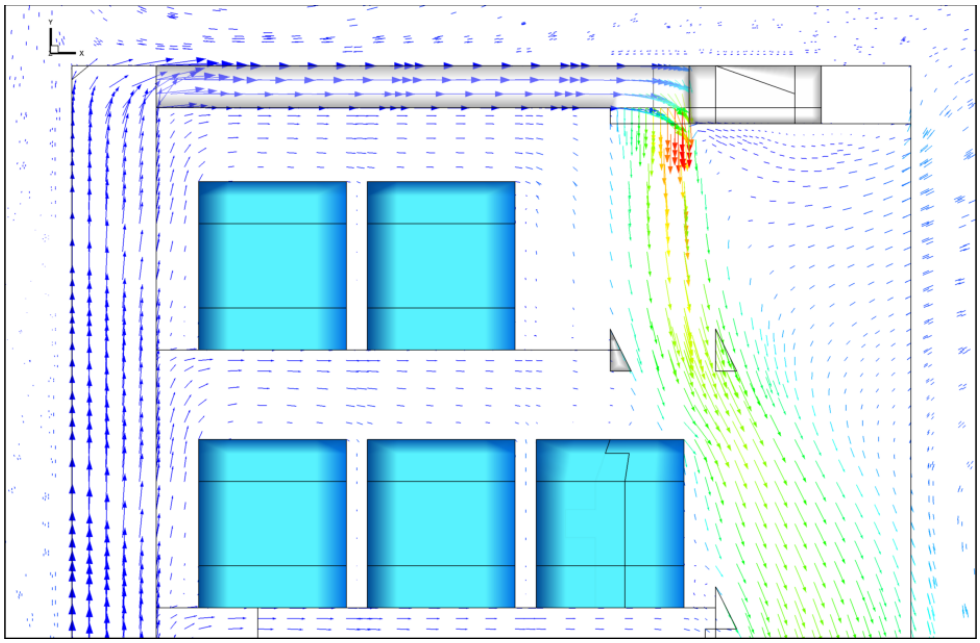

Figure 8.21 Base case having the DAG aligned with the first shelf only

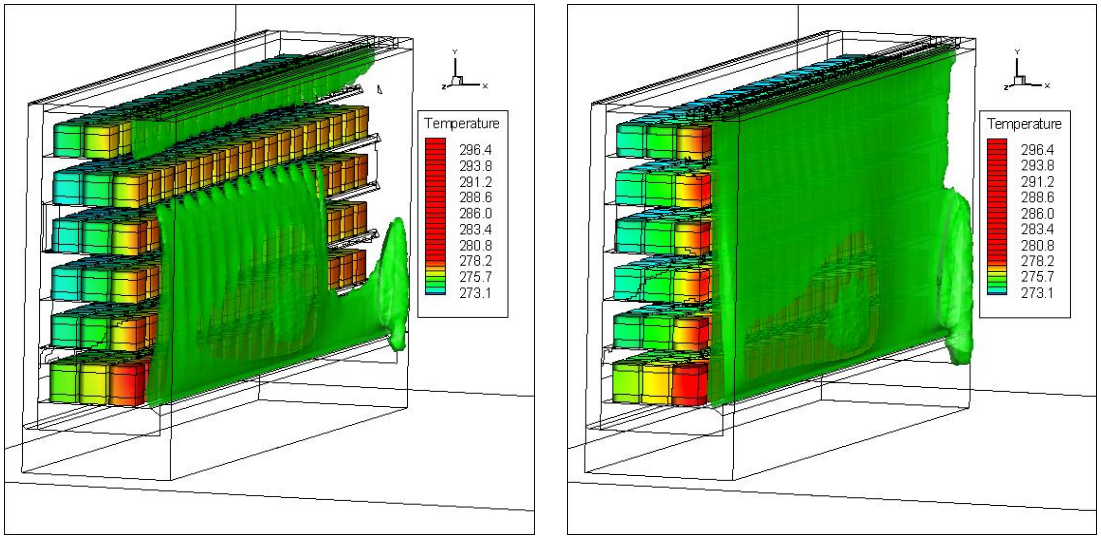

(a) Base-case (top shelf shorter)

(b) DAG shifted outwards (all shelves aligned)

Figure 8.22 Air curtain behaviour at an iso-surface having a downward (-y) velocity magnitude of 0.85 m/s before and after shifting the DAG outwards

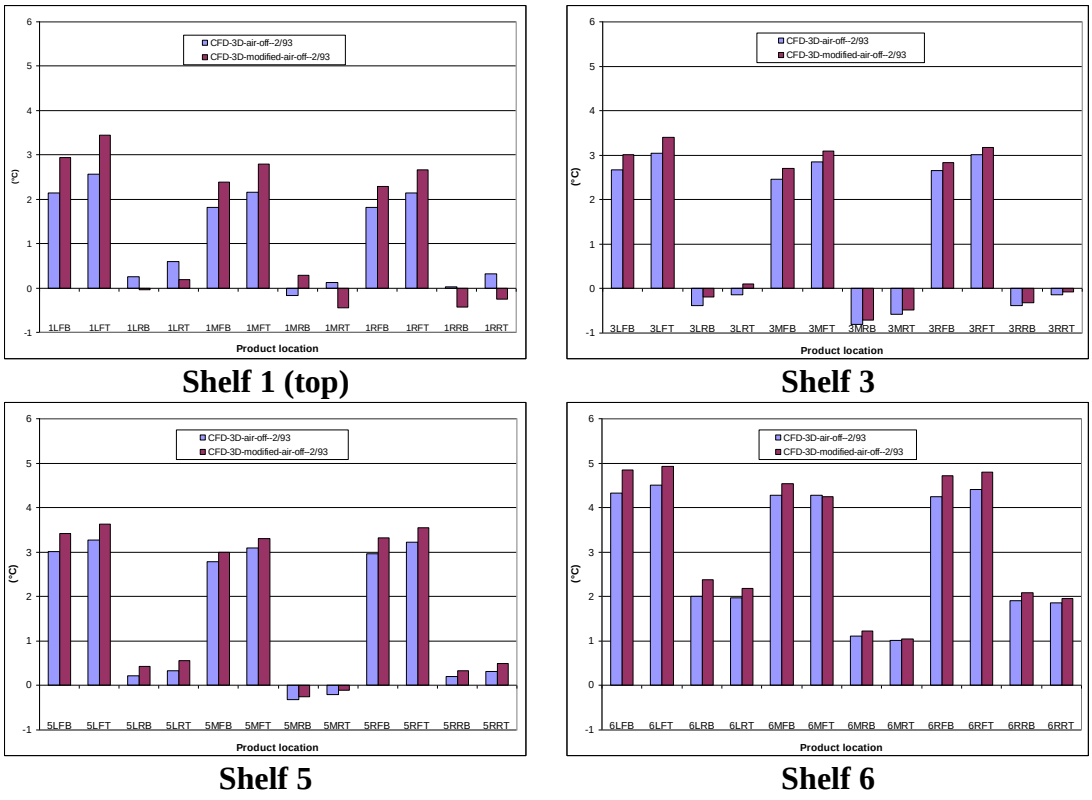

Shelf 1 (top) **Shelf 3**

Shelf 5 **Shelf 6**

Figure 8.23 Comparison of product temperature from CFD predictions before and after shifting the DAG outwards

8.7.3 Enhancing the velocity profile at the DAG

The purpose of utilising two air curtains is to minimise turbulence near the inner air curtain. Therefore, the outer most air curtain acts as a buffer to the inner one by minimising the velocity gradient. In this investigation, the 7.5 cm honeycomb is subdivided into two regions, where the outer one has smaller cross sectional area (and hence higher pressure drop) than the inner one. This way, the peak discharge velocity is shifted towards the cabinet creating an optimum velocity profile at the DAG.

8.8 Summary

This chapter presented an analysis and optimisation study on a dysfunctional open low-front display cabinet. Numerical simulations of the steady-state air flow and heat transfer were performed using a complete three-dimensional model, and the results were found to be in good agreement with experiment. It was found that in its original design, the second shelf onwards obstruct the flow of the air curtain. By simply shifting the DAG outwards (towards the ambient) and increasing the width of the first shelf (so that the DAG inner edge is aligned with all the selves), the path of the air curtain was not restricted, which resulted in the formation of a complete and effective air curtain. To further produce an efficient air curtain, a wider DAG was proposed (going form a DAG of 7.5 cm to 10 cm), with a profile having the peak velocity shifted closer to the cabinet. In addition, the aspect ratio of the existing honeycomb was found to be 2.5, and a thicker honeycomb having an aspect ratio of at least 10 must be used. This will result in straightening and also focusing the air leaving the honeycomb, which allows it to travel further down and seal the whole height of the display area.

CHAPTER 9
CONCLUSIONS, RECOMMENDATIONS, AND FUTURE WORK

"With confidence, you can reach truly amazing heights; without confidence, even the simplest accomplishments are beyond your grasp"

(Jim Loehre)

The previous chapters illustrated the effect of entrainment and infiltration on the performance of open low-front refrigerated display cabinets, and introduced methods to quantify them. This chapter summarises the findings of the whole thesis, and provides suggestions for future work aiming at reducing the energy consumption of such cabinets.

9.1 Thesis overview

This research makes a contribution to the overall effort to reduce the high energy demand associated with open low-front refrigerated display cabinets by improving the performance of their air curtains. This was done by providing a better understanding on the entrainment and infiltration processes through the use of advanced numerical and experimental techniques. The performance of such cabinets is highly dependent on the efficiency of their air curtains. Infiltration of warm ambient air was found to be responsible for the largest share of the cabinet cooling load when tested against ISO standard conditions. In retrospect, any enhancement to the efficiency of the air curtain will also improve the comfort conditions for the staff and customers by minimising the cold air spillage from the cabinets, hence improving the overall energy consumption of the supermarket.

The commercially available CFD software, Ansys Fluent, was used for the pre-processing and solving of 2D and 3D models, while the results were generated using Tecplot, a powerful post-processing software. As for experimentation, PIV was used to map the air flow field of the air curtain, while IR thermography was used to

determine the temperature distribution. All experiments were conducted in a thermally controlled test room where different ISO climate conditions could be created. Being able to merge the numerical and experimental techniques by using the experimentally obtained results as boundary conditions for the numerical approach reinforced the confidence in the simulation results.

Due to the highly complex air flow mechanics at the display opening, the entrainment process was first studied through an idealisation of the display cabinet. A solid vertical wall was numerically and experimentally placed at the outer edge of the shelves to represent a fully packed cabinet. This assumption was considered valid since entrainment is mainly a result of the interaction between the air curtain and the relatively warm ambient air. Ambient air infiltration into the cabinet was proven to constitute the largest share among the major cooling load components, and was successfully quantified by introducing two new methods.

As a final exercise, the numerical and experimental techniques developed were applied on an existing open low-front display cabinet having a display opening height of 150 cm. At first, the cabinet failed to perform in accordance with M-pack class M1 when tested against climate class 3 of the ISO standard. This was mainly due to the design of the shelves, which obstructed the flow of the air curtain and prevented it from sealing the entire height of the display opening.

This work also extended the validation effort of CFD results using data obtained from experiment. CFD modelling was proven to accurately predict the product temperatures, air flow patterns, and cooling loads of open display cabinets, and its accuracy was within engineering limits especially when the boundary conditions are obtained from experiment. The accuracy in this work however was limited by the lack of turbulence intensity at the air-off section and the pressure drop across the perforated back panel. The ability to apply experimental data to fine-tune the boundary conditions of a CFD modelling was of paramount importance in producing quantitative rather than qualitative results.

9.2 Summary of main conclusions

The following are the main conclusions of this work:

1. Open low-front display cabinets have more tendency to suffer from entrainment than cabinets of typical display height. This is due to the increase in the amount of entrained ambient air, which is proportional to the distance travelled by the air curtain. It was found that 31% of the entrained air through the air curtain infiltrates into the cabinet. The percentage of cabinet cooling load attributed to ambient air infiltration is nearly 85%, which is relatively higher than that found in cabinets of ordinary display heights.

2. Entrainment through the air curtain is mainly momentum driven, and is highly sensitive to the airflow characteristics at the Discharge Air Grille (DAG), and less sensitive to buoyancy effects. Among the different discharge parameters examined in this work, the velocity profile was found to have the most profound effect on the entrainment rate. It was found that, for a given mass flow rate, a ramp velocity profile having maximum velocity near the cabinet gives the least entrainment rate. This emphasizes the fact that a high velocity gradient at the air curtain borderline triggers mixing, leading to the enhancement of the entrainment action.

3. For the application of PIV to open display cabinets where the average velocity in the vicinity of the display area is in the order of 1 m/s, an interrogation area of 64x64 pixels having an overlap of 25% was found to offer the best results when the camera was placed about 125 cm away from the laser sheet.

4. Although the IR camera used in this work was calibrated, the emissivity of the screen, which was made of cardboard, was not known beforehand, and a value of 0.85 gave the closest results with the CFD simulation.

5. All variants of the k-ε turbulence model underestimated the air curtain's expansion rate and overestimated the stream-wise peak velocity. The Standard k-ε model however showed the closest results to those obtained by the PIV technique.

6. Cross-flow has a detrimental effect on the performance of low-front open display cabinets. This impact is amplified for cabinets of short span due to the effect of vortices on the flow of the air curtain.

7. The large amount of air emanating from the perforated back panel of low-front cabinets has a significant impact on the functionality of the air curtain. A consistent but insignificant decrease in peak velocity was noticed, although the distance travelled was relatively high. This is due to the contribution of air from the perforated back panel, which tends to augment the momentum along the flow path.

8. The air leaving the evaporator should have the highest permissible temperature and lowest mass flow rate to preserve the integrity of the products. This is to both minimise the refrigeration load and also the entrainment rate through the air curtain.

9. By analysing the air distribution in the low-front cabinets tested in this work, a DAG/PBP ratio of 40/60 produced the lowest infiltration rate since it produces a low-velocity air curtain and also assures full protection of the top shelf.

10. The optimum ratio of the open display height to DAG width was found to be in the range from 15 to 17, according to the two cabinet configurations tested in this work.

9.3 Suggestions for future work

This thesis has covered many alternative parameters related to the design of the DAG, and their effect on the entrainment and infiltration rates of the cabinet. However, other design aspects may be as beneficial to the airflow dynamics around open low-front refrigerated display cabinets, and may further enhance their performance. Research must be conducted to assess the feasibility of using perforated shelves, perforated canopies, and slanted back panels. In addition, the effect of the horizontal offset distance between the DAG and the shelves and the horizontal offset distance between the DAG and the Return Air Grille (RAG) must be studied.

It is logical to design and specify the refrigeration duty of a cabinet for a fully stocked scenario. The air curtain is more stable in this case since having more products tends to support its flow as it travels downward to the RAG. Moreover,

fully stocked shelves allow the air ejecting from the perforated back panel to fill less refrigerated volume, and this air aids in further stabilisation of the air curtain by pushing it away from the shelves. On the contrary, more shelved products may lead to the storage of more heat within the refrigerated zone due to the availability of more thermal mass to store radiation heat. Therefore, a study must be carried out to determine the optimum product loading in the cabinet.

All the numerical work in this thesis has been conducted using steady state simulations. However, the entrainment process is transient in nature and an unsteady state simulation must be conducted to faithfully represent the intrusions and protrusions of ambient air through the air curtain. Achieving this allows for studying the entrainment process through mass transfer rather than mass diffusion.

One of the main issues in this field is the ambiguity in the use of some dimensionless numbers among researchers. The use of the Reynolds number for example as a parameter to gauge the performance of the air curtain was shown to be misleading, especially when the DAG width is used as the characteristic length. Further studies must be commenced to study the performance of open display cabinets on the basis of correct non-dimensional quantities in order to come up with a generalised conception applicable to cabinet design in general.

The use of optimisation tools such as Genetic Algorithms in the study of open display cabinets is important, especially when coupled with CFD. A rich collection of data can be obtained and serve as correlation figures for the design of energy efficient cabinets.

Although the flow of the air curtain is considered to be highly random and turbulent on the microscopic level, some sort of repetitive trend was found during the PIV experiments. It is postulated here that if an intermittent flow is supplied by a small air curtain at the outer side of the main air curtain with the same frequency of those of the initiation of the intrusions, this might negate the triggering of the entrainment (engulfment) into the air curtain. An advanced feature in the new release of the DynamicStudio software is the Dynamic Mode Decomposition, which is a mathematical method that enables the extraction of coherent modes from experimental data, without reliance on governing equations. This feature can thus be

applied to capture temporal (or spatial) linear evolution dynamics of the air curtain, and a pulse of air flow can be applied at the right frequency to reduce the detrimental effect of turbulence and hence entrainment into the air curtain.

References

Adams, P. (1985). Intereffect of supermarket refrigeration and air conditioning. *ASHRAE transactions, Volume 91, Part 1B, Pages 423-433.*

Amin, M., Dabiri, D., and Navaz, H. (2009). Tracer gas technique: A new approach for steady state infiltration rate measurement of open refrigerated display cases. *Journal of Food Engineering, Volume 92, Issue 2, Pages 172-181.*

ANSYS Inc., Gambit v 2.3.16 (2006). User Guide.

ANSYS Inc., Fluent v 6.3.26 (2006). User Guide.

ASHRAE Handbook-Fundamentals (2009). *American Society of Heating, Refrigeration and Air-conditioning Engineers, Inc.*

Austin-Davies, J. (2005). Retail refrigeration? The good, the bad and the ugly. *Food Solutions: Europe.*

Awbi, H. (2003). Ventilation of buildings. *2nd edition. Taylor and Francis.*

Baker, N. (2004). How green is your supermarket? A guide for best practice. *Lib Dem Shadow Environment Secretary. http://greenlibdems.org.uk/resources/sites/217.160.173.25-3f0016a052c515.23380913/Environment%20Team%20Papers/Norman+Baker's+Report+on+Supermarkets.pdf.*

Bhattacharjee, P. and Loth, E. (2004). Simulations of laminar and transitional cold wall jets. *International journal of heat and fluid flow, Volume 25, Issue 1, Pages 32-43.*

Cengel, Y. and Boles, M. (2007). Thermodynamics: An Engineering Approach. *McGraw-hill.*

Chanson, H. (1996). Air bubble entrainment in free-surface turbulent shear flows. *Academic Press, Inc.*

Chui, E. and Raithby, G. (1993). Computation of radiative heat transfer on a non-orthogonal mesh using the finite volume method. *Numerical heat transfer, Volume 23, Part B, Pages 269-288.*

Cortella, G. (2002). CFD-aided retail cabinets design. *Computers and Electronics in Agriculture, Volume 34, Issues 1-3, pages 43-66.*

Cortella, G., Manzan , M. and Comini, G. (2001). CFD simulation of refrigerated display cabinets. *International Journal of Refrigeration, Volume 24, Issue 3, Pages 250-260.*

Costa, J., Oliveira, L., and Silva, M. (2006). Energy savings by aerodynamic sealing with a downward-blowing plane air curtain-A numerical approach. *Energy and Buildings, Volume 38, Issue 10, Pages 1182-1193.*

D'agaro, P., Cortella, G. and Croce, G. (2006). Two- and three-dimensional CFD applied to vertical display cabinets simulation. *International Journal of Refrigeration, Volume 29, Issue 2, Pages 178-190.*

El Moueddeb, K., Barrington, S., and Bathakur, N. (1997). Perforated ventilation ducts: Part 1, A model for air flow distribution. *Journal of Agricultural Engineering Research, Volume 68, Issue 1, Pages 21-27.*

El Moueddeb, K., Barrington, S., and Bathakur, N. (1997). Perforated ventilation ducts: Part 2, Validation of an air distribution model. *Journal of Agricultural Engineering Research, Volume 68, Issue 1, Pages 29-37.*

Enhanced Capital Allowance (ECA) Scheme for Energy Efficient Technologies. Energy Technology Criteria List for Refrigerated Equipment (2009).

Evans, J., Scarcelli, S., and Swain, M. (2007). Temperature and energy performance of refrigerated retail display and commercial catering cabinets under test conditions. *International Journal of Refrigeration, Volume 30, Issue 3, Pages 398-408.*

Faramarzi, R. (1999). Efficient display case refrigeration. *ASHRAE Journal, Volume 41, Issue 11, Pages 46-54.*

Faramarzi, R., Coburn, B. and Sarhadian, R. (2002). Performance and energy impact of installing glass doors on an open vertical deli/dairy display case. *ASHRAE Transactions, Volume 108, Part 1, Pages 673-679.*

Fernandez, J., Elicer-Cortes, J., Valencia, A., Pavageau, M. and Gupta, S. (2007). Comparison of low-cost two-equation turbulence models for prediction flow dynamics in twin-jets devices. *International Communications in Heat and Mass Transfer, Volume 34, Issue 5, Pages 570-578.*

Field, B. and Loth, E. (2004). An air curtain along a wall with high inlet turbulence. *Journal of Fluids Engineering, Transactions of the ASME, Volume 126, Issue 3, Pages 391-398.*

Field, B. and Loth, E. (2006). Entrainment of refrigerated air curtains down a wall. *Experimental Thermal and Fluid Science, Volume 30, Issue 3, Pages 175-184.*

Foster, A, Madge, M, and Evans, J (2005). The use of CFD to improve the performance of a chilled multi-deck retail display cabinet. *International Journal of Refrigeration, Volume 28, Pages 698-705.*

Gaspar, P., Gonçalves, L., and Pitarma, R. (2010). Experimental analysis of the thermal entrainment factor of air curtains in vertical open display cabinets for different ambient air conditions. *Applied Thermal Engineering, Article in press.*

Ge, Y. and Tassou, S. (2001). Simulation of the performance of single jet air curtains for vertical refrigerated display cabinets. *Applied Thermal Engineering, Volume 21, Issue 2, Pages 201-219.*

Gosney, W. and Olama, H. (1975). Heat and enthalpy gains through cold storage room doorways. *Proc Inst Refrig, Volume 72, Pages 31-41.*

Gray, I., Luscombe, P., McLean, L., Sarathy, C., Sheahen, P. and Srinivasan, K. (2008). Improvement of air distribution in refrigerated vertical open front remote supermarket display cases. *International Journal of Refrigeration, Volume 31, Issue 5, Pages 902-910.*

Hadawey, A. (2006). Design of chilled food display cabinets for better temperature integrity and longer product shelf life. *PhD thesis, Brunel University.*

Hadawey, A., Datta, D. and Tassou, S. (2005). Determination of display shelf life of sandwich components. *IIF-IIR, Pages 341-348.*

Hayes, F. and Stoecker, W. (1969, a). Heat transfer characteristics of the air curtain. *ASHRAE Transactions, Volume 75, Part 2, Pages 153-167.*

Hayes, F. and Stoecker, W. (1969, b). Design data for air curtains. *ASHRAE Transactions, Volume 75, Part 2, Pages 168-180.*

Hetsroni, G., Hall, C., and Dhanak, A. (1963). Heat transfer properties of an air curtain. *ASAE Transactions, Volume 6, Issue 4, Pages 328-331.*

Hetsroni, G. and Hall, C. (1964). Further studies of the air curtain. *Quarterly Bulletin Michigan Agricultural Experimental Status, Volume 46, Issue 3, Pages 438-452.*

Hill, J. and Lau, A. (1993). Performance of supermarket air-conditioning systems equipped with heat pipe heat exchangers. *ASHRAE Transactions, Volume 99, part 1, Pages 1315-1330.*

Howell, R. (1993, a). Effects of store relative humidity on refrigerated display case performance. *ASHRAE Transactions, Volume 99, Part 1, Pages 667-678.*

Howell, R. (1993, b). Calculation of humidity effects on energy requirements of refrigerated display cases. *ASHRAE Transactions, Volume 99, Part 1, Pages 679-693.*

Howell, R. and Shibata, M. (1980). Optimum heat transfer through turbulent recirculated plane air curtains. *ASHRAE transactions, Volume 86, Pages 188-200.*

Howell, R., Van, N., and Smith, C. (1976). Heat and moisture transfer through turbulent recirculated plane air curtains. *ASHRAE transactions, Volume 82, Part 2, Pages 191-205.*

ISO 23953-1:2005, Refrigerated display cabinets, Part 1: Vocabulary.

ISO 23953-2:2005, Refrigerated display cabinets, Part 2: Classification, requirements and test conditions.

Issa (1986). Solution of the Implicitly Discretised Fluid Flow Equations by Operator-Splitting. *Journal of computational physics, Volume 62, Pages 40-65.*

James, S. and James, C. (2010). The food cold-chain and climate change. *Food Research International, Volume 43, Issue 7, Pages 1944-1956.*

Johnson, D. (1998). What are some benefits of an air curtain? *AMCA Supplement to ASHRAE Journal, Pages 40-43.*

Kosar, D. and Dumitrescu, O. (2005). Humidity effects on supermarket refrigerated case energy performance: A database review. *ASHRAE Transactions, Volume 111, Part 1, Pages 1051-1060.*

Launder, B. (1989). Second-moment closures: present and future? *International Journal of heat and fluid flow, Volume 10, Pages 282-300.*

Launder, B. and Spalding, D. (1974). The numerical computation of turbulent flows. *Computer methods in Applied Mechanics and Engineering, Volume 3, Pages 269-289.*

Lawton, E. and Howell, R. (1995). Energy savings using air curtains installed in high-traffic doorways. *ASHRAE Transactions, Volume 101, Part 2, Pages 136-143.*

Loerke R. and Nagib H. (1976). "Control of free stream turbulence by means of honeycombs: a balance between suppression and generation". *Journal of Fluids Engineering, Transactions of ASME, Volume 98, Ser I, Issue 3, Pages 342-353.*

Macdonald, N. (1983). Utilization of condenser heat for desiccant dehumidifiers in supermarket applications. *ASHRAE Transactions, Volume 89, Part 2A, Pages 225-235.*

Maidment, G., Missenden, J., James, R., and Tozer, R. (1998). Influence of thermal radiation on weight loss in delicatessen cabinets. *IIF-IIR Commission D2/3, with D1-Cambridge, UK, pp. 226-234.*

Maki, A. and Tassou, S. (2005). Design optimisation and evaluation methodology of vertical multi-deck open display cabinets. *IIF-IIR conference, Pages 55-62.*

Navaz, H., Faramarzi, R., Gharib, M., Dabiri, D. and Modarress, D. (2002). The application of advanced methods in analyzing the performance of the air curtain in a refrigerated display case. *Journal of Fluids Engineering, Transactions of the ASME, Volume 124, Issue 3, Pages 756-764.*

Navaz, H., Amin, M., Dabiri, D. and Faramarzi, R. (2005). Past, present, and future research toward air curtain performance optimization. *ASHRAE Transactions, Volume 111, Part 1, Pages 1083-1088.*

Navaz, H., Henderson, B., Faramarzi, R., Pourmovahed, A. and Taugwalder, F. (2005). Jet entrainment rate in air curtain of open refrigerated display cases. *International Journal of Refrigeration, Volume 28, (2), 267-275.*

Navaz, H., Amin, M., Rasipuram, S. and Faramarzi, R. (2006). Jet entrainment minimization in an air curtain of open refrigerated display case. *International Journal of Numerical Methods for Heat and Fluid Flow, Volume 16, Part 4, Pages 417-430.*

Nesvadba, P., (1985). Radiation heat transfer to products in refrigerated display cabinets. *Proc. International Conference IIF IIR Commissions C2, D3, Pages 323-329.*

Norton, T. and Sun, D. (2006). Computational fluid dynamics (CFD) - an effective and efficient design and analysis tool for the food industry: A review. *Trends in Food Science and Technology, Pages 600-620.*

Orphelin, M. and Marchio, D. (1997). Computer-aided energy use estimation in supermarkets. *Proceedings of the fifth international conference: International Building Performance Simulation Association, Prague.*

Orphelin, M., Marchio, D. and Bech, S. (1997). Significant parameters for energy consumption in frozen area of large supermarkets. *Proceedings of Clima 2000 Conference.*

Pappas, T. and Tassou, S. (2003). Numerical investigations into the performance of doorway vertical air curtains in air-conditioned spaces. *ASHRAE Transactions, Volume 109, Part 1, Pages 273-279.*

Patel, J. (1996). Simulation of honeycomb sections using the porous media model. *Final year project, Brunel University, London.*

Patankar, S. and Spalding, D. (1972). A calculation procedure for heat, mass, and momentum transfer in three-dimensional parabolic flows. *International Journal of Heat and Mass Transfer, Volume 15, Pages 1787-1806.*

Purvis, A. (2004). Loaded! Why supermarkets are getting richer and richer. *http://www.guardian.co.uk/lifeandstyle/2004/jan/25/foodanddrink.shopping3*.

Raffel, M., Willert, C., Wereley, S. and Kompenhans, J. (2007). Particle Image Velocimetry – A practical guide. *Springer, second edition.*

Shah, N. (1979). New method of computation of radiation heat transfer in combustion chambers, *Ph.D. Thesis, Imperial College of Science and Technology, University of London.*

Shih, T.-H., Liou, W. W., Shabbir, A., Yang, Z., and Zhu, J. (1995). A New k-ε Eddy Viscosity Model for High Reynolds Number Turbulent Flows. *Computers and Fluids, Volume 24, Issue 3, Pages 227-238.*

Smale, N., Moureh, J. and Cortella, G. (2006). A review of numerical models of airflow in refrigerated food applications. *International Journal of Refrigeration, Pages 911-930.*

Stribling, D. (1997). Investigation into the design and optimisation of multi-deck refrigerated display cases. *PhD thesis.*

Stribling, D., Tassou, S. and Marriott, D. (1997). A two-dimensional CFD model of a refrigerated display case. *ASHRAE Transactions, Volume 103, Part 1, Pages 88-94.*

Tassou, S. (2006). Potential for Solar Energy in Food Manufacturing, Distribution and Retail, *Report to DEFRA, AC0405.*

Tassou, S., Chaer, I., Sugiartha, N., Ge, Y., and Marriott, D. (2007). Application of tri-generation systems to the food retail industry. *Energy Conversion and Management, Volume 48, Issue 11, Pages 2988-2995.*

Tassou, S. and Datta, D. (1999). Influence of supermarket environmental parameters on the frosting and defrosting of vertical multideck display cabinets. *ASHRAE Transactions, Volume. 105, Part 1, Pages 491-496.*

Tassou, S., Datta, D. and Marriott, D. (2001). Frost formation and defrost control parameters for open multi-deck refrigerated food display cabinets. *Proceedings of the Institution of Mechanical Engineers, Part A: Journal of Power and Energy, Volume 215, Part 2, Pages 213-222.*

Tassou, S. and Xiang, W. (2003). Interactions between the environment and open refrigerated display cabinets in retail food stores - Design approaches to reduce shopper discomfort. *ASHRAE Transactions, Volume 109, Part 1, Pages 299-303.*

The enhanced capital allowance scheme (2004). Refrigerated Display Cabinets.

The international organization for standardization (ISO), standard number ISO 23953-1, 2005. Refrigerated Display Cabinets-Part 1: Vocabulary . *ISO 23953-1.*

The international organization for standardization (ISO), standard number ISO 23953-2, 2005. Refrigerated Display Cabinets-Part 2: Classification, requirements and test conditions. *ISO 23953-2.*

ThermaCAM™ S60 infrared camera operator's manual, Emissivity Tables.

Van, N. and Howell, R. (1976). Influence of initial turbulence intensity on the development of plane air-curtain jets. *ASHRAE Transactions, Volume 82, Part 1, 208-228.*

Versteeg, H. and Malalasekera, W. (2007). An introduction to computational fluid dynamics-the finite volume method. *Second edition.*

Walker, D. and Baxter, V. (2003). Analysis of advanced, low-charge refrigeration systems for supermarkets. *ASHRAE Transactions, Volume 109, Part 1, Pages 285-292.*

Watkins, R., Tassou, S., and Datta, D. (2004). Life cycle analysis of a commercial refrigerated display cabinet. *Third international conference on heat powered cycles.*

Whitehead, E., (1985). Outdoor air treatment for humidity control in supermarkets. *ASHRAE Transactions, Volume 91, Part 1B, Pages 434-440.*

Xiang (2003). Performance Improvement of Multi-deck Display Cabinets and Reduction of Their Impact on the Store Environment. *PhD thesis, Brunel University.*

Yakhot and Orszag (1986). Renormalization Group Analysis of Turbulence. *Journal of Scientific Computing, Volume 1, Number 1, Pages 3-51.*

Yu, K., Ding, G. and Chen, T. (2007). Simulation of air curtains for vertical display cases with a two-fluid model. *Applied Thermal Engineering, Volume 27, Parts 14-15, Pages 2583-2591.*